New methods and applications in time-resolved X-ray absorption spectroscopy

A dissertation in fulfillment of the
requirements for the degree of doctor in the faculty of
mathematics and natural science

submitted to the department of physics
of the
Bergische Universität Wuppertal

by
Dipl.-Phys. Jan Eric Stötzel
from Bochum

Wuppertal
2011

Die Dissertation kann wie folgt zitiert werden:

urn:nbn:de:hbz:468-20120404-113458-5
[http://nbn-resolving.de/urn/resolver.pl?urn=urn%3Anbn%3Ade%3Ahbz%3A468-20120404-113458-5]

Table of Contents

1 Introduction

X-ray absorption spectroscopy (XAS) is a standard tool in material science to analyze the atomic structure of solid, amorphous, liquid or gaseous samples. Thereby it is possible to investigate the local structure around the atoms of a selected element in a range up to several angstroms. Thus, XAS is a complementary structure analysis tool to X-ray diffraction (XRD), which is rather probing the long range order by resolving the lattice structure and to small-angle X-ray scattering (SAXS), which is used for the investigation of inhomogeneities in the order of several nanometers. Prerequisite for XAS is an intense and polychromatic photon radiation as generated at modern synchrotron radiation facilities, where electrons are accelerated to almost the speed of light and stored on a circular path by bending magnets and electron focusing optics. By passing the bending magnets or additional periodic magnet structures the electrons experience an acceleration perpendicular to their flight direction, so that they emit an intense polychromatic photon beam in the actual direction of movement due to relativistic effects. This beam is very intense so that even with the application of a monochromator it can still pass materials with thickness of typically some micrometers. To measure XAS the photon energy is tuned over several hundred electron-volts at a selected absorption edge of an element in the sample. Thereby, it is possible to accurately measure characteristic oscillations appearing above the edge. These so-called extended X-ray absorption fine structure (EXAFS) oscillations are caused by interference effects of the initial quantum state of the generated photoelectron, determined by the selected edge, and the final quantum states of the photoelectron scattered at the potential of neighboring atoms within the material. The EXAFS oscillations reveal the sort of neighboring atoms, their distance to the absorbing atom, and their structural and/or thermal disorder. Furthermore, features close to the absorption edge (XANES) reveal the oxidation states and the electron configurations of the absorbing atoms as well as bonding angles.

A prerequisite for XAS is the X-ray monochromator, which allows tuning the photon energy by Bragg reflection from single crystals. Changing the crystal angle is

conventionally performed step-by-step, which features the disadvantage that mechanical vibrations occur, caused by each change in position. These vibrations have to settle down before the absorption value can be measured. Thus, a typical acquisition time of 20-40 min has to be considered for a single absorption spectrum. The idea of QEXAFS is to continuously move the monochromator crystals and thus to avoid the time-consuming settling times. Thereby, the acquisition time for one spectrum can be reduced to some seconds, when using stepper motors. With dedicated setups for time-resolved measurements it is even possible to decrease the acquisition time to some milliseconds, which enables studying very fast processes. Various monochromator designs for the crystal oscillation mechanics were conceived in the past. One promising approach was the application of piezo-crystals to achieve very fast oscillations. Lately, mechanics based on eccentric discs have proven to yield very fast and also very stable crystal oscillations. Thereby, the energy range of the spectra can be adjusted by interchanging discs with various eccentricities. Today, several QEXAFS monochromators can be found around the world working with such mechanics, which are also relevant for the technical advancements presented within this work.

Acquiring absorption spectra during some milliseconds in a continuous way is a challenging issue for several reasons. Apart from customized monochromator designs, the speed of detectors and the acquisition electronics have to be capable to process the generated data. Moreover, carefully conceived data analysis software is required in order to properly analyze the resulting huge amounts of data. Several experimental approaches towards better performance and more user-friendliness in each of the mentioned fields will be introduced and evaluated within this work. This includes the application of a fast angular encoder system inside the QEXAFS monochromator to monitor the Bragg angle of the crystal during the QEXAFS oscillations. Thereby, the aim is to obtain accurate energy values synchronized with the acquired absorption data. Furthermore, new flexible mechanics will be described which provide the possibility to arbitrarily adjust the energy range of the spectra within seconds and without the need to open the monochromator vacuum vessel. A new stand-alone data acquisition system will be introduced for the synchronized acquisition of the encoder signal and the sampled absorption values. Hardware and software developments of this system aim at high sampling rates, as well as easy access to all experimental settings, e.g. of detectors, monochromator and sample stages. Finally, new QEXAFS data analysis software with the purpose to provide all algorithms required to perform the typical steps of EXAFS data analysis on files with thousands of spectra will be introduced. Additional software filters and tools purposely included for the analysis of time-resolved absorption spectra will be evaluated.

Advanced applications for QEXAFS will also be examined in this work. With QEXAFS it is possible either to drastically reduce acquisition times for absorption spectra of static

samples or to investigate dynamic processes in physics and chemistry. Thereby, chemical reactions and phase transitions can be monitored with sub-second time resolution. Catalysis, sol-gel reactions, electric storage devices, and thermal decompositions cover typical scientific fields that benefit from QEXAFS. Even tomographic pictures were obtained by combining QEXAFS with focusing X-ray lenses in the past. The application of QEXAFS in catalysis has an exceptional importance, as will also be shown by presenting many characteristic examples within this work. Thereby, the Heck reaction catalyzed by Pd/Al_2O_3 catalysts will be investigated, which is an important reaction to achieve C-C couplings required to artificially produce molecules. Furthermore, kinetic oscillations in the conversion of reactants during catalytic partial oxidation of methane on Pd and during the extinction of CO oxidation on Pt will be studied. Such oscillations are promising candidates to gain new insights into the structure-performance relationships of catalysts. Modulated experiments with catalysts allow applying advanced data analysis techniques, such as the modulation excitation spectroscopy and phase-sensitive detection. The benefits of these approaches for QEXAFS will be evaluated by studying a Pt-Rh catalyst under switching reaction gas conditions during catalytic partial oxidation of methane and a Cu catalyst under oxidizing and reducing conditions. The fast thermal decomposition of metal oxalates is another challenging application for QEXAFS that will be discussed for the case of Co oxalate decomposition in various gas atmospheres.

The absorption and dispersion of a material are directly linked to each other, so that the structure of a sample cannot only be determined by measuring the absorbed but also the reflected beam intensity. By changing the experimental geometry of XAS experiments from transmission to reflection mode, investigations of surface structures or layered systems become feasible. Measuring XAS in total reflection under grazing incidence (GIXAS) provides structural information of a volume ranging only few nanometers from the surface into the sample, whereby the exact penetration depth can be adjusted conveniently by the incident angle. Apart from determining the structure of the surface, it is possible to study the thickness of thin single- or multi-layers and the surface roughness at each interface. Time-resolved processes on the surface, for example oxidation of metal surfaces or the absorption and desorption of specific atoms or molecules, can be investigated in situ and time-resolved with a combination of GIXAS and QEXAFS. This is a promising approach, since neither vacuum is required, as e.g. for depth-profiling with X-ray photoelectron spectroscopy (XPS), nor perfectly plane single crystal surfaces, as e.g. for scanning tunneling microscopy (STM). Furthermore, it is also applicable to study surface growth processes in situ by measuring spectra during layer deposition. Several pioneering experiments in the sub-second time regime will be presented to demonstrate the capabilities of this approach. For this purpose QEXAFS spectra in reflection mode will be analyzed during Cu layer deposition via dc magnetron sputtering and during the oxidation of freshly sputtered Cu films at various temperatures.

2 Theory

In the following chapter the theoretical background is summarized, which is a prerequisite to understand the technical advancements and applications presented within this work. Section 2.1 deals with the basics of X-ray absorption spectroscopy, starting with the absorption mechanisms of photons in condensed matter. Thereafter, the occurrence of element specific absorption edges at certain energies is explained within a phenomenological approach based on the rules of quantum mechanics. This approach is also leading to the so-called EXAFS formula that describes the observable oscillations in absorption appearing energetically above the edges. Finally, the experimental setup to measure these oscillations is introduced. In section 2.2 X-ray reflection on rough layered surfaces will be discussed to evaluate the possibilities of measuring EXAFS oscillations in this mode. It will be demonstrated how the approach based on the Fresnel formalism and the distorted-wave Born approximation helps to determine the structure, the thickness and roughness of thin layers on substrates. In the last section of this chapter the specific experimental challenges of time-resolved X-ray absorption spectroscopy will be evaluated. Thereby, the two different experimental approaches of QEXAFS and DEXAFS are introduced, before QEXAFS monochromator mechanics and typical applications for time-resolved EXAFS are discussed.

2.1 X-ray absorption spectroscopy

X-ray absorption spectroscopy (XAS) is a commonly used technique in the discipline of material science to determine the short range atomic order around the atoms of a selected element. With the advent of synchrotron radiation facilities, yielding very bright and brilliant X-ray beams, photon statistics became sufficient to analyze absorption effects

close to absorption edges as function of energy in full detail. The edges appear as soon as the photon energy is high enough to open a new absorption channel, which means that electrons of the next inner shell in the electron configuration of the atom can be excited to the continuum level. These electrons propagate as photoelectron waves and are backscattered at the potentials of neighboring atoms. Interference patterns at the position of the absorber atom are the consequence and yield a varying probability, whether the photon is absorbed or not, as function of photon energy. This is predicted by the transition probability in Fermi's Golden Rule and observable as oscillations in the absorption above the edge. The oscillations yield element specific information of the local atomic arrangement in terms of coordination numbers, bond lengths and angles as well as the valence state of the absorbing atom. Complementary to techniques revealing the long range order in materials, as e.g. X-ray and electron diffraction, XAS benefits from the fact that it can be also applied to systems with only short range order as e.g. small particles, amorphous or liquid materials. Combined with the rather intuitive experimental setup and the straight forward data analysis it is not surprising that XAS has become a standard tool in materials science. In the next subsections the basic principles of XAS will be explained in more detail.

2.1.1 Absorption mechanisms

The attenuation of X-rays passing a material of thickness d in x-direction is described by the law of Lambert-Beer

$$I_1(E) = I_0(E) exp\left[-\int_0^d \mu(E,x)dx\right]. \tag{2.1}$$

The attenuated intensity of the transmitted photon beam $I_1(E)$ and of the incident beam $I_0(E)$ are illustrated in Figure 2.1a. The exponential decrease of intensity is parameterized by an integral along the beam path over the absorption coefficient $\mu(E,x)$ in the most general case. However, in practical XAS applications samples that are homogeneous along the beam path are preferably used. In that case the absorption coefficient is only dependent on the photon energy E, leading to the simplified exponent $-\mu(E)d$ in Eq. (2.1). Henceforth, the absorption coefficient can be obtained in a straight forward way by calculating the logarithm of the quotient of $I_0(E)$ and $I_1(E)$. In addition to the absorption coefficient μ one often finds the mass absorption coefficient in literature, which is simply the absorption coefficient divided by the density of the sample material. Dealing with XAS means to measure and study the absorption coefficient, which is the sum of photon scattering and photoionization effects.

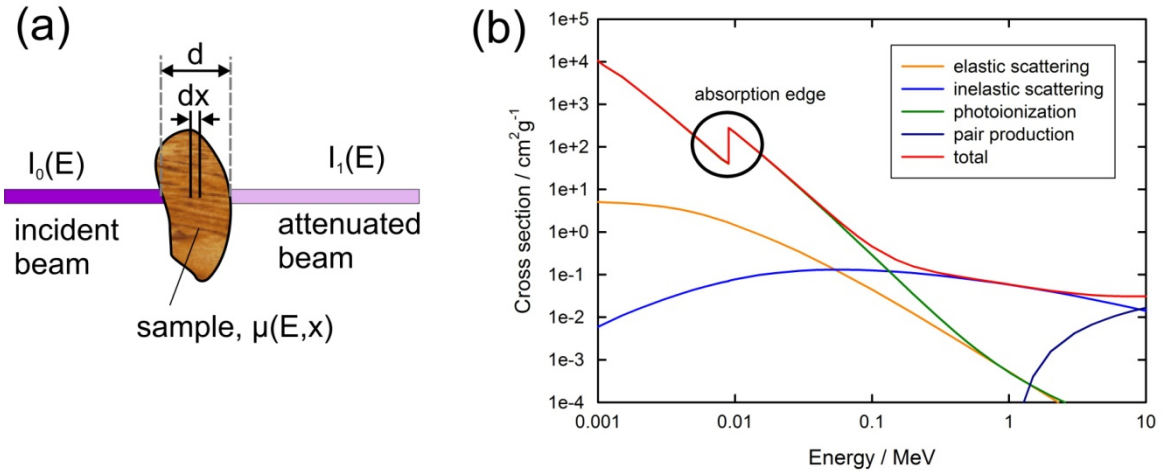

Figure 2.1: (a) Schematics to illustrate X-ray attenuation according to the law of Lambert-Beer and (b) cross sections of the different interactions of photons with solid Cu contributing to the absorption coefficient as function of photon energy (calculated with XCOM [Sal88, Ber11]).

As shown in Figure 2.1b, the total cross section for photon absorption generally consists of elastic scattering (Rayleigh/Thomson), inelastic scattering (Compton), pair production [Fra09c, Jen11] and photoionization. The latter one is the dominant effect in the energy regions of several keV, which is of particular interest for XAS measurements. These energies are well below the critical value of 1.02 MeV required for electron-positron pair production and both scattering effects only contribute to a slowly varying background as function of energy. Moreover, the scattering background turns out to be some magnitudes smaller than the cross section for photoionization. It is thus justified to describe and analyze X-ray absorption spectra mainly with photoionization. Apart from the absorption edges, which will be taken into account within the next section, it turns out that the absorption coefficient is a strictly decreasing function with increasing energy. This function was described in a phenomenological way by Victoreen [Vic48] for a material with density ρ, the atomic mass of the absorbing element A, the corresponding atomic number Z and the element specific parameters C and D as

$$\mu(E) \approx \frac{\rho Z^4}{A}\left(\frac{C}{E^3} - \frac{D}{E^4}\right). \tag{2.2}$$

This formula (especially the strong Z^4 dependency) is important especially with respect to the disciplines of X-ray imaging techniques, where contrast between different elements is decisive. In XAS applications Eq. (2.2) serves as fit function to get rid of the undesired background appearing in the spectra.

2.1.2 Absorption spectra

As soon as the photon energy is high enough to excite a bound electron from the electron shells of the absorbing atom to the continuum level, the absorption probability drastically increases. Thus, so-called X-ray absorption edges appear as function of photon energy. The nomenclature for naming these edges is determined by the initial state of the electron. Accordingly, the edge is called K-edge in those cases, where the most tightly bound electrons from the $n = 1$ shell can be removed, L-edge for the $n = 2$ shell and so forth. Since the $1s$ state is the only possible state for $n = 1$, only one K-edge appears for each element, which is also the edge with the highest energy as in this case the electron closest to the core is removed from the atom. For $n = 2$ three L-shells exist with decreasing energy starting at the $2s$-state (L_1-edge), followed by the $2p_{1/2}$-state (L_2-edge) and finally the $2p_{3/2}$-state (L_3-edge). Consistently, five M-shells appear for $n = 3$. However, for the majority of XAS experiments either the K- or the L-shells are considered which are typically found within a photon energy range between 1 keV and 40 keV for the most elements of interest.

An exemplary spectrum of a Pd metal foil measured at the K-edge is shown in Figure 2.2. The absorption spectrum can be divided roughly into three regions, which are the region of energies below the absorption edge, the edge itself with the X-ray absorption near edge structure (XANES[1]) ranging up to about 50 eV above the edge and the extended X-ray absorption fine structure (EXAFS) [Lyt65] for energies ranging several hundreds of eV above the XANES region. Each of these three regions contains important information, which will be further evaluated within this section. In addition to XANES and EXAFS, the abbreviation XAFS is also found in literature and was introduced by Rehr et al. [Reh86] to serve as general term for the entire fine structure including XANES and EXAFS. After subtracting the fitted and interpolated pre-edge from the whole spectrum $\mu(E)$, the XAFS spectrum is given by

$$\chi(E) = \frac{\mu(E) - \mu_0(E)}{\mu_0(E)} \quad or \quad \chi(E) = \frac{\mu(E) - \mu_0(E)}{\Delta\mu_0}, \tag{2.3}$$

(depending on the further steps in data analysis) with the atom-like background absorption $\mu_0(E)$ and the absolute increase of absorption at the investigated edge $\Delta\mu_0$. This is also illustrated in Figure 2.2.

Pre-edge region

The region located energetically below the absorption edge is called pre-edge region and is affected by the background absorption that mainly depends on the contribution of lower

[1] Also named near edge X-ray absorption fine structure (NEXAFS) in literature.

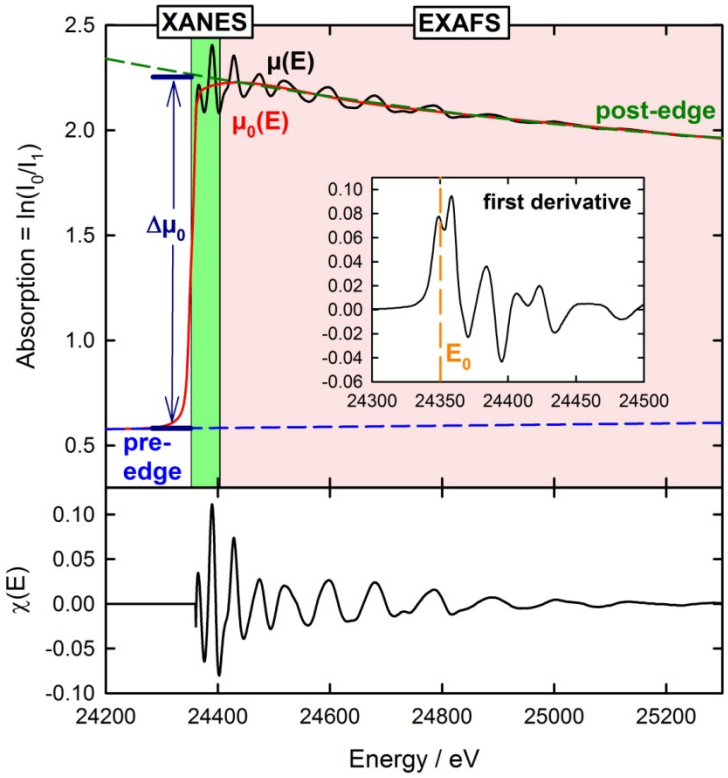

Figure 2.2: Absorption spectrum of a Pd metal foil measured at the K-edge. The inset shows the first derivative close to the edge. The extracted EXAFS as function of photon energy is displayed in the lower graph.

absorption edges and furthermore on the specific experimental setup. Any material located along the beam path between the detectors measuring $I_0(E)$ and $I_1(E)$ comes along with characteristic absorption cross sections contributing to the pre-edge. Such materials can be gases, windows or special materials that act as sample container or support for the investigated material. Fitting the pre-edge and subtracting the fit function from the whole spectrum allows removing all these undesired signals from the absorption spectra, which is a prerequisite before the EXAFS signal can be properly extracted.

Edge position

The edge position yields information about the binding energy of the corresponding electron in its specific orbital within the electron configuration around the atom core. This energy is e.g. affected by the oxidation state of the atom. An oxidized atom has already suffered a loss of electrons, so that more energy is required to further remove a core electron resulting in edges shifted to slightly higher energies. This means that the edge position can be used as indicator to study systems with varying oxidation states. However, the edge position also depends on resonances caused by electron transitions within the potential of the absorbing atom. These transitions significantly depend on the mixing of orbitals due to the characteristic bonding geometry determined by the positions of the neighboring atoms. Thus, conclusions which are based only on the edge position cannot

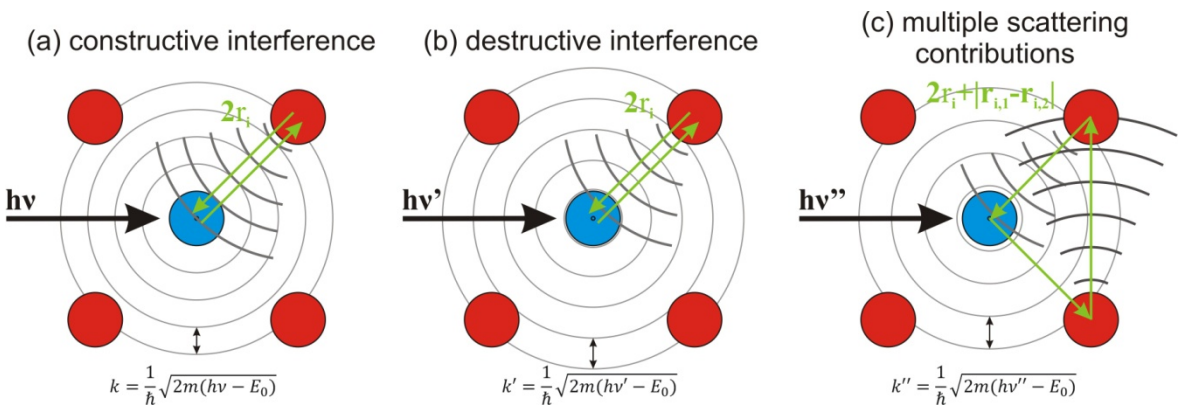

Figure 2.3: Schematics to explain EXAFS: The center atom (blue) absorbs a photon. The freed photoelectron propagates as wave and is scattered at the potential of neighboring atoms (red). Considering single path scattering, (a) constructive and (b) destructive interference of outgoing and scattered waves (depending on wavelength and distance between the atoms) yield maxima and minima in the absorption spectrum. Additional contributions from higher shells and (c) multiple scattering paths have all to be summed up to calculate the final absorption value at each energy.

always be drawn unambiguously. In the region around the edge some features, which correspond to excitations to states below the continuum level, can be typically observed. Some of these features already appear below the absorption edge as it is for example the case for various Cr or Ti compounds, but also in the edge itself as for example observable at the Cu K-edge. Valuable conclusions can be extracted from these features as will exemplarily be shown for Cu within the application part of this work (see section 4.1.4). However, the appearance of such features plainly shows that it is not possible to unambiguously determine the binding energy. This also leads to various ideas of what feature in the edge should be used to fix the binding energy, which contributes to the EXAFS data analysis as the important value E_0. In this work, as far as not stated differently, the edge position is determined by the first inflection point of the edge, as also demonstrated in Figure 2.2.

EXAFS

The absorption process results in both an excited atom with a core hole and a free photoelectron with a kinetic energy given by

$$\frac{p^2}{2m} = h\nu - E_0, \tag{2.4}$$

where p is the momentum and m the mass of the electron, h Planck's constant, ν the X-ray photon frequency and E_0 the binding energy of the initial-state electron. Accordingly, the freed photoelectron propagates as a photoelectron wave with a wavelength λ determined by the de Broglie relation $\lambda = h/p$. As shown schematically in Figure 2.3, this wave is

scattered at the potentials of neighboring atoms and the superposition of the outgoing and all scattered waves at the position of the absorbing atom yields the absolute absorption probability. The absorption probability is proportional to the X-ray absorption coefficient, which is the accessible value in XAS experiments. The total amplitude of the electron wave at the absorbing atom, and thus the overall X-ray absorption, depends on the amplitudes and phases of the backscattered and outgoing photoelectron waves. Since the wavelength and thus the phases vary as function of energy, an interference pattern in the absorption as function of photon energy can be observed. This pattern, which is the already mentioned EXAFS, appears in an energy range from 50 eV to about 1000 eV or more above the absorption edge. Valleys in the EXAFS correspond to destructive interference of outgoing and backscattered photoelectron waves, while peaks correspond to constructive interference. Since the distance of neighboring atoms as well as their element specific backscattering amplitudes and phases contribute to the EXAFS, it is possible *vice versa* to extract this information from the measured spectra.

The theory of EXAFS covering single and multiple scattering paths beyond 20-30 eV above the edge is well understood and summarized in the EXAFS equation [Reh90, Reh92, Zab95]. A heuristic derivation is given in the following paragraphs to explain in which way the lattice structure affects the EXAFS, which is exploited in the various applications presented in this work. For more details about the EXAFS equation excellent review literature is available [Lee81, Teo86, Kon88, Reh00]. Considering a photoelectron propagating from an atom at r_0 as spherical wave with $k = 2\pi/\lambda$, the amplitude of the backscattered wave is proportional to

$$\frac{e^{ik|\vec{r}_i-\vec{r}_0|}}{|\vec{r}_i-\vec{r}_0|}T_i(2k)\frac{e^{ik|\vec{r}_0-\vec{r}_i|}}{|\vec{r}_0-\vec{r}_i|}, \tag{2.5}$$

with the backscattering atom i located at $\vec{r}_i$. The first factor describes the outgoing wave at $\vec{r}_i$, while $T_i(2k)$ is the backscattering amplitude of the atom i and the last factor is the backscattered wave at the absorber atom propagating from $\vec{r}_i$. Setting $\vec{r}_0 = 0$ and $r_i = |\vec{r}_i|$ simplifying (2.5) leads to the expression

$$T_i(2k)\frac{e^{i(2kr_i+\Phi_i(k)-\frac{\pi}{2})}}{r_i^2}. \tag{2.6}$$

Since the electron is not moving in a constant potential, but in the specific potentials of center and backscattering atoms, it turns out that an additional phase shift has to be taken into account which is denoted here with $\Phi_i(k) - \pi/2$ and also included in (2.6). Thus, an expression is found, which describes the modification of the amplitude at the center atom.

The real part of (2.6) is thus proportional to the EXAFS denoted as $\chi_i(k)$ with a constant of proportionality K via

$$\chi_i(k) = K\frac{T_i(2k)}{r_i^2}\sin[2kr_i + \Phi_i(k)]. \tag{2.7}$$

Furthermore, the lifetime of the core hole and the photoelectron have to be taken into account, since they determine the coherence of outgoing and scattered wave at the central atom. The lifetime τ of the core hole is intrinsically limited by the fact that electrons from higher shells will refill the vacant state close to the core, and amounts to $\tau \approx 10^{-15}s$ in a crude approximation [Kes74]. The refilling of the vacant state is accompanied either by an emitted photon (radiative transition) or by an emitted secondary electron (Auger transition). Considering the Heisenberg uncertainty principle, the finite lifetime of the core hole is directly linked to a certain width of the absorption energy level. This is observable as broadening of the spectrum in the order of typically several eV. The lifetime of the photoelectron is extrinsically limited by interaction with or excitation of surrounding electrons as well as collective excitations as e.g. plasmon production. All mentioned lifetime effects are included in the description of EXAFS in a phenomenological way by an additional multiplication with the mean free path expression $exp[-2r_i/\lambda(k)]$. Here, $\lambda(k)$ is the mean free path of the photoelectron as function of k and should not be mixed up with the X-ray or photoelectron wavelength. Nowadays, *ab initio* calculations are used to include the described inelastic losses [Lee77].

It also has to be taken into account that the distance between center and backscattering atom is not really a fixed value. Thermal vibrations of the atoms in a lattice appear for temperatures above 0 K, so that only a mean distance value is preserved between them. Additionally, many absorbing atoms along the beam path are contributing to the EXAFS. Thus, structural disorder has to be considered contributing to a ‘smearing out’ of the mean distance value r_i. Both effects lead to a dephasing which can be included by introducing a Debye-Waller type factor consisting of a Gaussian distribution $N_i exp[-2k^2\sigma_i^2]$. Here σ_i is the root mean square deviation of r_i and N_i the number of atoms (of the same element) with this averaged distance r_i around the absorbing atom. On the one hand, the Debye-Waller factor worsens the situation with respect to the accurate determination of bond lengths and numbers of neighboring atoms. On the other hand it can be exploited to follow the evolution of structural disorder in a sample, which might turn out to be a valuable help to understand certain processes. This will also be demonstrated in the application part of this work (see section 4.1.1). For strongly disordered systems an asymmetric distribution of the distance values has to be considered (see e.g. [Yev10]), which can be technically accomplished by adding higher orders of the mean square deviation to the Debye-Waller factor cumulant expression [Zab95].

The importance to include many-body effects in the description of EXAFS is already evident from the discussion of the photoelectron lifetime, which depends on interactions with other electrons in the material. In addition to these effects, it has to be considered that with each "active" photoelectron many "passive" electrons remain in the absorber atom. With the final state of the photoelectron the passive electrons experience a new core potential approximately of the same dimension as it would be the case in an atom with one more proton in the core. Furthermore, the photoelectron may lift a passive electron to a higher vacant state inside the atom ("shake-up process") or even induce the emission of a passive electron ("shake-off process"). The product of the initial and final states of the passive electrons is then below one, since these are normalized states which only yield one if initial and final states are exactly the same. The resulting reduction factor is typically denoted with S_0^2 and is more or less only dependent on the central atom which makes it possible to determine it for each element with standard reference samples. The S_0^2 value typically amounts to about 0.6 - 0.9 [Kon88].

Finally, all factors are put together and yield one expression, the so-called EXAFS equation. By summing up single path scattering paths at the K-edge it can be written as

$$\chi(k) = \sum_i S_0^2 N_i \frac{|f_i(k)|}{k r_i^2} e^{-2r_i/\lambda(k)} e^{-2\sigma_i^2 k^2} \sin(2kr_i + \Phi_i(k)), \tag{2.8}$$

where $\Phi_i(k) = 2\delta(k) + \phi_i(k)$ contains twice the phase shift $\delta(k)$ the photoelectron experiences by leaving and entering the potential of the central atom and once the phase shift $\phi_i(k)$ due to the backscattering at a neighbor atom. The EXAFS equation was first formulated in a closely related form by Sayers et al. [Say71], who were also the first to show that a Fourier transformation of this equation yields a radial distribution function (after phase correction) with peaks corresponding to the next neighboring atoms.

To derive Eq. (2.8) in a more formal way, one possibility is to deal with the incoming photons as perturbation of the Hamiltonian for the electrons inside the absorbing atom. By assigning an electric field polarization $\vec{E}$ in z-direction to the photons, this perturbation can be included with the term $eE_0 z \cos \omega t$ with the angular frequency of the photons ω. The transition rate of the photoelectron from the initial state $\langle i|$ to its final state $|f\rangle$, which is proportional to the absorption coefficient, is then given by Fermi´s Golden Rule:

$$\mu(E) \propto \sum_f |\langle i|E_0 z|f\rangle|^2 \, \delta\big(E_i - E_f - \hbar\omega\big). \tag{2.9}$$

The dipole values E_0 and z of the photons are included here, as well as the energy dispersive density of the final states, which is given by the δ-function in this case, where

$E_f = E_i + \hbar\omega$ is the energy of the final and E_i of the initial state. The dipole matrix elements in Eq. (2.9) will only be non-zero if the core state is non-zero, which means at the center of the absorbing atom. Since $z = r\cos(\theta)$ and the initial state is a s-state in the case of K-shells, the final state has to be a p-state in that case. To further evaluate the final state, and thus derive the EXAFS equation, a muffin-tin approximation can be applied for the potential of the atoms. This potential is spherically symmetric around the atoms and exhibits a constant value outside these spheres. Basically, these are all requirements to derive the EXAFS equation. The inclusion of lifetime and disorder effect is quite laborious and can be followed e.g. in [Kon88, Reh00]. In the end, all calculations lead to the expression already formulated in Eq. (2.8). The fact that Eq. (2.8) is also valid for the $L_{2,3}$-edges is not obvious, since for these shells ($l = 1$) two different final states have to be considered with s- and d-character. However, the transition to the s-state turns out to be negligible compared to the d-state transition [Szm78, Kon00], so that it is still a reasonable approach to calculate the EXAFS with a single phase shift as presented in Eq. (2.8).

To use the EXAFS equation for data analysis it is essential to know the specific backscattering amplitudes $f_i(k)$ and phase shifts $\phi_i(k)$ defined by the investigated sample geometry. These can be calculated *ab initio* with software tools such as FEFF [Reh92, Reh00]. Today, such tools are very accurate, since they also consider multiple scattering paths and curved electron waves. Taking multiple scattering into account is of particular importance for linearly arranged atoms, where the multiple scattering paths yield a significant amount to the overall backscattering amplitudes. It was shown that Eq. (2.8) can be generalized to include contributions of multiple scattering paths with an effective path length $2r_i$, so that Eq. (2.8) is still valid for EXAFS analysis [Reh90]. Curved waves have to be considered, since the atoms are not point-like and especially for low distances and high wavelengths it is an inaccurate approach to use calculations based on a plane wave front. This refinement can also be included in the EXAFS equation, although it was originally derived with a plane wave approximation. This is attributed to the fact that only the backscattering amplitudes and phases are affected by the curved wave theory [Reh86, Reh90]. Considering all this theoretical advancements, *ab initio* calculations of EXAFS become very accurate and can be refined by fitting these calculations to measured data. Thereby, bond lengths can be determined with uncertainties of a few hundredths of Angstrom and coordination numbers with uncertainties of about 10-30 % [Reh91] or even 5 % [LiG95].

Before the measured X-ray absorption spectra can be analyzed with the calculated amplitudes and phases of a suggested structure model, it is required to extract and transform the EXAFS oscillations. The $\chi(E)$ can be extracted after fitting and subtracting the background absorption and using a spline function as demonstrated in Figure 2.2 and Eq. (2.3). Thereafter, the $\chi(E)$ has to be transformed to k-space via

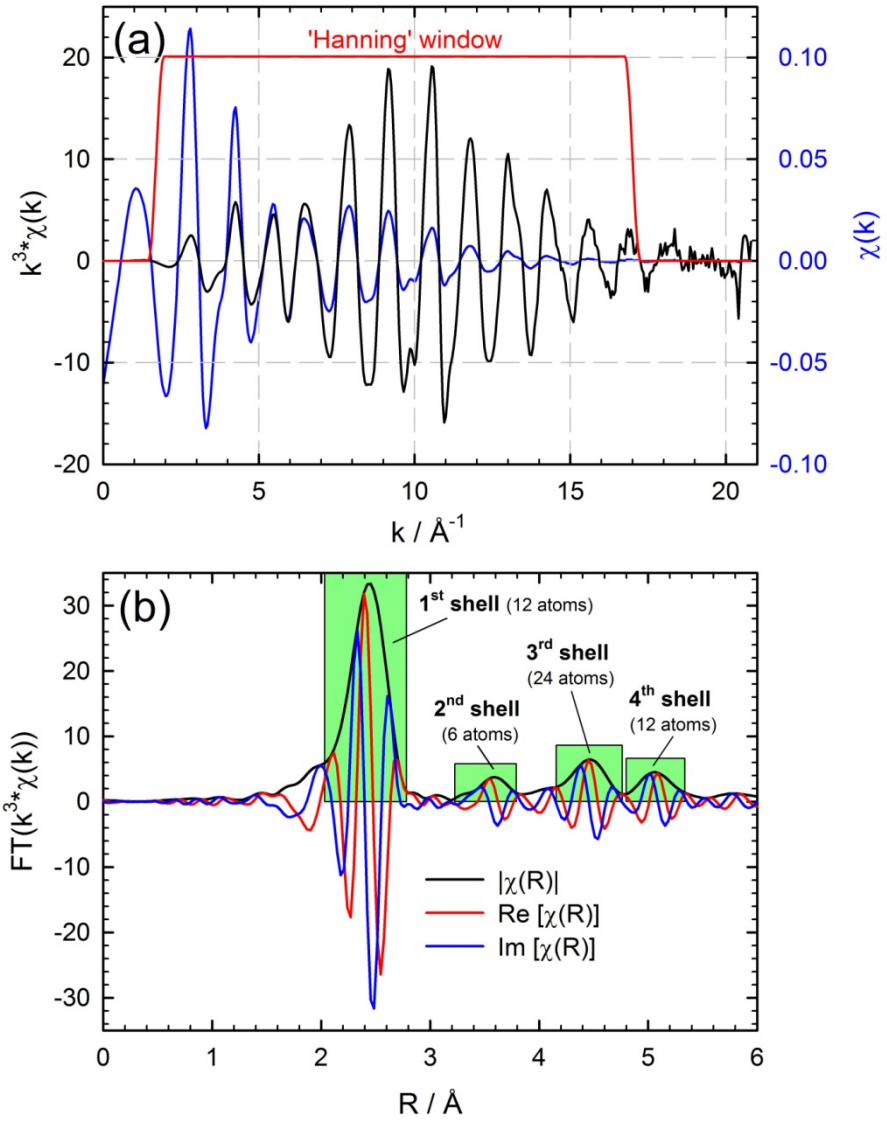

Figure 2.4: Typical EXAFS data processing applied to an X-ray absorption spectrum of pure Pd metal measured at the K-edge: (a) EXAFS oscillations transformed to k-space without k-weighting (blue) and with k^3-weighting (black), (b) Fourier transformation of the $k^3\chi(k)$ spectrum using the window as shown in (a).

$$k = \frac{1}{\hbar}\sqrt{2m(E - E_0)}, \tag{2.10}$$

with E_0 e.g. selected as inflection point in the edge, as discussed earlier. Since the oscillations fade out at higher k-values it is often useful to weight $\chi(k)$ with k^x, where x is typically picked out of 1, 2 or 3. A reasonable weighting yields more or less constant amplitudes of the EXAFS oscillations, so that all features are equally taken into account by the performed EXAFS fits. This is demonstrated in Figure 2.4a, where the absorption spectrum of metallic Pd at the K-edge, which was already presented in Figure 2.2, was further processed without k-weighting and with k^3-weighting. The application of different k-weightings on the same data set can also be used to distinguish between heavy and light

backscattering atoms. The backscattering amplitude of light atoms drops quickly with increasing energy, so that the contributions of lighter atoms are much less enhanced by a high k^3-weighting compared to the contributions of heavier atoms [Kon88].

Since the EXAFS function is a superposition of sine terms, it is useful to calculate the Fourier transformation of the EXAFS. This yields a radial distribution function in R-space making the interpretation of EXAFS much easier. The Fourier transformation is typically performed with the equation

$$FT(R) = \frac{1}{\sqrt{2\pi}} \int_{-\infty}^{\infty} k^x h(k) \chi(k) e^{i2kR} dk. \tag{2.11}$$

The additional window function $h(k)$ can be used to adjust the borders for the Fourier transformation, since e.g. the higher k-regions are often affected by noise, which should not contribute to the transformation. Typical window functions are the 'Kaiser-Bessel' and the 'Hanning' windows, which are most often combined with regions of constant 1 for the middle part of the data range. In the case of the 'Hanning' window this results for example in

$$h(k) = \begin{cases} \sin^2\left(\dfrac{\pi(k-(k_1-\Delta k))}{2\Delta k}\right), & k_1 - \Delta k < k < k_1 \\ 1, & k_1 < k < k_2 \\ \cos^2\left(\dfrac{\pi(k-k_2)}{2\Delta k}\right), & k_2 < k < k_2 + \Delta k \end{cases} \tag{2.12}$$

where k_1, k_2 and Δk can be specified to adapt the shape of the window. The Fourier transformed EXAFS extracted from a measured spectrum of metallic Pd is shown in Figure 2.4b, while the used window function in k-space is plotted in Figure 2.4a. It is often possible to draw important conclusions from the amplitude of the Fourier transformed spectra without performing any fits at all. In the case of metallic Pd it is for example possible to immediately assign the peaks in the amplitude of the Fourier transformed EXAFS to the first four shells as also marked in Figure 2.4b. However, it is important to note that the Fourier transformation yields an imaginary number with a certain amplitude and phase. When fitting the data in R-space it is thus required to check both real and imaginary contributions.

XANES

Analyzing the XANES in a similarly accurate way as the well-understood EXAFS is more difficult for two reasons. First, the mean free path of the photoelectrons drastically increases below about 30 eV, which is e.g. displayed in [Reh00]. Thus, the XANES is

highly affected by contributions of multi-scattering paths making it very sensitive to the local geometry around the absorbing atom. Second, close to the absorption edge inner atomic transitions to free orbitals respectively excitations to Rydberg states are very likely. These transitions are strongly affected by mixed orbitals or specific band structures and are thus sensitive to the chemical state of the absorbing atom. Both described effects make it very hard to perform *ab initio* calculations of the XANES, as it is standardly done in EXAFS analysis. In addition, the many characteristic wiggles appearing in the XANES region can be effectively exploited for so-called *finger-print* techniques. In this context, it is a typical approach to fit the measured XANES data with a linear combination of XANES spectra of well-defined reference materials to resolve the sample composition. This is especially interesting for time-resolved applications where only the XANES is measured in order to achieve a higher time resolution. The linear combination analysis (LCA) and other XANES analysis techniques, as the principal component analysis (PCA), will be discussed in more detail in section 3.3.

2.1.3 Experimental design

The typical beamline and experiment layout required for EXAFS experiments is schematically sketched in Figure 2.5. Prerequisite for EXAFS measurements is the polychromatic ('white') X-ray beam available at beamlines in dedicated synchrotron radiation facilities. In these facilities either electrons or positrons are accelerated almost to the speed of light and thereafter stored with constant kinetic energy in a vacuum ring, which is the so-called storage ring. To keep the electrons/positrons on a circular trajectory, they have to be permanently accelerated into the direction of the ring center. Thus, storage rings typically consist of bending magnets, which are used to deflect the electrons/positrons. Furthermore, the straight sections between the bending magnets are equipped with refocusing multipole magnets to keep the naturally diverging electrons on a narrow beam path. Every accelerated charge radiates photons and thus every bending magnet in the ring structure is a radiation source. The characteristic Hertzian dipole radiation of accelerated electrons/positrons in their inertial system is transformed to a narrow beam in the forward direction of the electrons in the rest frame according to the theory of relativity and due to the fact that the speed of the stored electrons/positrons is close to the speed of light. The natural beam spread angle of synchrotron radiation generated by bending magnets is of the order of $2/\gamma$ with

$$\gamma = \left(1 - \frac{v^2}{c^2}\right)^{-1/2}, \tag{2.13}$$

where v is the speed of the electrons and c the speed of light.

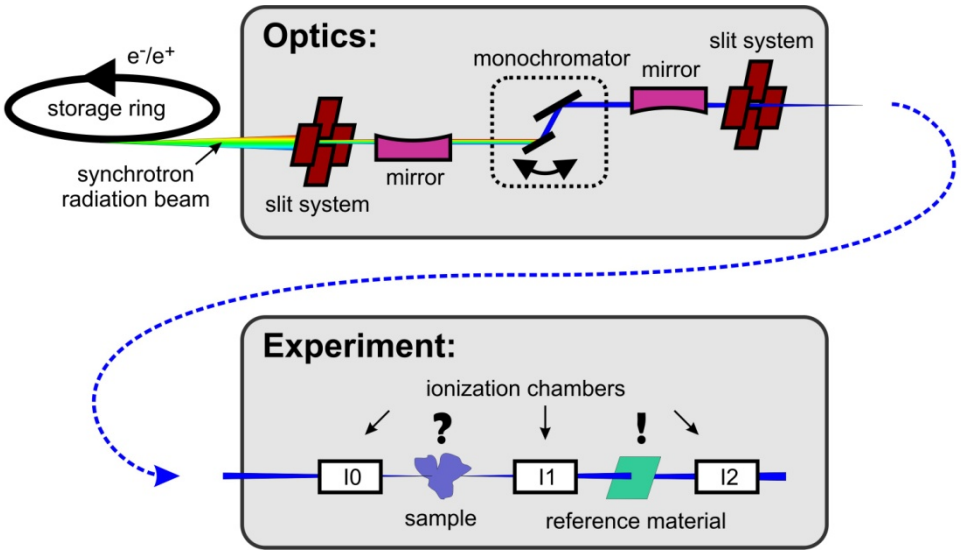

Figure 2.5: Typical design of a beamline dedicated to EXAFS experiments.

A second source of radiation that is typically found at storage rings is given by the so-called insertion devices that are installed in the straight sections of the ring structure. These devices consist of a system of electromagnets with periodically alternating field directions along the beam path. These magnets are often superconducting to achieve stronger magnetic fields. Passing these magnetic structures, the electrons/positrons are forced on a sinusoidal path, because of the applied permanently changing acceleration force perpendicular to the beam direction. Again, the acceleration is the source of radiation, but with the periodic magnet structures the emitted photons of each period can overlay coherently resulting in much higher beam intensities than achievable with bending magnets for electrons with the same kinetic energy. In the case of insertion devices one distinguishes between wigglers and undulators. For maximum angles between the electron directions in the insertion device and the beam orbit equal or below $1/\gamma$ the device is called undulator, otherwise it is called wiggler. All data of the present work were measured with a bending magnet, so that a deeper understanding of insertion devices is not required for further reading. More information about this topic and also the properties of storage rings in general is given e.g. in [Wil96].

The polychromatic photon beam, generated by a bending magnet or insertion device, typically passes various optical elements as also outlined in Figure 2.5. These are consisting of slits, mirrors and one or more monochromators. A first slit is often used to cut off scattered beam intensity from the bending magnet or insertion device and a filter system to suppress low energy contributions. Next in the beam path a bent X-ray mirror is preferably used to make the divergent photon beam parallel before it is reflected by the monochromator crystal/crystals. The mirror is especially important for the energy resolution of the X-ray monochromators, which exploit the principle of X-ray diffraction on single crystals according to Bragg's law (see e.g. [War91])

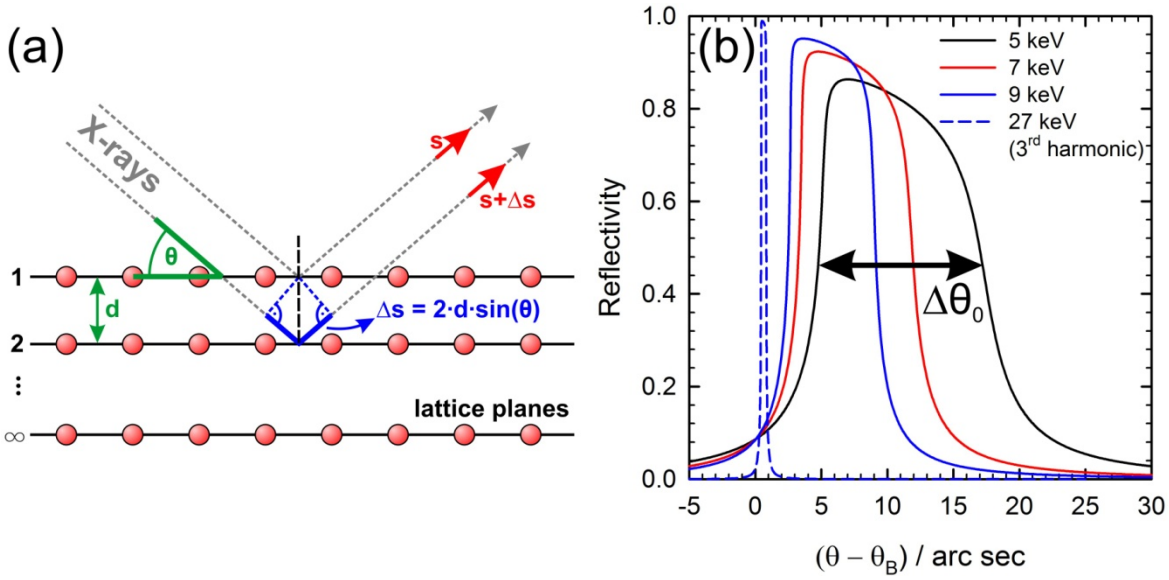

Figure 2.6: (a) Schematics to explain the Bragg equation for X-rays reflected on the lattice planes of single crystals, (b) first order reflection (Darwin) curves of X-rays with various energies reflected on a Si(111) single crystal in the angular region of the corresponding Bragg angle θ_B. The third harmonic for the 9 keV curve is added as dashed line.

$$n\lambda(E) = 2d_{hkl}\sin\theta. \tag{2.14}$$

Here, n is the order of the reflection and $\lambda(E) = hc/E$ the wavelength of the photons with energy E, while d_{hkl} is the distance between two lattice planes according to the Miller indices (hkl) and θ the angle between beam and lattice plane. Accordingly, the crystal angle defines an energy value which is reflected due to constructive interference, as illustratively shown in Figure 2.6a. The amplitude of the reflection is proportional to the structure factor, which is given by [Kit05]

$$F_{hkl} = \sum_m f_m(\theta) e^{-2\pi i(hx_m + ky_m + lz_m)}, \tag{2.15}$$

where the atomic form factor $f_m(\theta)$ includes the scattering properties of each atom m in the unit cell of the investigated lattice. No Bragg reflection is observed for $F_{hkl} = 0$, which is e.g. the case for the second order of a $Si(111)$ crystal.

The energy resolution of a monochromator crystal can be illustratively explained with the number of lattice planes contributing to the reflected beam. The more lattice planes contribute, the sharper the constructive interference becomes, so that the penetration depth of the beam into the crystal primarily determines the energy resolution. The theoretical correct approach is given by the dynamical diffraction theory [War91, Als00, Aut04] and results in the curves as displayed in Figure 2.6b (calculated with [San04]) for various X-

ray energies reflected on a $Si(111)$ single crystal. Thereby, the width of the reflection curves, which is also known as Darwin width, is given by [War91]

$$\Delta\theta_0 = \frac{2e^2\lambda^2}{\sin(2\theta_B)m_e c^2 \pi V} |Re(F_{hkl})| e^{-M}, \tag{2.16}$$

as long as the plane defined by incident and reflected beam is perpendicular to the beam polarization given by $\vec{E}$. With $\vec{E}$ parallel to the reflection plane an additional factor $|\cos(2\theta_B)|$ has to be considered. The Bragg angle θ_B, the volume of the crystal unit cell V and the Debye-Waller factor e^{-M} to account for the crystal temperature all contribute to the Darwin width. Typical values for $\Delta\theta_0$ as shown in Figure 2.6 range from about 4.5" at 13 keV to about 12.7" at 5 keV. To fully understand the shape of the reflection curves absorption effects have to be considered, leading to maxima of the reflection curves below 100%. The curves are not symmetric as the reflectivity significantly decreases at higher angles. This is attributed to the standing wave field build up by the incoming and reflected photon beam. This field exhibits a higher absorption if it is in phase with the reflecting lattice planes (maxima at the positions of the atoms), which is occurring towards the energetically lower limit of the Bragg reflection. The reflection curves are shifted to slightly higher values than the exact Bragg angle, due to the non-vanishing refraction of X-rays in condensed matter leading to refraction indices slightly below 1.

With Eq. (2.14) and (2.16) it is possible to calculate the energy resolution of a monochromator crystal via

$$\frac{\Delta E}{E} = \Delta\theta_0 cot\theta_B = \frac{4e^2 d_{hkl}^2}{m_e c^2 \pi V n^2} |Re(F_{hkl})| e^{-M}. \tag{2.17}$$

In a rough approximation about 10^4 lattice planes contribute to the reflected beam using a $Si(111)$ crystal and with dynamical diffraction theory the intrinsic resolution can be calculated to $\Delta E/E = 1.33 \cdot 10^{-4}$ [Bea74]. For $Si(311)$ the resolution is about one magnitude better (on the cost of less reflected intensity) as the corresponding planes exhibit a lower density of atoms. Thus more lattice planes are penetrated by the beam and thus contribute to the reflection. The intrinsic resolution of the crystal, expressed in Eq. (2.17), has to be modified by adding the divergence of the X-ray beam $\Delta\theta_B$. Another term $\Delta\theta_T$ accounts for additional thermal effects caused by the heat transfer of the beam to the crystal surface, which results in local deformations of the lattice structure. A detailed study of these effects and further information about the cooling of the crystals can be found e.g. in [Bil00, Lee94]. Accordingly, the final energy resolution is given by

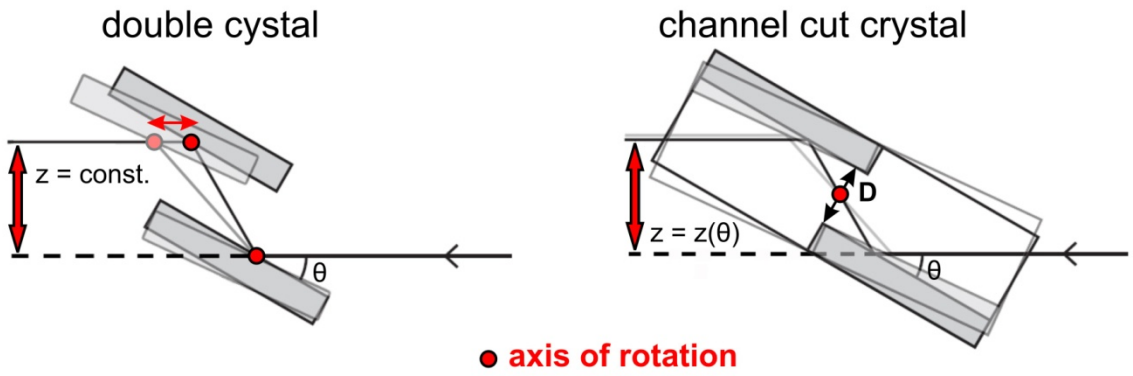

Figure 2.7: Schematics to demonstrate the different beam exits of double crystal and channel cut crystal monochromators.

$$\frac{\Delta E}{E} = (\Delta\theta_0 + \Delta\theta_B + \Delta\theta_T)\cot\theta_B. \tag{2.18}$$

One crystal surface is sufficient to reflect a selected energy of the polychromatic synchrotron radiation. However, a second crystal parallel to the first one is typically used to reflect the beam back into horizontal direction. As shown for the crystals in Figure 2.7, this double reflection results in a vertical offset of the beam z which depends on the crystal angle θ for the channel cut crystal via

$$z(\theta) = 2D\cos\theta, \tag{2.19}$$

where D is the perpendicular distance between the crystal surfaces. In Figure 2.8 the change of this offset between the start and end value of a spectrum covering 1 keV and 0.5 keV with a median energy ranging from 4 keV to 32 keV are plotted for $D = 10mm$ for $Si(111)$ and $Si(311)$ channel cut crystals. The beam travels vertically over the sample in the order of typically less than 0.1 mm. Measuring for example a spectrum at the Cu K-edge (8979 eV) from 8.9 keV to 9.4 keV results in a 52 µm movement of the beam over the sample. At the Pd K-edge (24350 eV) from 24.3 keV to 25.3 keV the displacement amounts to only 19 µm with a $Si(311)$ crystal of the same geometry. Considering a typical beam height of about 500 µm, the displacements are negligible in most cases, as long as the samples are not extremely inhomogeneous. One possibility to entirely solve this issue is to use a vertical slit in front of the sample, which is always fully illuminated by the beam. However, this is slightly decreasing the number of photons available for the experiment and a decreased signal-to-noise ratio is the consequence. In the case of conventional double crystal monochromators an alternative solution was developed, whereby the second crystal is moved along the beam, synchronized to the crystal angle. This approach grants a fixed exit height of the beam as also demonstrated in Figure 2.7. In many double crystal monochromators it is possible to detune the angle of the second crystal a few arc seconds with respect to the first one. As a result the two resulting

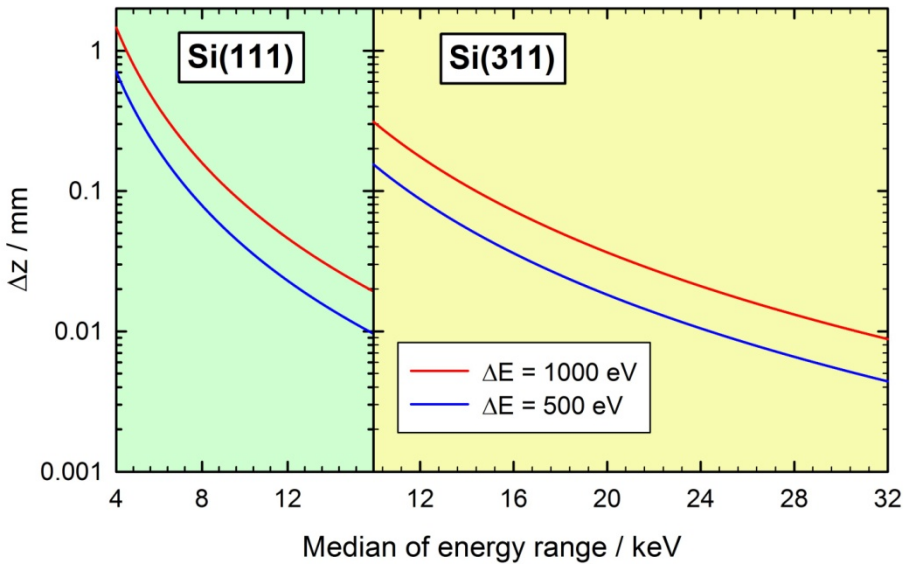

Figure 2.8: Vertical displacement of the beam on the sample during the acquisition of spectra covering an energy range ΔE as function of the median energy value (calculated for Si(111) and Si(311) channel cut crystals with D=10 mm).

reflection curves, as shown in Figure 2.6, are shifted relative to each other and do no longer perfectly overlap. Accordingly, the smaller overlap of both curves yields an overall decreased reflected intensity of the first order. However, with this approach the higher order reflection curves, which are much narrower (see the third harmonic in Figure 2.6), hardly overlap at all, which is leading to an effective suppression of these contributions. Elsewise, small amounts of undesired energies are added to the monochromatic beam.

Behind the monochromator another bent mirror can be used to focus the beam onto the sample. In combination with a final arrangement of vertical and horizontal slits this mirror defines the beam size at the sample position, given that the acceptance of the mirror is suitable for this purpose. In this way XAFS of the sample can be measured in absorption as well as fluorescence or indirectly in the reflected beam under grazing incidence geometry (see section 2.2). Each setup requires a slightly different arrangement of sample and detectors as it is also discussed in the context of the data acquisition system (see Figure 3.11). Similar for all setups is the requirement to measure the beam intensities, which is typically done either with ionization chambers, which are preferably used as long as transmitted beam intensity is measured, or with photodiodes, typically applied in the case of fluorescence measurements, where the yielded intensity is distributed over a certain dihedral angle.

Ionization chambers are constructed and connected as sketched in Figure 2.9. The X-ray beam enters the gas-filled chamber by traversing a Kapton window. Thereafter, a certain amount of photons is absorbed by ionizing the inserted gas, while the remaining photons leave the chamber through another window. Each ionization process generates a positively

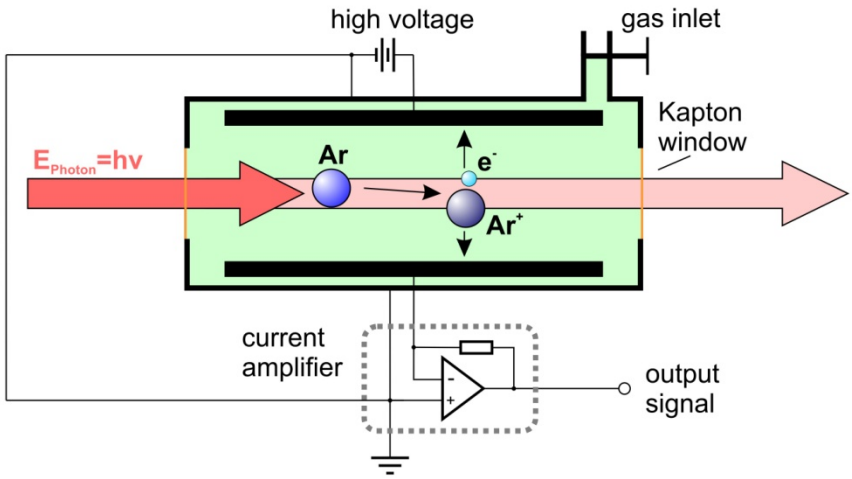

Figure 2.9: Schematic drawing of an Ar-gas filled ionization chamber and the ionization process induced by absorbing X-ray photons.

charged ion and a negatively charged electron. With high voltage applied to the chamber plates it is possible to separate these charges and to accelerate them towards the plates, where they can be measured as a small current from one plate to the other one. This current typically amounts to about 10^{-7} – 10^{-10} A and has thus to be amplified by V/A current amplifiers, before the signal can be digitized.

The main advantage of ionization chambers, compared to other detectors such as photodiodes, is that the percentage of absorbed photons can be adjusted by the inserted gas mixture and gas pressure. Thus, it is possible to set up several chambers in a row along the beam path and to measure intensity in all chambers at the same time. In a typical EXAFS experiment, the first chamber is used to measure the incident beam intensity by only absorbing about 10% of the beam intensity. The remaining photons penetrate the sample and about 90% of the photons that reach the second chamber are absorbed there in order to accurately measure the transmitted beam intensity. The remaining photons can be used to measure an additional reference material for energy calibration. Typical gases used for the ionization process in chambers are e.g. N_2, He, Ar, Kr and Xe, which have all different effective ionization energies between 22 eV for Xe and 41 eV for He [Tho09]. With this ionization energy E_{Ion}, the photon energy E, the length of the chamber L and the measured current I it is possible to calculate the photon flux ϕ via

$$\phi = \frac{I}{e}\frac{E_{Ion}}{E}(1 - e^{-\mu_{gas}L}). \tag{2.20}$$

By mixing gases and varying their pressure, the optimum gas mixture can be found at each absorption edge within the typical EXAFS range of 4-40 keV. Furthermore, each sort of ions has a different mobility and thus requires a different amount of time to reach the chamber plates [Blu08]. This is an important issue in time-resolved applications, since this

effect can lead to distortions in the spectra, as will be discussed in section 3.2.3 in more detail. In contrast to that, the electrons are about three magnitudes faster due to their lower mass and thus do not cause similar problems.

2.2 Grazing incidence XAFS in reflection mode

Generally, there are two approaches to obtain EXAFS information from the surface in grazing incidence geometry. The first one is the energy dispersive detection of yielded electrons which are photo, Auger and secondary electrons. Due to the short mean free path of the electrons in condensed matter, information from only a few nanometers below the surface is available using this technique, which is known as surface EXAFS (SEXAFS). In the second approach the reflected X-rays respectively the fluorescence signal is measured by using external total reflection geometry, which is also known as grazing incidence X-ray absorption spectroscopy (GIXAS) and is probing the surface up to some tens of nanometers depending on the incident angle. This approach was used in the present work and will be discussed in more detail within the following subsections.

2.2.1 X-ray reflectivity

Reflectivity of X-rays on condensed matter has already been discussed in section 2.1.3 in the context of X-ray monochromators, where reflection on single crystals plays a crucial role. Thereby, only photons within a small band of energies are reflected due to Bragg scattering, dependent on incident angle and lattice plane distances (see Eq. (2.14)). In grazing incidence geometry, with angles in the order of some tenths of degrees, Bragg scattering is scarcely contributing, so that the optical properties of a material can be described by the refraction index n [Jam67, Bor80]. Considering different atoms i with atomic number Z_i, the refraction index for X-rays with energy $E = hc/\lambda$ can be written as

$$n = 1 - \frac{N_A e^2 h^2}{2\pi m_e E^2} \sum_i \frac{\rho_i}{A_i} f_i\,(E), \tag{2.21}$$

where A_i is the relative atomic mass, $f_i(E)$ the atomic scattering factor and ρ_i the partial mass density of each sort of atom, while e is the elementary charge, m_e the electron mass and N_A the Avogadro constant.

The atomic scattering factor contains all information of how a specific atom is scattering photons of energy E. It incorporates dispersive contributions as well as absorbing contributions and is thus an imaginary number

$$f_i(E) = Z_i + f_i' + if_i'' \tag{2.22}$$

as well as the refraction index, which can be also written as

$$n(E) = 1 - \delta(E) - i\beta(E) \tag{2.23}$$

with the dispersive (real) contribution

$$\delta(E) = \frac{N_A e^2 h^2}{2\pi m_e E^2} \sum_i \frac{\rho_i}{A_i} (Z_i + f_i') \tag{2.24}$$

and the absorbing (imaginary) contribution

$$\beta(E) = \frac{N_A e^2 h^2}{2\pi m_e E^2} \sum_i \frac{\rho_i}{A_i} f_i''. \tag{2.25}$$

The absorbing contribution is directly linked to the absorption coefficient introduced in Eq. (2.1) via

$$\beta(E) = \frac{\mu(E) hc}{4\pi E}. \tag{2.26}$$

The real and imaginary part of the atomic scattering factor and thus also of $\beta(E)$ and $\delta(E)$ are linked to each other via the Krames-Kronig-Transformations (KKT) (see e.g. [Jac06])

$$f'(E) = \frac{2}{\pi} P \int_0^\infty \frac{E' f''(E')}{E^2 - E'^2} dE' \tag{2.27}$$

and

$$f''(E) = -\frac{2E}{\pi} P \int_0^\infty \frac{f'(E')}{E^2 - E'^2} dE', \tag{2.28}$$

whereby P is the Cauchy principal value defined as

$$P \int_0^\infty := \lim_{\epsilon \to \infty} \left[\int_0^{E-\epsilon} + \int_{E+\epsilon}^\infty \right]. \tag{2.29}$$

Thus, the knowledge of *f',* or respectively *f",* over an energy range as wide as possible, is the only requirement to calculate the corresponding unknown part. With respect to Eq. (2.24) and (2.25) this also means that all structural information in the absorption data is also available in the corresponding reflectivity data and vice versa. As a consequence, the acquisition of EXAFS in reflection mode reveals the local atomic structure to the same extent as achievable with the more established transmission mode. However, the reflection spectra have to be transformed according to Eq. (2.27), before the structural information can be extracted correctly with the steps of conventional EXAFS data analysis, as presented in section 2.1.2. This means that the reflection approach is somehow more sophisticated than the transmission approach concerning the setup as well as the data analysis.

The real part of the refraction index is below one, when dealing with X-rays. According to that and by additionally considering the law of Snellius, the so-called external total reflection appears below a critical angle. For reflection of X-rays in vacuum on a surface this critical incident angle can be approximated with

$$\alpha_c \approx \sqrt{2\delta}. \tag{2.30}$$

In the hard X-ray range the critical angles are typically found between 0.1° and 1°. However, due to the non-vanishing absorption, caused by the evanescent wave field penetrating the uppermost nm from the surface, the measured reflectivity is always slightly lower than 1, even in the case of total reflection.

2.2.2 Reflection by rough multilayers

Considering visible light the reflected and transmitted intensity of photons at interfaces between two materials can be calculated with the Fresnel equations and it can be shown that these equations are also valid for X-rays [Par54]. Accordingly, with A_m as incident and A'_m as reflected X-ray amplitude (photon polarization perpendicular to the reflection plane), the normalized reflected amplitude r and transmission t at the boundary between two adjacent layers m and $m+1$ are given by

$$r_{m,m+1} = \frac{A'_m}{A_m} = \frac{n_m \sin(\alpha_m) - n_{m+1}\sin(\alpha_{m+1})}{n_m \sin(\alpha_m) + n_{m+1}\sin(\alpha_{m+1})} \xrightarrow{\alpha_m \ll 1} \frac{k_{z,m} - k_{z,m+1}}{k_{z,m} + k_{z,m+1}}, \tag{2.31}$$

$$t_{m,m+1} = \frac{A_{m+1}}{A_m} = \frac{2\, n_m \sin(\alpha_m)}{n_m \sin(\alpha_m) + n_{m+1}\sin(\alpha_{m+1})} \xrightarrow{\alpha_m \ll 1} \frac{2k_{z,m}}{k_{z,m} + k_{z,m+1}}, \tag{2.32}$$

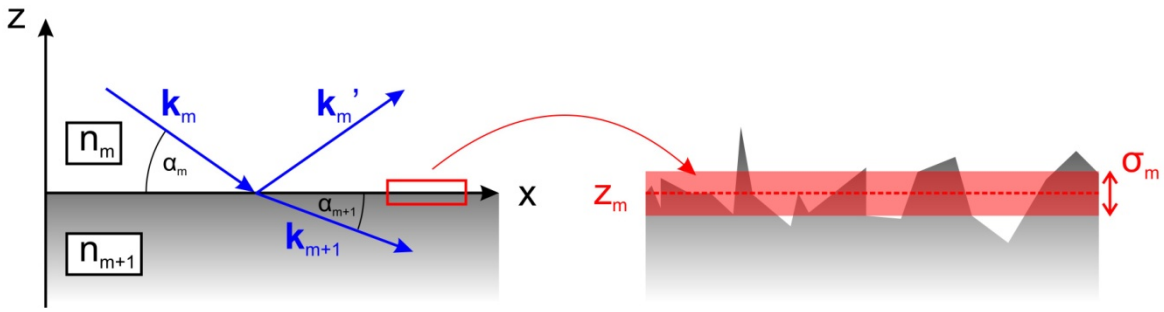

Figure 2.10: Sketch to explain the reflection of X-rays on surfaces and how the roughness of surfaces is characterized.

where k represents the corresponding wave vectors and α the angles, as displayed in Figure 2.10, while n_m and n_{m+1} are the imaginary refraction indices of the two adjacent media. In the region relevant for total reflection α_m is small, so that the approximation $\sin(\alpha_m) \approx \alpha_m$ can be used. This leads to the expressions on the right side of Eq. (2.31) and (2.32), which also results in $t_{m,m+1} = 1 + r_{m,m+1}$. In the special case of reflection on the uppermost surface in vacuum, which means that $n_1 = 1$, the relation $\alpha_2 = (\alpha_1^2 - 2\delta - 2i\beta)^{1/2}$ can be used, leading to the reflection coefficient R and the transmission coefficient T [Par54]

$$R = |r_{12}|^2 = \left| \frac{\alpha_1 - \sqrt{\alpha_1^2 - 2\delta - 2i\beta}}{\alpha_1 + \sqrt{\alpha_1^2 - 2\delta - 2i\beta}} \right|^2, \tag{2.33}$$

$$T = |t_{12}|^2 = \left| \frac{2\alpha_1}{\alpha_1 + \sqrt{\alpha_1^2 - 2\delta - 2i\beta}} \right|^2. \tag{2.34}$$

For incident angles α_1 smaller than α_c the beam penetrates the material with an exponentially decreasing evanescent wave field in the order of a few nanometers. With Eq. (2.34) the distance, where the photon amplitude decreases to $1/e$ can be calculated to

$$l = \frac{\lambda}{\sqrt{2}\pi} \left[\sqrt{(\alpha_1^2 - \alpha_c^2)^2 + 4\beta_2^2} - (\alpha_1^2 - \alpha_c^2) \right]^{-\frac{1}{2}}. \tag{2.35}$$

Thus, it is obvious that the penetration depth of the beam can be adjusted via the incident angle. When measuring in grazing incidence geometry, it is possible to control the information depth, so that space resolved structure determination in z-direction is possible. This is especially useful for the investigation of multilayer systems.

To study multilayer systems, as e.g. a thin film on a substrate in the simplest case, the Fresnel approach can be generalized with the recursion formula for the layer $m + 1$

$$R_{m+1} = \frac{1}{t_{m,m+1}}\left[T_m r_{m,m+1} e^{-i\left(k_{z,m+1}+k_{z,m}\right)\cdot z_m} + R_m e^{-i\left(k_{z,m+1}-k_{z,m}\right)\cdot z_m}\right], \qquad (2.36)$$

$$T_{m+1} = \frac{1}{t_{m,m+1}}\left[T_m e^{-i\left(k_{z,m+1}-k_{z,m}\right)\cdot z_m} + R_m r_{m,m+1} e^{-i\left(k_{z,m+1}+k_{z,m}\right)\cdot z_m}\right], \qquad (2.37)$$

which is known as Parratt algorithm [Par54]. Thereby, the Fresnel coefficients $r_{m,m+1}$ and $t_{m,m+1}$ can be determined with the small angle approximation in Eq. (2.31) and (2.32).

Up to here, all calculations were performed for ideal plane surfaces. However, surfaces typically exhibit a specific roughness in the dimension of a few Å, which is significantly affecting the reflection of X-rays with wavelengths in the same order of magnitude. As a result, one gets a specular reflex, which is the coherent part of the reflected waves, and additionally non-specular scattered intensity, which is the incoherent part. The specular reflex can be described quite accurately within the Fresnel formalism, as explained above. However, it has to be additionally accounted for the surface roughness e.g. in the framework of the Névot-Croce model. In this model a multiplication term is introduced including the root mean square roughness σ, which is actually the standard deviation of the surface height profile with respect to the mean height of the surface [Név80, deB91] (see also Figure 2.10). The final Fresnel coefficients are accordingly given by

$$r'_{m,m+1} = r_{m,m+1} exp\left(-2k_{z,m}k_{2,m+1}\sigma_m^2\right), \qquad (2.38)$$

$$t'_{m,m+1} = t_{m,m+1} exp\left(\frac{1}{2}\left(k_{z,m} - k_{z,m+1}\right)^2\sigma_m^2\right). \qquad (2.39)$$

In order to completely describe the reflection of rough layered surfaces, the distorted-wave Born approximation has to be applied [Hol93, Hol94], where the surface roughness is taken as disturbance acting on the transition from the undisturbed (plane surface) incident and final plane waves. It turns out that the reflected waves not only depend on σ, but additionally on the lateral correlation Λ, whereby the latter one mainly affects the non-specular scattered intensity [Hol94] and is thus not discussed here in more detail, as all presented applications in section 4.3 are measured with the specular reflex. It was shown that Eq. (2.38) can also be evaluated within the distorted-wave Born approximation for specular reflection and is thus still valid [deB94]. Measuring EXAFS in grazing incidence total reflection geometry allows measuring the specular reflex as well as non-specular scattered intensity, e.g. with angles of 2θ adjusted to the Yoneda-Peak [Yon63]. Examples of EXAFS measured in Yoneda-Peaks can be found in [Kei05].

2.3 Time-resolved EXAFS

Adding time-resolution to EXAFS grants access to a wide field of new applications. Prerequisite are the high photon fluxes provided by modern synchrotron radiation facilities of the third generation. Acquiring EXAFS spectra with 10^3 – 10^4 signal-to-noise ratios in less than a second is statistically feasible and provides invaluable opportunities. The most obvious one is the possibility to obtain a deeper structural insight in time-dependent phenomena in physics, chemistry and biology. Furthermore, fast EXAFS scanning is favorable for economic reasons, because more samples can be investigated during the limited time available for a user at a beamline in the framework of a scientific project. Last but not least, even in the case of static samples it is preferable to measure many spectra instead of one spectrum with the same overall integration time. Unexpected changes of the sample structure during about 20 min in the beam cannot always be avoided, e.g. due to the penetration of the beam leading to radiation damage, which is especially an issue in the case of biological samples. The sample can also change due to vibrations if it is a not very densely packed powder or present in a liquid state, so that stirring and bubbles might affect the measurements. Furthermore, random distortions can occur in a spectrum caused by e.g. spontaneous electrical noise, a sudden vibration of the sample or even a sudden beam loss in the storage ring. Measuring many spectra allows controlling and in many cases also filtering out these unexpected events. This will be evaluated in more detail theoretically in section 3.3.3 and with an application example in section 4.1.1. In spite of all these advantages that come along with time-resolved EXAFS approaches, the experimental techniques and also the treatment of generated data are much more complicated as it is the case for conventional EXAFS measurements. This will be further discussed here, and especially with the introduction of new solutions for this issue in chapter 3.

2.3.1 Experimental techniques

Mainly, there are two approaches to perform time-resolved EXAFS measurements, which are the quick-scanning EXAFS (QEXAFS) technique and the energy-dispersive EXAFS (DEXAFS, EDE) technique. The basic idea behind QEXAFS is to rapidly oscillate the monochromator crystals with frequencies of some Hz [Fra88, Fra89, Bor99, Ric02, Fra05, Stö08b, Stö10a]. During each oscillation period of the crystal, two spectra are acquired with increasing Bragg angle (up-spectrum) and decreasing Bragg angle (down-spectrum).[2] Thus, crystal oscillations of e.g. 10 Hz result in a time resolution of 1 spectrum each 50 ms. DEXAFS beamlines are equipped with curved monochromator crystals, which are used in combination with divergent X-ray beams to reflect different energies into different directions, whereby all directions are focused on a point at the sample position. Behind the

[2] Note that according to this convention spectra measured in decreasing energy direction are the up-spectra.

sample, the beam fans out again and a detector array (typically consisting of photodiodes) is used to measure the absorbed intensity in an energy-dispersive way. Thereby, all energy values of the spectrum are sampled at the same instant [Mat80, Mat81, Hag89, Den02, New02, Lab07]. Both techniques are in application at various synchrotron facilities and both feature specific advantages and disadvantages. Although DEXAFS is basically the faster technique, since no mechanical movements have to be considered, QEXAFS turns out to be more flexible and accurate. First of all, with QEXAFS it is easy to switch between different absorption edges and different energy ranges in a few seconds, without having to change the monochromator crystal. Furthermore, it is possible to measure the intensity of the incident beam, which was denoted with $I_0(E)$ earlier, synchronized to the absorbed intensity. No time-outs for reading the detector have to be considered and there are no specific requirements concerning the sample thickness and homogeneity. All these issues turn out to be critical in DEXAFS. Last but not least, it is possible to measure fluorescence [Lüt01, Gru01b], to conceive experiments in reflection geometry [Hec96, Lüt06] and to add focusing optics as e.g. X-ray lenses [Len99, Len01] or KB-mirrors to the experiment. Therefore, QEXAFS is the preferable choice for most sample systems, as long as a time resolution down to about one spectrum each few milliseconds is sufficient. This is e.g. the case for catalytic applications due to gas diffusion limitations. If faster measurements are required, DEXAFS is currently still the more suitable choice with the available instrumentation.

2.3.2 Monochromator designs

The development of QEXAFS monochromators started with the advent of the QEXAFS technique itself more than two decades ago [Fra88, Fra89]. Monochromators for conventional EXAFS measurements typically work with stepper-motors which are moved in a step-by-step fashion to measure a single spectrum. In that case an integration time of about 1 s for each data point has to be considered. Furthermore, between two adjacent data points it has to be waited for 0.5 – 1 s to allow mechanical vibrations to settle. Thus, a spectrum of 500 data points and 1 keV spectral width is typically measured in about 15 min or longer. It is not possible to significantly reduce the time span between two subsequent motor positions due to the mechanical vibrations, which would otherwise lead to increased noise and non-reproducible energy positions. However, it was shown that quasi-continuously moving the motors allows dropping the acquisition time for one spectrum down to a few seconds, while maintaining the high accuracy of conventional EXAFS scans [Fra88, Fra89]. This approach yields decent results as evident from many studies (see e.g. [Cla98]) and accordingly today most commercial EXAFS monochromators provide a quick-scanning mode in addition to the conventional step-by-step scanning mode.

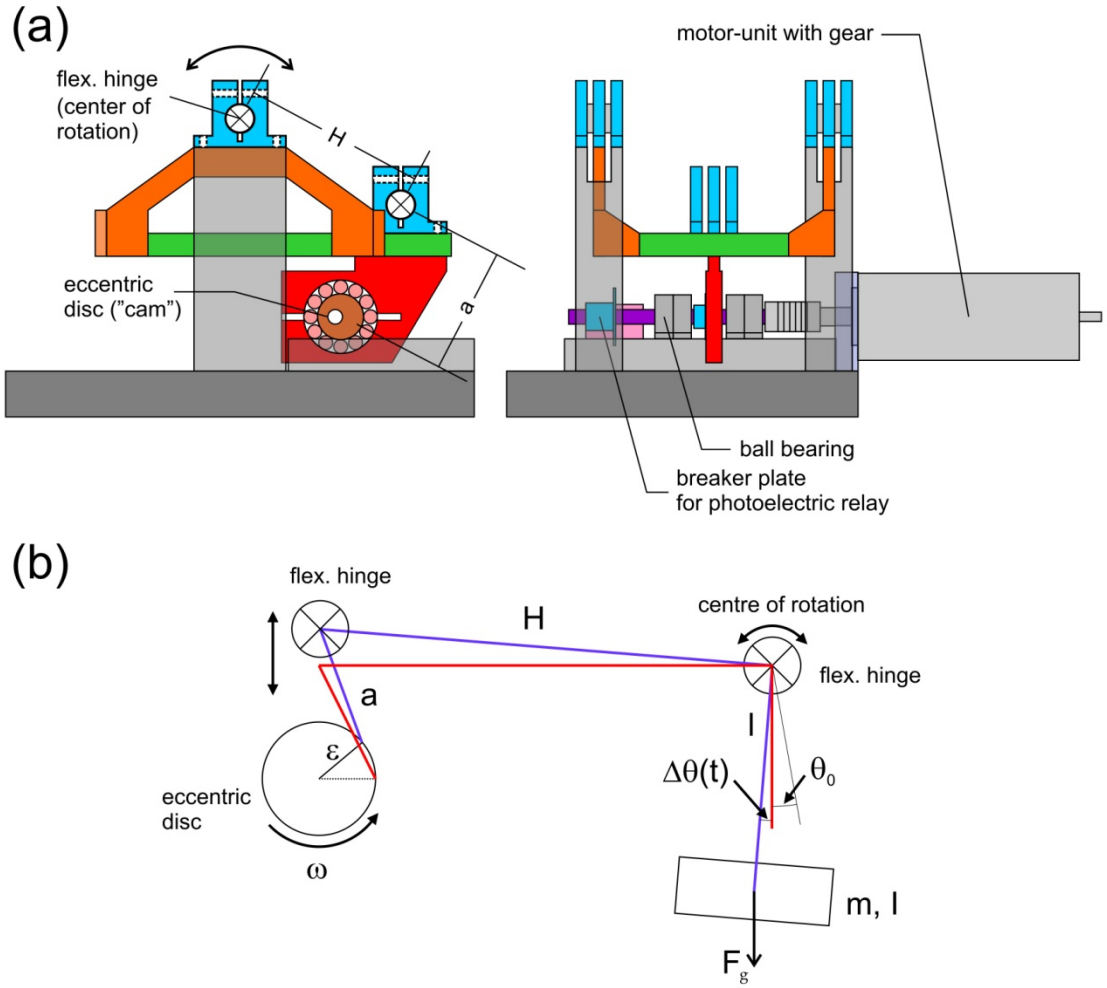

Figure 2.11: Schematics of the QEXAFS mechanics based on eccentric discs: (a) different views on the tilt table geometry, which is used to translate the rotation of the motor unit to an oscillatory tilt movement of the crystal mounted on the green plate, (b) sketch of the mechanics to calculate the Bragg angle $\theta_B(t)$ dependent on the geometrical parameters (both based on [Ric03]).

To further improve the time resolution and reduce the scan times for absorption spectra, covering XANES and EXAFS regions, to some ms, dedicated mechanics had to be developed. First, this goal was achieved with monochromator crystals mounted on piezo-driven tilt tables for XANES [Bor99] and EXAFS measurements [Ric02]. By applying an oscillatory voltage to the piezo translators repetitive energy scans could be performed. This setup features the advantage that very rapid oscillations are possible. Crystal oscillation frequencies of up to 111 Hz could be realized in the past [Bor99], which is also the record in the QEXAFS technique up to now. Several scientific examples have proven the workability of this setup [Ric01, Gru01a, Lüt01]. However, the durability and hysteresis of the piezo translators turns out to remain a problem, while also the achieved angular amplitude of the oscillations is limited to values covering only the XANES region in most cases.

In a second approach mechanics based on rotating eccentric discs were used to perform oscillations of a channel-cut crystal [Fra05]. A wider range of angular amplitudes is achievable with such a setup using a set of various eccentricities. Moreover, the setup also provides a much higher durability in comparison to the piezo-driven mechanics. Nevertheless, crystal oscillation frequencies of up to about 40 Hz are feasible. A drawing of the setup based on eccentricities with all crucial parts of the mechanics is shown in Figure 2.11. Actually, the shown construction is mounted on a vertical goniometer to adjust the mean Bragg angle, which corresponds to the mean energy value of the spectra. The eccentricity is provided by discs with an out-of-center borehole mounted on a rotating shaft of a dc motor. Two flexible hinges, which are also shown in Figure 2.11, define the rotation axis of the setup while another one is required to translate the out-of-center movement of the disc to the tilt table. On the tilt table itself a channel-cut crystal and the required cooling devices for the crystal are mounted. These are not shown in the drawing but e.g. presented in Figure 3.1. As presented in [Ric03] the crystal angle θ_B as function of time t can be written as

$$\theta_B(t) = \theta_0 + \gamma \sin \omega t + \sqrt{\frac{a^2}{H^2} - \gamma^2 \cos^2 \omega t} - \sqrt{\frac{a^2}{H^2} - \gamma^2}, \tag{2.40}$$

where $\varepsilon = H\gamma$ is the eccentricity, θ_0 the mean Bragg angle and ω the crystal oscillation frequency, while a and H are the geometrical parameters as displayed in Figure 2.11b. Thus, a sinusoidal crystal oscillation is achieved in a first order approximation. By changing the eccentric discs the angular amplitude can be adjusted stepwise to different values. The accessible range of angular amplitudes, respectively spectral widths, as function of the mean energy value of the spectrum is displayed in Figure 3.5 in section 3.1.2. Several published examples exist, which are demonstrating the benefits of this setup with respect to achievable scientific results (see e.g. [Bri05, Lüt05a]). The disadvantages are that (i) the width of the spectra can only be changed in discrete steps, which does not allow flexible adjustments, (ii) changing the width of the spectra requires the installation of a new disc, which takes several hours to regain operation conditions, and (iii) no intrinsic information about the crystal angle is available as e.g. in the case of the piezo-driven mechanics, where the applied piezo voltage can be linked to the Bragg angle. Instead, only a breaker plate mounted on the motor shaft and a light gate are used to get a signal synchronized to the starting point of each crystal oscillation. These problems and the corresponding solutions developed during the last years are described in more detail in section 3.1.1 and 3.1.2.

Currently, dedicated QEXAFS monochromators are in operation at the NSLS [Kha10], SOLEIL [Bri11], Swiss light Source (SLS) [Fra09a] and SPring-8 [Uru07]. The latter one

Table 2.1: Examples for QEXAFS studies sorted with respect to the application field.

Application	Examples
Catalysis	[Cla98, Gru01a, Den02, Lüt05a, Sin08, Fra09b, Gru09a, Sil09, Ban09, Föt11]
Surface structures	[Fra91, Hec96, Bru05, Lüt05b, Lüt06]
Sol-gel science, amorphous/liquid samples	[Pic00, Stö10b]
Diluted systems, high pressure/temperature applications	[Den95, Mur95, Sap00, Lüt01]
Biology, radiation damage	[Asc03, Pop03, Hau05]
Tomography	[Sch03a, Ric03]
Other topics in physics and chemistry	[Fra92, Mar04, Bri05, Mar07, Oku08, Kat09, Fuj09, Zho10a, Bau10, Gol11]

represents the only case, where the monochromator technique is not based on the concept of eccentricities. Instead, galvano-scanners are used, quite similar to those applied in discotheques to rapidly move mirrors. A small channel cut crystal is mounted on the rotation axis of the galvano-scanners, whereby it has to be noted that the crystal is not actively cooled.

2.3.3 Typical applications

There are many suitable applications for the QEXAFS technique. Basically, all applications for conventional EXAFS can be investigated, since they can also be studied with QEXAFS. However, the possibility to study time critical phenomena further expands this field significantly. An overview with some outstanding references sorted in order of QEXAFS application field is given in Table 2.1. This list is by no means complete and is certainly expandable with many interesting studies. However, here its sole purpose is to give a short overview of how many groups and disciplines are nowadays benefitting from this technique. Moreover, various examples will also be presented in the application chapter of this work, covering several applications in catalysis, thermal decompositions and also surface science applications as layer growth studies and surface oxidation.

3 Experimental work

For a successful application of QEXAFS in material science as structure resolving tool with millisecond time resolution, the monochromator design plays an outstanding role. Speed is certainly one important parameter for the further development of the QEXAFS technique and to decrease the acquisition time for a full EXAFS spectrum to less than a millisecond seems to be a reasonable goal for the next years. However, it also has to be noted that a better time resolution is for example not required for most applications in catalysis, which are currently forming by far the major application field for QEXAFS. Here the gas diffusion inside the catalytic reactor is typically limiting the required time resolution to some hundred milliseconds per spectrum. While this time resolution is easily achievable with nowadays QEXAFS monochromators, it is important to note that accuracy, flexibility and convenience are equally important components to further establish QEXAFS as a standard tool in materials science. The accuracy has to be comparable to the one of conventional EXAFS measurements otherwise certain scientific conclusions from the data will remain debatable. Flexibility is important on the one hand with respect to the broad field of applications resulting in a variety of experimental setups, and on the other hand with respect to the adjustments of spectral range and time-resolution during the experiments. User-friendly software is important to avoid that time-resolved EXAFS remains an exclusive tool for experienced users who are not only familiar with the electronics and devices of a QEXAFS data acquisition system, but also possess the required computing skills to handle the huge amounts of data that are typically generated during the experiments.

By considering all these important issues, several advancements and new developments were worked out during the last years and the results are summarized within this chapter. New QEXAFS monochromator developments will be presented, starting with the description of a novel rapid angular encoder system [Stö08b] in section 3.1.1. Thereafter,

in section 3.1.2 advancements in the eccentricity mechanics will be presented, which allow continuously adjusting the energy range of the acquired spectra [Stö10a]. A new data acquisition system was designed [Stö11] and is discussed in section 3.2. Finally, section 3.3 deals with the new QEXAFS data analysis software T-REX [Stö12b]. After introducing and explaining all these advancements, their benefits for novel QEXAFS applications will be demonstrated in chapter 4.

3.1 Advanced monochromator design

The presented developments are upgrades applied to an existent QEXAFS monochromator setup as introduced in section 2.3.2, which is driven by mechanics based on eccentricities. Basically, the presented new angular encoder can be immediately adapted to any kind of QEXAFS monochromator, as it was e.g. done at the SuperXAS beamline located at the Swiss Light Source (SLS) [Fra09a]. The new driving mechanics are a slightly more space-consuming modification, which is only applicable to monochromators already using eccentricities. Alternatively, they can be used as basic concept for the design of new QEXAFS monochromators.

3.1.1 Angular encoder

For several years, it has been one of the main goals to design rapid and reliable crystal oscillation mechanics for the QEXAFS technique. The focus on reliability was mainly attributed to the fact that it was not possible to monitor the angle of the crystal at each instant during the oscillation. Stepper motors with well-defined step-widths are used in conventional EXAFS monochromators and it is thus rather simple to derive the correct angle of the crystal from the motor positions. Generally, QEXAFS monochromators do not provide such information due to the continuously moving mechanics. This is especially the case, when rotating eccentric discs driven by a synchronous motor are used, as presented in section 2.3.2. Thus, in the past a perforated disc had been mounted on the motor axis and had been used in combination with a photoelectric gate to obtain at least one specific angular position of the crystal as reference position for splitting the spectra. Thereafter, the approximated theoretical equation for the crystal movement, which was given in Eq. (2.40), along with measurements of reference compounds served to determine the energy scale for the acquired spectra.

With well reproducible mechanics the calculation of energy scales is a reasonable approach as also demonstrated by several scientific investigations [Fra04, Fra05, Lüt05a]. However, one has to consider that the required calculations are rather time consuming and laborious. Furthermore, angular errors of a few arc seconds from one spectrum to the next one cause

major deviations in the acquired data. For example, 1 arc second deviation of a Si(111) crystal adjusted to an energy of about 10 keV corresponds to a deviation of about 0.24 eV in energy. Such deviations due to unpredictable mechanical clearance, vibrations, or changing temperatures have to be eliminated by carefully designing the mechanics as long as no encoder is available.

In previous setups it was also not possible to directly measure the amplitude of each oscillation so that only well-defined eccentricities of the mounted discs could be used and a variation of the amplitude was only possible in discrete steps. Thus, there are two answers to the question, why it is so important to measure the movement of the crystal synchronized to the absorption coefficient. First, one does not have to rely too much on the reproducibility of the mechanics, which means on the other hand that more flexibility in the design of new mechanics is gained. Second, the typical uncertainties for the determination of bond lengths and coordination numbers with EXAFS (see e.g. [Reh00]) are also valid for QEXAFS measurements, so that photon statistics and detector rise times remain the only restrictions for data quality in comparison to conventional EXAFS measurements.

Experimental considerations for the angular encoder system

The challenge of adding an angular encoder system to the QEXAFS monochromator is mainly caused by the high oscillation frequencies of the crystal in combination with a required angular resolution in the order of < 1 arc second. Thus, a very fast encoder and additionally very fast electronics are required in order to get the correct angular value synchronized to each absorption value. For this purpose an angular encoder system manufactured by Renishaw (New Mills, Gloucestershire, England) was used [Ren07], which operates under vacuum conditions (ca. 10^{-8} mbar) and yields an angular resolution of about 0.031 arc seconds with a setup as shown in Figure 3.1. Hereby, the bent scale tape of the encoder system is mounted on a circle section coaxially aligned to the rotation axis of the crystal.

During the oscillation of the crystal the scale tape moves closely over the read head, which is mounted on the non-oscillating part of the mechanics. The signal of the read head is interpreted by an interpolator interface located outside the vacuum vessel. The interpolator yields a quadrature square wave signal as output signal, which is a standard for encoders and can be analyzed in terms of direction and position/speed via clocked up-down counter electronics. The achieved angular resolution depends on the linear resolution S of the encoder, which amounts to 10 nm in the present case. Furthermore, the distance of the scale tape to the rotational axis is required, which is denoted with R in Figure 3.1 and amounts to (67.3 ± 0.3) mm in the shown setup. With these parameters the resolution corresponds to energy steps of only 0.0074 eV at 10 keV using a Si(111) monochromator

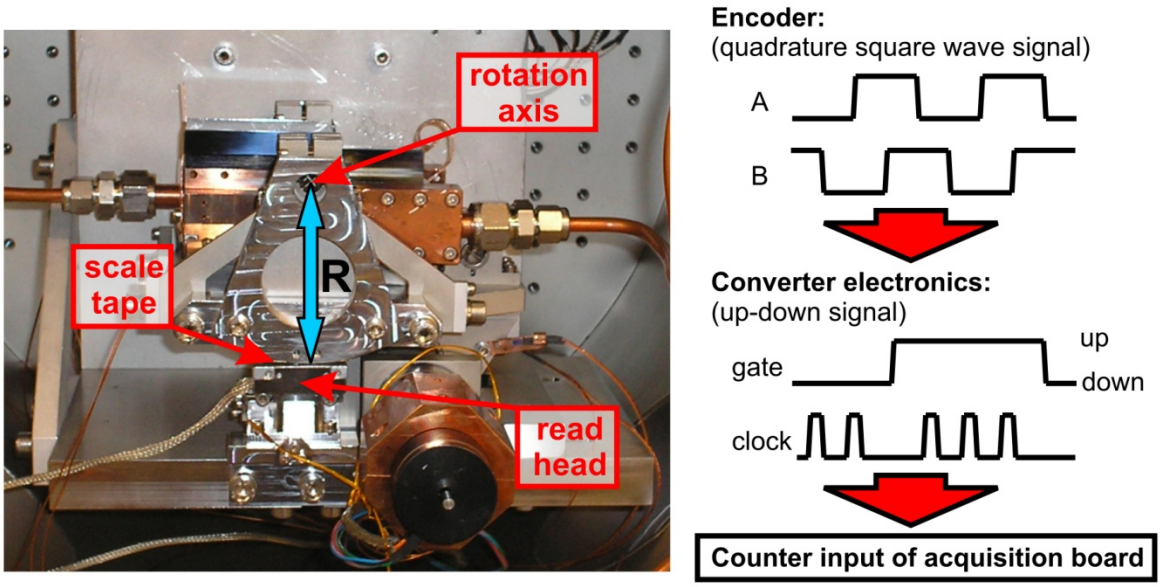

Figure 3.1: On the left side, the interior of the QEXAFS monochromator with the angular encoder is shown. On the right side, the typical quadrature square wave signal of the encoder is shown, which can be converted to an up-down signal by fast converter electronics. Inputs that can read the up-down signal are available on most multifunctional data acquisition systems.

crystal and is thus far below the intrinsic energy resolution of the crystal. At the SuperXAS beamline at the SLS (see section 3.4) a similar setup was chosen with a different encoder model (50 nm resolution) and a slightly different distance R yielding an angular resolution of 0.136 arc seconds corresponding to 0.03 eV at 10 keV using a Si(111) crystal. For typical crystal oscillation frequencies and amplitudes the output signal frequency of the encoder interface amounts up to several Megahertz demanding very fast electronics to read these quadrature square wave signals correctly. In the herein presented setup customized electronics were designed with a counter chip and a quartz oscillator defining the clock rate [Stö08a]. Concerning the required clock rate, with the nearly sinusoidal movement of the crystal as explained in section 2.3.2, the maximum speed of the scale tape with respect to the read head can be calculated by

$$v_{max} = 2\pi f \cdot A \cdot R, \tag{3.1}$$

where f is the crystal oscillation frequency and A the crystal oscillation amplitude. Dividing Eq. (3.1) by the resolution S of the encoder yields the maximum signal frequency which should be at least multiplied by a factor 2 to estimate the required clock rate of the electronics. Considering for example 0.3° amplitude and 20 Hz crystal oscillation frequency, clock rates of close to 9 MHz have to be considered with the setup presented in Figure 3.1 and thus an acquisition board with appropriate inputs has to be chosen (see also section 3.2.1). It has to be noted that meanwhile also multifunctional data acquisition boards with specific inputs for quadrature square wave signals are available. However, it

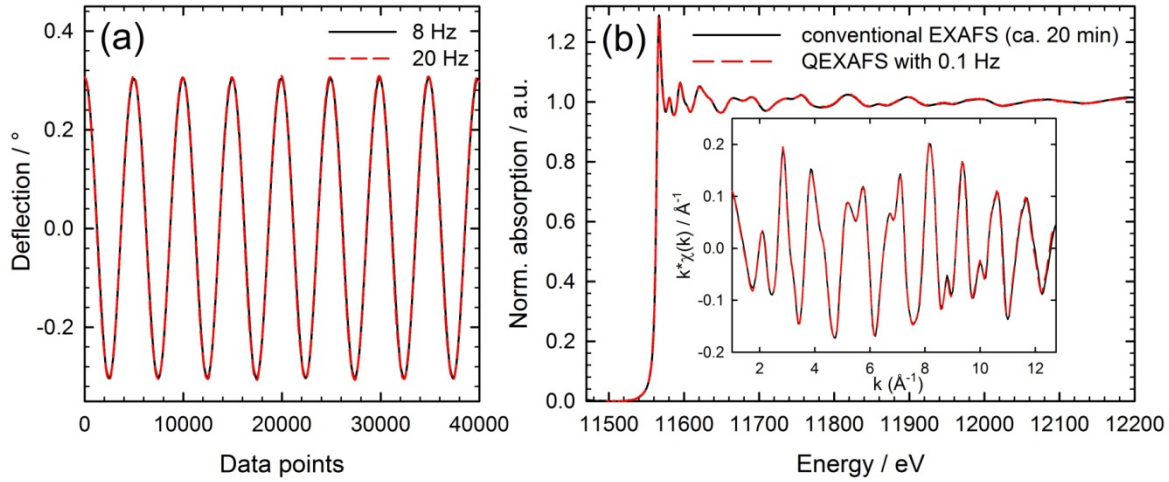

Figure 3.2: Test measurements to check the capabilities of the new angular encoder hardware: (a) signal of encoder acquired during crystal oscillation with 8 and 20 Hz, (b) normalized absorption spectra and extracted EXAFS of Pt metal foils measured at the Pt L_3-edge with a conventional EXAFS measurement and with a 0.1 Hz QEXAFS measurement (after averaging over 11 spectra).

still has to be evaluated, whether such boards are a suitable alternative for the QEXAFS data acquisition by means of the required speed and accuracy.

Characterization of angular encoder system

In Figure 3.2a the signal yielded by the encoder during crystal oscillations with frequencies of 8 and 20 Hz is shown. No steps are lost, although the required counter frequency to read the encoder signal during the 20 Hz oscillations is close to the limit of 9 MHz provided by the used acquisition board. Furthermore, Figure 3.2b shows absorption spectra of Pt metal foils at the Pt L_3-edge, one measured with a conventional EXAFS monochromator at the DELTA storage ring [Lüt09] and one measured with 0.1 Hz with the herein presented QEXAFS monochromator, which had temporarily been installed at the SAMBA beamline at the SOLEIL storage ring [Bri11]. The energy values of the QEXAFS spectrum were calculated with the signal of the angular encoder. In the extracted EXAFS signal it is plain to see that the encoder yields at least similarly accurate results as the conventional stepper motor EXAFS monochromator. While this improved accuracy is an important aspect of the installed encoder system in order to achieve most reliable results, it also enables the design of new and more flexible driving mechanics for QEXAFS monochromators as shown in the next paragraph. Furthermore, it has a deep impact on the design of a new data acquisition system and on the QEXAFS data analysis software as shown in the sections 3.2 and 3.3.

3.1.2 Mechanics with flexible eccentricity

Driving mechanics based on eccentricities have proven to be a very successful approach for the QEXAFS technique (see section 2.3.2). They provide a stable and reproducible crystal movement while the angular amplitude of the oscillation can be adjusted in discrete steps by changing the eccentric disc. Depending on the setup, changing the eccentric disc requires opening the vacuum vessel of the monochromator resulting in a time loss of typically several hours. First of all, before opening the vessel, the mechanics have to be heated up to avoid water condensation on the water- or cryogenically cooled elements. Afterwards changing the eccentric disc takes a considerable amount of time, and finally the vessel has to be evacuated again to a pressure compatible with the pressure in the other X-ray optical devices along the beamline. Such a delay is most unwelcome during a beamtime which is typically restricted to a few days. Additionally, if the decision to change the eccentric disc proves to be disadvantageous, e.g. due to a worse signal-to-noise ratio, there is no way to switch back to the old settings without further loss of valuable beamtime. Khalid et al. report on a setup where the eccentric disc is located outside the vacuum vessel to solve this problem [Kha10]. However, the disadvantages of such a setup are that still (i) the amplitude cannot be changed continuously and (ii) the change of amplitude is only possible after interrupting the measurements.

A continuous change of the amplitude is preferable, since it enables the user to optimize the spectral width for each specific experiment. This is especially helpful when considering signal-to-noise limitations defined by the required time-resolution and the provided photon statistics of the beamline. For example, the user might have to decide spontaneously, whether full EXAFS spectra with a lower time resolution or only XANES spectra with a higher time resolution might be more promising to study the specific dynamic evolution of interest. In each case, the opportunities provided by variable oscillation amplitudes allow optimizing the ranges of the spectra, so that the entire photon flux is used for exactly the energy region of the absorption spectra which is important for data analysis. Apart from that, a flexible eccentricity offers completely new scientific opportunities for QEXAFS which becomes obvious by considering the following two practical cases:

(i) In many applications, where e.g. the transition between two oxidation states is observed, it is sufficient to determine the structure of the initial and the final state by acquiring and analyzing full EXAFS spectra. Then, the transition between these states can be followed with rapidly scanned XANES spectra, which are suitable to study the dynamics of the process and the appearance of possible intermediates.

(ii) In other applications it might be desirable to follow a process at two different absorption edges. With a fixed eccentric disc switching to a different absorption edge results in a change of spectral width. A peak-to-peak amplitude of 0.6° in

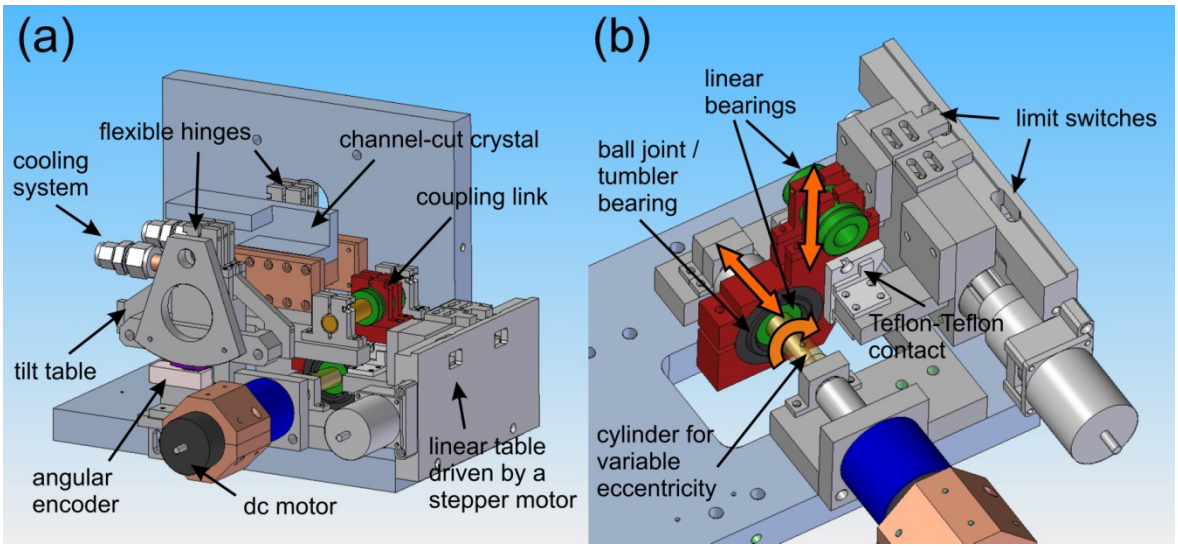

Figure 3.3: Construction drawing of new flexible eccentricity mechanics: (a) Overview of the entire tilt table, (b) focused view on the essential parts of the mechanics. The parts highlighted in different colors are crucial to understand the concept of flexible eccentricity, while the wider arrows indicate the directions of movement.

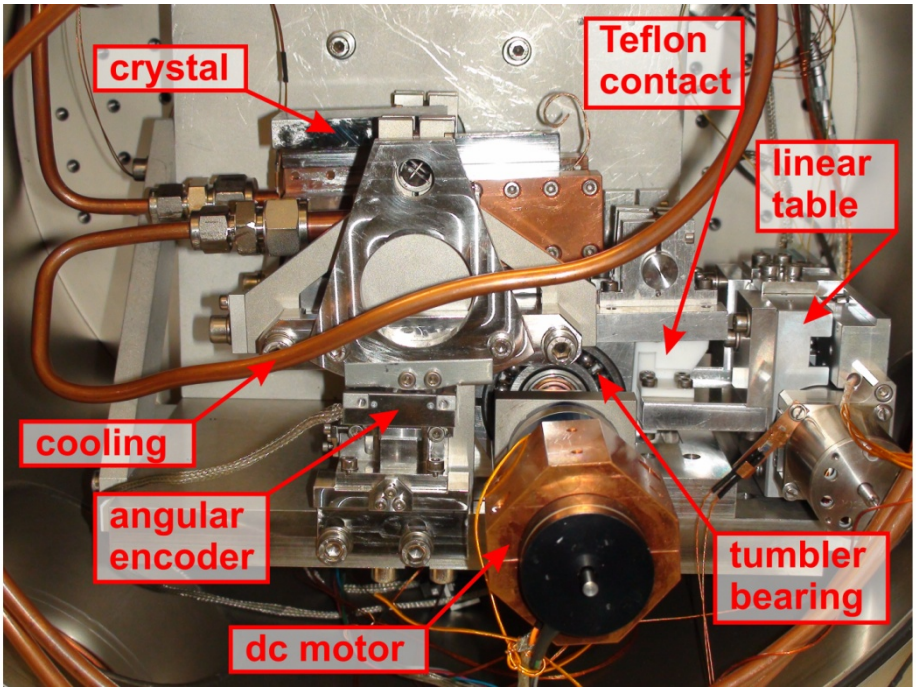

Figure 3.4: Elements of the new QEXAFS monochromator with flexible eccentricity.

Bragg angle corresponds to a width of 100 eV at the Ti K-edge, 400 eV at the Cu K-edge and 700 eV at the Pt L_3-edge. With a flexible eccentricity one can easily change the settings to get the same energy range at each edge.

Due to all these considerations, a new QEXAFS monochromator design with flexible eccentricities was developed as presented within the following paragraphs.

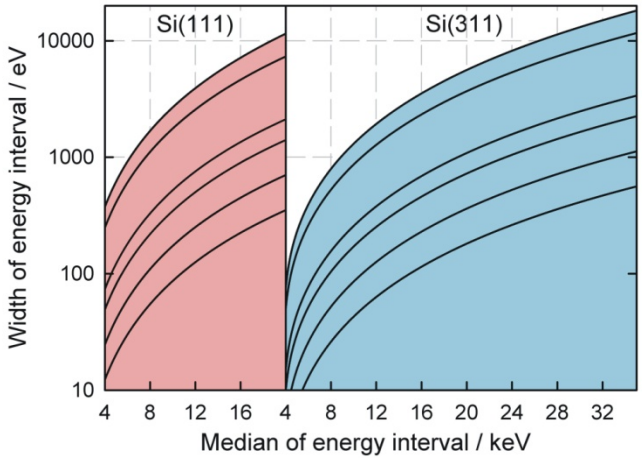

Figure 3.5: Graphical demonstration of the accessible spectral ranges with the new flexible eccentricity mechanics as function of the median energy value of the spectrum using Si(111) and Si(311) monochromator crystals. The black lines correspond to the accessible ranges with the previous setup, while the colored areas represent the accessible ranges of the new setup.

New design for QEXAFS mechanics

The advanced monochromator setup was designed to investigate absorption edges in the range from about 4 keV to 40 keV with Si(111) and Si(311) monochromator crystals. The full Bragg angle range for each spectrum should be continuously tunable between 0° and 3° with oscillation frequencies up to 40 Hz, or respectively 80 spectra each second. To achieve the goal of a variable eccentricity, a cylinder with the length of 30.5 mm was conceived with a borehole slightly tilted by 4.37° with respect to the cylinder axis. If the motor axis of the applied dc motor, which had already been used in the previous setup, is now coaxially fixed inside the borehole, a variation in eccentricity from 0 to 2.3 mm along the cylinder can be achieved by using the setup as drawn in Figure 3.3 and as also presented within the photo in Figure 3.4. Depending on the position of the coupling link along the cylinder the Bragg angle range can be varied within the limits defined above.

For the linear movement along the cylinder axis a linear translation table with a stepper motor and adjustable limit switches was attached. The contact surfaces between linear table and coupling link were made of Teflon because of the low friction provided by this material. Thus, the coupling piece is not restricted in its vertical movements which are caused by the oscillations of the tilt table. At the same time an unhindered movement along the cylinder is possible without significant mechanical clearance when changing directions. The coupling link itself is fixed to the cylinder with a combination of a tensible linear bearing to grant movement along the cylinder and a ball joint, respectively a tumbler bearing, to handle the out-of-center movement of the rotating tilted cylinder. The option of using ball joint or tumbler bearing will be further discussed in the next section. Another tensible linear bearing is attached to the coupling piece to realize the connection to the tilt

table. Figure 3.3b shows how the coupling piece is connected to the linear table and the cylinder while the wider arrows indicate the directions of movement. The entire setup in Figure 3.3a with the addition of the angular encoder as shown in Figure 3.1 is mounted on a stable goniometer, which is used to adjust the mean Bragg angle of the oscillation. This angle directly corresponds to the mean energy value of the acquired spectra, while the tilt table movement determines the spectral width. In Figure 3.5 the accessible width of energy depending on the mean energy value of the spectrum is plotted. While the dark lines represent the accessible regions with the fixed eccentricities, the shaded areas are entirely accessible with the new setup. Moreover, changing the amplitude takes only a few seconds now, while switching between the dark lines caused a delay of several hours for the experiments before.

Characterization of the new mechanics

All presented measurements to characterize the new monochromator mechanics were performed at the Optics Beamline at the Swiss Light Source [Fle09]. The monochromator was installed at a distance of about 16.5 m from the bending magnet source. The unfocussed beam emitted by the bending magnet passed two 100 µm thick diamond windows and finally an 80 µm thick Kapton window as beam exit. The beam size was defined by a slit system, which was located right in front of the monochromator, to about 3 mm horizontally and 0.5 mm vertically. The monochromator vessel was vacuum technically decoupled from the rest of the beamline by using two 80 µm Kapton entrance and exit windows. Inside the vessel, a water-cooled Si(111)-crystal was mounted on the tilt table. A pressure of 10^{-7} mbar was achieved inside the monochromator vessel during the experiments. Behind the monochromator the beam intensity was measured in front of and behind the sample with two ionization chambers (15 cm length), the first filled with N_2, the second with Ar, both at ambient pressure. The intensity of the monochromatic beam was in the order of 10^{11} photons/s during all performed experiments.

In Figure 3.6 the results of a measurement are shown, where the amplitude of the crystal oscillation was tuned stepwise from 0.04° to 1.45° and back to 0.04°, while the oscillation frequency was kept constantly at 1 Hz. The tumbler bearing was used as part of the coupling link for these measurements. As described in section 3.1.1 the angular encoder can be used to accurately measure the deflection of the crystal. Thus, in a first approach it is useful to study the encoder signal, which is accordingly plotted as function of time in Figure 3.6a in order to demonstrate the workability of the mechanics. In this experiment a Cu metal foil was used as sample and measured at the Cu K-edge at 8979 eV.

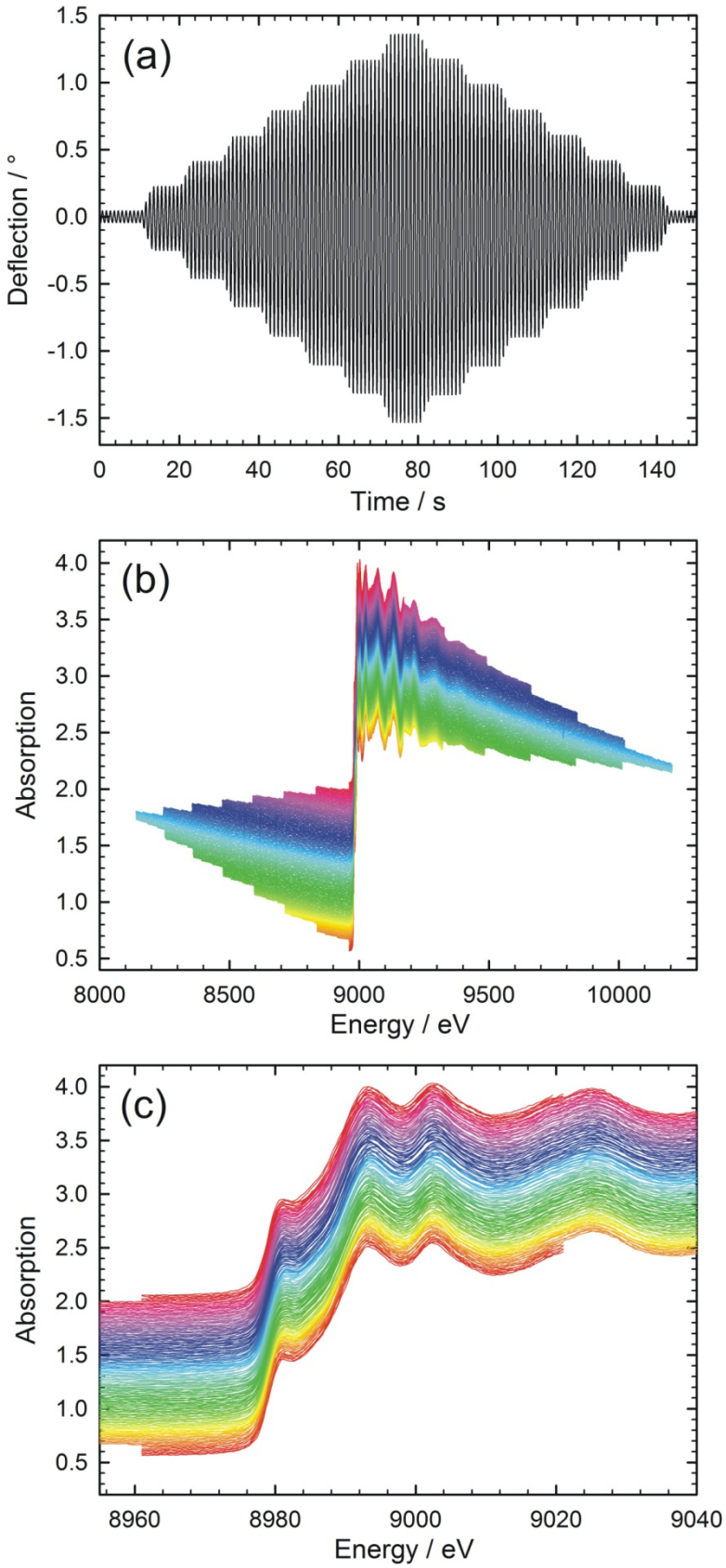

Figure 3.6: Scan of a Cu metal foil at the Cu K-edge with variable energy ranges: (a) signal of angular encoder, (b) and (c) acquired absorption spectra with different horizontal scalings, both with vertically shifted spectra to make changes visible. Every 10 s the amplitude was changed in equidistant steps.

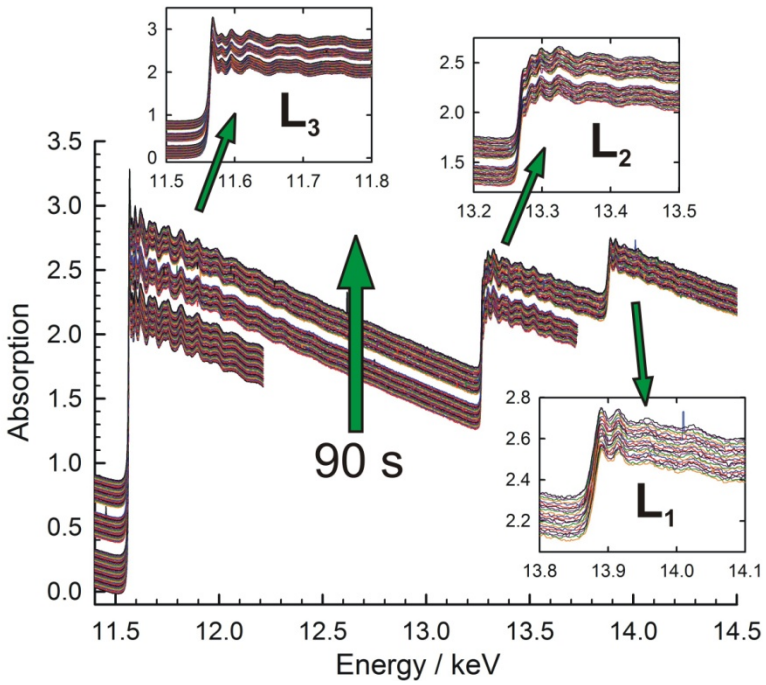

Figure 3.7: Pt metal foil measured with a scan sequence consisting of three different spectral widths covering only the L_3-edge, both L_3- and L_2-edges and finally all three L-edges during an overall time period of 90 s.

The resulting absorption spectra are shown in Figure 3.6b and again with a focus on the XANES region in Figure 3.6c. In both cases, the spectra were consecutively shifted on the vertical axis to make the variation in spectral width visible. The energy range reaches from 60 eV to 2070 eV in the presented experiment. With the results in Figure 3.6a and b it is demonstrated that the oscillation amplitude and thus the spectral width can be changed reproducibly in a very short time without interrupting the oscillations at all. Furthermore, the change of amplitude works equally well in both directions along the cylinder. Figure 3.6c especially demonstrates the stability and reproducibility of the mechanics since the Cu K-edge XANES is well reproduced independent of the chosen spectral width.

A second example demonstrates how the new mechanics based on eccentricities can be used for customized scan sequences. In this specific scan sequence a Pt metal foil was measured at the Pt L_3-edge in a first step, then with a new scan range covering the L_3- and L_2-edges, and finally with a scan range covering all three L-edges. Each step was measured for 30 s yielding an overall cycle period of 90 s. One full cycle is shown in Figure 3.7, and again the spectra were shifted vertically to visualize the changing energy range. For this measurement the ball joint was used as part of the coupling link and is obviously also a reasonable alternative for the mechanics. Figure 3.7 indicates that scan sequences work well and thus can be used for applications, in which it is e.g. required to alternately measure the sample at two edges which is relevant in some catalytic systems [Fra04].

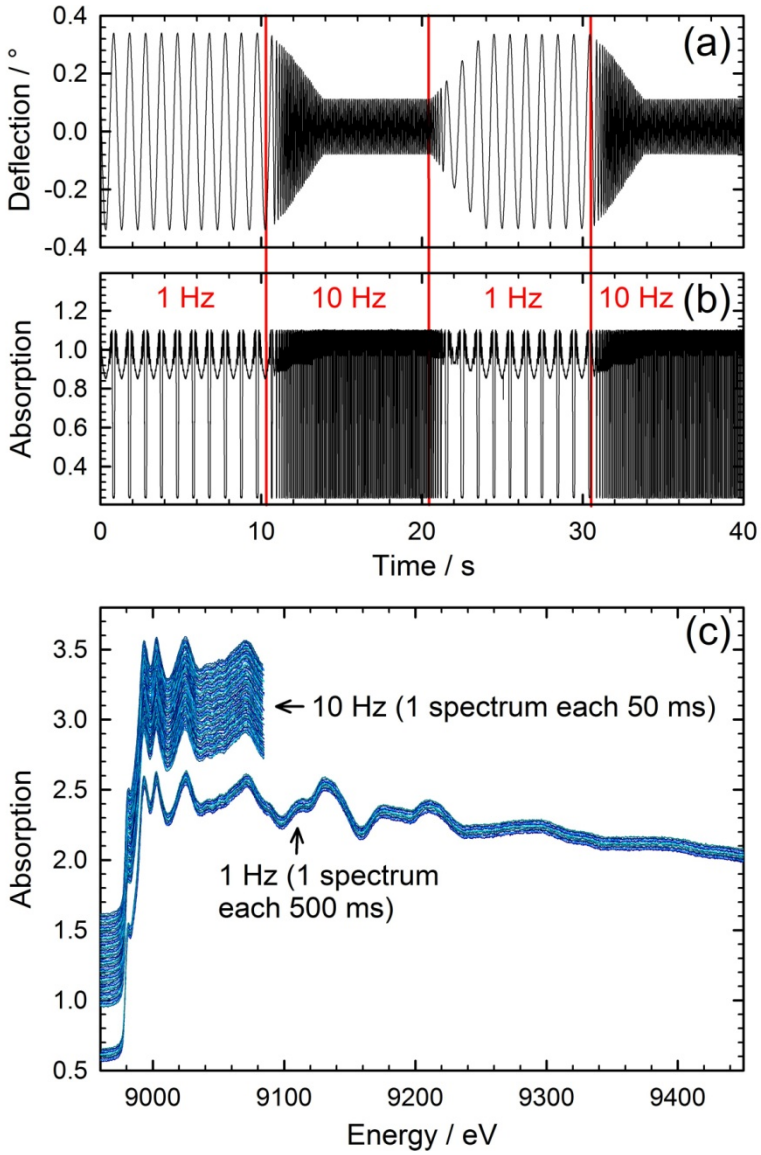

Figure 3.8: Absorption spectra of a Cu metal foil measured at the Cu K-edge with a scan program of varying crystal oscillation frequency and amplitude: (a) angular encoder signal, (b) absorption spectra as function of time and (c) absorption spectra as function of energy (vertically shifted).

A third example demonstrates a scan sequence, where also the oscillation frequency is varied. Again a Cu metal foil was measured at the Cu *K*-edge alternately for 10 s with an oscillation frequency of 1 Hz and 10 s with an oscillation frequency of 10 Hz. At the same time the spectral width was reduced from about 500 eV to about 150 eV. The results are shown in Figure 3.8 and demonstrate that even with higher oscillation frequencies everything works in a stable and reproducible way. There are many applications which might benefit from such scans in the future. Typical examples are given e.g. in the application section of this work, where changes in a catalytic sample are induced by periodically changing gas compositions (see also [Stö09a, Stö09b]). Scans synchronized to mass flow controllers or gas switching devices could e.g. measure full EXAFS spectra in the stable regions of the catalytic cycle where no significant changes occur, while the

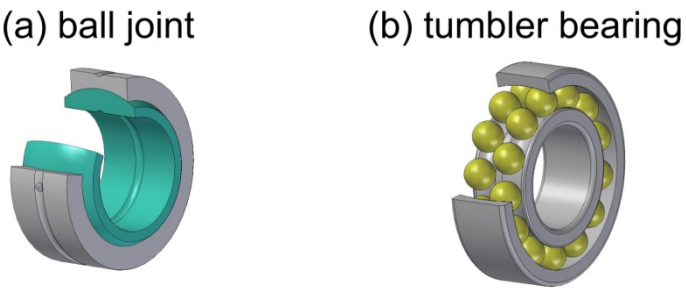

Figure 3.9: (a) Ball joint (steel-steel friction surface) and (b) tumbler bearing as the two options in the new flexible eccentricity mechanics for compensating the out-of-center movement of the rotating cylinder.

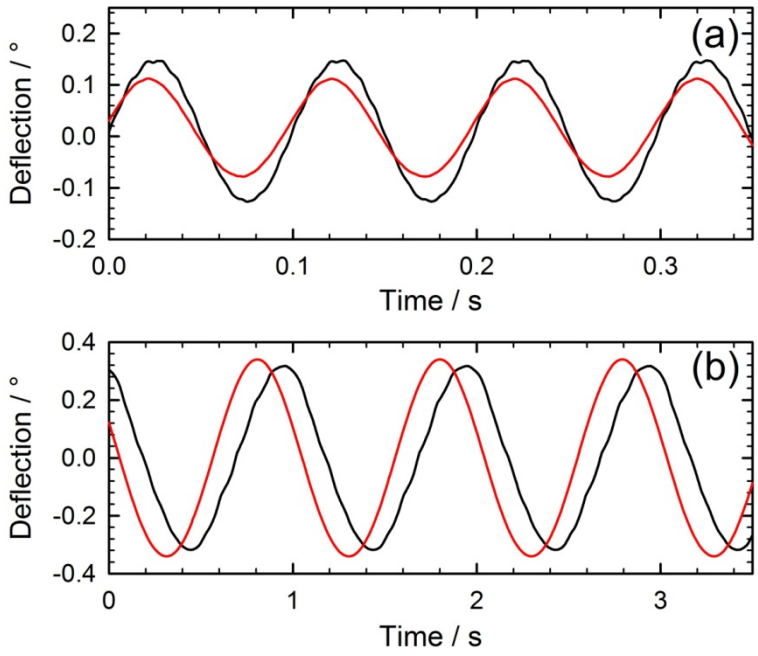

Figure 3.10: Comparison of encoder data acquired during crystal oscillations using the ball joint (black) and the tumbler bearing (red) as part of the new flexible eccentricity mechanics: (a) amplitude of about 0.2° with 10 Hz frequency, (b) amplitude of about 0.3° with 1 Hz frequency.

structural transitions in the sample could be monitored with very fast XANES scans. Such a flexibility is unique in the discipline of time-resolved EXAFS and thus also a further strong argument for the application of the QEXAFS technique in materials science in general.

A crucial part of the advanced mechanics is the handling of the out-of-center movement of the rotating tilted cylinder. A ball joint and a tumbler bearing were considered for this task and both are shown as constructional drawing in Figure 3.9 (see also Figure 3.3 for ball joint and Figure 3.4 for tumbler bearing implementation). The ball joint provides advantages concerning the tilt movement, while on the other hand it is very difficult to achieve high rotation frequencies due to the friction between the steel surfaces, even with

the application of vacuum compatible grease. Thus, the linear bearing has to be fixed to the cylinder with a rather high tension. However, this turns out to be a tightrope walk, because too much tension entirely inhibits the movement along the cylinder axis, which is prerequisite to change the amplitude. The tumbler bearing as second option provides much less friction towards the rotational movement and also less mechanical clearance, so that it is much easier to find an adequate level of tension for the applied linear bearings. On the other hand the tumbler bearing is somewhat stiffer considering the tilt movement.

Since mechanical considerations could not finally resolve the issue, whether tumbler bearing or ball joint is the better choice, both versions were evaluated during experiments with respect to easier handling and stability. A comparison of both versions is demonstrated with angular encoder data in Figure 3.10. Principally, both options are feasible, which has already been shown in Figure 3.6 and Figure 3.7. This is confirmed here, where oscillation frequencies of 1 Hz and 10 Hz were applied with varying amplitudes. However, it turns out that the encoder data was much smoother whenever the tumbler bearing was used, while ripples appeared in the case of the ball joint. Actually, these ripples do not seem to be a big issue for the sake of the angular encoder, but considering long-term stability it is certainly preferable to use the tumbler bearing, which is in addition easier to adjust as has been stated above. Furthermore, under certain conditions the ripples in the encoder signal might be accompanied by unpredictable rapid movements, which might consist of frequencies beyond the speed limits of the encoder, respectively the encoder electronics. All in all, no reasons were found to prefer the ball joint over the tumbler bearing, so that the latter one is considered as the best choice for the presented advanced monochromator mechanics.

3.2 Data acquisition system

The design of a data acquisition system for QEXAFS comes along with several challenges. The most obvious one is certainly to acquire, store and visualize the huge amounts of raw data which are typically generated during quick-scanning EXAFS experiments. A continuous stream of recorded data is required to properly investigate reactions that take several hours to be completed. Furthermore, visualization of the data is a main issue prior as well as during the QEXAFS experiments. Displaying at least one spectrum every second is a prerequisite for each specific experiment, because it provides a reasonable refresh rate to immediately observe, how changed parameters affect the acquired spectra. The preparation works cover the setup of beamline optics as e.g. slit systems, mirrors and the monochromator, as well as detector settings, especially gains and filter rise times of the current amplifiers, but also gas filling and high voltage supply for the ionization chambers. Last but not least, attention has also to be paid to the sample thickness and the sample

alignment in the beam. Here again, visualization with high refresh rates is very helpful, for example in order to find a suitable position on the sample. During the measurements, the visualization capabilities of the software are required to control, whether everything works the way it was planned or if e.g. saturation limits are exceeded. It also helps to draw preliminary conclusions about the investigated sample, which sometimes turn out to be very important for the further planning of the experiments.

Another challenge for the design of a QEXAFS data acquisition system is to control the other involved hardware components as the QEXAFS monochromator, the current amplifiers and the sample stages. In all QEXAFS experiments, adjustment scans are required to align the samples relative to the beam. Considering for example catalytic experiments, the sample container is often a very thin capillary with a diameter less than a millimeter. These capillaries have to be carefully aligned in order to measure in their center, where a maximum amount of material contributes to the signal. Furthermore, scan programs should be provided for example to investigate a sample at different positions during the experiment. Apart from the sample stage, communication with the QEXAFS monochromator controls is desirable to measure systems at two different edges or to perform scans with varying time resolution and/or spectral width as exemplarily shown in several examples within section 3.1.2. Adjusting the current amplifier setting with the same software is not only convenient, but also a first step towards automating QEXAFS measurements, which is especially useful with respect to the filter settings as described below. Another important aspect is the documentation of all settings for each measurement, which is most easily achievable by including all settings in the data acquisition software.

3.2.1 System requirements

Using the QEXAFS monochromator setup with mechanics based on eccentric discs scan rates of up to 20-80 spectra each second, where each spectrum covers an energy range of about 1 keV, have to be considered for the design of a reasonable data acquisition system. As explained in section 2.1.3 the typical experimental setup consists of three ionization chambers, which have to be read out simultaneously. Additionally, the importance to read out the angular encoder inside the QEXAFS monochromator synchronized to the absorption data was explained in section 3.1.1, as well as the fact that special hardware is required providing counter inputs capable to process signals of up to about 10 MHz. With 16-bit resolution for the data of the ionization chambers and 32-bit resolution for the angular encoder at least 0.4-1.6 Megabytes of data each second have to be processed by the electronics to acquire spectra with 2000 data points. Acquiring less data points is not recommendable, because they are not evenly distributed over the energy range due to the sinusoidal crystal movement. However, more data points are always helpful considering

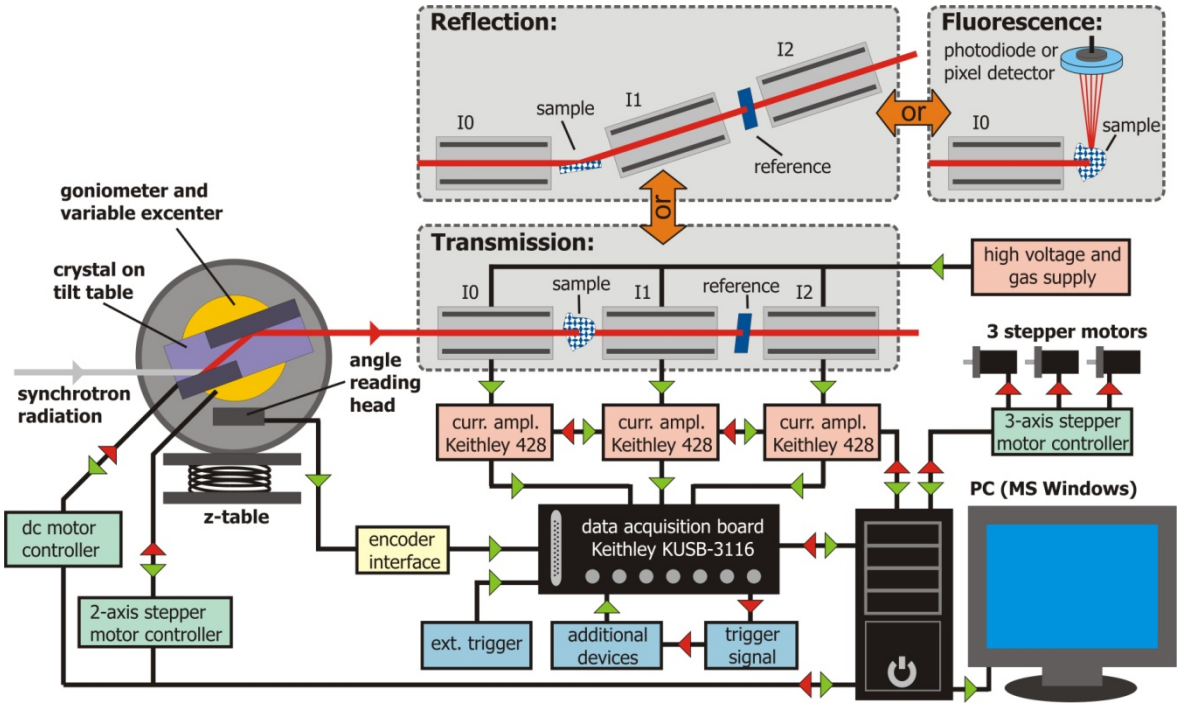

Figure 3.11: Drawing of an entire QEXAFS data acquisition setup. Arrows indicate the communication direction between all components.

digital filtering (see section 3.3.3). Thus, files sizing a few hundred Megabytes are generated within few minutes as long as stored in binary format. However, binary data require subsequent conversion to ASCII, which is time consuming and also causes serious problems, if for some reason the converter software is not available, which will make the files practically unreadable. Thus, acquiring the data directly in ASCII format is preferable, although the file sizes amount to about one order of magnitude more in that case. The QEXAFS data acquisition system has to be capable to process the high data transfer rates continuously over several hours because in some experiments it is not obvious right from the beginning, whether a certain process is over after a few seconds or significant structural changes are still observable after a much longer time period. Additionally, the system should be flexible enough to provide additional inputs for external data sources to measure e.g. temperatures, electrical resistances or the signal of a mass spectrometer synchronized to the EXAFS data. Managing external trigger inputs is as well important e.g. in automatic space-resolved experiments, where a new measurement has to be started as soon as the position of the sample has changed (see e.g. [Sch03a, Ric03]).

3.2.2 Hardware and software overview

Starting with the hardware, a complete overview including all devices typically involved in a QEXAFS data acquisition system is given in Figure 3.11. All devices are controllable with a single PC via Microsoft Visual C# software providing a graphical user interface (GUI) to grant convenient access to all required settings [Mic10]. Since all connections to

the PC are realized by USB or serial COM ports, there are no special hardware requirements so that the PC can be easily replaced in the case of malfunctions. Cable length limitations that come along with USB can be overcome either by setting up the PC close to the experiment and communicate with it via remote control or by using active USB extensions. It was decided to use an external ADC board, which can be conveniently connected via USB and is additionally preferable considering noise, since it is shielded from the other hardware components inside the PC. For a maximum of flexibility the multifunctional Keithley KUSB-3116 board was chosen. It provides analogue, digital and counter inputs, which can be sampled in a synchronized way with frequencies of up to 500000 16-bit values per second using a multiplexer (Keitley Instruments Inc., Cleveland, Ohio, USA) [Kei06]. As already stated earlier, three ionization chambers and a 32-bit counter for the angular encoder have to be considered for a standard QEXAFS experiment, so that a maximum of 100000 datapoints[3] per second can be acquired. Due to the multiplexer a time shift between the four values of each datapoint exists, which can either be corrected via a spline interpolation or can be reduced to a negligible level by sufficient oversampling. Furthermore, the acquisition board provides trigger inputs and outputs which are useful in experiments, whenever synchronization to other devices is required.

A three-axis stepper motor controller is additionally connected to the PC and enables very accurate sample positioning with micro-stepping resolution (Trinamic Motion Control GmbH & Co. KG, Hamburg, Germany). The hardware of the monochromator, which has already been described in detail in section 3.1.2, can also be controlled from the data acquisition PC. Furthermore, up to three Keithley 428 current amplifiers are connected and controllable via GPIB [Kei99]. These components are also schematically displayed in Figure 3.11.

The main GUI of the data acquisition software is shown in Figure 3.12. The purpose of the main GUI is to start and stop the measurements after setting up all required parameters for the acquisition and the plotting of the acquired data. Here it is possible to select one of the offered acquisition modes, which will be explained in more detail below. As soon as a new measurement is started, all settings will be documented within an information file, which is also important for the data analysis process as described in section 3.3. Generally, to enable continuous data acquisition, the collection of data is organized in buffers via predefined classes (Data Translation GmbH, Bietigheim-Bissingen, Germany) [Dat06]. After starting the measurement, the first buffer receives the sampled data. As soon as the first buffer is full, the second buffer continues receiving data, while simultaneously the data of the first buffer is written to the hard disc and sent to the plot window. When the first buffer is empty, it is again assigned to the waiting list and can be refilled. The size of

[3] Datapoint is defined as tuple typically consisting of one angular and three voltage values.

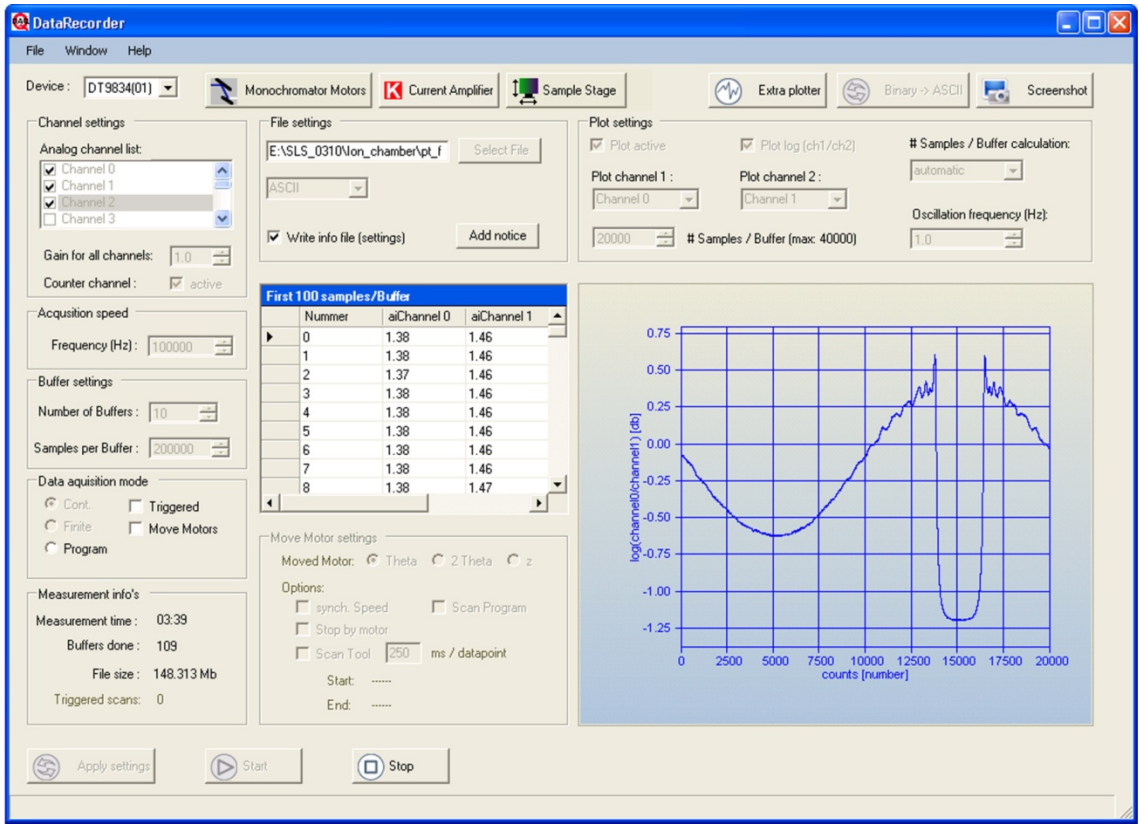

Figure 3.12: Main GUI of the new QEXAFS data acquisition software (see text for details).

the buffers can be manually set by the user and the smaller the size of the buffer, the more often the plot window is refreshed. However, with smaller buffer sizes the CPU more often has to organize the switching between buffers and the plotting of the data, which can cause the system to crash in extreme cases. The exact limits are defined by the PC hardware, but typical refresh rates of about one second are not an issue with the performance of contemporary PCs. The number of buffers is especially important in the case of finite scans of predefined duration, since this number defines the duration of the measurement. In the case of continuous sampling the number of buffers only has to be chosen high enough to ensure that there is always an empty buffer available in the waiting list.

The two most basic acquisition modes are finite and continuous scans, which can be combined with the trigger input of the acquisition board. For the continuous scan only the first trigger signal is considered as starting point for the scan, and it has to be aborted manually by the user. When initializing finite scans, the first trigger signal will start a finite scan according to the buffer settings. Afterwards the system waits for the next trigger signal which will start another scan with the same settings and accordingly the operation proceeds with consecutively numbered files. More advanced acquisition modes are available as soon as the communication with the three-axis motor controller for the sample stage is initiated. Thereafter, it is e.g. possible to use the scan tool which means that data is

acquired as function of the motor position. This is required, whenever sample alignment is necessary. It is also possible to acquire data while two motors move at the same time and are synchronized with respect to each other. This is an interesting option e.g. in combination with a reflectometer as described in section 4.3.1 to perform θ-2θ scans, because here sample and 2θ detector arm have to be moved synchronously. A third option is to program a scan with several motor positions so that data is acquired at each chosen position and data acquisition is stopped as long as the motors are moving. This last option is also available in combination with the monochromator motors and such programmed scans have already been described and studied in detail in section 3.1.2.

Additional sub-GUIs are available in order to enable controlling of the monochromator motors, the current amplifiers and the sample stage. These will not be further described here. More information and figures of each GUI as well as a more details about the plot functions of the software can be found in [Stö11].

3.2.3 Evaluation of data acquisition

Several successful scientific investigations have been already performed with the herein presented QEXAFS data acquisition system and prove that good results with real sample systems can be achieved, especially when dealing with catalytic applications (see e.g. [Stö09a, Stö10b, Sin10, Zho10a, Rei11]). In the following paragraphs, the capabilities and also some limitations of the setup will be discussed, mainly with the help of well-defined reference samples, which were measured at the SuperXAS beamline at the Swiss Light Source (SLS). Details about the beamline can be found in section 3.4. The applications presented within this work confirm the workability with respect to dealing with actual questions in materials science. All therein presented data was also measured with the data acquisition setup introduced and discussed within this section.

Acquisition speed

In order to evaluate the achievable data acquisition speed, Figure 3.13 shows absorption spectra of a Cu metal foil measured at the Cu K-edge at 8979 eV. Data acquired with different crystal oscillation frequencies are presented in three different zooming steps. The entire spectrum with a range of about 500 eV was measured thrice during 500 ms, 100 ms and 50 ms. First of all, it is obvious that no significant differences can be seen neither in the complete spectra in Figure 3.13a nor in the XANES region in Figure 3.13b. This can be seen as proof that the achievable acquisition speed of the setup is high enough to reproduce all features of the spectrum. With a focus on the edge feature in the Cu K-edge Figure 3.13c demonstrates that many datapoints are available in each spectrum, so that even with the best time resolution, corresponding to a total acquisition time of only 750 µs for the displayed region, no details get lost. With respect to the intrinsic energy resolution of a

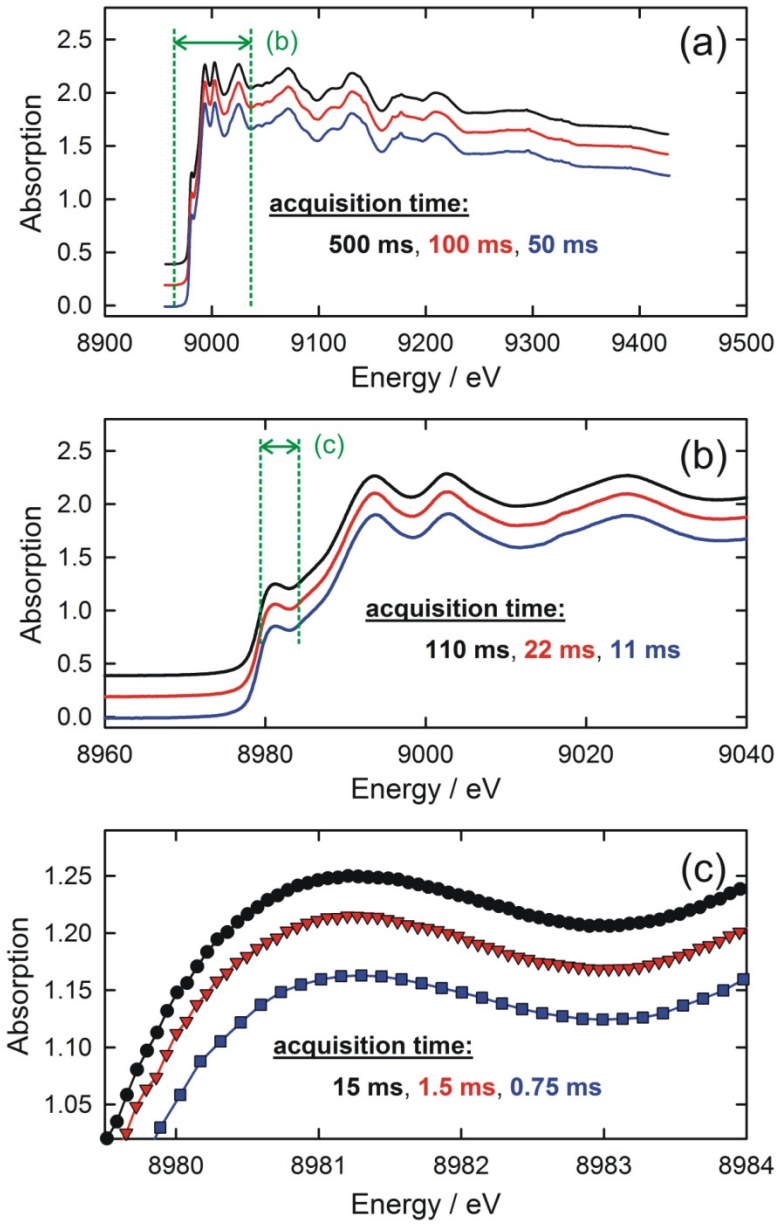

Figure 3.13: Absorption spectra of a Cu metal foil at the Cu K-edge measured with different crystal oscillation frequencies of 1 Hz (black), 5 Hz (red) and 10 Hz (blue). The three different zoom steps in (a), (b) and (c) demonstrate the high acquisition speed, yielding sufficient data points to reproduce all edge features in detail.

Si(111) crystal, which amounts to only about 1.5 eV at the Cu *K*-edge, this data density seems to be even slightly disproportionate. However, such oversampling is very important for the further data processing with digital filters as will be evaluated in detail in section 3.3.3. Another positive aspect of oversampling is the fact that the intrinsic time shift between the acquired values caused by multiplexed data acquisition is negligible.

Noise considerations

As in all time-resolved analysis tools, data quality is an important issue when dealing with QEXAFS. In general, this is a statistical issue due to the reduced integration times for each sampled data point. Moreover, QEXAFS spectra are typically acquired in the millisecond time regime, making it impossible to filter out the 50 Hz (or 60 Hz) ground noise from power supplies without affecting the EXAFS signal at the same time. Additionally, the implementation of the QEXAFS setup within the complex infrastructure of a storage ring and the many different devices contributing to the setup are an extraordinary challenge. This becomes even more evident with a list of noise sources that have to be considered in QEXAFS data acquisition:

- Ground signal at the synchrotron radiation facility: Connected storage ring devices such as HF cavities or primary accelerator devices can be sources of high-frequency noise in the ground signal.
- Ground loops: Using several power supplies with slightly different ground potentials causes leakage currents which affect the measured data.
- Environmental electrical fields and insufficient cable/detector shielding: Devices with high-frequency units or power transformers generate electrical fields which might affect e.g. the ions and electrons in the ionization chambers and/or the current in the cables.
- Mechanical vibrations of sample and/or detectors: Inhomogeneous samples moving relative to the beam path can be a source of noise, as well as a varying beam position in the ionization chambers with respect to the chamber plates.
- Pressure changes in the ionization chambers: Induced either by the connected gas filling system or by moving chamber windows, excited e.g. by acoustic vibrations due to the enhanced noise level inside the experimental hutch (caused e.g. by vacuum pumps or cooling systems), such changes affect the ion current and thus the detected signal.
- Power connection and electronics of high-voltage supplies, current amplifiers and data acquisition board: Each device with its specific electronic circuits might affect the acquired data with noise as long as it is not carefully designed for such applications.

These noise sources have to be checked carefully when designing a QEXAFS setup and preferably even prior to each experiment, since additional devices located close to the sample and the detectors can be sources of new perturbations. In this context, a reliable data acquisition system is a prerequisite in order to unambiguously identify noise sources.

One promising option to improve the signal-to-noise ratio of the acquisition system is the differential mode as sampling option, which is provided by the used acquisition board. In

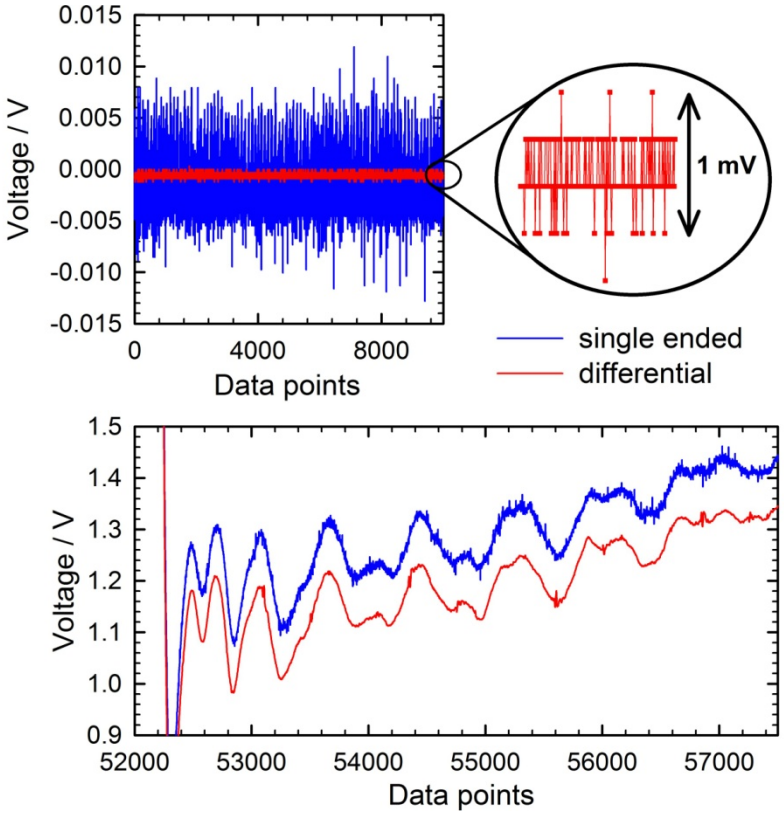

Figure 3.14: Scans performed in single-ended and differential mode measuring the 0 V reference signal (zero check) of a Keithley 428 current amplifier (top) and the amplified signal of an ionization chamber located downstream of a Pt metal foil, which was measured at the Pt L_3-edge (bottom). The signal was not yet normalized on the incident beam intensity.

this mode the incoming measured signal and ground signal are subtracted from each other in order to eliminate noise, which was e.g. induced in both wires by environmental fields. Since signal and ground are both treated equivalently as input signals in differential mode, the number of input channels is reduced from 16 to 8 compared to the single-ended mode. This is however still a sufficient number of analog channels for QEXAFS data acquisition.

In the case of the presently used multifunctional data acquisition board the differences in the achievable signal-to-noise ratios between both acquisition modes are surprisingly high. This is demonstrated in Figure 3.14 where the 0 V output signal of a Keithley 428 current amplifier was sampled using both modes. While the data points scatter in a band of approximately ±7 mV in the case of the single-ended mode, the noise level is reduced to the least significant bit of 0.31 mV[4] using the differential mode. Furthermore, in Figure 3.14 the signal of an ionization chamber located downstream a Pt metal foil is shown. Measurements with both acquisition modes were performed and obviously, the noise level can be significantly reduced within QEXAFS applications by using the differential mode.

[4] This value corresponds to 1 bit for a 16-bit ADC with a range of -10 to 10 V as used in this case.

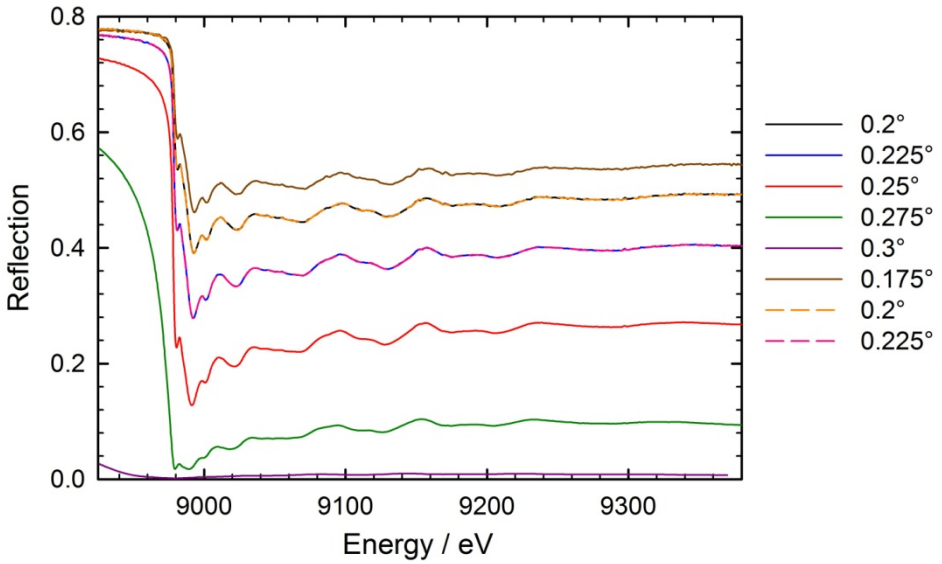

Figure 3.15: ReflEXAFS data of a thin Cu layer on glass at the Cu K-edge acquired during a periodic scan program with various incident angles. A crystal oscillation frequency of 1 Hz was used and the displayed spectra are the results of averaging over ten subsequent spectra. The two dashed spectra belong to a second cycle of the scan program and demonstrate the decent reproducibility of the experimental setup.

Scan options

The workability of the 'Scan Tool' and 'Scan Program' functions is best demonstrated within practical applications in a ReflEXAFS experiment. As explained in section 4.3.1 ReflEXAFS measurements require a thorough positioning of the sample in the beam which is typically achieved with the help of *z*-scans in vertical direction and angular rocking scans. The data shown in Figure 4.52 in section 4.3.1 was e.g. acquired with the implemented scan tool of the QEXAFS data acquisition system. An example for a scan program is given in Figure 3.15, where reflection spectra are displayed. Here a thin Cu layer sputtered on glass was measured in grazing incidence reflection geometry during a cycle with various different incident angles reaching from 0.175° to 0.3° in steps of 0.025°. At each angle reflection spectra were acquired with 1 Hz crystal oscillation frequency and one full cycle was performed during 90 s. Each spectrum in Figure 3.15 is the result of averaging over ten spectra and it is noteworthy that the scan program works in a very reproducible way as the spectra acquired during the second cycle are perfectly congruent with the spectra acquired during the first cycle. This specific scan program was primarily performed to characterize the new software implementations. However, such scan programs are very useful in future applications. Varying the incident angle in grazing incidence experiments results in a varying penetration depth as stated in section 2.2. Thus, it is for example possible to monitor the growth of an oxide layer in situ with such a scan program, so that time-resolved as well as space-resolved information of the layer is obtainable in situ in a single experiment.

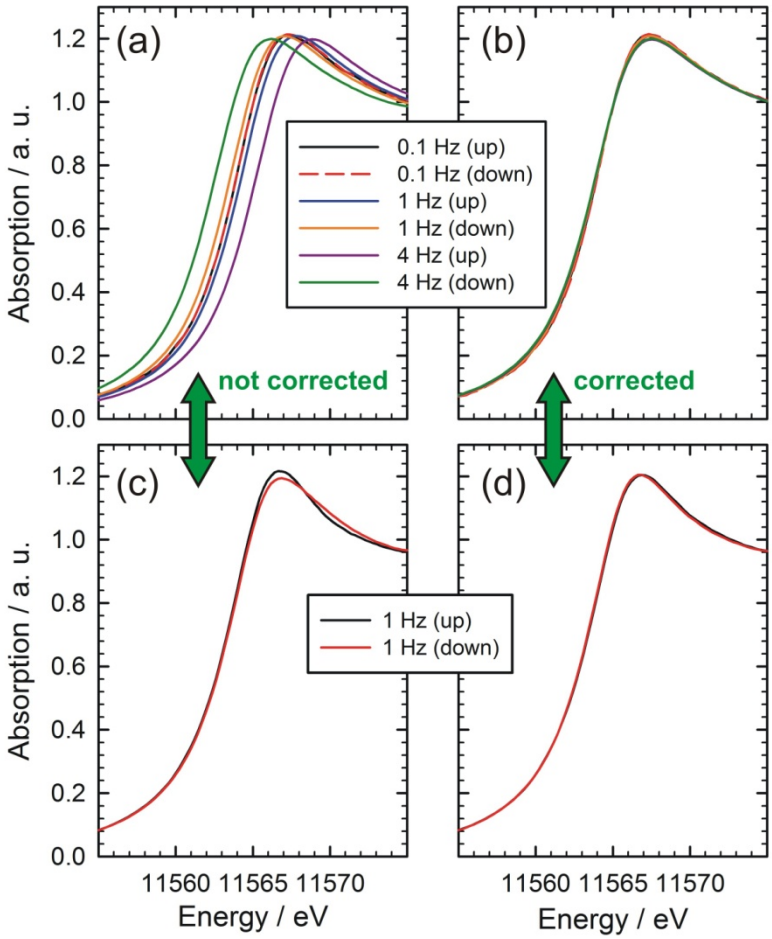

Figure 3.16: Absorption spectra of a Pt-containing sample (a and b) and a Pt metal foil (c and d) at the Pt L_3-edge before and after correcting the time shift caused by the ionization chamber response time.

Further details and examples for programmed scans synchronized to the sample stage or to varying monochromator settings are available in [Stö11].

3.2.4 Detector limitations

While it was shown that the introduced data acquisition system is fast and almost free of noise concerning the pure sampling capabilities, each element of the whole QEXAFS data acquisition system has to be considered to properly characterize the setup. Thus, this section deals with the detector system, consisting of high voltage supply, ionization chambers and current amplifiers. All these devices provide characteristics concerning response times, rise times and noise, so that they have to be chosen carefully in order to achieve a reliable working QEXAFS data acquisition system.

Response time

Although the acquisition of data from angular encoder and ionization chambers is perfectly synchronized by the means of acquisition electronics, a finite response time of the detector

system has to be taken into consideration. This means that the signals are slightly delayed with respect to the immediately obtained angular information. This time shift is constant as long as all detector and current amplifier settings remain unchanged and can only be recognized as energy shift between the spectra acquired in up- and down-direction of the crystal oscillation. It typically amounts to a few hundred microseconds. To investigate the described delay in more detail, a Pt-containing sample was measured with two ionization chambers along the beam path up- and downstream the sample. Additionally, a Pt metal foil was placed between the second ionization chamber and an additional Si photodiode (see [Pau11] for details) as a third detector in the beam path. The photodiode exhibits a significantly faster response time and the measured signals do not show the time shift relative to the angular data, as it is observable for the ionization chamber signals. The spectrum of the Pt metal foil was used to calibrate the energy scale and the resulting (averaged) spectra of the Pt-containing sample and the Pt metal foil are both displayed in Figure 3.16. The shift in energy between the spectra measured in up- and down-direction is well recognizable already for oscillation frequencies of 1 Hz and much more evidently for higher frequencies. Also the spectra of the Pt metal foil, which are based on the division of the signal of the photodiode by the signal of the ionization chamber, exhibit a different shape dependent on the scan direction.

The differences in the spectra dependent on the scan direction can be removed with a detector calibration by shifting the signal of the chambers backwards in time for 250 µs. The result of that correction is shown in Figure 3.16b and d. Now the spectra of the sample as well as the metal foil are almost perfectly congruent independent of the scan direction. Generally, the time shift can be easily corrected as explained late in section 3.3.2, but one has to keep in mind that the specific value of the time shift has to be determined anew as soon as any detector or amplification parameter is changed. It is also important to note that the described time shift is hardly observable as long as three detector systems with approximately the same response time are used, for example with three ionization chambers with the same filter rise times as typical for most transmission experiments. Nevertheless, if very accurate measurements are required and especially the spectra of both scan directions are taken into consideration for data analysis, the delay should not be ignored. As soon as different kinds of detectors are used in combination, as e.g. in all fluorescence applications, correcting the time shift is a prerequisite to obtain reasonable results, which is especially true for time resolutions in the sub-second time regime. Ionization chambers as QEXAFS detectors feature the important advantage that they can be used conveniently to measure the intensity of the incident and transmitted X-ray beam, while the percentage of absorbed photons in the chambers can be tuned by the gas filling. Nevertheless, for the sake of high-accuracy and high-speed QEXAFS data acquisition, alternative transparent detectors, as e.g. diamond foils, should be evaluated in detail in the near future.

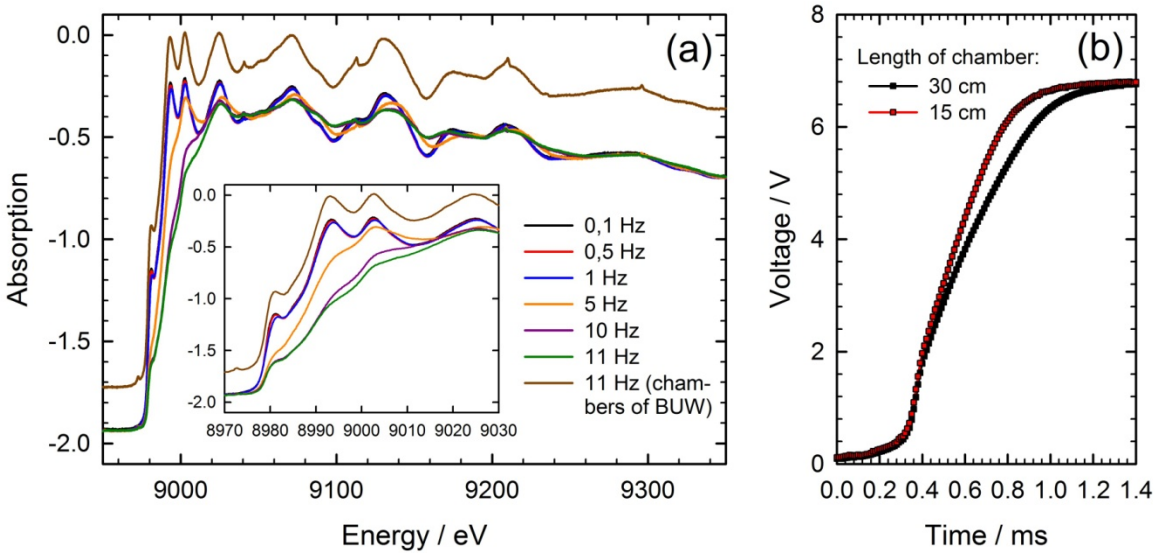

Figure 3.17: Investigations of rise times with different ionization chambers: (a) Absorption spectra of a Cu metal foil measured at the Cu K-edge (averaged over several subsequent spectra and measured with increasing energy), (b) response to an opening fast shutter (provided by the SLS) measured with a long and a short ionization chamber designed by the BUW.

Rise times of detectors

Even a very high data acquisition speed and corrected time shifts are insufficient for proper measurements as long as the signal rise time of the detectors is the limiting factor. Considering ionization chambers the rise time depends on the specific design, the gas filling as well as the applied high voltage. Concerning the design of the ionization chambers, it has already been shown in earlier studies that commercial ionization chambers do not always provide suitable conditions for QEXAFS measurements [Stö08a]. As shown in Figure 3.17a, beyond 1 Hz crystal oscillation frequencies the rise time of the investigated commercial chambers (FMB Oxford Ltd., Oxford, United Kingdom) [FMB07] lead to significant distortions in the spectra, which were scanned with increasing energy. At 11 Hz nearly all features of the Cu *K*-edge are smoothed out, while the chambers of the Bergische Universität Wuppertal (BUW) still yield perfect results at this frequency. Filter electronics of the commercial chambers consisting of electrical resistances and capacities, as well as the large distance between the two plates inside the chambers, are probably the reason for this effect, which does not only affect the XANES region as shown in Figure 3.17a, but also renders the EXAFS useless for higher crystal oscillation frequencies, as demonstrated in more detail in [Bri11]. All spectra in the present work were measured with the chambers of the BUW, except the ones shown in Figure 3.17a.

The size of the chamber plates also makes a difference due to the increased capacity which is decreasing the rise time. This is demonstrated in Figure 3.17b where the response to a rapidly opening shutter (provided by the SLS) was measured with two chambers from the

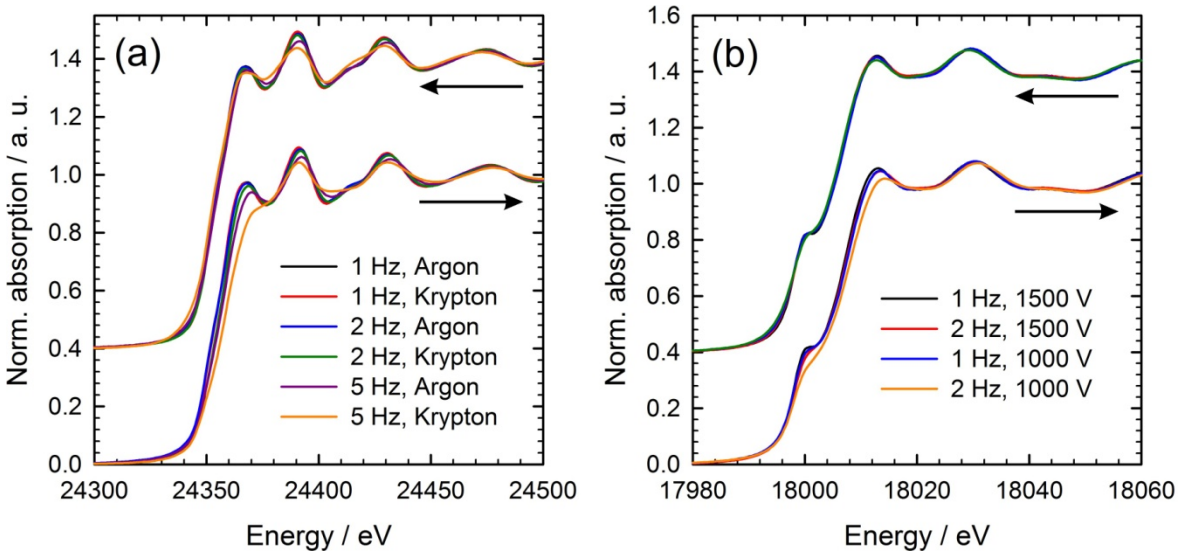

Figure 3.18: Normalized absorption spectra to demonstrate rise time effects of ionization chambers: (a) Pd metal foil at the Pd K-edge measured with Kr and Ar gas fillings and various oscillation frequencies, (b) Zr metal foil at the Zr K-edge measured with applied 1000 V and 1500 V high voltages using 1 Hz and 2 Hz crystal oscillation frequencies. The arrows indicate the scan directions.

BUW, one with 15 cm long plates (red) and one with 30 cm long plates (black), both with equal widths. First of all, there is a delay of the step-like increase of the signal of about 0.4 ms to the first visible increase, which is in good agreement with the earlier investigations of the time shift between ionization chambers and angular encoder. Furthermore, it can be distinguished between the region up to 0.4 ms, where both chambers show almost the same strong increase in signal strength and the following region, where the signal increases faster in the shorter chamber. The signal in the first region can be mainly attributed to the fast electrons generated in the ionization process. In this case the rise time of the current amplifier is the limiting factor and only minor differences between the signals of the two chambers are recognizable due to plate length. Thereafter, the slower ions are the only contributing to the rise of the signal and their mobility in combination with the low pass properties of the electric circuit are determining the rise time. Here, significant differences are observable, whereby short chambers with lower capacity are slightly faster than long chambers. The distance between the chamber plates and the application of additional grids have further to be considered in order to improve the performance of the ionization chambers for the application within the QEXAFS data acquisition setup [Kno00, Mül10].

The effects of the specific gas inside the ionization chamber and the applied high voltage on the shape of XANES spectra are shown in Figure 3.18. Spectra of a Pd metal foil at the Pd *K*-edge and of a Zr metal foil at the Zr *K*-edge were measured using a Si(311) channel cut crystal. The spectra at the Pd *K*-edge were all scanned with exactly the same settings except for the scan speed and the gas filling of the second chamber located directly behind

the sample. The shown XANES regions are selected from spectra covering a range of 1850 eV, and with the crystal oscillation frequencies of 1, 2 and 5 Hz the shown regions correspond to scan times of 67.5, 33.8 and 13.5 ms. The displayed spectra were the result of averaging over 20, 40 and 100 spectra and the highest scan speed at the absorption edge was 13100 eV/s during the 5 Hz measurement. The gas filling does not seem to affect the spectra significantly when using frequencies up to 1 Hz. At 2 Hz the spectra measured with Kr show some deviations from the slow scans, which are not observable in the measurements with Ar. More evident are the changes at 5 Hz where the spectrum measured with increasing energy and Kr inside the ionization chamber is looking quite distorted and even with Ar some features start to get lost.

In general it can be seen that the spectra measured with decreasing energy look less distorted. This is explainable in terms of a specific rise time. By scanning the absorption edge the signal changes very rapidly to a very different level (jump of several volts in the chamber behind the sample). If the detectors are not fast enough, the signal will approach the new signal level with a kind of exponential time scaling behavior defined by a certain rise time constant. When scanning in decreasing energy direction, this effect is scarcely disturbing, since there is only the already smooth pre-edge. However, in the other direction the sharp features of the XANES region directly follow the edge jump, while the signal is not yet on the level to reproduce these features correctly. The fact that the Kr causes a higher rise time than the Ar is well explainable with the reduced mobility of the larger Kr ions as e.g. measured by Sitar et al. [Sit93]. Accordingly, the Kr ions need significantly more time to reach the chamber plates and thus also more time until they contribute to the measured signal.

For the Zr metal foil shown in Figure 3.18b the oscillation frequency was adjusted to 1 Hz and 2 Hz, while additionally the high voltage was switched between 1000 V and 1500 V. The shown XANES spectra are cut out of spectra with a total range of about 980 eV. Accordingly, the shown region was scanned in only 21.3 ms, respectively 42.6 ms, resulting in 3400 eV/s as the highest scan speed at the absorption edge. Averaging over 20 and 40 spectra was carried out to make sure that observed deviations can be unambiguously assigned to the changed parameters and not to random noise. While hardly any differences are recognizable in the spectra scanned downwards in energy, the edge feature of the Zr K-edge is a good indicator to see changes in the other scan direction. With 1 Hz everything is still fine and independent of the applied high voltage. This is also true for the 2 Hz measurement with 1500 V. With 2 Hz and 1000 V however, significant deviations are observable, which clearly evidences that the voltage should be chosen as high as possible to avoid such effects, however without triggering sparkovers inside the chambers.

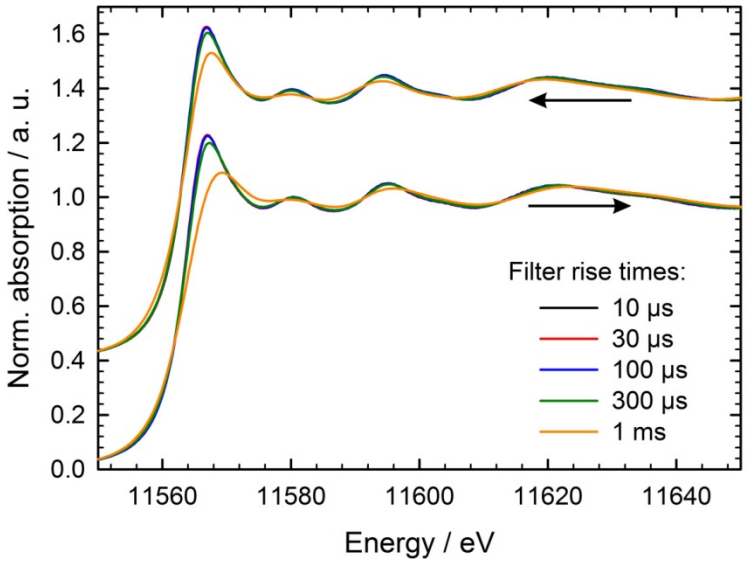

Figure 3.19: Measurements with 5 Hz crystal oscillation frequency and various filter rise times were performed at the Pt L_3-edge. The scan direction of the normalized Pt metal foil absorption spectra are indicated by the arrows, while the spectra are vertically shifted for clarity.

Rise times of current amplifiers

The settings of the current amplifiers are very important to optimize QEXAFS measurements. Especially the rise time, which is the time the signal requires to increase from 10 % to 90 % of the input signal, can be very helpful as it can be manually adjusted to filter out high frequency noise. However, the application of rise time filters is a mixed blessing. Sharp features in a spectrum, as e.g. the intense white line feature appearing right above the L-edges of transition metals, might be smeared out accidently. In most cases of EXAFS analysis this turns out to be a negligible effect, but in XANES analysis procedures this can cause serious problems, as soon as e.g. the acquired spectra have to be compared to spectra of reference materials measured with different settings. In Figure 3.19 spectra of a Pt metal foil measured at the Pt L_3-edge are shown, which were all measured with a constant crystal oscillation frequency of 5 Hz but with various filter rise times ranging from 10 µs to 1 ms. Up to 100 µs no differences in the spectra are observable, but with the rise time adjusted to 300 µs deviations appear in the white line intensity, while even the full XANES region is affected by distortions in the case of a selected rise time of 1 ms. The full scan range for the spectra shown in Figure 3.19 amounts to about 800 eV which leads to maximum scan speed of 6000 eV/s at the white line feature and of 12500 eV/s at the mean energy value of the spectrum. With the intrinsic energy resolution of a $Si(111)$ crystal at this energy, which amounts to about $\Delta E/E = 1.33 \cdot 10^{-4}$, the maximum feasible filter rise time t_{max} of the current amplifiers can be estimated by the formula

$$t_{max} \leq \left(\frac{\Delta E}{E}\right)\frac{E}{\dot{E}(E, E_0, E_A)} = \left(\frac{\Delta E}{E}\right)\frac{E}{2\pi f E_A\sqrt{1-\left(\frac{E-E_0}{E_A}\right)^2}}. \quad (3.2)$$

Here, E is the energy value, where the maximum energy resolution is required, which would be typically the absorption edge or the white line feature. E_0 is the mean energy value of the spectrum and E_A the energy range, which amounts to 400 eV in the present example. Accordingly, in the specific case of measuring the Pt absorption edge with 5 Hz the result for t_{max} is 222 µs, which is in a good agreement with the spectra shown in Figure 3.19, where the first deviations are observable with a filter rise time of 300 µs, while a value of 100 µs still yields decent results. It is thus shown that suitable filter rise times can and should be calculated prior to each experiment. Alternatively, it can also be advantageous to use the lowest achievable rise time for the acquisition of raw data and to apply software filters in the subsequent data analysis, which are much more flexible. Additionally, one has to be aware that there is a lower limit in the filter rise time depending on the chosen gain. For the Keithley 428 current amplifiers this lower limit amounts to 10 µs for gains of 10^6 and 10^7 V/A. However, the minimum rise time increases to 40, 100 and finally 250 µs for higher gains of 10^8, 10^9 and finally 10^{10} V/A [Kei99]. So if e.g. the measurements in Figure 3.19 shall be repeated with 20 Hz, amplifications of 10^8 V/A or less have to be used to not exceed the limits of the current amplifier which would elsewise cause deviations in the spectra.

3.3 QEXAFS data analysis software

The first sections of this chapter were dedicated to the topic of how to acquire as many spectra as possible of a reasonable quality. The invaluable scientific opportunities of such measurements were already discussed in section 2.3.3. However, the analysis of data files, which are typically consisting of several thousands of spectra, turns out to be rather tedious without the right software tools. For conventional EXAFS data analysis there is already excellent software available as e.g. WinXAS [Res98], the Athena/Artemis graphical user interface [Rav05] based on the IFEFFIT code [New01] or EXCURV [Bin98]. All these programs provide the functions required to analyze EXAFS spectra and some of them also include few options specifically designed for time-resolved EXAFS. However, they are beyond doubt not designed to conveniently deal with several thousand spectra. Thus, for many years the QEXAFS technique – at least in the subsecond time regime – has remained a somehow exclusive tool for those, who were skilled in programming. Unfortunately this is not the majority of users, who might rather want to use QEXAFS as complementary technique to better understand the physics, chemistry or biology of their sample systems.

For that reason, providing convenient and transparent software for the QEXAFS data analysis is a crucial advancement to further establish QEXAFS as a standard tool in material science.

In section 3.2.1 it was mentioned that the QEXAFS raw data files have file sizes in the order of several hundreds of megabytes up to several gigabytes. Such files, which typically contain four columns with about 10^6 - 10^9 rows, cannot be opened straight forward with common text editors or table calculation software as Excel, Origin or SigmaPlot, since these programs are limited by the random access memory of the computer. Reasonable QEXAFS software has to process the data files sequentially and to write intermediate results to the hard disc. Considering recent hardware developments as solid state discs, this is not a big deal with respect to the performance, but programming becomes more challenging. Additionally, the amount of required disc space is an issue, when considering concepts for storing a project. With several intermediate steps each project ends up with several huge data files, which in summation amount to about thrice the size of the original raw data file. If the user decides to create several projects with the same raw data to check out different settings, disc space in the order of several tens of gigabytes will be required for only one measurement, which was acquired in less than an hour of one entire beamtime.

Dealing with the huge number of spectra, which are generated during QEXAFS experiments, the challenge is not only to write reasonable algorithms. To a significant extent also the visualization of the data is an issue, since it is important to rapidly scan through the spectra and to find the regions of interest. On the other hand, the high numbers of spectra offer opportunities, which are exclusive for the QEXAFS technique and have certainly not yet been exploited to the full extent. In the following sections the QEXAFS data analysis software T-REX (Time-Resolved EXAFS analysis software) is presented, which is the result of almost four years of experience with the evaluation of various QEXAFS data sets, each one coming along with specific challenges of how to extract a maximum of information. It will be explained in detail, which functions were included and why they were considered as important. Many examples of these functions are given in the application chapter, where it is shown how scientific results can be obtained with T-REX. Thus, the description of software functions can also be regarded as a guidance, respectively a suggestion of receipts, how to proceed in the often not straight forward course of QEXAFS data analysis.

(a)

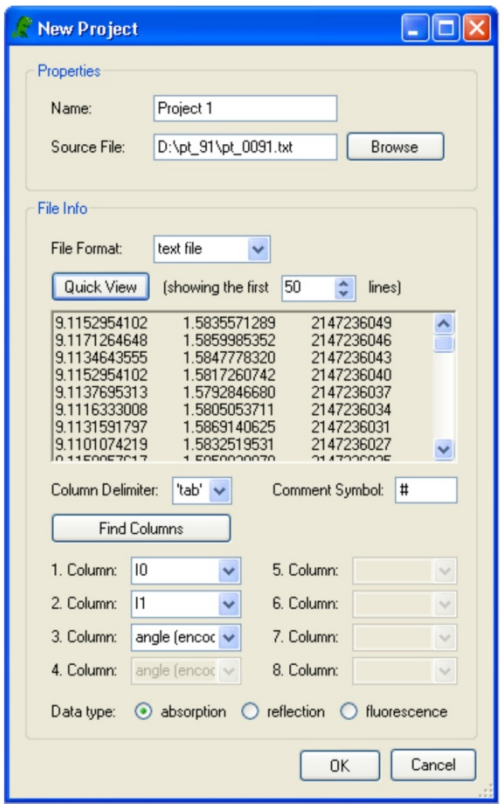

(b)

T-REX - chews up your QEXAFS data

Figure 3.20: (a) GUI for opening a new QEXAFS project: Selecting the raw data file, assigning the columns, choosing the measurement mode and naming the project are the required operations here, (b) icon/logo of the T-REX software.

3.3.1 General design considerations

The main goal of designing new software for QEXAFS data analysis was to grant access to the manifold information that can be extracted from QEXAFS data in a convenient way. Therefore, the GUI was designed rather simple as shown in various figures in the next sections (see e.g. Figure 3.22). On the left side, a tree view can be found, where all intermediate results and all steps performed during the data analysis are listed. This provides an overview of the performed steps and also allows navigating through the results by clicking on a specific step. A container with various tabs corresponding to the various steps of data analysis is found in the middle of the main window. All important settings and operations are located here, while a plot pane on the right side displays the results of each operation. The plot pane is an object taken from the ZedGraph class library, which is available under the LGPL[5] [JCh07]. Additionally, the plot window is linked to a horizontal scan bar, which allows conveniently skipping through the spectra with the mouse or with the arrow keys. This was recognized as a key feature to rapidly find the most interesting parts within the often confusing quantities of spectra.

[5] Lesser Gnu Public License

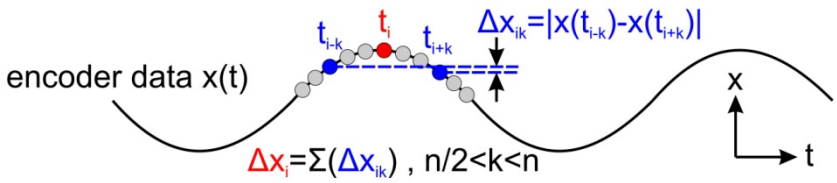

Figure 3.21: Drawing to explain the encoder splitting algorithm of T-REX: For each data point i close to a maximum or minimum the differences of each two neighboring data points within the same distance $|t_i - t_{i-k}| = |t_i - t_{i+k}|$ *are summed up in an adjustable interval with n/2<k<n. The data is split at the value* t_i *with the minimum sum* Δx_i.

Each QEXAFS raw data file is opened within a new project as shown in Figure 3.20. Thereby, it is possible to assign the columns, to choose the applied measurement mode and to assign a specific name to the project. These projects can be stored as binary file with a *.trx* file extension after each step of data analysis. All required settings of the software are stored within those files, so that it is possible to continue the data analysis after reopening the project. The amounts of data given by the raw data file in combination with the additional data generated by the analysis software are simply too huge to be also stored within these project files. Thus, the project files only work as long as they are not separated from the folder with the corresponding data files. The intermediate and final results are all stored as separate ASCII files, which can conveniently be imported by any plotting software. Alternatively, the graphs shown by the plot window can directly be exported to a printer. The various steps of data analysis and additional functions of the T-REX software will be described within the following sections.

3.3.2 Splitting and sorting the raw data

As explained in section 3.1.1, an angular value synchronized to each absorption value is acquired due to the application of a fast angular encoder inside the QEXAFS monochromator. This position value can be used to split the acquired data, to sort the spectra according to the scan direction and to accurately determine the energy value of each data point. Splitting the data is the very first step, before e.g. averaging over several spectra can be performed. In section 3.2.3 it was shown that a time shift between the encoder and the data of the detectors has to be considered and eventually corrected. This is best done during the first step, since data interpolation is required, which is most accurate before any data reduction is carried out. The herein presented software allows setting up time shifts for each channel individually, which is a reasonable approach, since each detector might exhibit a characteristic response time, as discussed in section 3.2.3. By applying time shifts to the raw data, each column is corrected with respect to the absolute measurement time via linear interpolation. During the splitting procedure it is also possible

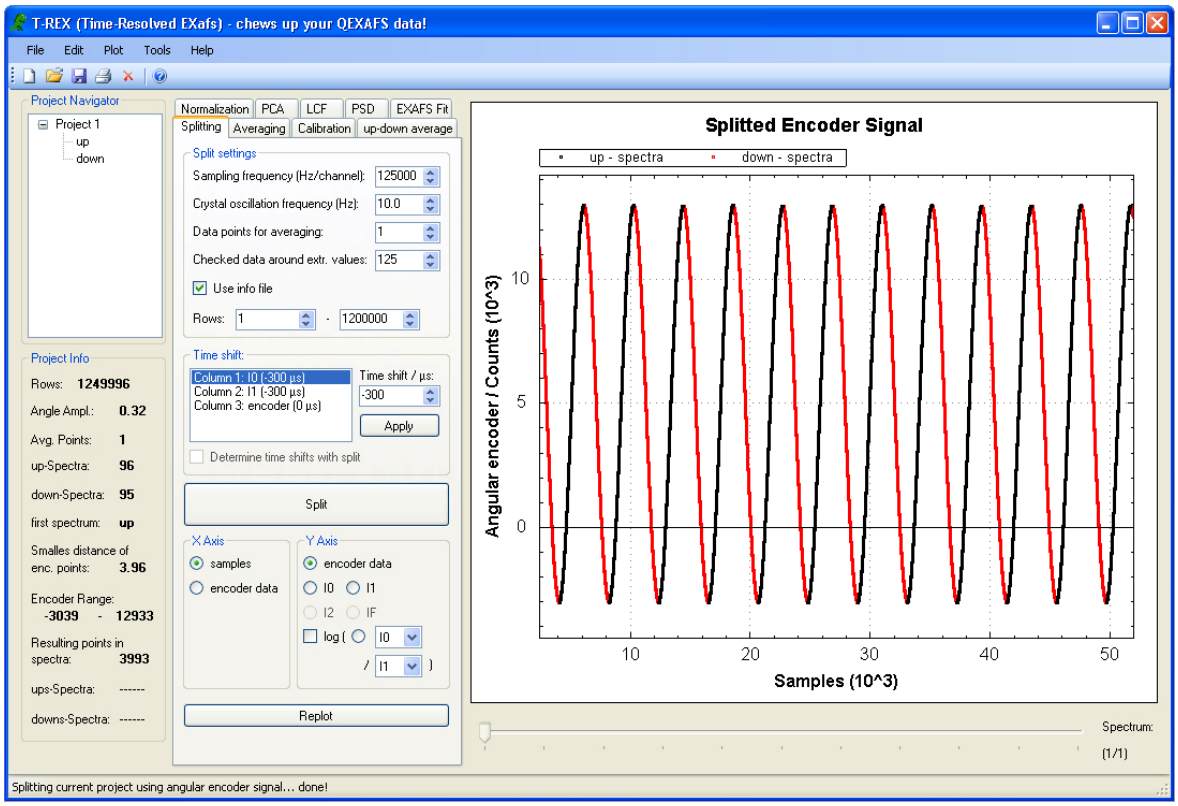

Figure 3.22: T-REX GUI for splitting the QEXAFS data: The field 'Checked data around extr. values' corresponds to the 'n' as defined in Figure 3.21. Additionally, it can be averaged over several data points and a time shift can be applied to each channel individually. After performing the splitting, the encoder signal is shown in the plot window, whereby the black parts correspond to the detected up-spectra and the red parts to the down-spectra.

to average over several data points, which is reasonable in cases, where the data density is significantly higher than actually required.

In order to split the data one possible approach is to fit the encoder signal with a sinusoidal function as suggested by Eq. (2.40). However, this approach encounters several difficulties. First of all, the file sizes are problematic for the fitting algorithm, but even more important is the fact that the new QEXAFS hardware presented in section 3.1.2 is flexible enough to perform scans with varying amplitude and frequency, which cannot be reproduced by a simple sinusoidal function. Thus, the more promising approach is to continuously move along the encoder data and thereby to look out for maxima and minima. The T-REX software checks a variable number of neighboring values at each encoder value and whenever these are all lower or all higher than the central value, this value will be considered as maximum or minimum.

One might think that it is sufficient to simply select the highest and lowest value in each oscillation period to determine the splitting positions. However, with high sampling frequencies several tens of values close to the extreme values might exhibit exactly the

same encoder value and can thus equally be considered as maxima or minima. Thus, for each candidate the difference of a selectable number of neighbor pairs (values with the same distance to the right and left side) are summed up as also explained in Figure 3.21. The value, where the summed up difference of neighboring pairs is lowest, is accordingly chosen as extreme value for symmetry reasons. This algorithm proved to be very stable and is even working for data files, where the encoder has lost some steps, which might happen either due to a bad hardware alignment of the encoder read head or due to frequencies that exceed the limits of the electronics. Furthermore, data sets with variable frequencies and amplitudes can be successfully processed by the algorithm as well. While the splitting operation takes some minutes to process a data file of some gigabytes, the adjustable number of checked neighbor values can be used to accelerate this step of data analysis. However, it has to be checked carefully, whether the results are still reasonable. Moreover, time should not be an issue at this point of data analysis, because generally it is sufficient to perform this step once per data file. In Figure 3.22 the GUI to perform the data splitting is shown. In the plot area it is possible to check, whether the splitting of the encoder data was successful, as the two directions detected by the algorithm are displayed in different colors.

3.3.3 Averaging/Smoothing spectra

Flexible averaging and smoothing operations applied to several subsequent spectra provide unique opportunities for controlling signal-to-noise ratios, especially when a high time-resolution is used, and can be seen as one of the most important steps in QEXAFS data analysis. The herein presented methods of signal analysis and processing can be found in various textbooks as e.g. [Kro91, Kam02, Wen04] and will be introduced for the application to QEXAFS here. Prerequisite is a rather high sampling frequency, since the data acquisition introduced in section 3.2 samples continuously and consequently yields slightly different energy values in each acquired spectrum. Thus, the data has to be interpolated on a uniform energy grid before averaging over several spectra can be initiated. Actually, it has to be decided for each data set individually, which sampling frequency is sufficient, but about 2000-5000 points for each full EXAFS spectrum covering ca. 1 keV have proven to yield a reasonable data point density. These points are not evenly distributed over the energy range in the raw data, as becomes clear when considering the non-linear crystal movement described by Eq. (2.40). Thus, lower sampling rates are not recommended. Furthermore, it is of advantage to acquire several additional spectra prior and after the actually interesting dynamic process during the performed experiment. This is not only important to avoid missing the process, but also because all filter techniques are working as (discrete) convolution of the measured spectra $x(t)$ with a specific kernel $h(t)$ according to

$$y(t) = \sum_{i=-\infty}^{\infty} x(t - t_i) \cdot h(t_i), \tag{3.3}$$

yielding the smoothed spectra $y(t)$. To avoid confusion, it has to be noted that here each spectrum is assigned to one constant time value t_i, although the spectra are actually scanned during a time interval Δt. However, this simplification is valid as long as only the spectra of one scan direction are considered for the averaging process, as it is the case in T-REX, where both scan directions are treated individually.

In QEXAFS applications a specific window width of M spectra is chosen for the kernel, because it is technically not feasible to use windows with infinite borders as suggested by Eq. (3.3). Accordingly, the kernel $h(t_i)$ is modified to

$$h'(t_i) = \begin{cases} h(i), & -\dfrac{M-1}{2} \leq i \leq \dfrac{M-1}{2} \\ 0, & else. \end{cases} \tag{3.4}$$

Since the spectra are measured at equidistant time intervals Δt, it is possible to replace t_i by i for an easier handling as long as it is kept in mind that i is actually $i \cdot \Delta t$. As a result, when starting the measurement with the first spectrum at $i = 0$, the first filtered spectrum contributing to $y(t)$ can be calculated for $i = (M-1)/2$. The same considerations have to be made at the end of the measurement at $i = N$, which means that the number of resulting spectra with respect to the measured spectra N is reduced by $M - 1$.

All averaging/smoothing processes over several spectra can be technically understood as low pass filtering. One simple approach for filtering is to sum up a certain number of spectra, which is practically a trade-off between time resolution and statistics. Thereby, the total number of spectra and thus the time resolution are reduced, which might be tolerable or even desirable in many cases. However, generally it is preferable to smooth the spectra and maintain the number of spectra, as becomes clear by considering the drawing in Figure 3.23. Here it is demonstrated that depending on where the averaging is started and depending on the original signal one gets completely controversal results. This effect is negligible in the case of random noise, where summing up spectra serves well as data reduction procedure. But in order to get unambiguous results it is preferable to restart the averaging process at each measured spectrum and display all resulting averaged spectra, as also illustratively displayed in Figure 3.23 with the orange circles. Technically, this can be understood as averaging with a moving window, which is equivalent to the discrete convolution of the spectra along the time axis as explained in Eq. (3.3). A rectangular function

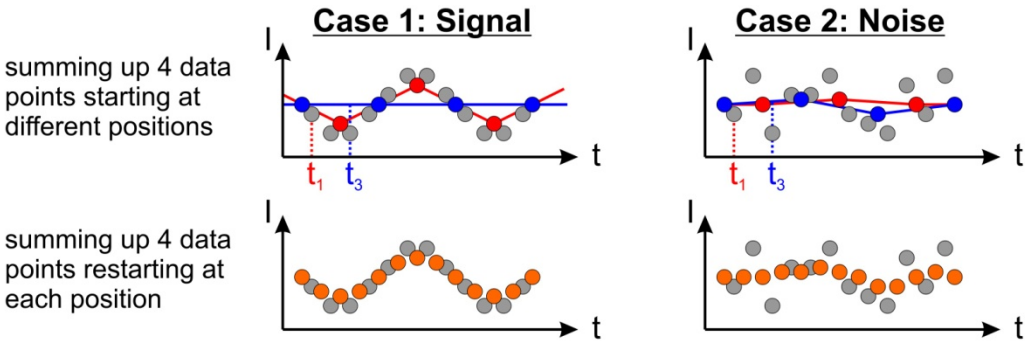

Figure 3.23: Scheme to demonstrate that summing up several spectra can lead to different results depending on the start value and the shape, respectively the frequencies of the signal. The grey circles represent the original data; the colored circles are the results of the specified averaging processes.

$$h_{rect}(t) = \frac{1}{M} \tag{3.5}$$

with a fixed width M is one possible kernel, which is displayed in Figure 3.24a (black line) and which was applied in Figure 3.23 to obtain the orange circles. The approach is comparable to summing up several spectra, but the process is restarted at each spectrum. Alternatively, a Gaussian window can be used as kernel

$$h_{Gauss}(t) = \frac{1}{\Sigma_{Gauss}} \frac{3}{\sqrt{2\pi}M} e^{-\frac{9t^2}{2M^2}}, \tag{3.6}$$

which is quite commonly used for digital low pass filtering and is also displayed in Figure 3.24a (red line). In this case, the window width M corresponds to a $\pm 1.5\sigma$ range, which is covering about 87% of the integrated Gaussian bell function. Furthermore, it is important to add the normalization factor, which can be calculated by

$$\Sigma_{Gauss} = \sum_{i=-\frac{M-1}{2}}^{\frac{M-1}{2}} h_{Gauss}(i). \tag{3.7}$$

A third kernel, also accessible in T-REX, is given by the so-called sinc-function in combination with a 'Hanning'-window

$$h_{sinc}(t) = \frac{1}{\Sigma_{sinc}} \cdot \underbrace{\frac{1}{2}\left(1 - \cos\left(\frac{2\pi(t - \frac{M}{2})}{M}\right)\right)}_{Hanning-window} \cdot \underbrace{\frac{\sin(2\pi f_g t)}{2\pi f_g t}}_{sinc-function}. \tag{3.8}$$

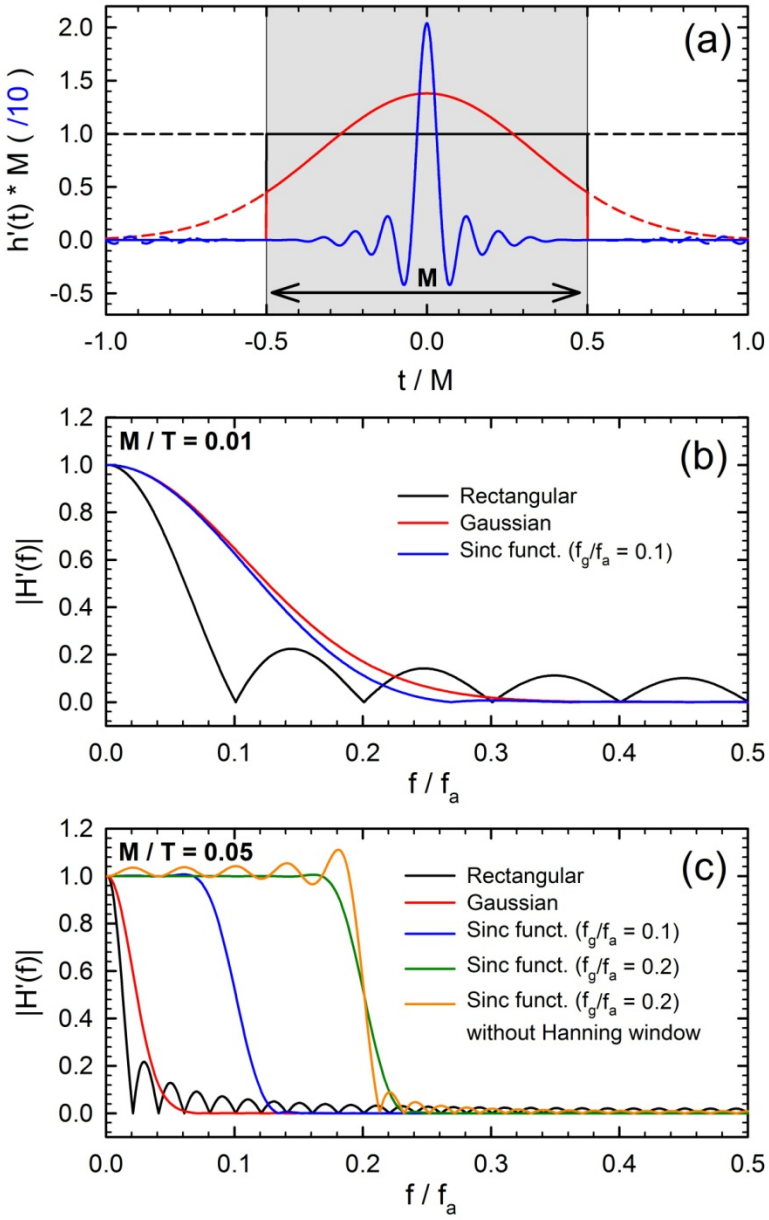

Figure 3.24: Rectangular, Gaussian and sinc-function filter in time and frequency space: (a) convolution kernel h'(t) of rectangle (black), Gaussian bell (red) and sinc-function (blue) with h(t) displayed with dashed lines, (b) transformation of the filters into frequency space with a window width of M/T=0.01 and (c) transformations with M/T=0.05 and two different cut-off frequencies for the sinc-function filter, which is also displayed without multiplied 'Hanning' window.

By displaying this filter in time space, as it is also done in Figure 3.24 (blue line), it is difficult to recognize the practical value of the sinc-function and the additional parameter f_g. However, this is a different matter in the frequency space, as explained in the next paragraph. The Σ_{sinc} normalization factor is calculated in a similar way as for the Gaussian kernel (see Eq. (3.7)).

In order to better understand the various kernels displayed in Figure 3.24a, i.e. how they affect the measured data, it is useful to study them in frequency space. This can be achieved with a discrete Fourier transformation of the kernels according to

$$H(f) = \sum_{n=-\infty}^{\infty} h'(t) e^{-in2\pi ft}. \tag{3.9}$$

In Figure 3.24b the amplitude $|H(f)|$ is shown for all presented kernels. The number of data points was set to $N = 1000$ and the window width to $M = 10$, respectively $M = 50$, for the demonstrated examples. According to the sampling theorem, the maximum analyzable frequency is given by $T/(2N)$, where T is the time during which the N data points were measured, i.e. $T = N \cdot \Delta t$. For simplicity reasons T was also set to 1000 in this example. It can be observed that the rectangular filter exhibits the strongest low pass character of all filters, when using similar window widths. On the other hand, it cannot be avoided that higher frequencies pass the filter, which is due to the fact that the borders of this filter are not approaching the zero level (Gibbs phenomenon). The Gauss filter exhibits a weaker low pass character than the rectangular filter, but here the higher frequencies are entirely suppressed. Thus, the Gauss filter yields the better results in most cases, except for measurements, where only a very small window width can be used and a strong low pass character is required.

Gauss and rectangular filters can both be seen as low pass filters, but actually they are affecting all frequencies, so that even for the lowest frequencies a certain degree of smoothing is achieved. To only suppress high frequencies, without affecting the lower ones, a rectangular shape in the frequency space is required with an adjustable cut-off frequency. This can be achieved with the sinc-function filter and the adjustable parameter f_g introduced in Eq. (3.8), as shown in Figure 3.24b for f_g equal to 0.1 and 0.2 of the maximum frequency $f_{max} = T/N$. Compared to the other filters, the sinc-function filter exhibits the advantage that the user can decide, which frequencies are suppressed, while the sharpness of this cut-off is adjustable by the window width. On the other hand, a broad window is required to realize a sharp cut-off, while for narrow windows the frequency characteristics are rather similar to the other filters. The combination of the sinc filter with a ‘Hanning’-window is very important, as also shown in Figure 3.24c, since otherwise overshoots appear in the frequency space, especially close to the cut-off frequency, but to a lower extent also at all other possible frequencies. In section 4.1.2 a practical example with the different averaging processes is given and it is also studied in more detail, how the results are affected. Thereby, ideas are introduced how to combine the results obtained with the application of various filters to shed light into the course of a reaction.

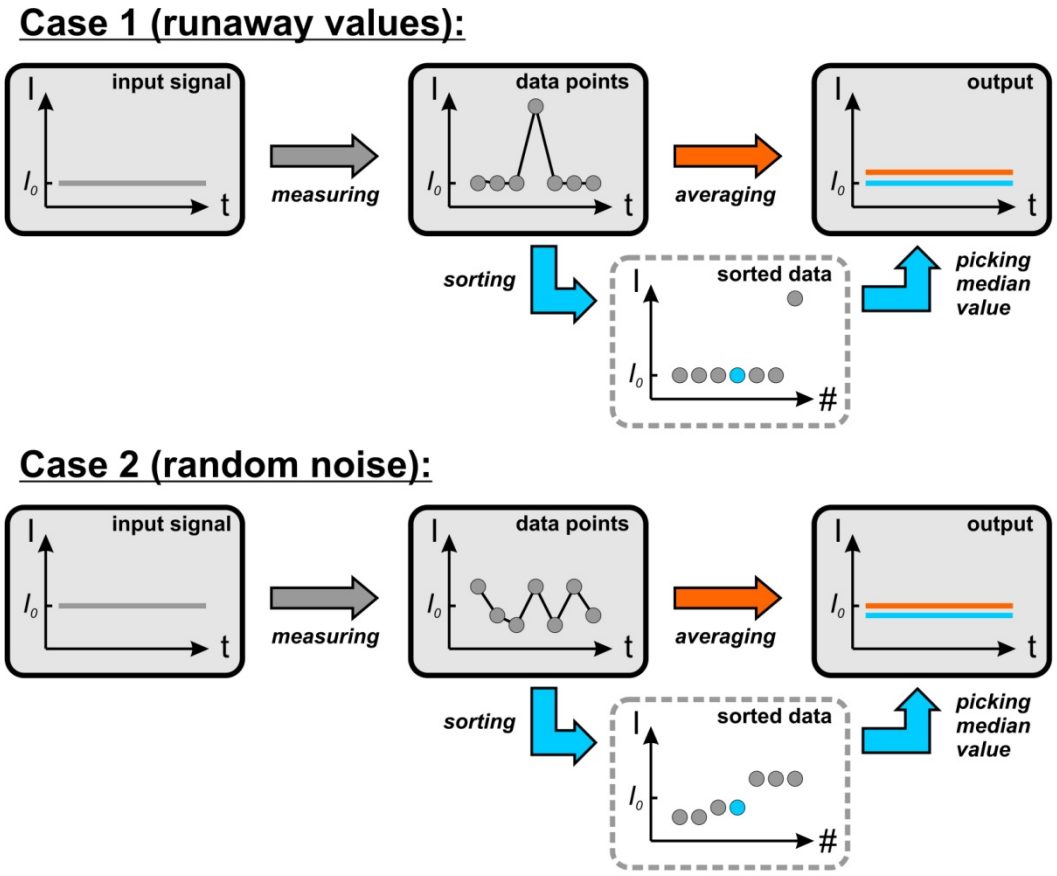

Figure 3.25: Schematics to explain the advantages and disadvantages of the median filter and the low pass averaging filter in the cases of runaway values and random noise.

While low pass filtering by summing up several spectra is generally very effective to improve data quality, in some cases it can unfortunately also make the situation worse. Apart from the obvious disadvantage that one might cut off frequencies which are not accounted to noise but to the dynamics of the investigated process, the occurrence of runaway values is problematic. This is shown in the first case drawn in Figure 3.25. When averaging over several data points including a runaway value is performed, the result is affected by this value as shown by the final orange line, which is located slightly above the original input signal. Such runaway values can be caused by sudden electrical disturbances in the data acquisition electronics, by a sudden vibration of the sample or naturally in liquid sample environments where particles or bubbles pass the beam path. For these cases a median filter was implemented in T-REX, which works, as also explained in Figure 3.25 via the path of the blue arrows. Instead of averaging, the data points are first sorted with respect to their values and thereafter the median value is picked as result yielding the blue line in Figure 3.25. While the median filter can help to achieve much better results in the case of runaway values, for random noise the low pass filtering is the better choice as explained by the second case drawn in Figure 3.25. Here the noise is randomly distributed around the original signal and it thus makes more sense to improve the statistics by

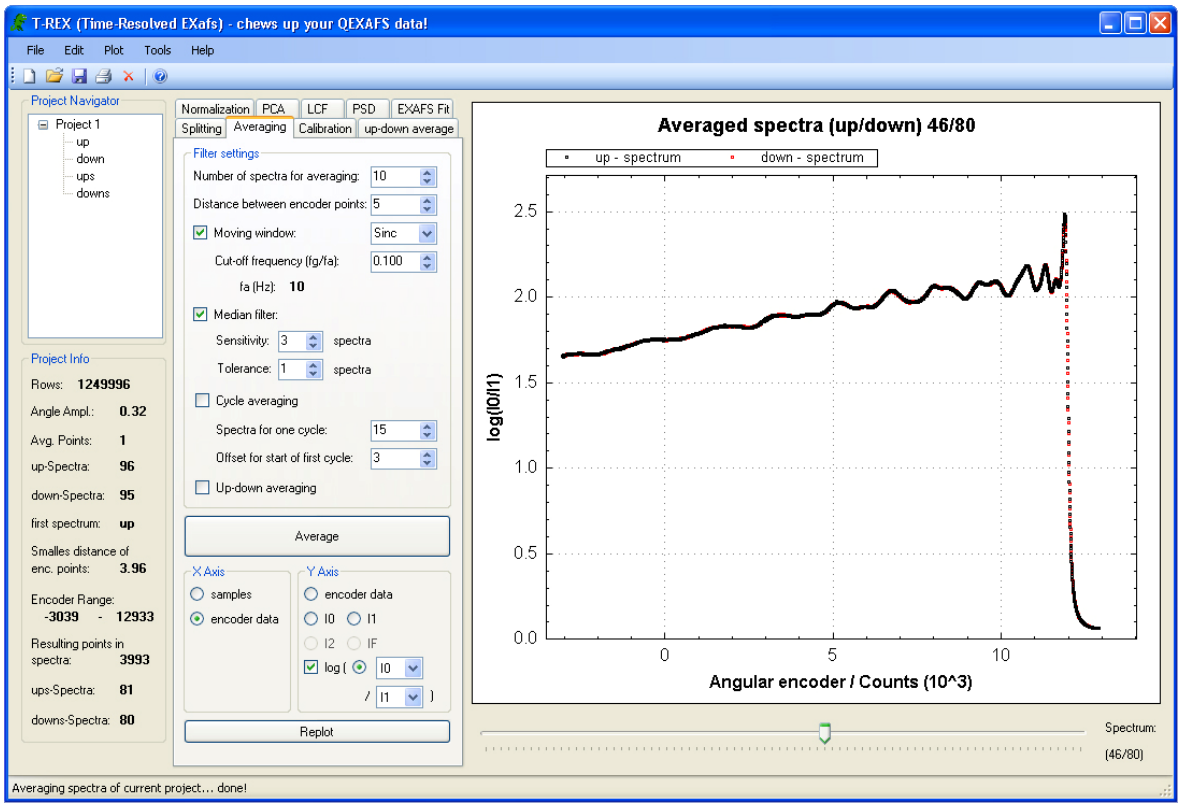

Figure 3.26: T-REX GUI for setting up the filters that can be applied to the QEXAFS spectra: Low pass filter, median filter, cycle averaging and averaging over both scan directions can be initialized and performed from within this tab.

summing up all data points. In section 4.1.1 the application of the median filter is demonstrated and it is shown that the median filter can be used to effectively suppress runaway values, which were not eliminated by low pass filtering. Such a procedure can grant access to data which was not analyzable before and is thus a valuable addition to the QEXAFS data analysis.

The GUI to initialize the filtering of QEXAFS spectra is shown in Figure 3.26. The uppermost part of the working tab includes the settings of the smoothing filters as presented in the beginning of this section. Thereafter, the median filter can be set up with a ‘Sensitivity’ value, which is defining how many neighboring spectra are considered for sorting before picking the median value. Additionally, a ‘Tolerance’ value can be selected for those cases, where it is wished that the actual value will only be replaced by the median value, if the actual value is e.g. located at the uppermost or lowermost end of the sorted values. Of course this option makes only a difference, when more than three values are compared, respectively when the ‘Sensitivity’ is higher than one. In addition to the low pass and median filter options, it can also be averaged over several cycles in the case of modulated experiments. This option will be further discussed in section 3.3.7. Furthermore, it can be averaged over both scan directions, which should only be done after properly correcting for the time shift of the detectors within the data splitting step, as explained in

the previous section. Otherwise, it is recommended to average over both scan directions after performing the energy calibration. This is also possible in T-REX within the 'up-down average' tab. It is important to note that the various filters can also be combined. Thus, it is e.g. possible to first sort out run-away values with the median filter, before averaging over many spectra is performed to reduce random noise. This was e.g. done to analyze data in section 4.1.1.

3.3.4 Energy calibration

The energy calibration of QEXAFS spectra is performed directly after the averaging/smoothing step. The minimum of the first derivative of sample or reference spectra as function of the encoder signal is determined to roughly locate the absorption edge[6]. In the region of the so-determined minimum the second derivative can be further calculated and the zero crossing can be determined. The corresponding value is selected as final encoder value of the absorption edge and is thus assigned to the reference energy value. In Figure 3.27 the GUI for these operations is shown with an example of a calculated second derivative displayed in the plot pane. An additional smoothing algorithm can be applied to noisy data, which helps to unambiguously determine the edge position. This smoothing is technically similar to the convolution with a Gaussian bell function as explained in the previous section, but here it is important to note that the smoothing is performed as function of energy and not time. It is also important to note that this smoothing is only temporarily applied to the data in order to find the absorption edge and does not affect the final calibrated spectra. However, as explained in section 3.2.3, smoothing the spectra along the energy axis, which is actually also a function of time in QEXAFS due to the scanning mode, might be preferable to hardware rise time filters provided e.g. by the current amplifiers. Thus, an additional function is included to permanently apply a Gaussian filtering to the data along the energy coordinate in parallel to the performed calibration process. In future upgrades, additional low or band pass filters could be implemented here, in order to e.g. filter out certain disturbing frequencies with band pass filters.

With well-designed encoder hardware and adapted electronics it is sufficient to carry out the calibration for one spectrum and to use the thereby determined position value to calculate the energy scale for all other spectra. However, it is also possible to carry out the calibration process for all spectra individually, which takes significantly more time, but can e.g. be used to determine the edge position of each sample spectra most accurately with respect to the reference sample. Such precise edge position determination provides important information about changes in the oxidation state of the sample during the

[6] Note that increasing encoder signal corresponds to decreasing energy.

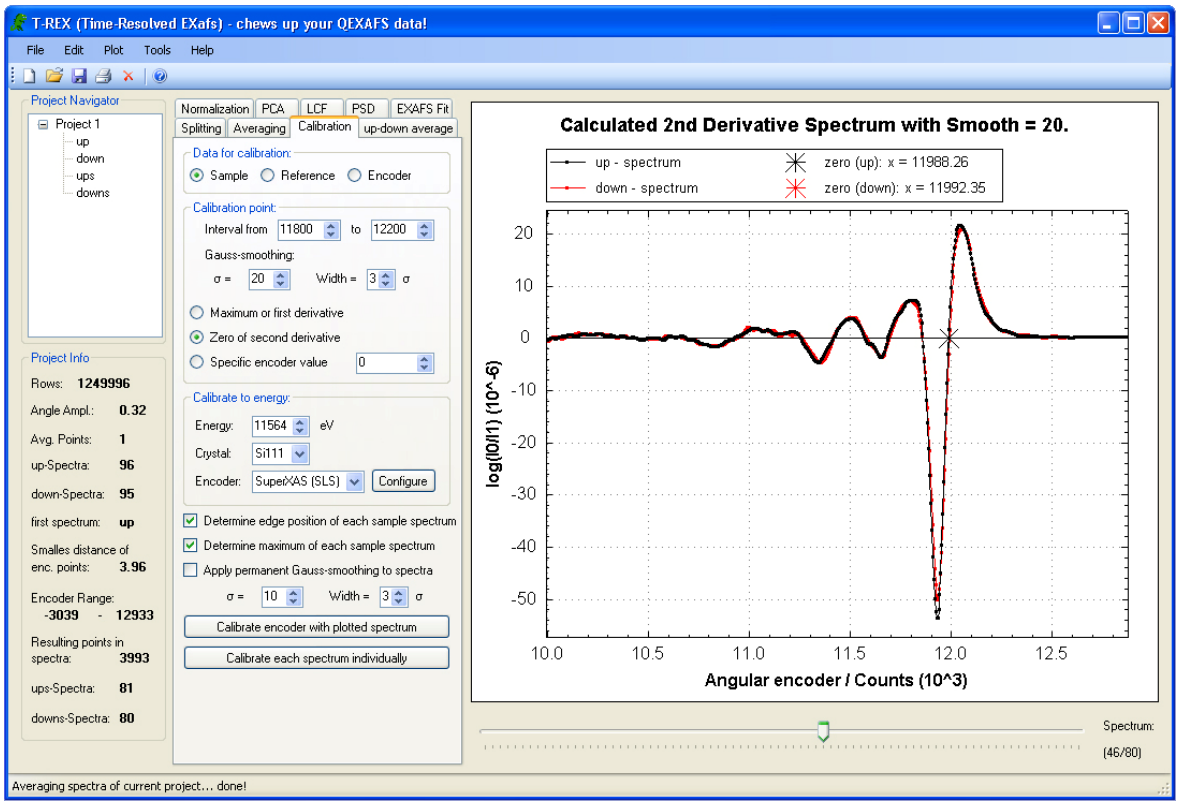

Figure 3.27: T-REX GUI for calibrating the QEXAFS spectra.

experiment as also discussed in section 2.1.2 and shown for a QEXAFS application example in [Oll12]. Sometimes it is also helpful to track the maximum of the spectra as function of time. Especially, for the *L*-edges of transition metals the white line intensity is strongly affected by the oxidation state so that very small changes in the oxidation state can be detected. An example of such an approach is given in section 4.1.3, where the white line intensity of the Pt L_3-edge was investigated to study a Pt-containing catalyst during oscillations of CO oxidation. Thus, a file with the corresponding data can also be created during the calibration process in T-REX.

3.3.5 Principal component analysis and factor retention criteria

The principal component analysis (PCA) is a statistical tool to extract the number of significant linear independent components in a set of data. Applying PCA to time-resolved XANES spectra is a convenient approach in order to evaluate, how many independent chemical components appear during a specific process (see e.g. [Fay92, Fer95, Res98, Stö12a]). The steps of PCA are e.g. described in detail in [Dil84, Smi02] and were correspondingly implemented within the T-REX software. For this purpose, the variance-covariance matrix of the QEXAFS data has to be determined. The data should be present as m vectors A_k $(k = 1, \ldots, m)$ corresponding to m measured spectra each one consisting

of n data points a_{kl} $(l = 1, \dots, n)$ on a uniform energy grid. After calculating the mean corrected data

$$a_{kl}^{*} = a_{kl} - \bar{a}_k = a_{kl} - \frac{1}{n}\sum_{i=1}^{n} a_{ki} \tag{3.10}$$

the elements of the symmetric $m \times m$ variance-covariance matrix Σ can be calculated via

$$c_{kk'} = \frac{1}{n-1}\sum_{i=1}^{n} a_{ki}^{*} a_{k'i}^{*}, \qquad \Sigma = \begin{pmatrix} c_{11} & \cdots & c_{1m} \\ \vdots & \ddots & \vdots \\ c_{m1} & \cdots & c_{mm} \end{pmatrix}. \tag{3.11}$$

By computing the eigenvectors of Σ an orthogonal basis is obtained, whereby the eigenvector with the highest eigenvalue represents the direction of the strongest correlation in the data and the one with the lowest eigenvalue represents the direction of lowest correlation. Thus, sorting and studying the eigenvalues of the variance-covariance matrix can be effectively used to decide how many independent components actually contribute to the input data. Defining an orthogonal matrix P, where the j^{th} column is the j^{th} eigenvector of Σ, leads to the relation

$$\Sigma = P\Lambda P^{-1} \tag{3.12}$$

where Λ is a diagonal matrix with the m eigenvalues of Σ as diagonal elements, while all other elements are zero. Since Σ and Λ are trace invariant and additionally the trace is equal to the sum of squared variances as well as the sum of all eigenvalues, normalizing the eigenvalues with respect to the trace directly yields the proportion of the corresponding eigenvector to the data set.

After deciding how many independent components contribute to the data, it is possible to reconstruct the data using only these selected components. First, the eigenvectors of the p chosen components are used as columns of a new $m \times p$ matrix R. Accordingly, the final reproduced data matrix $\tilde{A}$ contains again m spectra as columns and can be calculated via [Smi02]

$$\tilde{A}^{T} = R(R^{T}A^{*T}) + \bar{A}, \tag{3.13}$$

where $A^{*} = (A_1^{*}, \dots, A_m^{*})$ is the matrix with the m mean-corrected spectra as columns and $\bar{A}$ contains all the averaging data $\bar{a}_k$ required to reverse the mean value correction as previously performed according to Eq. (3.10).

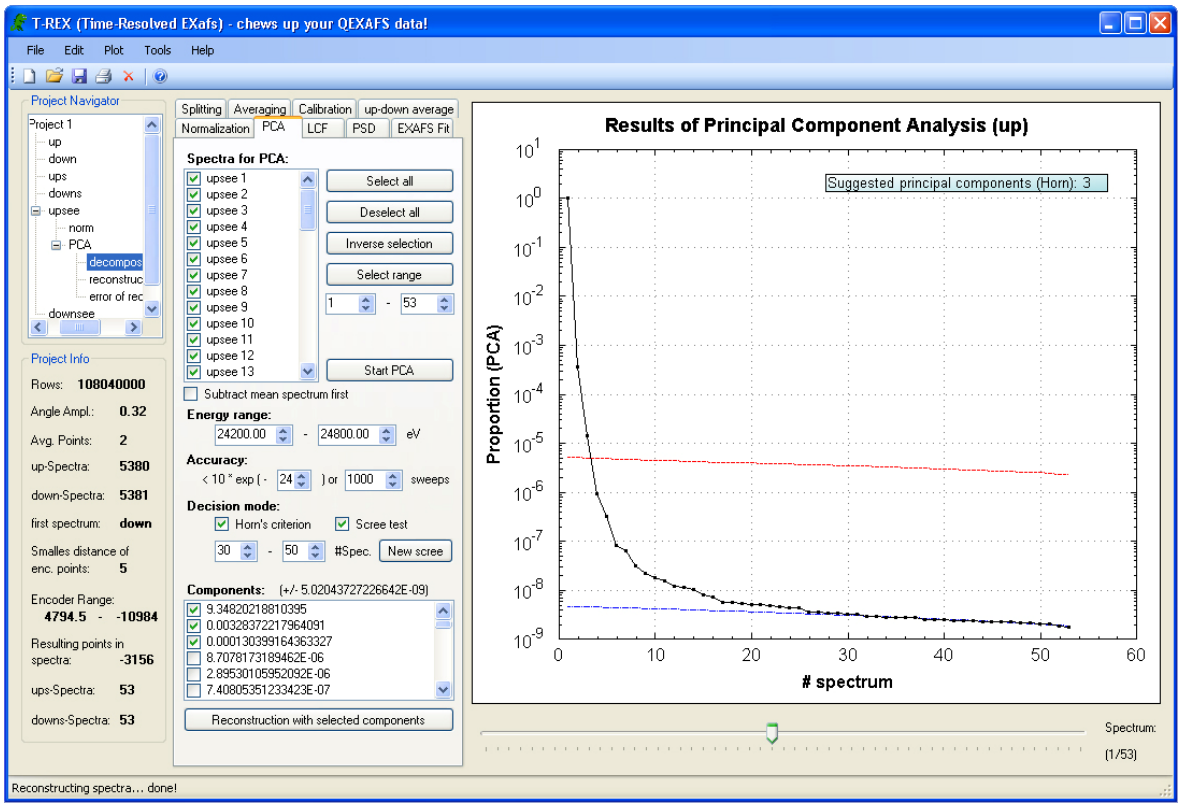

Figure 3.28: T-REX GUI to perform PCA with a selectable number of spectra in an adjustable energy range: The example is taken from a measurement at the bottom of the cell used to study the Heck reaction in section 4.1.1 (see Figure 4.12, blue line).

While the PCA is a well-established and invaluable procedure in many different fields as e.g. criminology and psychology, there is still an ongoing discussion about the interpretation of the results concerning the component retention criteria. A thorough overview over this topic is given e.g. by Hayton *et al.* [Hay04]. The criteria to decide, whether a component is significant are very important to prevent misinterpretations of the PCA results, which are very often not unambiguous. As a matter of fact, no decision criterion yields correct results in 100% of all cases. This is easy to understand considering components which appear in a very small amount compared to the noise level. Parallel analysis (PA) is one criterion and was introduced by Horn [Hor65]. It is based on the idea of constructing a second data set with the same dimensions as the original set, however filled with random noise. Afterwards the PCA is performed on both data sets and only components with eigenvalues above the ones resulting from the random data set are considered as significant.

PA was acknowledged as the criterion which yields correct results in most cases [Hay04] followed by the scree plot criterion [Cat66], which tends to overestimate the number of components. To apply the scree plot criterion the tail of the sorted eigenvalues of the variance-covariance matrix is fitted linearly and the first few components deviating from

this linearity are recognized as significant. Each criterion might be favorable depending on the specific data so that both criteria were implemented in T-REX. It is highly recommendable to check both criteria and to compare the results. As soon as there are inconsistencies, these should be discussed. Thereafter, to further check the results it is also a reasonable approach to reconstruct the spectra with the chosen number of components and to analyze the deviations between reconstructed and measured spectra. The curve representing these deviations should contain no significant maxima in the course of the reaction, which would indicate that not enough components were considered. This approach was e.g. presented and explained by Wang *et al.* [Wan08]. The importance of this approach becomes clear by considering that the input data for the PCA in QEXAFS are no random spectra but spectra as function of time, so that a kind of correlation can be found in the data. However, such correlation is not taken into account by the PCA algorithm. Thus, even small changes, which are recognized as noise by the retention criteria, might be actually an additional component, when it is possible to localize them in a specific time interval. In section 4.1.2, a complete PCA was performed with the tools presented here and the results and their interpretation are discussed in more detail.

The corresponding GUI to perform PCA is shown in Figure 3.28. The user can select the spectra that are considered by the PCA in a check list and also adjust the considered energy range. The most time consuming task of the PCA algorithm is to determine the eigenvalues. Thus, in T-REX it is possible to adjust the accuracy of the algorithm, which allows calculating the eigenvectors even for matrices corresponding to a few hundred spectra in a reasonable amount of time. Prior to the PCA, the user can choose the retention criteria. Since another PCA on a matrix with the same dimension as the one with the measured data has to be performed for PA, twice the calculation time has to be considered. The scree plot criterion can also be applied after performing the PCA and the user can arbitrarily adjust the borders for the scree fit. After performing the reconstruction with a selected number of eigenvalues, the reconstructed spectra can be plotted as well as the deviations between the reconstructions and the original data.

3.3.6 Linear combination analysis

With the help of PCA it is possible to narrow down the number of independent components that contribute to the investigated process. However, to identify these components the LCA is a more reasonable approach, which additionally yields the weights of the contributing components. Thereby, the measured XANES spectra are fitted with a linear combination of XANES spectra of well-defined reference materials. In T-REX all required parameters can be set up conveniently inside the LCA tab, which is exemplarily shown in Figure 3.29. The functions behind this GUI are mainly taken from the IFEFFIT package, which already provides all required algorithms [New01]. After normalizing the

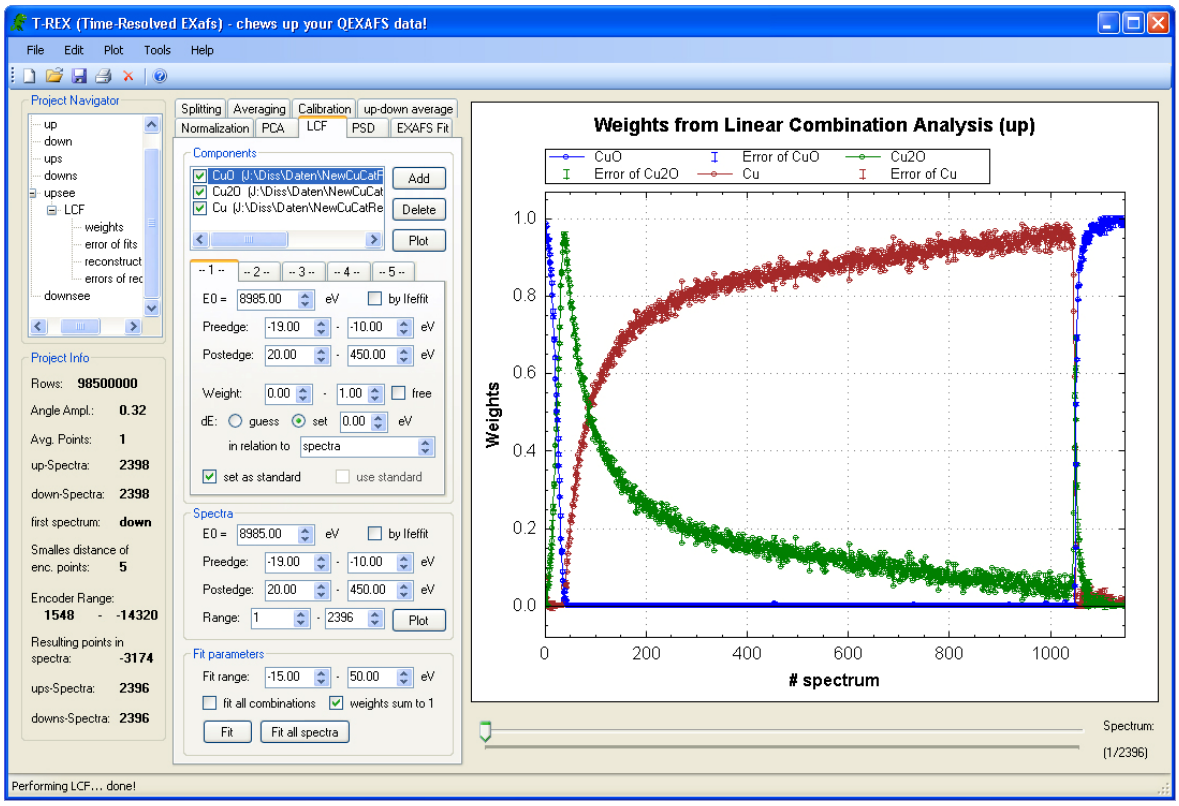

Figure 3.29: T-REX GUI for performing LCA fits for all spectra in the project with selected reference spectra. The reduction and oxidation behavior of supported Cu/Al_2O_3 is monitored here (see section 4.1.4 for more details)

measured spectra, it is possible to upload up to five reference spectra into the software. Thereafter, the references have to be normalized, possibly with the same parameters that were already used for the QEXAFS data, before the LCA process can be started. The software allows performing the LCA for a single spectrum in order to check, whether the correct references were considered, or respectively for as many spectra as required to follow the weights of each component as function of time. In the latter case an output file is produced with the results, which are also accessible via the tree view on the left hand side of the T-REX working area. Primarily, the LCA weights and the corresponding errors as function of time are plotted. However, it is also possible to plot the mean square deviation between fit and data as function of time, which can be also very helpful to analyze a process, as e.g. shown in section 4.1.3. Apart from that, several examples for the application of LCA in QEXAFS are given in chapter 4.

3.3.7 Phase-sensitive detection

Phase-sensitive detection (PSD) is a difference spectroscopy technique applicable to systems under observation that can be modulated in a reproducible way by a periodic excitation induced e.g. by varying temperature, pressure or gas composition. After applying an excitation with a defined period, it is possible to separate the measured data

into an ac and a dc contribution. The ac contribution consists of the basic frequency of the modulation plus higher harmonics, while the dc part contains all other frequencies that cannot be linked to the modulation and are thus considered as background signal. Subtracting the dc signal from the rest is then equivalent to removing all signals that can be unambiguously attributed to noise, which is the basic idea of modulation excitation spectroscopy (MES). Additionally, with PSD it is possible to investigate the phase lags and the amplitudes of the responses to the modulation that appear in the spectra. Introducing a controllable phase parameter ϕ_{PSD} and varying this parameter leads to a phase-resolution which allows distinguishing between different signals corresponding to different species. Considering e.g. an oxidation process with one intermediate step, the two transitions will exhibit different kinetics and thus different phases with respect to the excitation.

The theory of phase-sensitive detection was evaluated in many details and with many application examples in several references, mainly dealing with the application of PSD in infrared spectroscopy [Bau01, Ura06, Ura08]. A short summary of the theory based on the mentioned references will be given here, before the application in QEXAFS is discussed in more detail. Basically, all required theory is included in Fourier's theorem, which states that every periodic function, as e.g. the modulation of the system under observation, can be expressed as Fourier series (FS) according to

$$f(t) = a_0 + \sum_{k=1}^{\infty} [a_k \cos(k\omega t) + b_k \sin(k\omega t)] \tag{3.14}$$

with the frequency $\omega = 2\pi f = 2\pi/T$ where T is the period of the modulation in this case. The coefficients a_0, a_k and b_k are the Fourier coefficients, which are given by

$$a_0 = \frac{1}{T}\int_0^T f(t)dt, \tag{3.15}$$

$$a_k = \frac{2}{T}\int_0^T f(t)\cos(k\omega t)\,dt; \quad k = 1,2,\dots, \tag{3.16}$$

$$b_k = \frac{2}{T}\int_0^T f(t)\sin(k\omega t)\,dt; \quad k = 1,2,\dots. \tag{3.17}$$

The a_0 coefficient is the dc part mentioned above, while a_k and b_k are the contributions to the ac part. In terms of amplitude and phase lag $f(t)$ can be rewritten as

$$f(t) = a_0 + \sum_{k=1}^{\infty} c_k \sin(k\omega t + \varphi_k) \tag{3.18}$$

with c_k and φ_k given by

$$c_k = \sqrt{a_k^2 + b_k^2}\,, \qquad \varphi_k = \tan^{-1}\left(\frac{a_k}{b_k}\right). \tag{3.19}$$

Applying the modulation $f(t)$ to the sample during EXAFS measurements means that the time- and energy-dependent X-ray absorption $A_i(E,t)$ of each species i in the sample can also be written as FS. The overall X-ray absorption of the sample with N species is then given by

$$A(E,t) = \sum_{i}^{N}\left(A_{0,i}(E) + \sum_{k=1}^{\infty} A_{k,i}^{90^\circ}(E)\cos(k\omega t) + A_{k,i}^{0^\circ}(E)\sin(k\omega t)\right). \tag{3.20}$$

$A_{0,i}(E)$, $A_{k,i}^{90^\circ}(E)$ and $A_{k,i}^{0^\circ}(E)$ are the Fourier coefficients which are calculated in a similar way as already demonstrated for the modulation in Eq. (3.15) - (3.17). Eq. (3.20) can also be written in terms of amplitude and phase lag:

$$A(E,t) = \sum_{i}^{N}\left(A_{0,i}(E) + \sum_{k=1}^{\infty} A_{k,i}(E)\sin\left[k\omega t + \varphi_{k,i}(E)\right]\right). \tag{3.21}$$

In phase-sensitive detection $A(E,t)$ is multiplied with a sine function which inhibits the controllable phase angle ϕ_k^{PSD} before performing a normalized integration, yielding the so-called phase-resolved modulation spectrum

$$A_k^{\phi_k^{PSD}}(E) = \frac{2}{T}\int_0^T A(E,t)\sin(k\omega t + \phi_k^{PSD})\,dt \tag{3.22}$$

with the specified phase angle ϕ_k^{PSD} and frequency $k\omega$. After a few more conversions using trigonometric relations, the phase-resolved modulation spectrum can be re-written as

$$A_k^{\phi_k^{PSD}}(E) = A_k^{0^\circ}(E)\cos(\phi_k^{PSD}) + A_k^{90^\circ}(E)\sin(\phi_k^{PSD}) \tag{3.23}$$

or with phase and amplitude as

$$A_k^{\phi_k^{PSD}}(E) = A_k(E)\cos[\varphi_k(E) - \phi_k^{PSD}]. \tag{3.24}$$

It is important to note that all required information to perform PSD is actually included in the Fourier coefficients $A_k^{0^\circ}(E)$ and $A_k^{90^\circ}(E)$ for each order k.

It was already mentioned that PSD has been successfully applied in time-resolved IR spectroscopy and recently the application was also extended to Raman spectroscopy and XRD [Ura11]. Within this work, it will be discussed whether and how PSD might be a useful technique for QEXAFS data analysis. First approaches were carried out to analyze time-resolved EXAFS data of processes excited by a periodic modulation in [Stö09b], while first attempts to use PSD spectra were presented by Ferri et al. [Fer10]. The authors claimed that MES could be used to drastically reduce noise with the calculation of 1st order PSD difference spectra according to Eq. (3.22). The resulting spectra were compared to difference spectra of well-defined reference materials to analyze the investigated catalytic reaction. However, in order to properly evaluate the noise reducing capabilities of this approach, it is important to compare the results obtained with PSD to those that can be obtained with other smoothing techniques as presented in section 3.3.3. This is done in section 4.1.4 with the application on two complementary catalytic experiments, one with very small but slow and one with very fast but significant variations in the spectra.

In contrast to the approach presented by Ferri et al. [Fer10, Fer11], in T-REX Eq. (3.22) is not directly applied to the absorption data. Instead the Fourier coefficients according to Eq. (3.15), (3.16) and (3.17) are calculated. This enables the user to easily advance to the PSD spectra via Eq. (3.23), while it is also possible to remain in time dimension by reproducing the spectra via FS according to Eq. (3.14). It has to be noted that the FS approach is exactly as effective as the PSD approach as long as it is only aimed on investigating the system with the frequencies of the excitation. Furthermore, by correctly calculating the a_0, it is also possible to add this dc part to the PSD results afterwards, so that there is absolutely no reason to end up with difference spectra, which cannot be further processed with the conventional analysis tools that are typically applied to absorption spectra.

As recognizable in Eq. (3.20), the MES calculations are all performed for each energy value separately and correspondingly an individual set of a_0, a_k and b_k coefficients is obtained at each energy value of the acquired spectra. Thus, the MES options in T-REX offer to calculate the coefficients up to a specified order either for a defined energy, for the entire spectrum or for the white line feature only. The latter option is the only one, where MES is not performed along the energy axis, since the white line feature might exhibit a changing position in energy during the cycle. In each case, the Fourier coefficients are

written to a separate text file and the user is free to decide, whether to compute PSD or FS spectra or even the phase directly according to Eq. (3.19).

As a matter of fact, the actual idea of PSD is to phase-resolve changes in a spectrum. In the case of X-ray absorption spectra changes in the sample structure typically do not show up at certain energies, but affect the entire spectrum contrary to e.g. FTIR or Raman spectroscopy, where features appear well-separated in energy/wavelength. Thus, the R-space obtained after extracting and Fourier transforming the EXAFS function $\chi(k)$ is actually a more promising candidate for PSD, since the contributions of back-scattering atoms appear at distinct R-values. Furthermore, within the formulas of MES it makes no difference, whether they are applied as function of energy E or interatomic distance R. Therefore, this function was also included in T-REX and will also be discussed in detail in section 4.1.4.

3.3.8 Background subtraction

Each of the thousands of spectra that are typically acquired during one QEXAFS measurement contains all the information of an EXAFS spectrum as summarized in section 2.1.2. Thus, it also has to be analyzed in the same way to identify neighboring atoms and determine coordination numbers, bond lengths and/or lattice disorders. For this purpose, again the algorithms of IFEFFIT are used, in order to normalize the QEXAFS spectra, to extract the EXAFS signal $\chi(k)$ and to perform Fourier transformations. All these functions are found in the 'Normalization' tab of the T-REX software. Here, it is possible (i) to set up E_0, (ii) to fit the preedge with a linear fit, (iii) to fit the postedge with the Victoreen function (see Eq. (2.2)) and (iv) to calculate a spline function, which is used for EXAFS extraction. The spline function can be adapted by adjusting the spline 'clamps' individually for the lower and higher energy regions of the spectra. This regulates how rigorous the spline curve follows the data. Details about the spline function, which is part of the so-called AUTOBK algorithm, are given by Newville [New01] and within the IFEFFIT online documentation [IFE11]. After extracting the EXAFS it is possible to define borders in k-space and to choose a specific window, before the Fourier transformation can be performed. In Figure 2.2 and Figure 2.4 it has already been demonstrated, how the herein presented steps of EXAFS data treatment are applied to the absorption spectra. Each step, including normalization, extracting $\chi(k)$ and calculating Fourier transformations can be performed for the plotted spectrum only to find suitable parameters or afterwards also for all spectra of the project with the chosen parameters resulting in a multi-column file. The normalized spectra can be further evaluated with PCA, while the $\chi(k)$ data is especially required for the application of the EXAFS fitting functions.

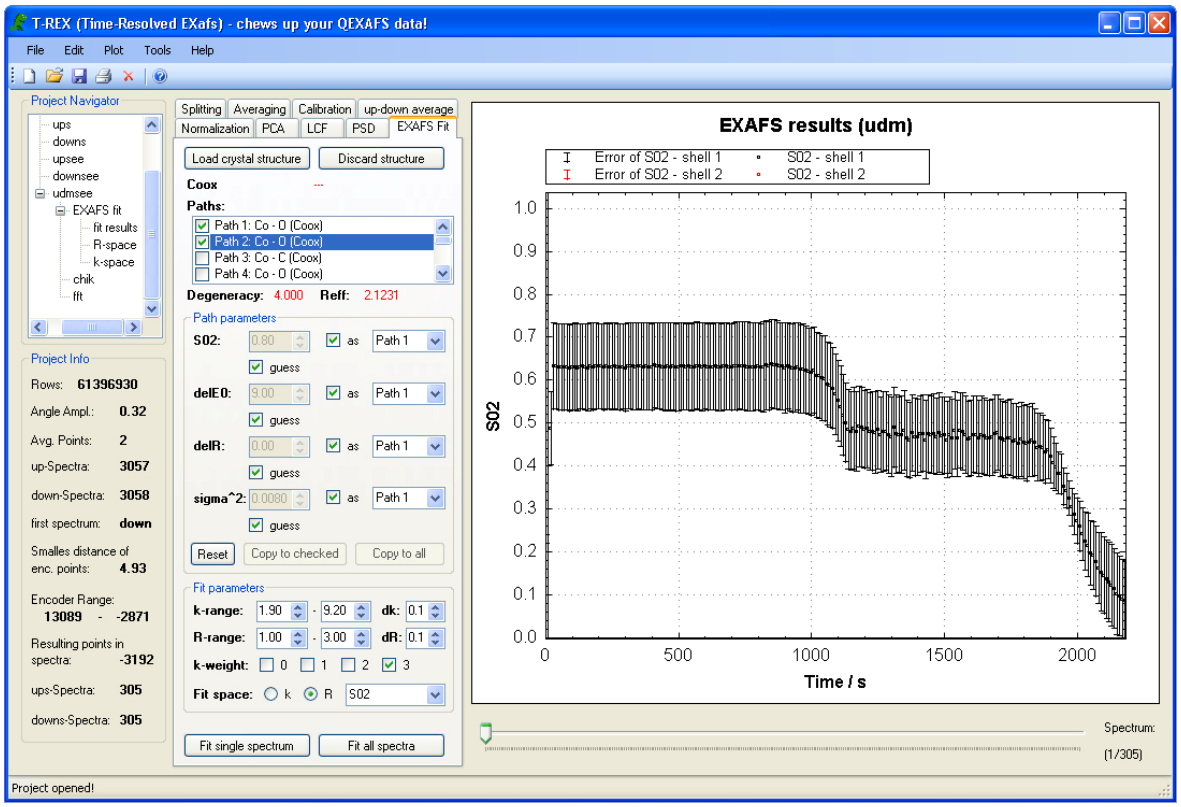

Figure 3.30: T-REX GUI for EXAFS fitting performed on the QEXAFS data: In this specific example the amplitude of the first two O shells were fitted during the thermal composition of Co oxalate, whereby the steps of dehydration and decomposition can be studied.

3.3.9 EXAFS fitting

After extracting the EXAFS data $\chi(k)$, as explained in the previous section, it is possible to perform EXAFS fits. Again the idea was to use the existent tools for EXAFS analysis and to provide an interface, so that these tools can be used in a convenient way for as many spectra as required. Accordingly, it is possible to import 'feff.inp' input files with the atomic structural data of a suggested model. This file is then processed with the FEFF6 code [Zab95] to calculate the scattering paths, which can then be further refined via the EXAFS fits. For each path it is possible to adjust the amplitude factor $N \cdot S_0^2$, the energy shift ΔE, the path length shift ΔR and the mean-square displacement σ^2 of the Debye-Waller factor. These parameters can either be set to a constant value or initialized with a starting value, which is further refined during the fit. After selecting a fit window in R-space, it is possible to fit a single spectrum and to study the results in the plotting window as it is e.g. well known from EXAFS analysis software like ARTEMIS [Rav05]. Moreover, in T-REX the fit can be automatically performed for all thousands and more spectra of the current project, so that changes in coordination number, distance of neighboring atoms and lattice disorder can be investigated as function of time.

In Figure 3.30 an example is shown to demonstrate the capabilities of the EXAFS fitting tool. In this example the first neighboring oxygen shells of Co were fitted during the dehydration and finally the decomposition of Co oxalate $Co(C_2O_4)*2H_2O$ as response to heating up the sample in hydrogen atmosphere (see also section 4.2 for more details). In this case, the amplitude of the shells is shown and it is easy e.g. to find the instance of dehydration at ca. 1000 s, where the coordination number decreases due to the removal of two of the overall six O neighbors. Afterwards, the decomposition can be easily detected, because the coordination number of O decreases to zero, as soon as the oxalate decomposes to pure metallic Co. Since all fit results are written into one text file it is easy to switch e.g. to the distance between the first O shell and the central Co atom. In contrast to conventional EXAFS fitting it is hardly possible to check each fit manually for a few thousand spectra. Thus, it is most important to investigate how the fit errors evolve as function of time. In this context, it has to be kept in mind that the starting model for the EXAFS fits is not necessarily the best model to fit the end of the reaction. In the case of Co oxalate the number of O neighbors decreases to zero, while the number of next neighbor Co atoms drastically increases with the formation of metallic Co. Here, as in many cases, it is suggested to fit the data several times with different models until a smooth transition and low fitting errors during the entire reaction time are achieved. This will be shown in more detail with a practical example in section 4.1.1.

3.3.10 Simulation tool for spectra measured in reflection mode

Measuring EXAFS spectra of thin films in total reflection under grazing incidence does not only allow determining the structure of these films, but also the thickness and roughness by refining simulated spectra until they show congruence with the measured ones. For this purpose a special fit tool was included in T-REX, which is shown in Figure 3.31. With this tool simulations based on the distorted-wave Born approximation (see section 2.2.2 and [Kei05]) can be performed for sample systems consisting of one layer deposited on a substrate. As input parameters the incident angle, the divergence, width and height of the beam, the vertical gap of the used slits (see Figure 4.48 in section 4.3.1), the length of the sample and the distance between sample and detector have to be entered. Further, the density, the roughness and horizontal correlation, as introduced in section 2.2, have to be chosen for the substrate as well as the deposited layer, while for the latter one also the thickness has to be defined. Additionally, the folder has to be selected, where the required fit tools are located and a file with the optical data $\delta(E)$ and $\beta(E)$ of the substrate material as well as the deposited layer. Finally it is possible to perform the simulations within an adjustable energy range, predefined by the limits in the file containing the optical data.

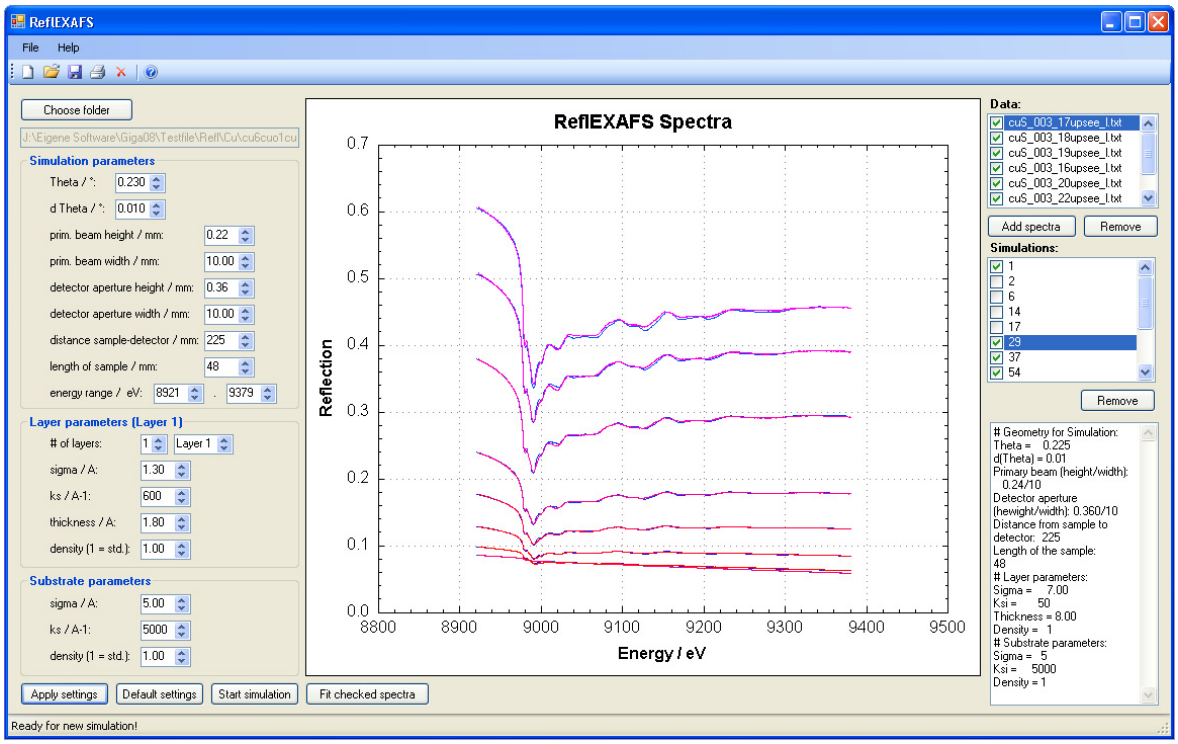

Figure 3.31: Tool in T-REX to simulate ReflEXAFS spectra and to refine these simulations by varying parameters until congruence with the measured data is achieved.

One advantage of the implemented simulation tool is the possibility to (i) load measured spectra, which are displayed in red colors and (ii) perform several calculations, which are displayed in blue colors. Thus, it is possible to conveniently vary parameters in a systematic way, which helps to rapidly find the right directions towards the best fitting parameters. It is also possible to export the data of chosen spectra and calculations into a multi-column text file, which can be further processed by conventional plotting software. Since the fitting of several reflection spectra can become very time consuming (which is easy to understand with respect to the number of input parameters), it is possible to store the current simulation project in a separate binary file, which includes all data of the project and can thus be easily shared together with the file including the used optical data.

3.3.11 Typical workflow for QEXAFS data analysis

The variety of data analysis tools provided by T-REX indicates that there is not one perfect path to analyze QEXAFS data, but that there are many and sometimes complementary approaches, which can help to get reasonable results. Which steps of data analysis can be performed strongly depends on the available data quality and also on what exactly the scientific questions are. The diagram in Figure 3.32 provides an overview over the typical workflow in QEXAFS data analysis using T-REX. The first part is starting with the raw data file and ending with the energy calibrated spectra. This part is rather linear and has to be completely exercised for each QEXAFS file. The paths marked by the colored arrows

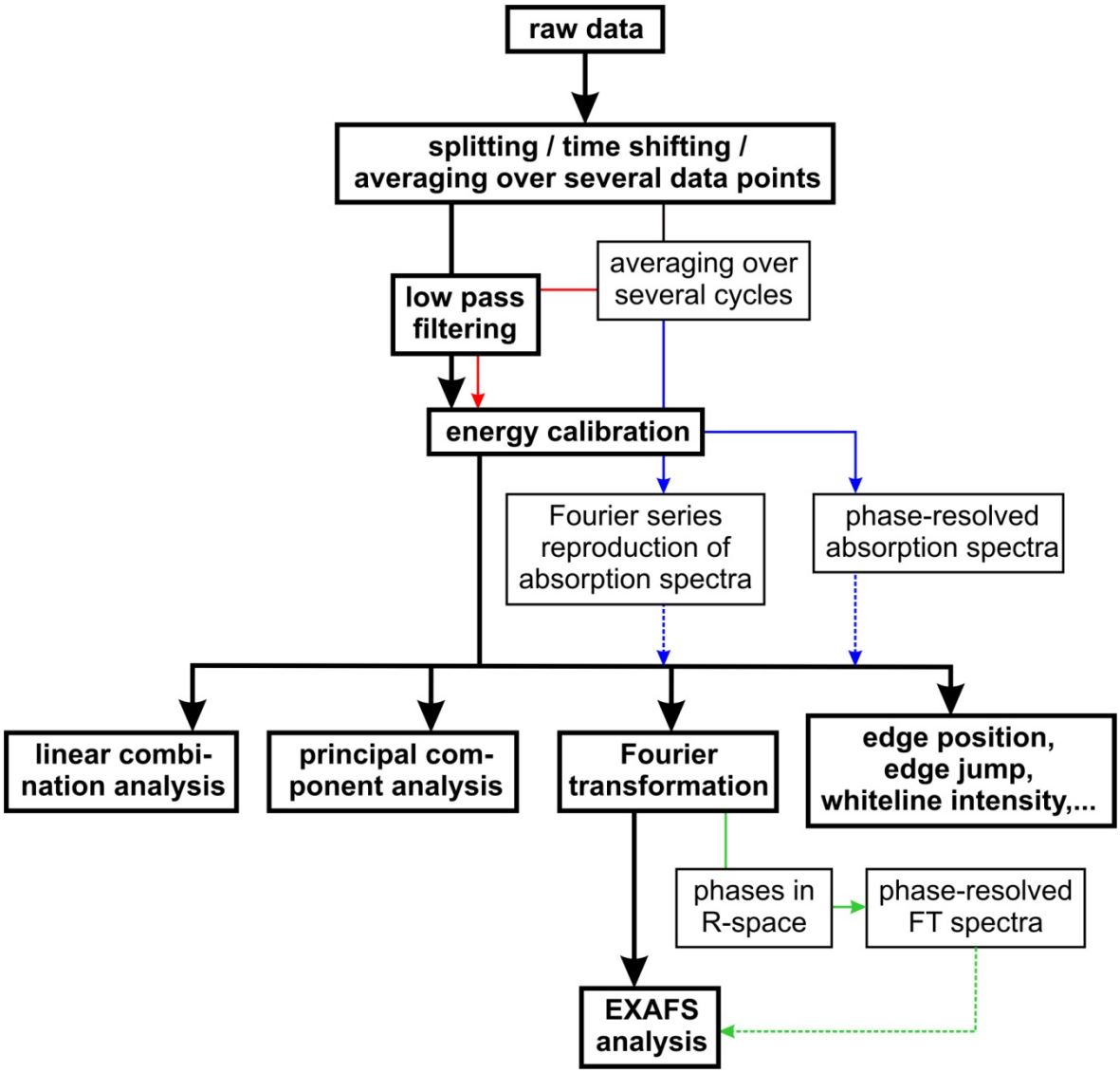

Figure 3.32: Steps of QEXAFS data analysis. The bold printed parts are standard tools for conventional QEXAFS data analysis, while the parts connected by the colored arrows are only relevant in modulation experiments.

are only available in modulation experiments and will be discussed in more detail in section 4.1.4. The second part of data analysis is more branched out as many options are available as soon as the calibrated spectra are prepared. The next chapter will provide many examples, where each of the herein presented tools is evaluated by applying it to measurements performed during scientific relevant experiments.

3.4 SuperXAS beamline

True to its name, the SuperXAS beamline at the SLS was purposely designed for XAS experiments [Fra09a, Pau11]. The source of this beamline is a super-bending magnet with 2.9 T. With the typical operation conditions of the SLS storage ring, which are 400 mA of

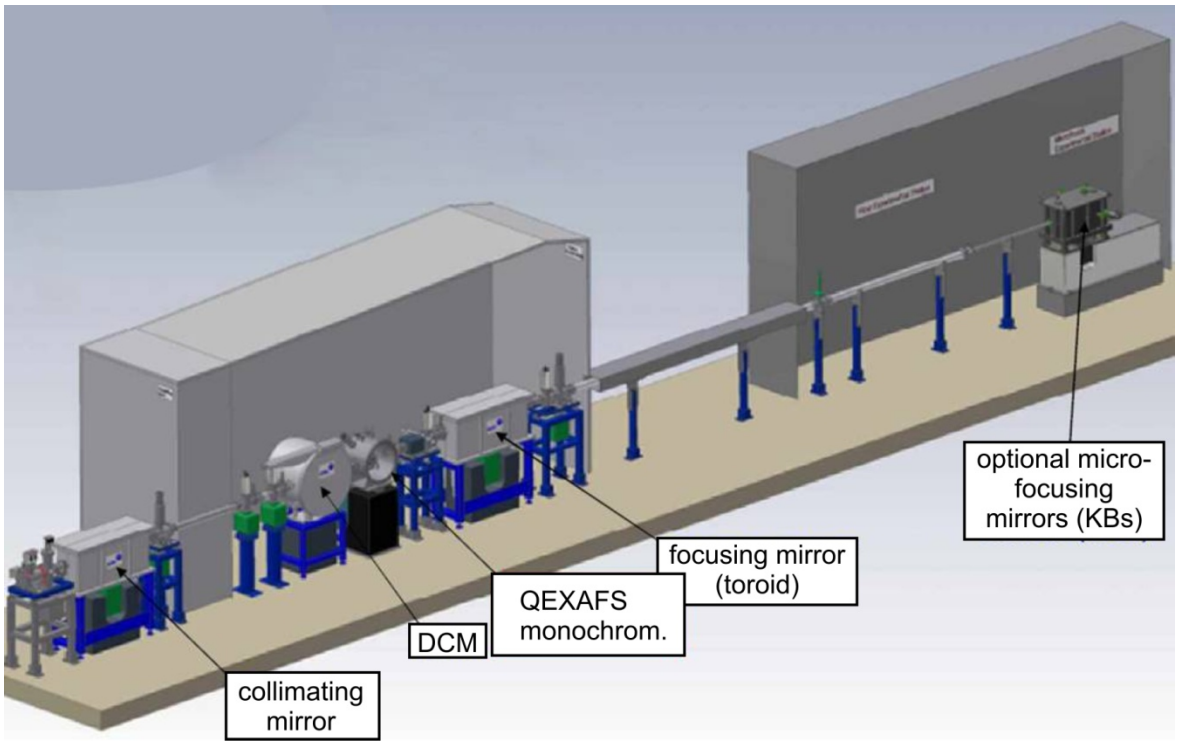

Figure 3.33: Sketch of the construction of the SuperXAS beamline optics as designed by ACCEL (now Bruker ASC) [Bru11].

2.4 GeV electrons, a flux of more than 10^{13} photons/(s · mrad^2 · 0.1%BW) is obtained covering an energy range from 4 to 30 keV, while a maximum of $3{\cdot}10^{13}$ photons/(s · mrad^2 · 0.1%BW) is achieved at the critical energy of 11.1 keV [Pau11]. Basically, the beamline is designed as already described schematically in Figure 2.5 and in a sketch on its construction in Figure 3.33. Close to the source, an initial graphite filter, which cuts off the low energy contribution of the synchrotron beam, is followed by primary slits, before a collimating mirror with either Pt or Rh coating is used to make the divergent beam more parallel. Next, the beam encounters the two installed monochromators, which are a conventional Si(111)/Si(311) fixed-exit double crystal monochromator (DCM) and a commercial channel cut crystal QEXAFS monochromator built by Bruker ASC [Bru11] in collaboration with the University of Wuppertal. An outstanding feature of the SuperXAS beamline is the possibility to switch between both monochromators in only 5 min, while maintaining the beam position on the sample.

Si(111) and Si(311) crystals can be mounted on the water-cooled tilt table inside the QEXAFS monochromator, which is driven by rotating eccentricities as explained in section 2.3.2 and [Fra05, Ric03], while an angular encoder system as described in section 3.1.1 and [Stö08b] is added to measure the Bragg angle. Crystal oscillation frequencies up to 40 Hz can be achieved, while a set of exchangeable discs with various eccentricities allows adjusting the energy range. A further upgrade to mechanics with flexible eccentricities as described in section 3.1.2 and [Stö10a] is already in the process of

installation. Behind the monochromators, a beam stop to block the Bremsstrahlung and a beam defining slit system are located. Finally, a toroidal focusing mirror, again with Pt and Rh coating, enables the user to focus the beam on the sample down to a beam spot of about 100 µm x 100 µm. Thereby, typically about 10^{12} photons/s are available at the sample position using the Si(111) crystal. Several detectors, as e.g. fast ionization chambers developed by the Bergische Universität Wuppertal, are available at the sample station. Further details about the beamline and source parameters plus diagrams of e.g. mirror reflectivity and photon flux can be found at [Pau11].

4 Applications

The experimental advances in the QEXAFS technique, which have been described in chapter 3, are aiming on expanding and improving the possibilities of time-resolved structure analysis with EXAFS. The broad field of applications for QEXAFS has already been discussed in section 2.3.3 and will be confirmed in this chapter with various examples especially of surface sensitive applications, including experiments in catalysis as well as the deposition and oxidation of thin Cu metal films. The main focus is on the specific approaches to analyze the data, so that this chapter serves as verification of the experimental work presented in chapter 3. However, also new scientific insights in the described processes with respect to the chemistry and physics are provided, which will be also discussed in detail in the following sections.

All QEXAFS data presented in this chapter were acquired at the SuperXAS beamline at the Swiss Light Source (SLS). This beamline was introduced in section. In section 4.1 several catalytic applications will be presented, starting with the famous Heck reaction in section 4.1.1. Thereafter, two examples of kinetic oscillations during catalytic reactions are given, which are the oscillations in structure and performance during (i) catalytic partial oxidation of methane on Pd/Al_2O_3 catalysts in section 4.1.2 and (ii) CO oxidation on a Pt/Al_2O_3 catalyst in section 4.1.3. In both cases new insights were obtained by applying the QEXAFS technique. Finally, experiments with modulated excitations of supported Cu and Pt-Rh catalysts on alumina will be presented and evaluated with respect to the new approaches in QEXAFS data analysis, which have been introduced in section 3.3.7. In section 4.2 the thermal decomposition of Co oxalate will be investigated in various atmospheres. The last part of this chapter deals with experiments accomplished with QEXAFS in reflection mode under grazing incidence to investigate layer growth of thin Cu films (section 4.3.2) and the oxidation of thin Cu films at various temperatures (section 4.3.3).

4.1 Catalysis

It is not only a pathetic statement that the world would be a very different place today without the developments in catalysis in the past. Most people are well aware of the catalyst in their cars used to accelerate the oxidation of CO, produced by combustion motors, to the less hazardous CO_2 [Far99]. However, this is just one catalytic application of many that affect the existence of mankind. The very first important catalytic reaction in industry was the ammonia synthesis also known as the Haber-Bosch process [Sch03b]. Ammonia is of major importance for the food and fertilizer production and the large scale production of ammonia, enabled by a magnetite catalyst, was one basis for the exploding world population in the last century. Today the production of fine chemicals, and thus also the corresponding industry, would not exist without catalysis and for that reason catalysts are also called the working horses of the chemical industry. One important reaction in this context is the formation of C-C bonds via catalyzed cross coupling reactions [Nob10], which are essential for the organic synthesis as e.g. required for the production of pharmaceuticals. Last but not least, for thousands of years many catalytic reactions have taken and still take place in living organisms, as e.g. during photosynthesis and in the conversion of food to energy, where proteins and enzymes serve as catalysts [Cam06]. A list of some typical catalytic reactions is presented in Table 4.1 to further demonstrate the high variety of applications affected by catalysis.

Catalysts are generally used to increase the speed of a reaction, while they do not change the thermodynamics which determine e.g. the equilibrium state. Thereby, the catalyst itself is not consumed and available for new reactions at the end of the catalytic process. In Figure 4.1 it is demonstrated schematically how a catalyst typically works with the example of molecules reacting on a solid surface, as e.g. described in [Cho03]. The two molecules *A* and *B* are the reactants that form the product *P* according to the lower Gibbs free energy of the product. Without the catalyst a huge energy barrier has to be overcome, which is only possible under difficult reaction conditions by means of high temperatures and/or pressures. With a catalyst it is possible to remove this barrier by providing an alternative path, which is in this case the surface, where the two molecules can be absorbed in an exothermic reaction. On the surface the molecules come close enough to react when overcoming the activation energy, which is much lower as it would be the case without the catalyst. Thereafter, the product is separated in an endothermic step and as a result the catalyst is free again to support a new catalytic cycle. This new energetically favorable way towards the product allows performing the reaction more rapidly and under industrially feasible conditions, which is a prerequisite for large scale production.

Table 4.1: A few examples of industrially relevant catalytic processes and the catalysts that are typically applied for each process [Cho03].

Reaction	Equation	Catalyst
Oxidation of CO and hydrocarbons	$2CO + O_2 \rightleftharpoons 2CO_2$	Pt, Pd
Ammonia synthesis	$N_2 + 3H_2 \rightleftharpoons 2NH_3$	Fe
Ammonia oxidation	$4NH_3 + 5O_2 \rightleftharpoons 4NO + 6H_2O$	Pt-Rh
Methanation	$CO + 3H_2 \rightleftharpoons CH_4 + H_2O$	Ni, Pd
Catalytic partial oxidation of methane	$2CH_4 + O_2 \rightleftharpoons 2CO + 4H_2$	Pd
Steam reforming of methane	$CH_4 + H_2O \rightleftharpoons CO_2 + 3H_2$	Ni
Water-gas shift reaction	$CO + H_2O \rightleftharpoons CO_2 + H_2$	Fe (oxide), Cu-ZnO

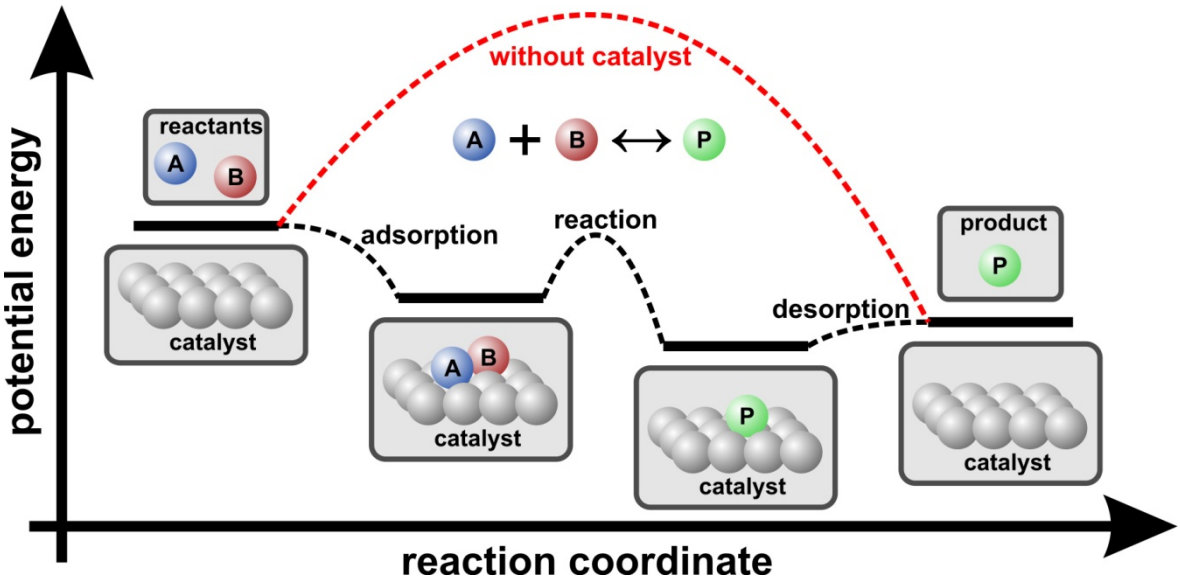

Figure 4.1: Drawing of the potential energy during a catalytic reaction of two molecules on the surface of a catalyst.

Apart from bio catalysis, which is working with enzymes and not further considered within this work, generally it is distinguished between homogeneous and heterogeneous catalysis. In homogeneous catalysis catalyst and reactants are present in the same phase, while in heterogeneous catalysis the catalyst is typically a solid and the reactants are gases or liquids. Heterogeneous catalysis is especially important for the chemical industry and was performed in all catalytic applications presented within this work. Thereby, supported catalysts were used, which consist of a macroscopic catalytic inactive support material as e.g. alumina (Al_2O_3) or boron nitride (BN) over which the catalytic material is distributed. Typically smallest catalytic particles, often only a few nanometers in diameter, are either attached by impregnating the support in a solution with subsequent drying of the sample

[Bai83] or by using flame spray pyrolysis [Str05, Han07]. The typical notation for a supported catalyst is X% Y/Al_2O_3, which means that X% of the total weight of the catalyst is assigned to the catalytic active metal Y, while the remaining weight is assigned to the alumina support.

For many years the development and optimization of catalysts has mainly been achieved by trial and error experiments. Only in the last few decades first steps were performed to understand catalysis on the atomic scale. Investigations in this direction were e.g. performed by G. Ertl who was rewarded with the Nobel price 2007 for his pioneering work in this field [Ert08]. However, such investigations were mostly limited to idealized conditions as e.g. plane surfaces with well-defined crystal structures and vacuum. The idea was to transfer these results in combination with density functional theory calculations, as e.g. performed by Reuter el al. [Reu03a, Reu03b], to technically relevant systems. However, this proved to be a more complicated issue than expected due to the complex dynamic processes in a macroscopic reactor.

Industrially relevant conditions are (i) catalysts made of very small particles and (ii) catalysts in gas streams or liquid environments. These differences to the afore mentioned idealized conditions became famous in the literature as *material gap* and *pressure gap* [Cho03]. The first condition is important because of the increased surface-to-volume ratio of small particles, which allows maximizing the performance of the catalyst while minimizing the required resources. This is especially useful, since the best catalysts typically consist of noble metals which are rare and thus very expensive. The second condition is important for a large scale conversion of reactants. Both mentioned conditions lead to a highly dynamic structure of the catalyst, which is strongly affecting the performance. The various contributing effects range from macroscopic transport phenomena within catalytic reactors to the highly dynamic behavior of smallest metal particles on the atomic scale. Thus, the investigation of catalysts under working conditions is crucial to find structure-performance relationships, which are crucial for the further development of optimized catalysts.

One of the most discussed topics in catalysis is the underlying catalytic mechanism in heterogeneous catalysis. The famous Langmuir-Hinshelwood mechanism proposes that the reactants are adsorbed on the metal surface before they react and are desorbed again, as it is also illustrated in Figure 4.1 and explained in more detail in [Cho03]. Is oxygen one of the reactants, it is also possible that the metal surface is oxidized first and the metal oxide serves as active intermediate, from which oxygen can be easily extracted for the catalytic reaction before being replenished by the surrounding oxygen atmosphere. This is described within the so-called Mars-Van-Krevelen mechanism [Mar54].

The number of investigation techniques applicable to catalysts at work is limited. Scanning tunneling microscopy (STM) and atomic force microscopy (AFM) are only applicable to plane surfaces. All techniques that require a primary electron beam and/or the detection of scattered electrons as e.g. X-ray photoelectron spectroscopy (XPS), low energy electron diffraction (LEED) or electron microscopy (SEM/TEM) are not suitable, since no vacuum conditions are available during the catalytic process under realistic conditions. X-ray diffraction (XRD) is one of the important tools to investigate crystal structures, but the highly dispersed catalytic particles are often too small for this technique to yield reasonable results. In that context, the XAFS technique proved to be the perfect choice, since it resolves the atomic structure within a short range of less than 1 nm around the selected element and is also not restricted to vacuum conditions. Since the most interesting processes on the catalyst surface are highly dynamic, the time-resolved EXAFS is most suitable to investigate catalysts at work as was shown with the DEXAFS (see e.g. [New07, New10, Igl11]) as well as the QEXAFS techniques (see examples in this chapter and section 2.3.3). Thereby, the required time resolution is limited by transport phenomena linked to the diffusion of the reaction gases through the catalytic reactor, which is typically in the order of a few hundred milliseconds up to some minutes. Thus, the dynamics correspond well to the time resolution provided by the QEXAFS technique. New application examples will be presented in the next sections and provide new insights in the complex behavior of catalysts by using advanced QEXAFS data analysis techniques.

4.1.1 Heck reaction

The discovery and development of Pd-catalyzed cross couplings in organic synthesis was awarded with the Nobel Prize in chemistry 2010, which demonstrates the importance of this process quite well. It allows high-precision forming of C-C bonds which is crucial for artificially producing molecules, as e.g., is required for large-scale production of numerous drugs [Hon93, Dan96]. Other applications can be found in agriculture and the high-tech sector, where it plays an important role in optimizing the blue light of organic light emitting diodes (see for example [Par11]). Figure 4.2 demonstrates how these cross coupling reactions on Pd work in the case of the Heck reaction presented in [Hec68] and the following three articles in the same journal. Bromobenzene and olefins in a precursor solution are attracted by the Pd atom so that intermediate Pd-C bonds are developed. Thereby the C atoms of bromobenzene and olefin come close enough to form a new C-C bond resulting in the product styrene which is e.g. used to build polystyrene, one of the most widely used plastics. During the process, the Pd is not consumed, and the released Pd can thus serve again as a catalyst for a new C-C bond formation.

Although the Heck reaction is usually catalyzed by homogeneous Pd complexes, the application of heterogeneous catalysts is often preferred due to their easier handling.

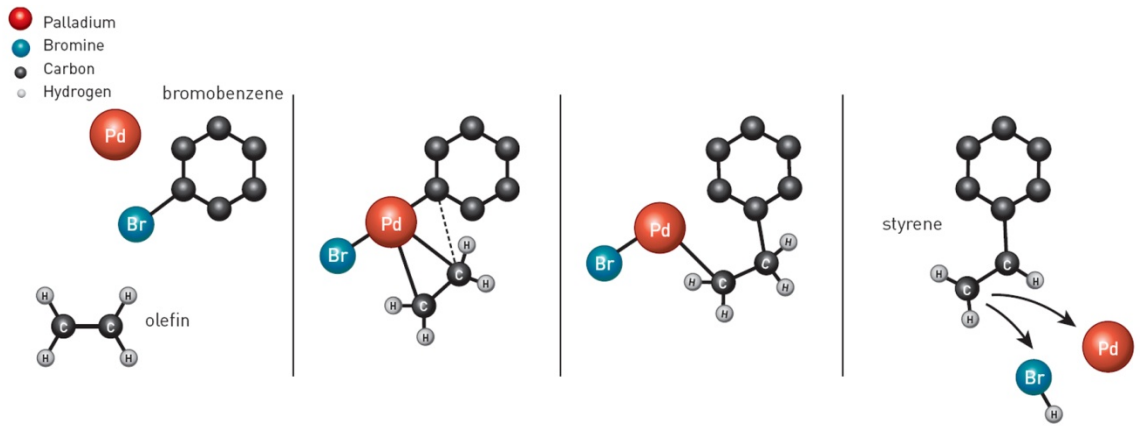

Figure 4.2: Connecting a short olefin to a ring of carbon atoms with the help of Pd as discovered by R. Heck (taken from [Nob10]).

However, the reaction mechanism of the heterogeneously catalyzed Heck coupling reaction is still a matter of discussion. One suggestion is that the Pd is leached from the heterogeneous catalyst into the liquid phase to form homogeneous complexes as the catalytic active species [Bif01, deV06, Ast07]. According to another suggestion, the Heck reaction is purely heterogeneously catalyzed [Kan90, Aug95]. Solving this issue is difficult, since the dynamic behavior of intermediate Pd species cannot be followed by ex situ methods [Köh07] and also because very small concentrations of the active Pd species are sufficient to catalyze the reaction, which might therefore be difficult to detect [Kle08]. Thus, spectroscopic in situ investigations are required to resolve the structural changes of Pd species within the course of the reaction [Mic05]. QEXAFS, which is an adequate technique for this purpose, was applied here since it allows investigating the reaction in situ under realistic conditions.

Experimental

A special cell, as shown in Figure 4.3, with two beam paths to probe the catalyst bed and the liquid phase was used to study the catalyzed Heck reaction [Gru05a]. While the cell itself is made of stainless steel, a polyether ether ketone (PEEK) inset was used to avoid reactions catalyzed by the cell. For the experiments about 168 mg of a flame-sprayed 5% Pd/Al_2O_3 catalyst [Han07] was loaded into the cell. Afterwards the cell was filled up with phenyl bromide (2.5 mmol, 0.393 g, 0.26 mL), styrene (3.75 mmol, 0.390 g, 0.43 mL) and 3 mL N-methyl-2-pyrrolidone (NMP) which altogether proved to yield a reasonable concentration of Pd in solution during the experiments for QEXAFS measurements. The reaction mixture was heated up to about 150 °C in air to start the catalytic reaction and was measured by passing the beam through the upper windows in a first experiment. The supported catalyst was measured during a second run of the experiment under the same conditions with the help of the lower window path. Thus, it was possible to resolve structural changes in the reaction solution as well as at the supported catalyst.

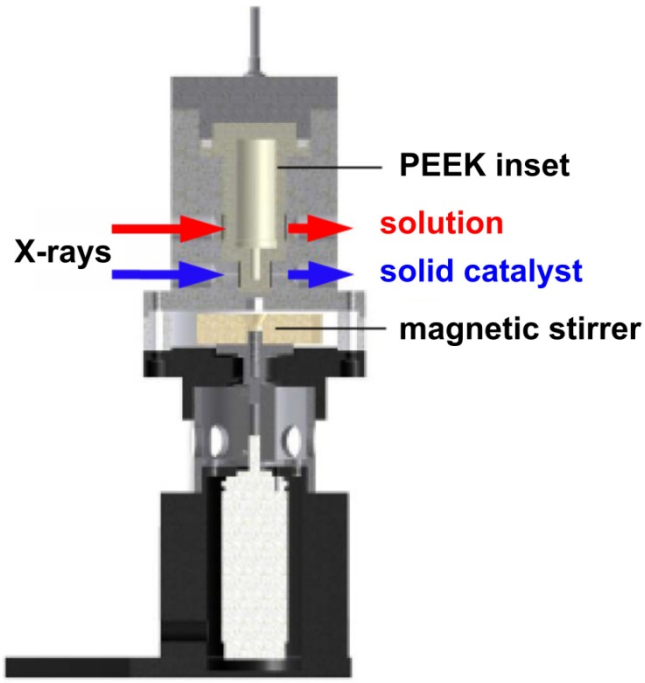

Figure 4.3: Design of the two beam path cell used to monitor the soluble Pd species in the reaction solution and the supported Pd catalyst at the bottom of the cell during the Heck reaction (see [Gru05a] for details).

All QEXAFS measurements were performed with the Si(311) crystal mounted on the tilt table inside the QEXAFS monochromator at the SuperXAS beamline (see section 3.4). The white beam was collimated with a Pt-coated mirror before it passed the monochromator. The applied eccentric disc yielded a peak-to-peak angular amplitude of 0.6°, corresponding to an energy range of about 1.7 keV for the spectra at the Pd *K*-edge (24.35 keV), which was scanned with 1 Hz crystal oscillation frequency. A second Pt-coated toroidal mirror was used to focus the beam onto the sample. The incident and transmitted beam were measured with two 15 cm long ionization chambers, the first filled with Ar and the second with Kr, both at ambient pressure, while a high voltage of 1.5 kV was applied to the chamber plates. A third chamber filled with Ar was used to measure a Pd metal foil in parallel to the sample in order to obtain an absolute energy value for the encoder calibration. Data analysis was performed with the techniques as explained in section 3.3. For the Fourier transformations a k-range from 0 – 14 $Å^{-1}$ was considered using a Kaiser-Bessel window. EXAFS fits were typically performed within a distance range of 1 – 3 Å, except for the third shell fits, where the fits were performed within a window of 4.2 – 4.8 Å. The PCA was performed with WinXAS [Res98] in this experiment, as well as the Fourier transformations of the spectra with very small edge jumps, since the AUTOBK algorithm provided by IFEFFIT did not yield reasonable results here. For these spectra a k-range of 2 – 10 $Å^{-1}$ was selected, due to the lower metal concentration resulting in less EXAFS signal. The S_0^2 value required to derive the exact coordination numbers from

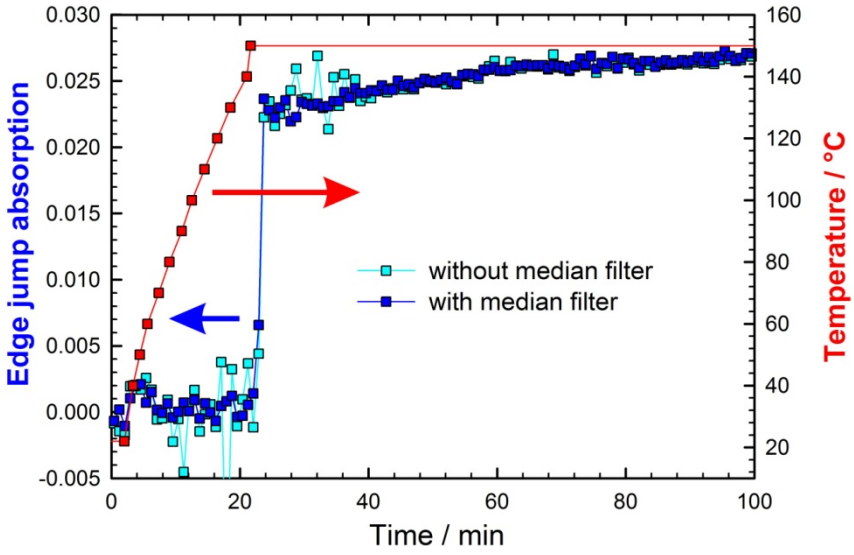

Figure 4.4: Jump in X-ray absorption at the Pd K-edge as function of time and temperature of the solution. The edge jump was calculated with and without applied median filter.

EXAFS analysis was determined by fitting a spectrum of the Pd metal foil after carrying out the same data treatment as for the sample spectra.

Results

Starting with the results of probing the reaction solution with the X-ray beam passing through the upper windows, Figure 4.4 shows the jump in absorption at the Pd *K*-edge as function of time and temperature. Averaging over 100 spectra, resulting in an effective time resolution of 50 s, was performed here due to the low concentration of Pd along the beam path. In the beginning no edge is recognizable at all, which means that no Pd was present in the solution at this early stage of the reaction. During the applied heating of the solution up to 150 °C there is also no edge observable, which evidences that all Pd observed in the course of the reaction has to be leached Pd from the heterogeneous catalyst. Finally, at about 22 min a sudden increase of Pd is observable during a time interval of only about 1 min. The edge jump further increases slowly up to about 60 min of total reaction time, before the amount of probed Pd remains on a more or less constant level, which corresponds to about 14% of the total amount of Pd in the system. This value was calculated with the measured jump in absorption of about 0.027, the cell dimensions, the volume of the solution and the total weight of 168 mg 5% Pd/Al_2O_3 that was loaded into the catalyst bed.

In Figure 4.5 the normalized absorption spectra measured up to about 100 min are shown. To achieve appropriate quality for further data analysis, averaging over 400 spectra had to be performed in this case. As observable in Figure 4.5a, the spectra acquired during the initial increase of the Pd concentration in the liquid phase still look rather distorted probably due to superheating of the liquid phase. It takes another 20 min before the system

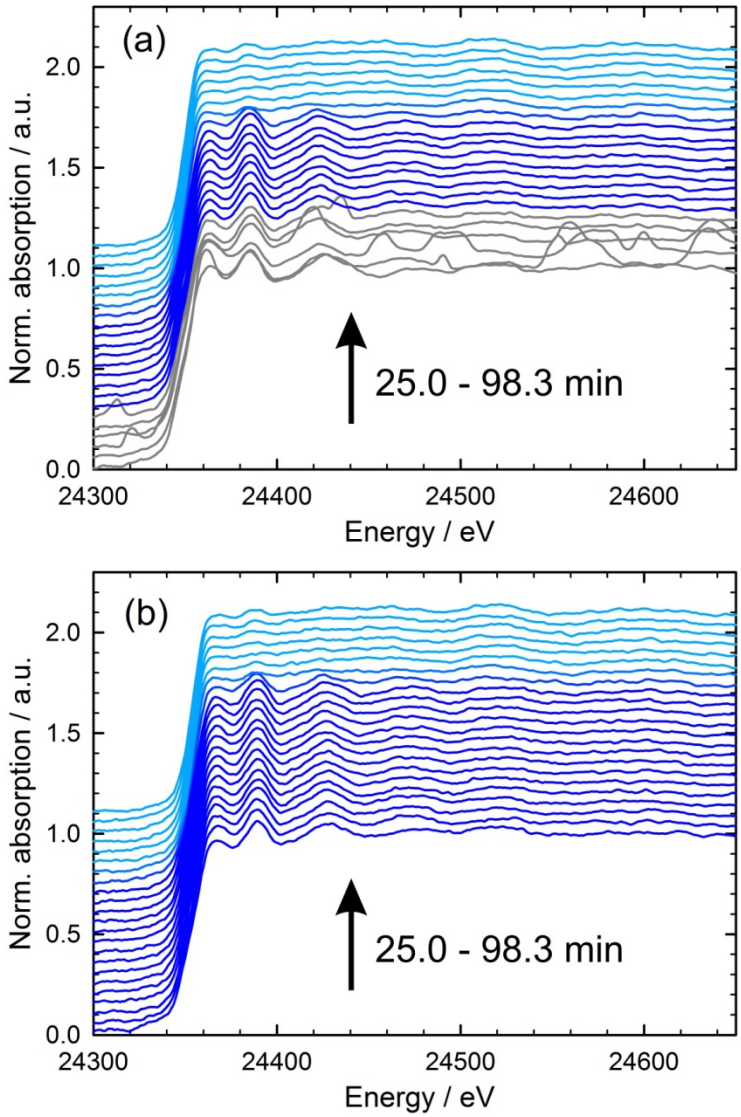

Figure 4.5: Normalized spectra of the Pd species in the solution during the reaction: (a) without and (b) with the application of the median filter. The spectra are shifted vertically to better show the evolution during the reaction.

has equilibrated and the spectra become smoother. However, the distortions are randomly distributed over the spectra and in section 3.3.3 it was explained how a median filter can be effectively used to suppress such artifacts. In the present case, a median filter checking the next two neighboring spectra was applied to the data before again averaging over 400 spectra was performed and the result of this operation is shown in Figure 4.5b, demonstrating that the data quality could be improved significantly.

After applying the median filter, all spectra could be used for further data analysis, e.g. for the determination of the edge jump, as shown in Figure 4.4. The corresponding results are shown together with the results that are achievable without the median filter. The obvious success of the median filter is an important result, also with respect to measuring conventional EXAFS in liquid systems, because fluctuations in the concentration are

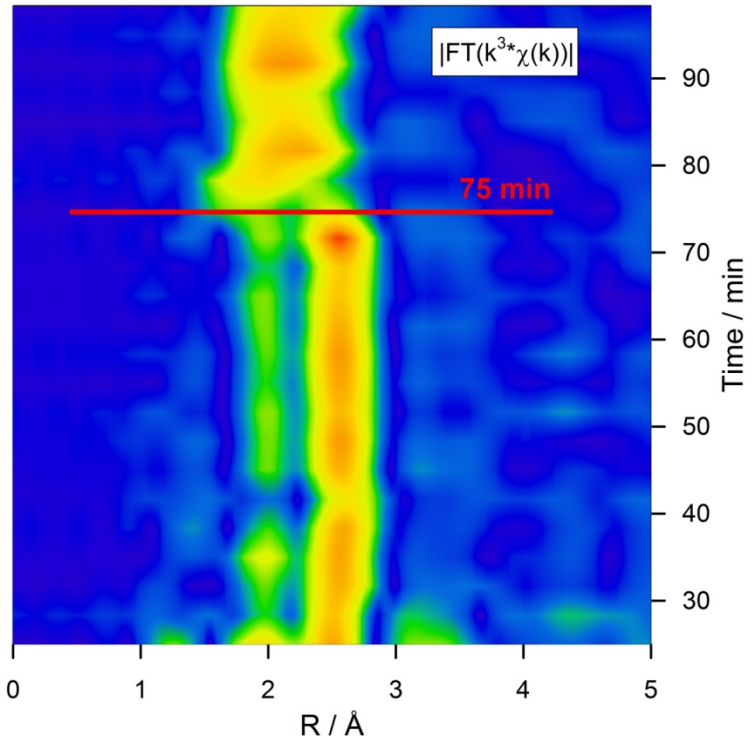

Figure 4.6: Fourier transformed EXAFS spectra of the reaction solution as function of time measured during the Heck reaction.

hardly avoidable during 20 min acquisition time. With such fluctuations the whole data set can become useless. From a statistical point of view, the same data quality can also be achieved by acquiring a few hundred spectra during these 20 min, while additional sudden fluctuations can be effectively removed with a median filter. Similar considerations can be made for the appearance of other random artifacts in EXAFS spectra, which might be caused e.g. by spikes in the electronics, sudden mechanical vibrations or beam losses. Thus, even for static sample systems, using QEXAFS in combination with the herein presented software tools provides advantages in comparison to conventional EXAFS measurements. The median filter only works well as long as the time resolution is high compared to the observed dynamics, so that the neighboring spectra have approximately the same shape as the one with the artifacts. Thus, this experiment is an example of how to alternatively exploit the high time resolution provided by contemporary QEXAFS systems, apart from investigating very rapid processes.

With the filtered spectra in Figure 4.5b it is now possible to observe that no significant changes occur after the first appearance of Pd up to about 75 min of total reaction time. Thereafter, the XANES features disappear almost instantly, while the EXAFS region still remains structured. Since the Pd concentration does not change significantly at this point, which is evident with the edge jump investigations in Figure 4.4, the observed changes can be assigned to structural changes of the leached Pd. It was ensured that none of the measured Pd was deposited Pd on the windows of the cell, since no edge jump could be

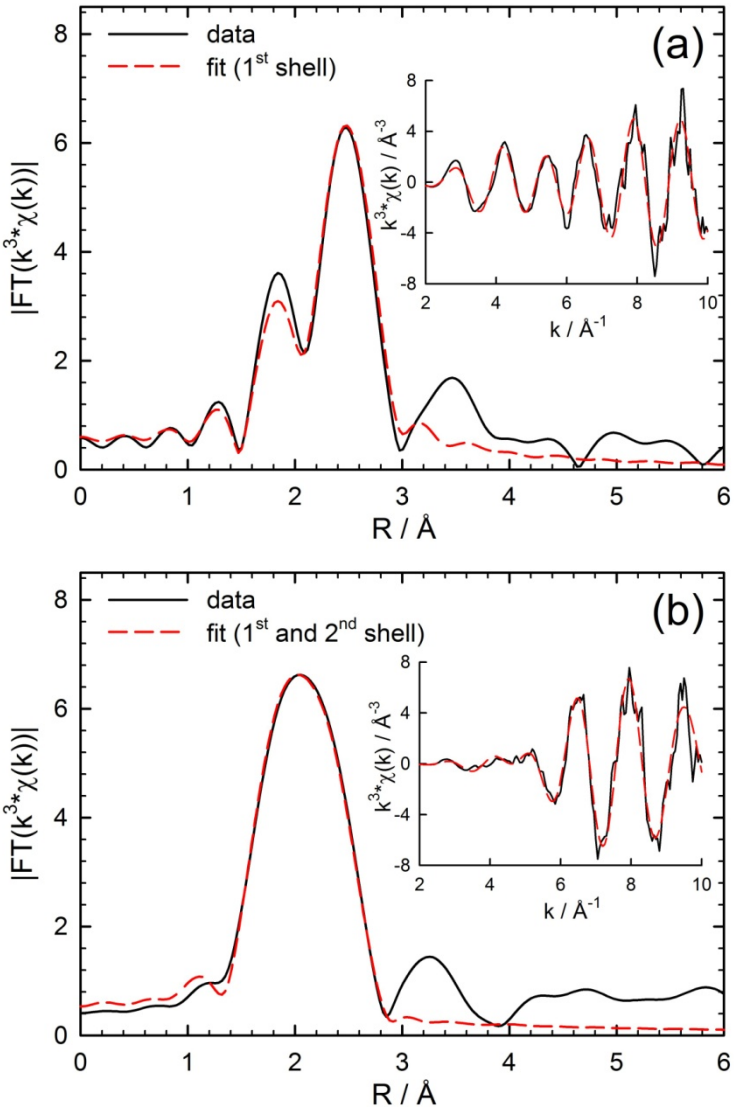

Figure 4.7: EXAFS fits of the two states observed in the reaction solution in R- and k-space: The shown data corresponds to the time intervals of (a) 60 – 67 min and (b) 93 – 100 min.

observed by measuring the empty cell after the experiment. The yields of the formed products of the catalytic reaction and the conversion of the PhBr were additionally investigated with gas chromatography (see [Rei11]). The resulting data is in good agreement with the studied behavior of the edge jump and the absorption spectra. The conversion of PhBr starts after about 22 min, which corresponds to the first appearance of Pd in the solution. After about 75 min almost no more formation of the products can be observed and this corresponds to the time region, where the distinct changes in the EXAFS spectra appear.

An EXAFS analysis of the two observed states in the liquid phase was performed to resolve in each case the local structure around the absorbing Pd atoms. The Fourier transformed data during the reaction is shown in Figure 4.6 and again the two already observed stages (cf. Figure 4.5b) can be recognized. Up to about 75 min two well-

Table 4.2: EXAFS fit results derived from the fits shown in Figure 4.7. Coordination numbers (CN), mean-square deviations (σ^2) and interatomic distances (R) of the Pd species in the solution are displayed.

State of reaction	Shell	CN	σ^2 / 10^{-3} Å^2	R / Å
active phase	Pd	8.7 ± 1.1	10.0 ± 0.9	2.733 ± 0.005
inactive phase	Br	2.7 ± 0.7	2.6 ± 1.8	2.423 ± 0.019
	Pd	2.2 ± 1.2	5.4 ± 3.6	2.792 ± 0.028

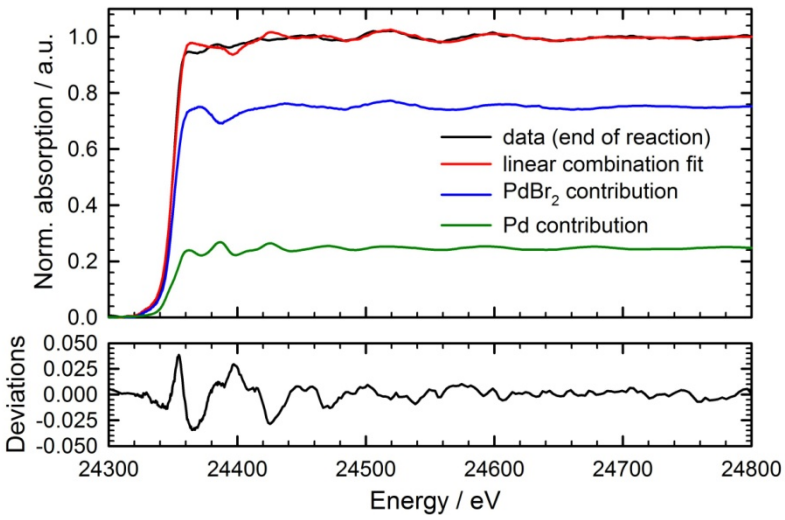

Figure 4.8: Linear combination fit with crystalline $PdBr_2$ and pure Pd metal reproducing a spectrum at the end of the reaction in the liquid phase. The lower plot window shows the deviations between fit and measured data.

separated backscattering contributions with constant intensity at 1.8 Å and 2.5 Å appear and thereafter only one broad signal at 2.0 Å remains. Since no significant variations during the two observed stages are recognizable, it was further averaged over now 800 spectra before performing the EXAFS fits, which are shown in Figure 4.7a and b. The first stage proved to be best fitted with a straight forward model of bulk fcc Pd, whereby only the first shell was considered for the fit. The broad signal of the second stage could not be fitted with a reasonable quality by using a single Pd-Pd, Pd-O or Pd-Br scattering path. However, a good fit could be accomplished with a combination of Br and Pd shells. For this purpose the amplitudes and phases of the first shell of bulk Pd and the first shell of $[PdBr_4]^{2-}$ were taken into consideration for the fit. The important fit results are all summarized in Table 4.2.

As a result of the EXAFS fits it can be concluded that most of the leached Pd is present as small Pd colloids during the active phase of the Heck reaction. According to the diagrams calculated by Jentys [Jen99] for the fcc structure, the coordination number of about 8.7 corresponds to average particle sizes of about 2 nm considering more or less spherical

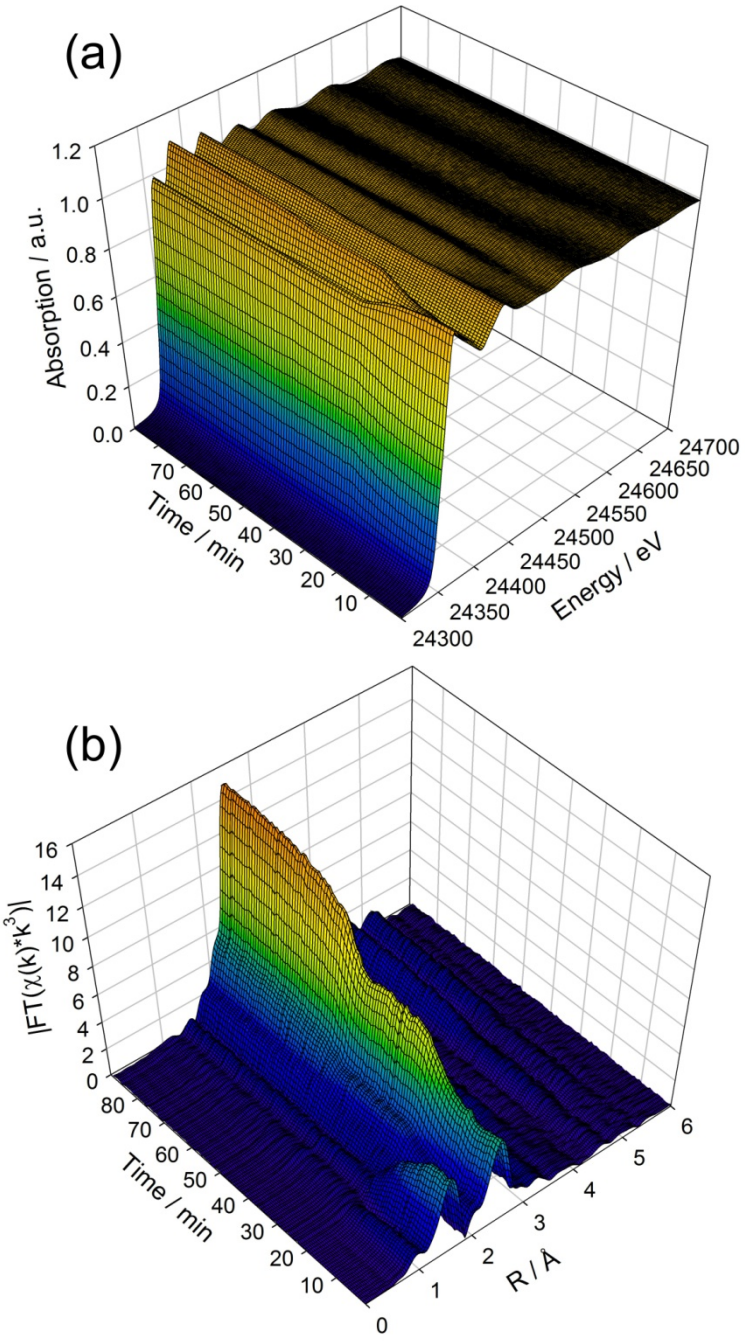

Figure 4.9: QEXAFS investigations of the solid catalyst at the bottom of the cell: (a) Normalized absorption spectra, (b) Fourier transformed EXAFS.

shaped particles. This was confirmed by scanning transmission electron microscopy investigations shown in [Rei11]. During the inactive stage, a Pd-Pd distance close to the one typical for bulk Pd metal results from the fit [Kit05]. However, the coordination number is rather low with 2.2. Considering the same spherical Pd particles as suggested for the active state this value corresponds to only about 30% Pd particles, respectively 20% Pd when considering bulk Pd as dominant species.

The fitted Pd-Br distance is in good agreement with the structure of $[PdBr_4]^{2-}$ (see e.g. [Mar75, Lan06]) and even slightly better with $[Pd_2Br_6]^{2-}$ (see e.g. [Zhu07]), which might be present here as well. The coordination number of 2.7 corresponds to about 70% $[PdBr_4]^{2-}$ and/or $[Pd_2Br_6]^{2-}$ species, which agrees very well with the remaining 20% – 30% Pd represented by the Pd-Pd shell. The mean-square displacement for the Pd-Pd scattering path, also shown in Table 4.2, is lower during the inactive stage. Although the fit uncertainties are rather high, this evidences that the Pd colloids are substantially larger at this point of the reaction, which would be in good agreement with the growing particle size of the catalyst powder (see below). To confirm the fit results the normalized absorption spectra were also analyzed with the complementary approach of LCA using a spectrum of pure Pd metal and solid crystalline $PdBr_2$ as reference spectra. The result is shown in Figure 4.8 and the amount of 75% $PdBr_2$ is in good agreement with the results of the EXAFS fits. The almost featureless structure of the XANES can be reproduced by the LCA fit, while remaining deviations may be attributed to the small size of Pd colloids and the structural differences between solid $PdBr_2$ and the dissolved bromo-palladates.

In the next step the solid 5% Pd/Al_2O_3 catalyst at the bottom of the reactor was investigated with the help of the lower beam path provided by the in situ cell (see Figure 4.3). Therefore, the Heck reaction was repeated with exactly the same conditions and the resulting normalized absorption spectra acquired during the reaction are displayed in Figure 4.9a. First of all it was observed that in this case the Pd concentration is much higher compared to the results obtained inside the solution, so that much better data quality could be achieved. Nevertheless, since the dynamics of the studied reaction are rather slow, it was averaged over 100 spectra (50 s time resolution), which yields a decent data quality for further analysis. The rather strong white line feature at the beginning of the reaction indicates that the catalyst was initially present in an oxidized state, which is a realistic assumption due to oxidation in air [Rei10].

The initial sample composition was quantified by LCA using spectra of bulk PdO and Pd as references to fit the XANES region from 24335 – 24385 eV. The resulting amounts of each species as function of reaction time are monitored in Figure 4.10 starting with an initial mixture of about 70% PdO and 30% Pd. The amount of PdO decreases to about 5% during the heating process up to about 25 min, indicating a reduction of the PdO with increasing temperature. Between 25 min and 50 min the amount of PdO remains at about 5% before it further decreases. However, these results have to be interpreted carefully because of the increasing fit error after 15 min. It will be shown below with the help of EXAFS fits that the detected 5% PdO are actually an erroneous effect induced by the small sizes of Pd particles present at this stage of the reaction. Correspondingly, the spectra are better fitted with a low contribution of PdO in the LCA instead of pure bulk Pd, although actually no more oxygen is present at this stage of the reaction.

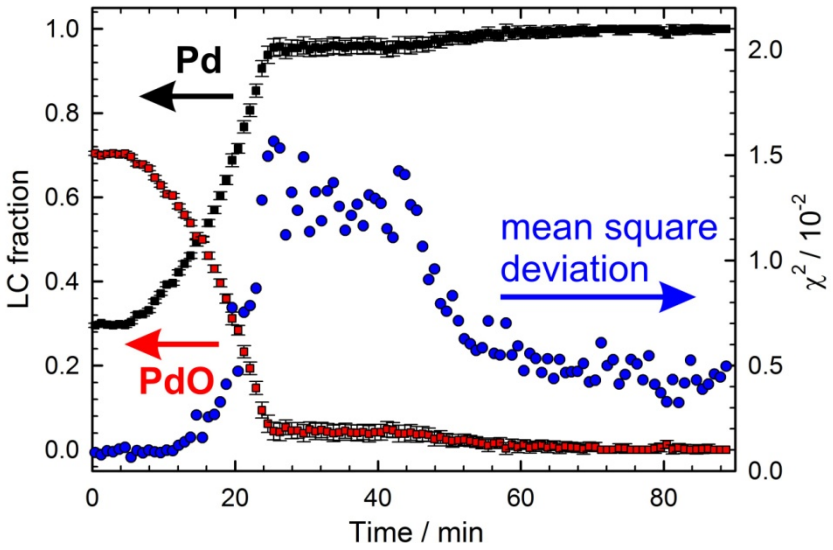

Figure 4.10: Results of fitting the normalized EXAFS spectra with a linear combination of bulk Pd metal (black) and PdO (red) spectra. The blue dots represent the mean square deviation between fits and measured data.

The Fourier transformed EXAFS spectra shown in Figure 4.9b exhibit two signals at distances of 1.55 Å and 2.45 Å. The one at 1.55 Å can be assigned to an Pd-O scattering path, while the other one corresponds to the first Pd neighbor atoms. In the beginning of the reaction the first peak decreases and the second peak increases as expected for the reduction of the catalyst, which has already been observed within the LCA results. However, after about 43 min the contribution of the Pd-Pd path further increases. To quantitatively analyze the Fourier transformed spectra, EXAFS fitting was performed with a combination of the first shell of PdO and the first shell of bulk Pd. The resulting coordination numbers, atomic distances and mean square displacements are shown in Figure 4.11. During the first 25 min the coordination number of Pd increases from 3 to 8, while the one of O decreases from 2 to 0. This corresponds to an initial Pd/O ratio of 1.5 which is in good agreement with the LCA results, which yield an initial Pd/O ratio of 1.4. The mean square displacement of the Pd-Pd shell increases linearly during the heating stage. This could be expected due to the applied linear increase of temperature, which causes an increased thermal disorder. It is difficult to make similar observations for the Pd-O path, since the fit errors drastically increase with the vanishing contribution of oxygen atoms. The fitted distances of Pd-O and Pd-Pd are close to the values expected for bulk PdO and Pd metal [Was53, Kit05]. Finally, to make sure that no intermediate state was overlooked during the first 35 min, a PCA was applied to the spectra and the results suggest only two components during this time interval, as demonstrated in Figure 4.12 (black line).

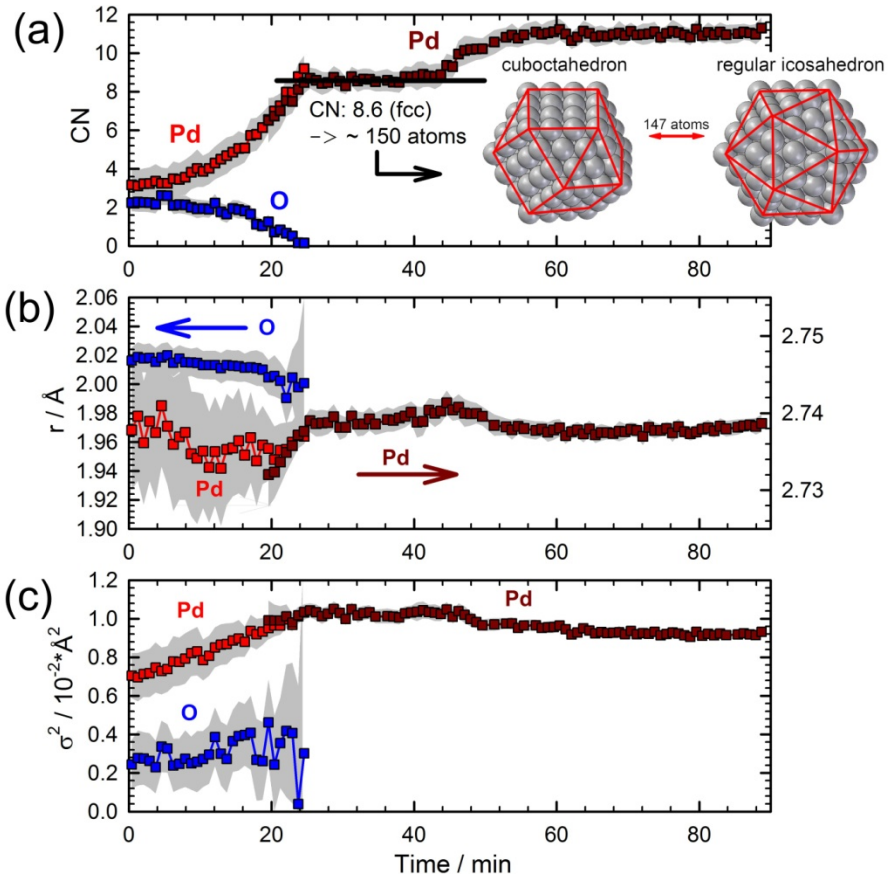

Figure 4.11: Results of EXAFS fits performed for all spectra of the solid catalyst at the bottom of the cell during the Heck reaction: (a) Coordination numbers, (b) interatomic distances and (c) mean-square deviations. The grey areas represent the errors of the values as determined by the fit algorithm.

The EXAFS fit model was changed after the reduction, as soon as no more oxygen could be detected. Accordingly, the remaining part of the reaction was fitted with the sole contribution of the first shell of bulk Pd. The results are in good agreement with the ones of the initial time interval, as can be seen by the 5 min overlap region in Figure 4.11. With the theoretically calculated diagrams of Jentys [Jen99], the average number of Pd atoms in the Pd nanoparticles could be estimated using the coordination number yielded by the EXAFS fits. For the plateau appearing after 25 min (see Figure 4.11a) the Pd particles consist of about 150 atoms. This is close to the magic number of 147 spherical atoms, which are required to build a perfect cuboctahedron or a regular icosahedron with four atoms in each edge as shown by Mackay [Mac62]. By additionally fitting the third shell, it is also possible to estimate the particle shapes [Jen99]. In the present case of the observed plateau a coordination number of about 13.6 is obtained with the fits shown in Figure 4.13 leading to a ratio of $N_3/N_1 = 1.6 \pm 0.3$. Although the fit errors are rather high, this value still supports the assumption of particles with approximately spherical shapes. Thus, the above mentioned geometries, which are also drawn in Figure 4.11a, are suggested to be the dominant species here. The corresponding particles exhibit a size of about 2 nm in

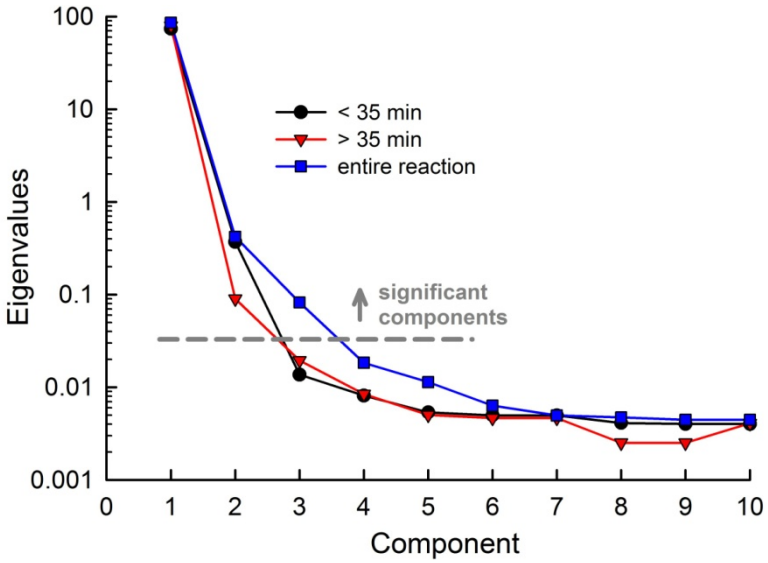

Figure 4.12: PCA results of the normalized X-ray absorption spectra of the solid catalyst at the bottom of the cell by considering various time intervals.

diameter. This is in good agreement with earlier studies using scanning transmission electron microscopy yielding particle sizes between 2 – 3 nm for the solid catalyst reduced in flowing hydrogen.

After the observed plateau at about 43 min the coordination number of Pd further increases. The Fourier transformed spectra (see Figure 4.9b) do not indicate any new species, so that this increase can be unambiguously attributed to particle growth. This is also supported by the decreasing mean square displacement observed after 43 min, which is caused by the higher lattice order provided by bigger particles. The upper limit of accurate particle size determination is at about 5 nm and this limit is clearly exceeded at the end of the reaction. However, since the calculated values are still below 12, which is the expected number for bulk fcc Pd, it is obvious that still small Pd particles are present at the end of the reaction. Scanning transmission electron microscopy pictures of the catalyst at the end of the reaction confirm this assumption, since they show particles with a diameter of 5 – 8 nm and even bigger ones with more than 20 nm [Rei11]. To finalize the analysis, a PCA was performed again for the time interval after 35 min and again only two components are suggested, whereby the second one exhibits a rather small contribution (Figure 4.12, red line). Thus the particle growth is assumed to be the only process occurring during this stage of the reaction for the solid catalyst at the bottom of the cell.

Discussion

Based on the QEXAFS results, the scheme of the Heck reaction could be further refined, as described in detail in [Rei11] and as it is here summarized in Figure 4.14. Since the focus of this work is set on the QEXAFS spectroscopy, only a short illustrative overview of the results will be given to demonstrate how an extensive analysis of QEXAFS data can help

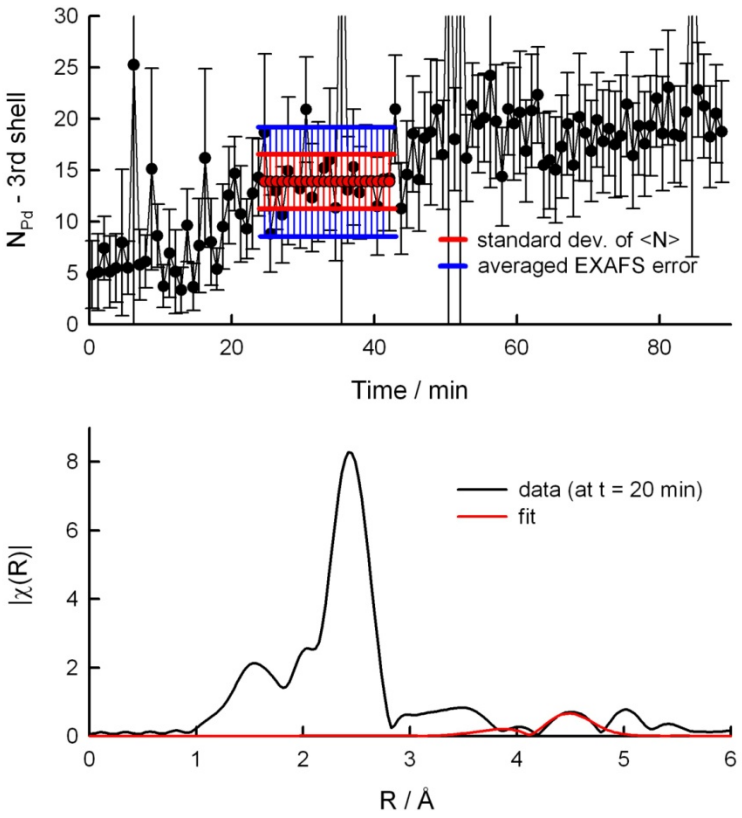

Figure 4.13: Third shell fit results of the solid catalyst at the bottom of the cell. The averaged coordination number at the plateau amounts to 13.6, while the averaged error of the fits is 5.3 and the values scatter with a standard deviation of 2.6. The lower plot window shows an exemplary fit in R-space.

to explain processes in chemistry. At the start of the reaction, it can be seen that the reaction solution has some reducing capabilities, since the supported Pd catalyst is entirely reduced during the initial heating stage. Concerning the Heck reaction itself, homogeneous Pd complexes leached from in situ colloids were considered as active species [deV06, Ast07, Köh07]. It was also stated out in earlier investigations that the generation of phenyl-bromo-palladate as active species in the Heck reaction is initiated by the interaction of the aryl halide with the surface of the supported catalyst, which causes leaching of Pd into the liquid phase [Ree00, Gni05]. It has to be noted that the oxidative addition of aryl halide can only take place on Pd(0) [Köh06, Köh07], which explains that the Heck reaction cannot start before the catalyst is fully reduced. As soon as the leaching of Pd(0) starts, the Heck reaction proceeds according to the well-known mechanism [Oes09, deV06].

At the end of the Heck cycle, the released Pd(0) is prone to aggregation, leading to the formation of Pd colloids. Since only colloidal Pd is detected in the solution during the active stage, the oxidative addition of PhBr seems to be too slow to prevent the formation of these colloids and thus the dissolution of Pd from the formed colloids can be considered as the rate determining step. This also means that the Pd colloids take an active part within the Heck cycle. As the Heck reaction fades out with the vanishing base, the composition of

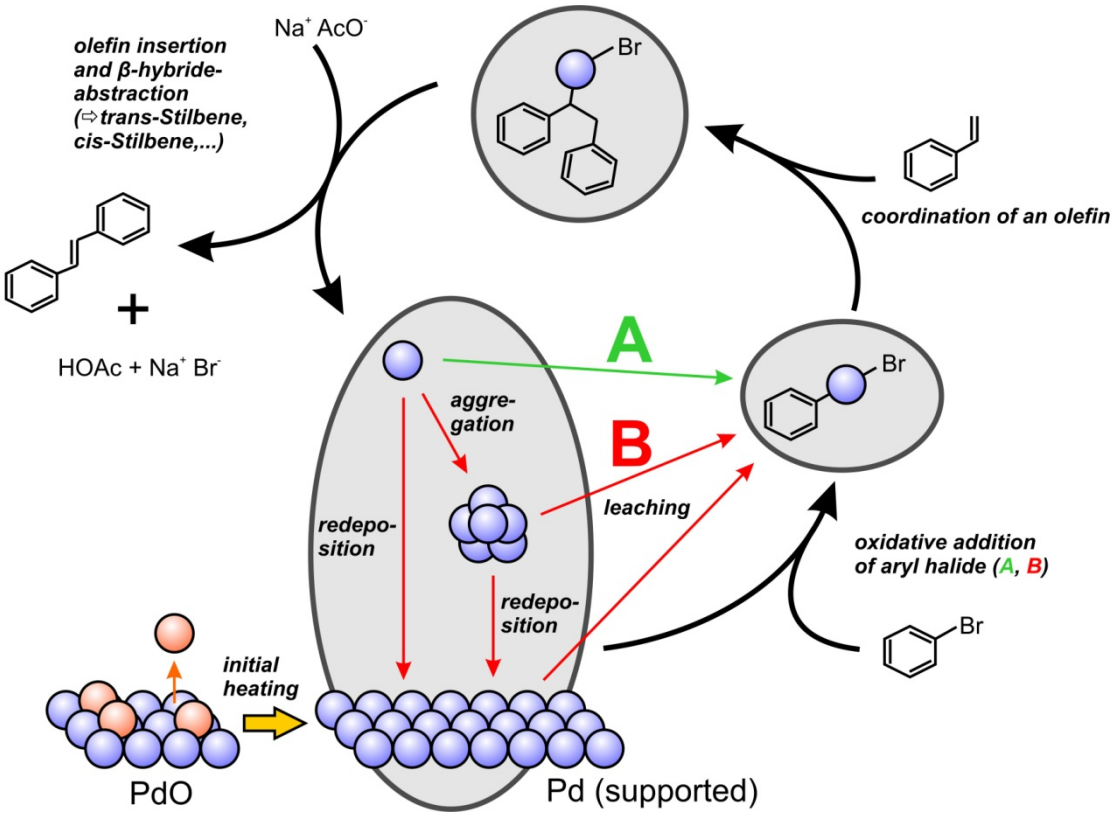

Figure 4.14: Scheme of the investigated Heck reaction: After the initial heating and a complete reduction of the supported catalyst Pd is leached and the Heck cycle starts with the oxidative addition of bromo benzene. The released Pd at the end of the cycle can either be directly involved in the next cycle (A, green) or it aggregates to Pd colloids, which serve as reservoir for further leaching of Pd atoms (B, red).

the solution changes in favor of homogeneous Pd complexes. On the one hand this proves that the leaching of Pd proceeds at a rather high rate and on the other hand it also shows that the formation of Pd colloids is favored by the completion of the Heck reaction and the thereby released Pd(0). The particle growth in the catalyst bed can be explained with an increased rate of redeposition towards the end of the active stage. During the active stage there is a stable dissolution/redeposition ratio, which finally shifts towards the redeposition with the increased concentration of homogeneous complexes until equilibrium between colloids and homogeneous species is reached. However, since no decrease in Pd concentration could be observed in the solution, an additional equilibrium between the leached Pd and the supported Pd particles is suggested.

It was shown that QEXAFS can be effectively used to eliminate time-dependent fluctuations that can appear during a reaction with a heterogeneous mixture. Additional insights into the reaction mechanism can be gained by applying a median filter in combination with additional smoothing algorithms. Moreover, the application of high time resolution, in combination with a reasonable set of software tools, has proven to provide the most flexible approach for such experiments, since the user can decide afterwards, how

much time resolution is required and how much of it can be spent in order to obtain better statistics. Thus, it is on the one hand possible to detect fast processes, as for example the initial leaching of Pd observed in the solution, but on the other hand also to perform accurate EXAFS analysis to resolve all the involved species.

4.1.2 Chemical oscillations during catalytic partial oxidation of methane

Chemical oscillations in the conversion of reaction gases on catalysts are a long-known phenomenon and often discussed in literature for idealized systems by means of plane surfaces and also industrially relevant conditions [Ert82, Eis86, Sch93, Sli94, Imb95, Gru97, Imb08]. To a certain degree it is possible to describe the oscillations within a theoretical approach, as e.g. performed by Reuter et al. with density-functional theory [Reu03a, Reu03b]. Thereby, oscillations are suggested to appear within bistable regions of surface phase diagrams, which appear in a narrow pressure regime of the reactants. This could be confirmed experimentally and it was shown that the width of such bistable regions are explainable by a hysteresis, which means that the catalytic behavior at a certain point in this region depends on the direction of changing reactants pressure to reach this point [Zhd02, Joh04]. Moreover, it was shown that the regions of bistability become narrower with an increasing number of defects leading to a more pronounced effect of oscillations and chaotic behavior in the case of nanoparticles [Joh04]. Within the bistable regions, a slow process is determining the oscillatory behavior. Several suggestions exist for this process as summarized by Zhdanov [Zhd02], involving adsorbate induced surface restructuring [Zhd99], oxide formation [Sal82] or carbon deposition [Col87]. Recently, it was also shown that roughening and smoothing processes of the catalytic surface have to be considered to be the source of kinetic oscillations [Hen10].

Considering experimental studies, it is important to note that in macroscopic systems and under technically relevant conditions additional non-linear terms can play a role and that various different surface structures are present on each nanoparticle. Thus, it is difficult to reliably predict and explain oscillations based on theoretical models, and it well explains why in situ investigations are so important. Such investigations were performed here for oscillations in the conversion of methane during catalytic partial oxidation (CPO) on a supported Pd catalyst [Stö12a] as well as oscillations during the extinction of CO oxidation on a supported Pt catalyst [Sin10]. For a deeper insight in structure-performance relationships of catalysts it is important to better understand the nature of these oscillations, which e.g. helps to technically improve reactor designs.

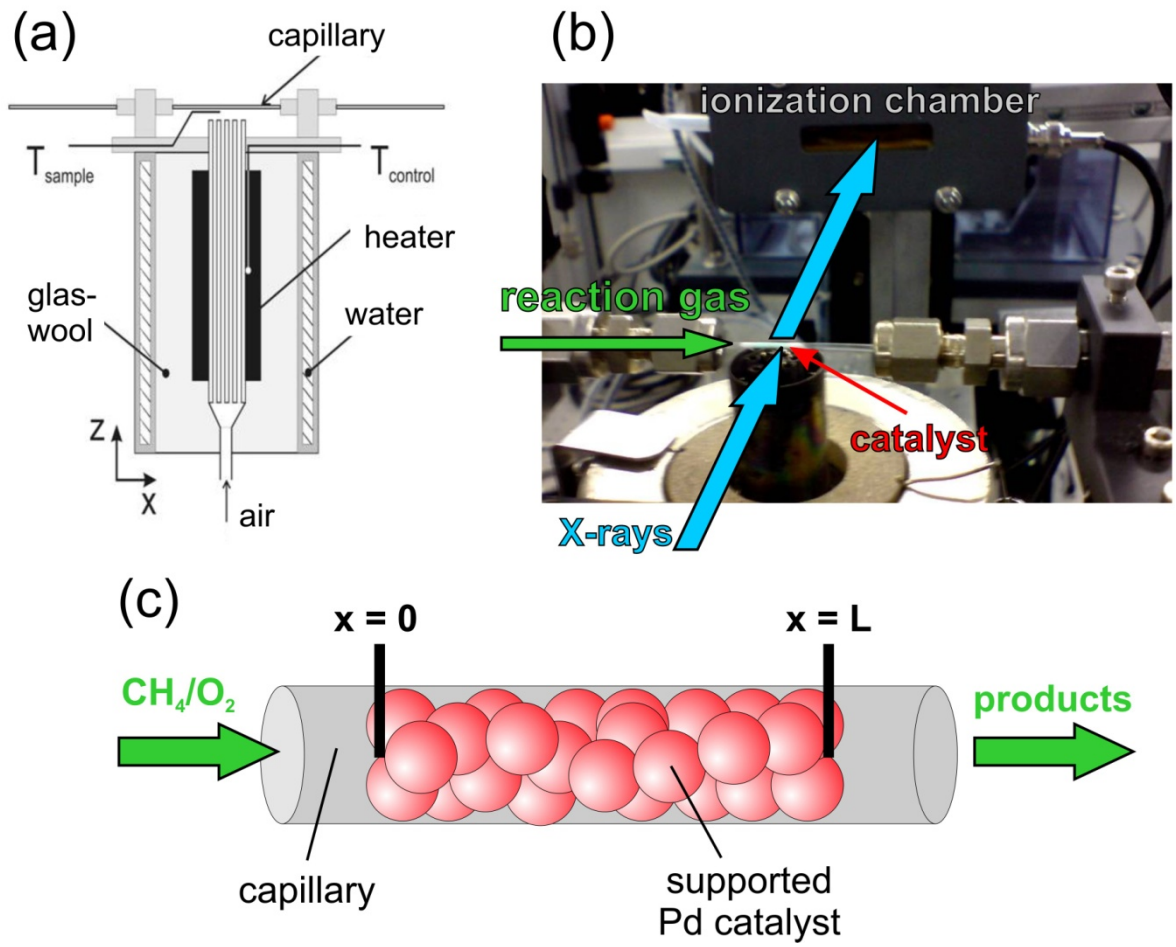

Figure 4.15: Capillary reactor for the investigation of catalysts at work with X-ray absorption spectroscopy: (a) Schematic drawing of the cell (taken from [Gru04]), (b) photography of the cell as it was installed at the SuperXAS beamline at the SLS during the experiments and (c) drawing of the capillary with the fixed catalyst bed.

Introduction

The CPO of methane is an alternative process to steam reforming, which is used to convert methane to hydrogen, as also shown in Table 4.1. A lot of interesting applications come into consideration for the CPO of methane. For example, every day a lot of methane is released during oil production, which has to be burnt down to the less harmful climate gas CO_2. A conversion to hydrogen, which is an important and valuable synthesis gas for the chemical industry, would be very welcome for economic as well as ecological reasons. Another interesting application for CPO is the on-board generation of synthesis gas for fuel-cell driven cars [Rec98, Bas01]. Furthermore, the CPO can be regarded as initial step in the conversion of methane to liquid products as methanol, dimethyl ether and synthetic fuels.

The dynamic behavior of oscillations during methane conversion is especially interesting for better understanding the CPO due to the various reactions that are typically involved in

such non-linear phenomena. Oscillations during the conversion of methane were observed on many transition metal catalysts [Byc06, Byc07] and one of the first reports on oscillations during the oxidation of methane on Pd was published by König et al. [Kön94]. Several studies in this scientific field were published [Ozk97, Gra99, Den99, Zha03, Zha05, Byc09], but it was already explained in the introduction of this section that only a few structure analysis techniques are applicable for in situ investigations of catalysts. Thus, in situ QEXAFS investigations of oscillations on a supported Pd/Al_2O_3 catalyst under working conditions were performed here with time and spatial resolution. The results will be presented in the following sections.

Experimental

Oscillations were observed and investigated on a commercial 5% Pd/Al_2O_3 catalyst (Johnson Matthey 324, mean particle size 3.4 nm, as determined by TEM) and a 5% Pd/Al_2O_3 catalyst prepared by flame spray pyrolysis (FSP catalyst) [Str05, Han07]. TEM investigations of samples with similar particles produced by FSP yielded particle sizes of 2 – 4 nm. In both cases, the catalytic powder was pressed, crushed and sieved to fractions between 100 and 200 µm and afterwards about 5 mg were loaded as a fixed bed into a quartz glass capillary (Markröhrchen, Hilgenberg GmbH, 1 mm diameter, wall thickness of 20 µm). As shown in the drawing in Figure 4.15a the capillary was mounted on a gas blower used for heating the sample, while the temperature was measured via a thermocouple located below the capillary [Gru04]. The gas inlet of the capillary was connected to the reaction gas supply, whereby the flow rate was adjusted by mass flow controllers (Brooks) and additionally measured at the outlet of the capillary with a gas flow meter (7-gas flow meter, Raczek). A 27 mL/min gas flow of 3% O_2 / 6% CH_4 / He was typically applied to the reactor during the herein presented studies as long as not stated otherwise. At the gas outlet of the reactor the gas mixture was measured with a mass spectrometer (Balzers Thermostar). Oscillations of the two Pd/Al_2O_3 catalysts were studied time and space resolved with various temperatures and gas compositions, while the dependence on the age of the catalyst was also investigated. In Figure 4.15c the capillary is schematically drawn to explain the relative position x/L which will be further used within this section.

For the performed QEXAFS experiments the settings of the optics at the SuperXAS beamline were adjusted to the same settings as already described for the Heck reaction and again spectra were acquired with 1 Hz crystal oscillation frequency. The moderate photon statistics, mainly caused by the extended scan range of 2 keV, were compensated by the variable averaging/smoothing procedures introduced in section 3.3.3 resulting in a reduced effective time resolution. The $\chi(k)$ spectra were extracted from the absorption spectra via the AUTOBK algorithm provided by IFEFFIT [New01]. After Fourier transforming the k^3-weighted EXAFS signal within a Kaiser-Bessel window from 1.6 – 11.9 $Å^{-1}$, the data was

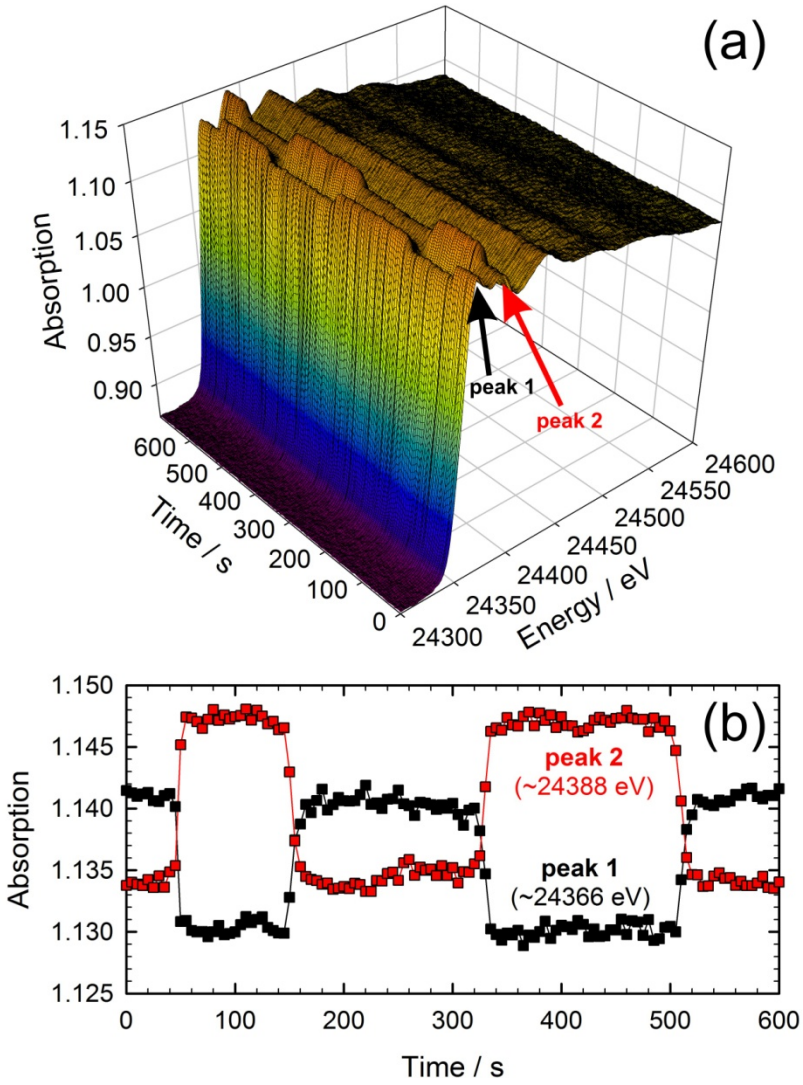

Figure 4.16: QEXAFS spectra acquired during CPO oscillations on Pd/Al_2O_3 measured at the Pd K-edge: (a) 3D overview and (b) intensity of the XANES peaks as function of time as marked by the arrows in (a). The data was acquired with the FSP catalyst at x/L = 0.93 and 410 °C.

fitted in *R*-space from 1.2 – 3.2 Å using phase and amplitudes calculated with FEFF6 [Zab95]. To exactly determine the coordination numbers of the sample the reduction factor S_0^2 is required and was determined to 0.81(5) here by fitting the first shell of a Pd metal foil spectrum. For the performed LCA fits, the E_0 was kept constant, while the components were forced to sum up to 100%. PCA was performed as described in section 3.3.5 with the application of both presented retention criteria.

Results

A series of QEXAFS spectra acquired during oscillations in the conversion of methane to hydrogen are shown in Figure 4.16a for the FSP catalyst, measured within a 27 mL/min gas flow at 410 °C close to the end of the catalyst bed (x/L = 0.93). Each shown spectrum is the result of averaging over 5 raw data spectra, resulting in a time resolution of one

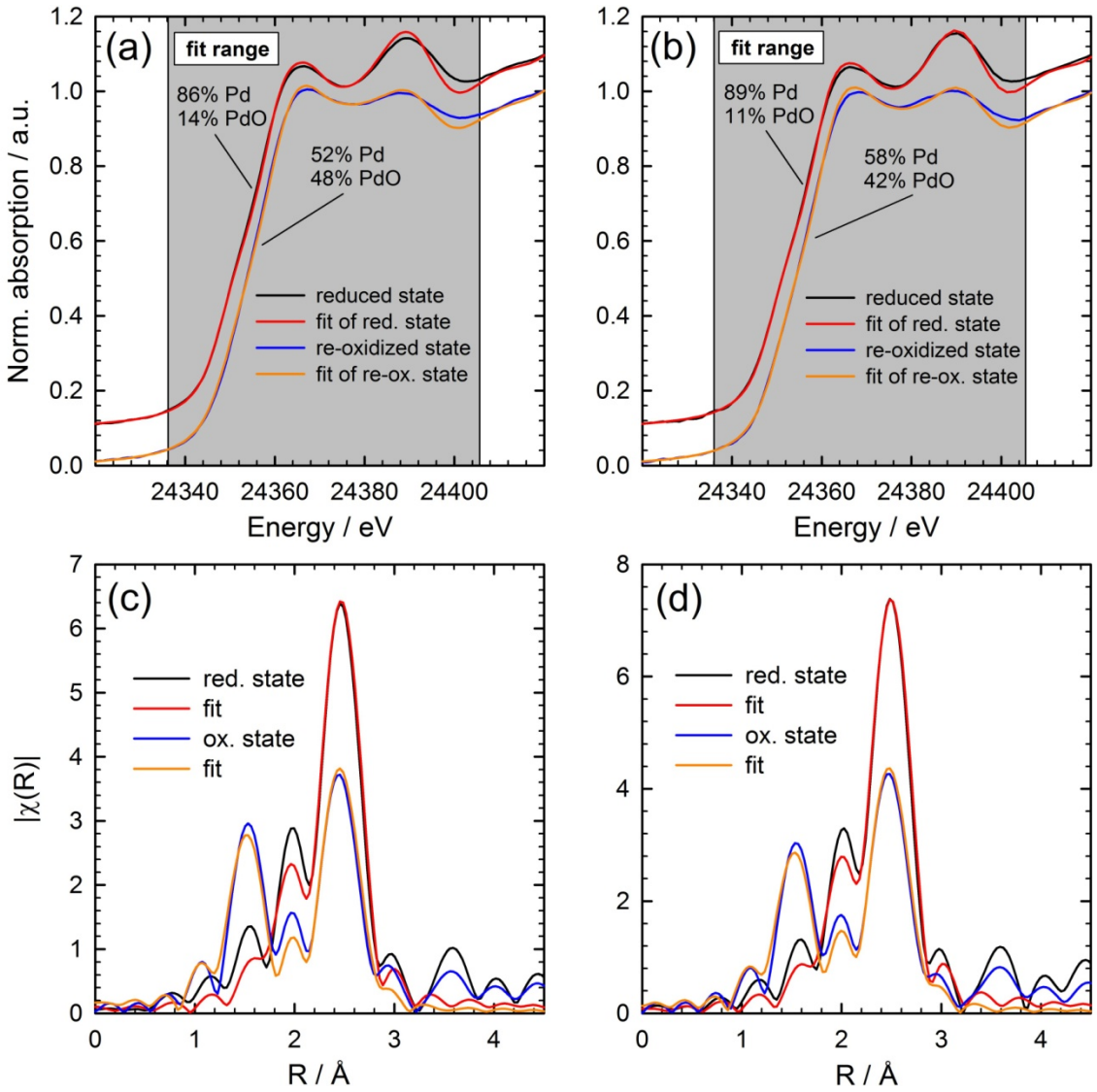

Figure 4.17: Linear combination fits (first row) and EXAFS fits with the first shell paths of bulk metallic Pd and PdO (second row) of the averaged reduced and partially oxidized states observable during CPO oscillations: (a),(c) FSP catalyst (same data as in Figure 4.16a) and (b),(d) commercial catalyst at the end of the catalyst bed at 385 °C.

spectrum each 5 s. Following the XANES structure as function of time, two different states (oxidized and reduced) can be clearly separated. While these states are rather stable for a few hundred seconds, the transitions between them proceed on a much faster scale of a few seconds. This becomes evident by following the two maxima in the XANES (Figure 4.16b), which correspond to the $1s \rightarrow 5p$ (Peak 1) and the $1s \rightarrow 4f$ (Peak 2) electron transitions in the Pd atom. In more detail, it can be recognized that the reduction process, observable at about 50 s, respectively 330 s, proceeds in less than 5 s, while the oxidation is slightly slower in the order of about 15 s.

At the beginning of the herein presented data analysis, the focus will be set on the properties of the oscillations, as far as they can be explained with the behavior of the two

stable states (reduced and oxidized) under various experimental conditions. The second part will deal with a more precise view on structural changes of the catalyst during the oscillations as function of time. The structure of the more or less stable reduced and oxidized states can be resolved either with the application of LCA fits in the XANES region or with path refinement fits in the EXAFS region. For this purpose it was averaged over all spectra contributing either to the reduced or to the oxidized state of one measurement covering about 6 oscillation periods. As a result two very smooth and representative spectra are obtained. The XANES region of these spectra and LCA fits with spectra of bulk metallic Pd and PdO are displayed in Figure 4.17a for the FSP and b for the commercial catalyst. Generally, the features of the XANES structure are well reproduced by the fits, but some deviations appear as a logical consequence to the nanometer sized catalytic particles, leading to less significant scattering features. Furthermore, the differences in temperature between the used references and the sample spectra have to be considered. Thus, a systematic error is expected to appear in the LCA results, which has to be quantified by the complementary EXAFS analysis in order to correctly resolve the structure. On the other hand, the relative changes of sample composition, which are indicating the transition between the reduced and oxidized states, are not affected, so that the LCA results provide a convenient access to study the temporal character of the oscillations. According to the results shown in Figure 4.17a and b, a stronger contribution of Pd can be observed for the commercial catalyst in both states. This can be explained with slightly larger particles of the commercial catalyst compared to the highly dispersed FSP catalyst, which directly results in a higher PdO/Pd ratio in the oxidized state of the FSP catalyst according to the higher surface-to-volume ratio.

The EXAFS fit results presented in Figure 4.17c, d and Table 4.3 for the FSP and the commercial catalysts can be used to further refine the structure of the oxidized and reduced states. Here it is important to note that no oxygen contribution could be observed in the reduced state of both catalysts. This is not in contradiction to the LCA results, since it has already been stated that a systematic error in the LCA results was to be expected. Thus, now it can now be concluded that fully reduced Pd nanoparticles are the dominant species in the reduced state. Furthermore, a higher coordination number of Pd was obtained in the case of the commercial catalyst, which confirms the suggestion that the catalytic Pd particles of the FSP catalyst are smaller than the ones of the commercial one (see [Jen99] for particle size dependence on coordination number). The oxidized state is best fitted with the combination of a Pd-O and a Pd-Pd scattering path. The results yield a lower ratio of O to Pd than could be expected for bulk PdO [Was53], which is further evidence that only the surface of the particles is oxidized, as already suggested by the LCA results. However, according to the fit results and the PdO structure presented in [Was53] about 82% of the particles are still reduced in the case of the FSP catalyst, which means that the LCA results are still overestimating the amount of PdO. More or less spherical particles with a fcc

Table 4.3: EXAFS fit results for the reduced and oxidized states of the FSP and the commercial catalyst. Coordination numbers (CN), mean-square deviations (σ^2) and interatomic distances (R) are displayed.

State of reaction		Path	CN	σ^2 / 10^{-3} Å^2	R / Å
FSP	reduced	Pd-Pd	8.4 ± 0.9	12.4 ± 0.7	2.717 ± 0.005
	oxidized	Pd-O	1.1 ± 0.2	1.7 ± 1.6	1.991 ± 0.008
		Pd-Pd	6.2 ± 0.7	13.8 ± 1.1	2.710 ± 0.006
commercial	reduced	Pd-Pd	8.8 ± 0.7	11.8 ± 0.5	2.726 ± 0.004
	oxidized	Pd-O	1.1 ± 0.2	1.9 ± 1.3	1.992 ± 0.006
		Pd-Pd	6.9 ± 1.4	13.7 ± 0.8	2.715 ± 0.005

structure and diameters of about 2 – 3 nm, as determined below for the FSP catalyst, consist of about 147 or 309 particles considering regular icosahedrons or cuboctahedrons as typical particle geometry [Mac62]. In such particles only 38.4% – 48.5% of all atoms are not located at the surface, so that it can be concluded that only surface atoms are oxidized here. A stronger contribution of Pd can be observed for the commercial catalyst, where about 84% of the particle's volume is still reduced in the oxidized state. This is in agreement with the LCA results, where, however, about 6% more Pd metal was observed in the oxidized state compared to the FSP catalyst.

A systematic LCA analysis of the QEXAFS data allows investigating and comparing the structure of the catalyst at different positions along the capillary. In Figure 4.18 this was done for the FSP catalyst at 410°C and the results obtained at both ends of the catalyst bed are shown together with the synchronized signals of H_2 and O_2 acquired with the mass spectrometer. First of all, it is obvious that the observed oscillations in the structure of the catalyst and the oscillations in the catalytic activity occur simultaneously and the transitions between the states appear rather regularly. Furthermore, at the end of the catalyst bed the catalyst is reduced almost as long as the corresponding H_2 signal persists, while the duration of the reduced state is much shorter than the duration of the corresponding H_2 signal at x/L = 0. This is demonstrated by the green boxes in Figure 4.18 and suggests that a reducing front moves from the end to the beginning of the catalyst bed and thereafter back again towards the end, which is in good agreement with earlier studies [Kim10, Gru10]. It is also evident that hydrogen production can be observed no longer than some particles of the catalyst are in the reduced state at x/L = 1, which is in agreement with earlier studies of the ignition behavior of CPO on Rh and Pt catalysts [Gru09a, Kim09]. Especially at the beginning of the catalyst bed it can be observed how closely related the oxidation state of the catalyst and the catalytic activity really are, since

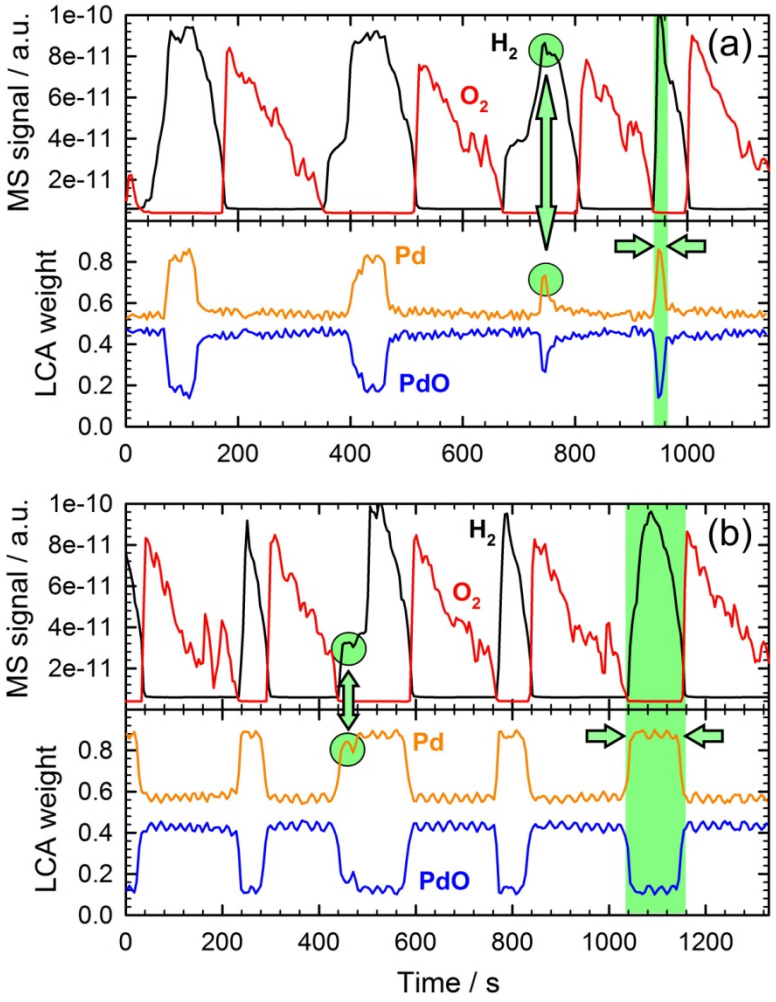

Figure 4.18: Results of LCA performed for all QEXAFS spectra during CPO oscillations on the FSP catalyst at 410 °C measured at (a) the upper part of the fixed bed (x/L = 0) and (b) the lower part of the fixed bed (x/L = 1). Additionally, the synchronized MS signals of H_2 and O_2 are shown.

characteristic features appear simultaneously in the QEXAFS data as well as in the MS data. This is demonstrated by the green circles in Figure 4.18.

The systematic LCA analysis can also be used to determine the relative duration of the reduced state during one oscillation period at various positions along the catalyst bed and for variable temperatures. For this purpose, the length of the oscillation period T or respectively the oscillation frequency f was determined with the help of the H_2 signal in the MS data. In Figure 4.19a the relative duration of the reduced state is displayed, while the logarithmic oscillation period is plotted as function of the reciprocal temperature in Figure 4.19b. Generally, it can be observed that the relative duration of the reduced state is longer at higher temperatures. Moreover, it also varies stronger along the catalyst bed with increasing temperature. At 418 °C the catalyst is reduced for more than 80% of the full oscillation period at the end of the capillary, while it is reduced during only 20% of the period at x/L = 0. Concerning the relative length of the reduced state of the commercial

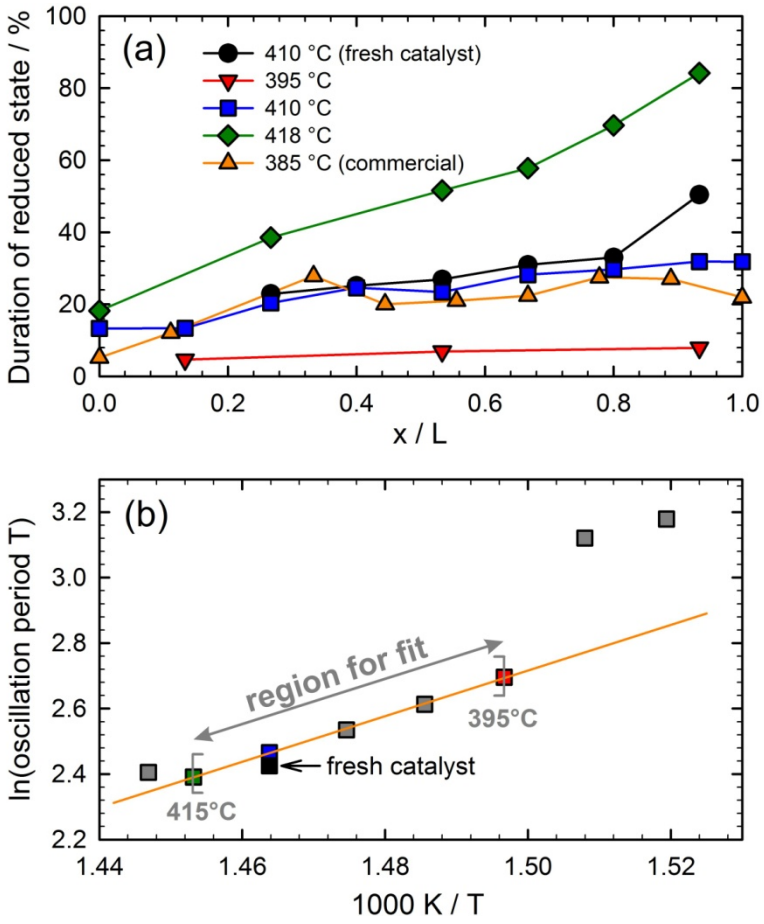

Figure 4.19: (a) Relative duration of the reduced state in each oscillation period for the commercial catalyst and the FSP catalyst at different temperatures. (b) Logarithm of the oscillation period as function of the reciprocal temperature for the FSP catalyst and linear fit in the region between 395 K and 415 K.

catalyst, it is noteworthy that it behaves at 385 °C like the FSP catalyst at 410 °C. The frequency of the oscillation increases as function of the temperature to a maximum of about 0.004 Hz at about 415 °C / 418 °C. Above about 420 °C the catalyst stops to oscillate, which is also true for temperatures below about 385 °C, where no ignition occurs. Between 395 °C and 415 °C the oscillations are stable and reproducible. Considering that some reaction with rate constant k is controlling the frequency f of the oscillations, and is thus the rate determining step, the Arrhenius equation

$$k = A\ exp\left(-\frac{E_a}{RT}\right) \Leftrightarrow T = f^{-1} = A' \exp\left(\frac{E_a}{RT}\right) \tag{4.1}$$

can be applied with the constant A, respectively A'. This was first suggested by Zhang et al. [Zha03] to describe the oscillation period as function of the temperature with activation energy E_a. In the present case, the linear fit in Figure 4.19b yields E_a = 58 kJ mol^{-1} for the FSP catalyst, which is a slightly lower value as detected for Pd metal foils and wires (68 kJ mol^{-1}). The fresh catalyst oscillates a bit faster than the aged catalyst at the same

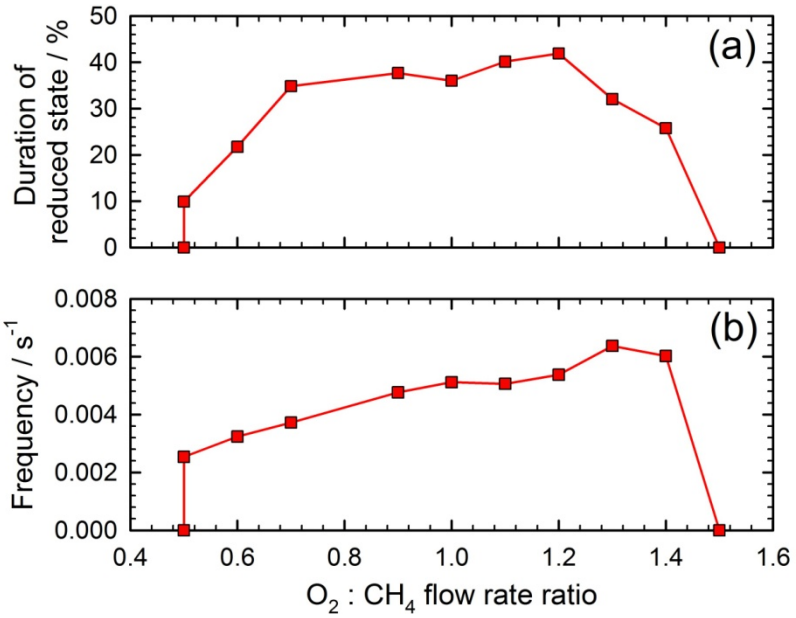

Figure 4.20: (a) Relative duration of the reduced state in each oscillation period and (b) frequency of the oscillations as function of the reaction gas composition measured with the FSP catalyst at 400 °C and x/L = 0.67.

temperature, which can be assigned to a smaller particle size (see below). A higher oscillation frequency of 0.005 – 0.006 Hz was measured for the commercial catalyst, but the oscillations are also less stable in this case. The lesser amount of Pd in the capillary with the FSP catalyst might be the reason for the lower oscillation frequency.

The dependence of the oscillations on a varying $O_2 : CH_4$ flow rate ratio was also investigated and again the relative duration of the reduced state and the oscillation frequency were determined. Both are shown in Figure 4.20 as function of the flow rate ratio. No oscillations were observable for $O_2 : CH_4$ ratios below 0.5 and above 1.5. The relative duration of the reduced state is rather symmetric around a ratio of 1.0, while the frequency is increasing linearly as function of the ratio from about 0.0025 Hz at 0.5 to 0.006 Hz at 1.4.

Concerning the age of the catalyst, up to now it has only been shown that the oscillation frequency is slightly higher for the fresher catalyst. By determining the averaged coordination number and structural disorder of the first Pd shell in the reduced state, respectively the first O shell in the oxidized state, with the help of EXAFS analysis, further conclusions with respect to the age of the catalyst can be drawn. The results as function of the position on the capillary are shown in Figure 4.21 and the corresponding fits are similar to those exemplarily shown in Figure 4.17. The coordination numbers of Pd, determined for the fresh catalyst after only 4 h in the gas stream, range from about 7.0 to 7.5 along the catalyst bed. This corresponds to particles with fcc structure consisting of about less than 100 atoms which would correspond to sizes of less than 2 nm in diameter [Jen99, Mac62].

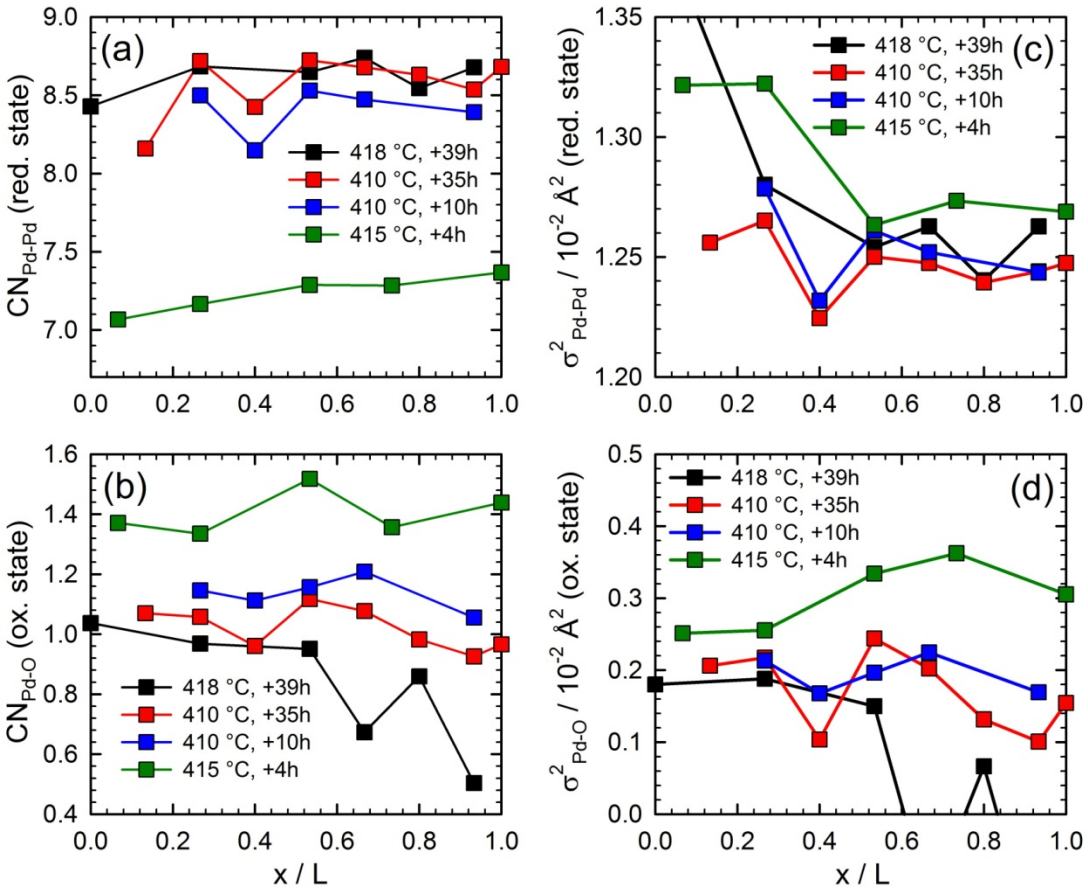

Figure 4.21: Results of first shell EXAFS fits performed for the reduced and oxidized state during the oscillations under various conditions: (a) Coordination number (CN) of Pd in the reduced state, (b) CN of O in the oxidized state, (c) mean square deviation (σ^2) of the Pd-Pd shell in the reduced state and (d) σ^2 of the Pd-O path in the oxidized state.

After 10 h in the gas stream the coordination number is significantly higher with about 8.4 and the value further increases to about 8.7 after 39 h in the gas stream, which corresponds to particles with about 150 atoms and ca. 2 – 3 nm in diameter. With respect to the TEM results, which were rather suggesting particle sizes of 2 – 4 nm, an underestimation by EXAFS analysis can be recognized. This is a well-known phenomenon in catalysis research with Pd nanoparticles under working conditions when using EXAFS techniques [Igl11] and was recently assigned to anharmonic contributions to the Debye-Waller factor caused by surface disorder [Yev10]. Moreover, it is a crude approximation to consider the catalytic particles as spheres. Morphology studies of catalytic particles on supports rather suggest that the particles are shaped as slabs and also change the shape during varying reaction conditions [Gru00, Lop04, Han02]. Deviations from spheres also result in an underestimation of particle sizes [Jen99].

Independently of the accuracy of the absolute values, the particle size obviously increased during the experiments due to sintering. The uncertainties of the determined coordination numbers are naturally rather high for highly dispersed systems measured at high

temperatures due to anharmonic contributions to the Debye-Waller factor which affect the low k-region of the EXAFS spectra [Cla00]. However, Figure 4.21a also shows that the relative errors are not that high, since the values obtained at different positions along the catalyst bed are not scattering that much and especially the curves obtained for the catalyst after 10 h and 35 h on stream exhibit exactly the same features. Thus, the EXAFS error turns out to affect the results in a systematic way and accordingly, all results might be shifted to higher or lower coordination numbers, while the observation of sintering still remains valid. Sintering of Pd/Al_2O_3 catalysts in methane was also suggested by Demoulin et al. [Dem08], who measured the CO chemisorption on the catalyst after heating the catalyst to 550 °C and letting it cool down to room temperature again. The average coordination number of O in the oxidized state decreases with larger particles as shown in Figure 4.21b. This can be explained by the fact that only the outer surface of the Pd particles is oxidized and accordingly the sample composition shifts to higher amounts of bulk Pd with larger particles. Thus, this effect can be considered as further confirmation of the observed sintering effect.

By fitting the Debye-Waller factor it is possible to analyze the thermal and structural disorder of the system as explained in section 2.1.2. The results for the FSP catalyst are also displayed in Figure 4.21 for the first Pd shell in the reduced and the first O shell in the oxidized state. During the reduced state disorder is highest at the beginning of the catalyst bed and decreases towards the end. This is in agreement with an increased thermal disorder at the beginning of the catalyst bed due to an evolving hot spot as detected in studies using IR thermography [Kim10]. The results for the oxidized state rather indicate a maximum towards the end of the capillary, probably because the catalyst heats up along the axial direction due to the exothermic methane combustion. At 418 °C the oxidized state was too short to achieve reasonable data quality for EXAFS fits at the end of the capillary.

With the achieved time resolution and data quality it is also possible to analyze the ignition and extinction behavior during the oscillations in more detail. Up to now, the oxidized and reduced states were treated as stable states. This has to be further refined with respect to Figure 4.22, where a closer look at the evolution of the LCA weight of PdO is given at different temperatures and a fixed position along the catalyst bed. To obtain these results it was averaged over several oscillation periods. Figure 4.22a demonstrates that for the first 60 s the oxidation proceeds similarly at all temperatures with an exponential growth, as describable by

$$\%PdO(t) = \%PdO(t \to \infty) \cdot [1 - e^{-bt}] \tag{4.2}$$

with a time constant b that does obviously not depend on the temperature. The PdO contribution further increases to a maximum, which is reached after 60 s at 410 °C and

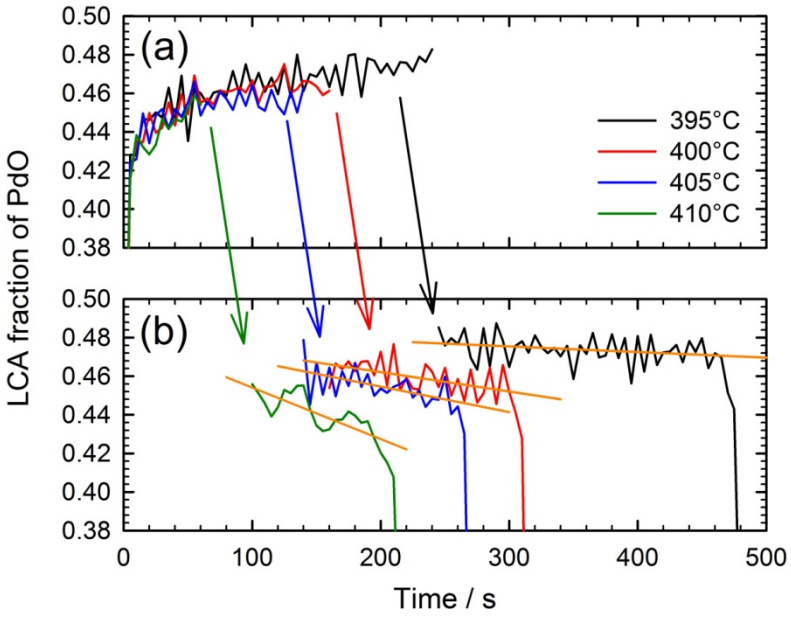

Figure 4.22: Relative amount of PdO in the oxidized state of the oscillation as determined with LCA after averaging over 3 oscillations: (a) first part with increasing PdO amount directly after the oxidation and (b) second part with decreasing amount leading to the reduction.

after 240 s at 395 °C. The data in Figure 4.22 was cut at the maximum and the second half of the oxidized state is shown in Figure 4.22b together with linear fits. Evidently, the amount of PdO decreases linearly until the catalyst reduces. Thereby, the amount of PdO decreases faster at higher temperatures. The behavior in Figure 4.22a can be explained by the fact that the deactivation occurs above a temperature threshold of the hot spot at the beginning of the reactor, which is similar in all cases [Gru07]. For the activation of CPO the oven temperature is the decisive parameter, because it supports the evolution of a hot spot and thereby the whole reduction process.

The results in Figure 4.16 indicate that it might be sufficient to describe the dynamics in the structure of the catalyst with only two states as characterized in Figure 4.17. On the other hand, various adsorbed molecules as CH_4, CO, CO_2 or O_2 are known to appear during the oscillations due to the active catalytic reaction. Such adsorbates cause only minor changes in the absorption spectra and are thus difficult to detect [Res97]. Furthermore, PdC_x is suggested to appear during the oscillations [Byc09], which is also difficult to detect, since it provides EXAFS features that resemble those of metallic Pd [McC93a], while the XANES structure is also quite similar for Pd supported on alumina with and without incorporated carbon [McC93b]. As hydrogen is produced by the partial oxidation of methane, the diffusion of hydrogen into the Pd lattice also has to be considered, since it is known that hydrogen can fill up the vacancies in the Pd lattice that are not occupied by C leading to PdC_xH_y compositions, whereby x and y are linearly linked to each other [Vog11]. For all these reasons, a good data quality is required in order to

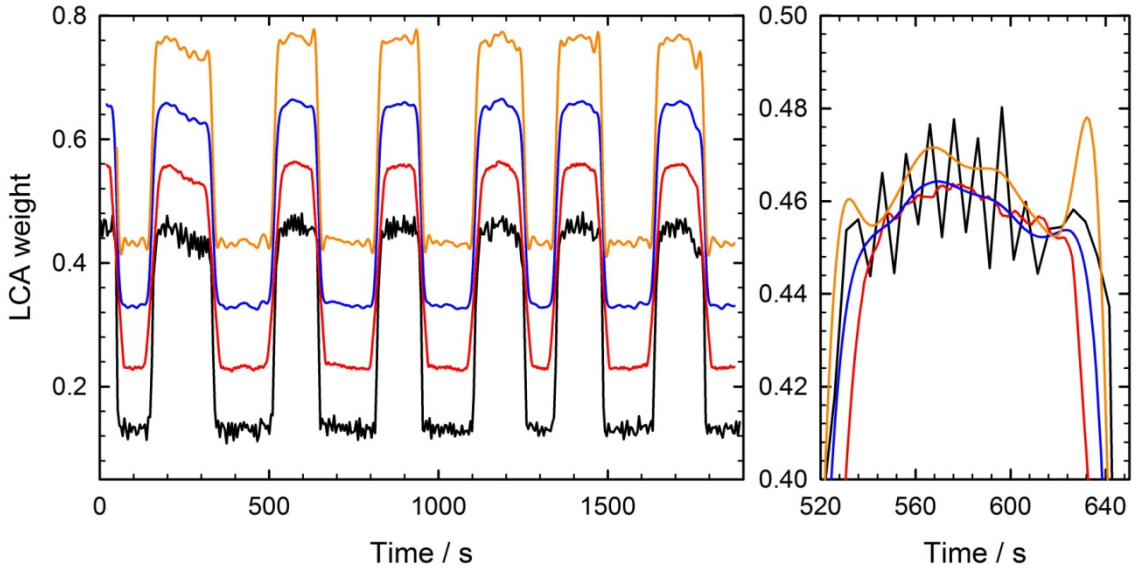

Figure 4.23: Resulting LCA weights of PdO (same data as used for Figure 4.16) after applying different smoothing filter algorithms on the raw data with the T-REX software prior to the LCA fits: (black) data reduction by averaging over 5 spectra, (red) convolution of the spectra along the time axis with a moving rectangular window of 40 spectra width, (blue) convolution with a moving Gaussian window of 40 spectra width and (orange) low pass filtering with a cut-off frequency of 0.04 Hz. On the left side, the spectra are shifted vertically with respect to the black curve to make changes visible.

discuss any additional species, which can only be achieved with advanced smoothing procedures as implemented in T-REX and described in section 3.3.3.

In Figure 4.23 the LCA weight of PdO is shown after performing low pass filtering by averaging with a moving rectangular window and a moving Gaussian window, both with a window width of 40 spectra. Additionally, a low pass filter with a cut-off frequency of 0.04 Hz was applied to the data. All three filter techniques yield improved signal-to-noise ratios with respect to the data, where averaging over only 5 spectra was performed. However, using the rectangular window, high frequency noise can still be observed in the results (see Figure 4.23, on the right side, red curve). This is in good agreement with Figure 3.24, where the filters were investigated in frequency space and it is clearly shown that high frequency contributions pass the rectangular filter. At the same time, the low pass character of the rectangular filter is already too strong in this case, because the fast transitions between the reduced and oxidized states are not reproduced correctly. The Gaussian filter yields better results, as the transitions are not that strongly affected, while there is absolutely no more high frequency noise. The sinc-function filter with the chosen cut-off frequency performs equally well in suppressing high frequency noise as the Gaussian filter, but it is possible to further decrease the cut-off frequency. Thus, it is also possible to investigate features close to the transitions between reduced and oxidized states, which would have been either lost in noise or been removed by applying the other

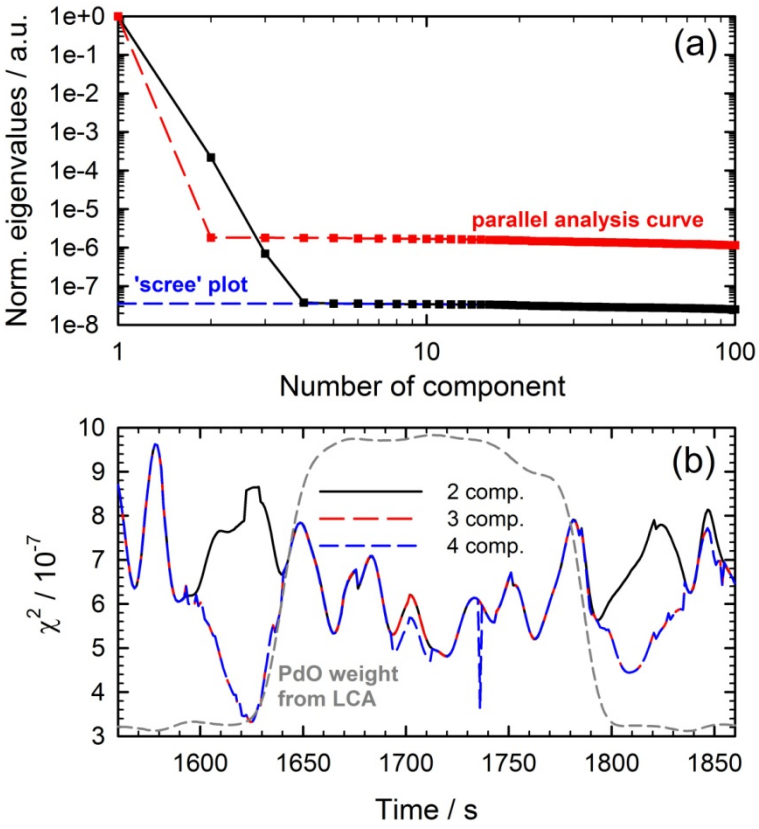

Figure 4.24: PCA applied to one period of CPO oscillation within the Gaussian smoothed data as introduced in Figure 4.23: (a) Eigenvalues of the components normalized on the sum of all eigenvalues (similar to proportion of each component) and applied factor retention criteria (parallel analysis in red, fit of the 'scree' in blue), (b) Resulting mean square deviation after reconstructing the sample spectra with different numbers of PCA components and the PdO contribution to the sample composition as calculated in Figure 4.23, here in arbitrary units (grey, dashed).

filters. Thereby, it is noteworthy that sharp overshoots appear prior and after the transitions, which can be explained by the fact that the surface coverage of the catalyst is removed prior to the transitions. Consequently, e.g. a stronger bulk Pd character can be observed shortly prior to the oxidation.

To reveal additional species during the oscillations a PCA was applied to the Gaussian smoothed data to check the number of independent components, which contribute to one period of the CPO oscillations. The results are shown in Figure 4.24a, where the two retention criteria presented in section 3.3.5 were applied. The parallel analysis curve suggests that only two independent components contribute, while the 'scree plot' criterion yields 3 or maybe even 4 independent components. This inconsistency can be resolved by reproducing the spectra with various numbers of components and afterwards analyzing the mean square deviations between reproduced and measured spectra as function of time. The results are displayed in Figure 4.24b together with the PdO weight as calculated by LCA in arbitrary units. A third component significantly improves the reproduced spectra prior to

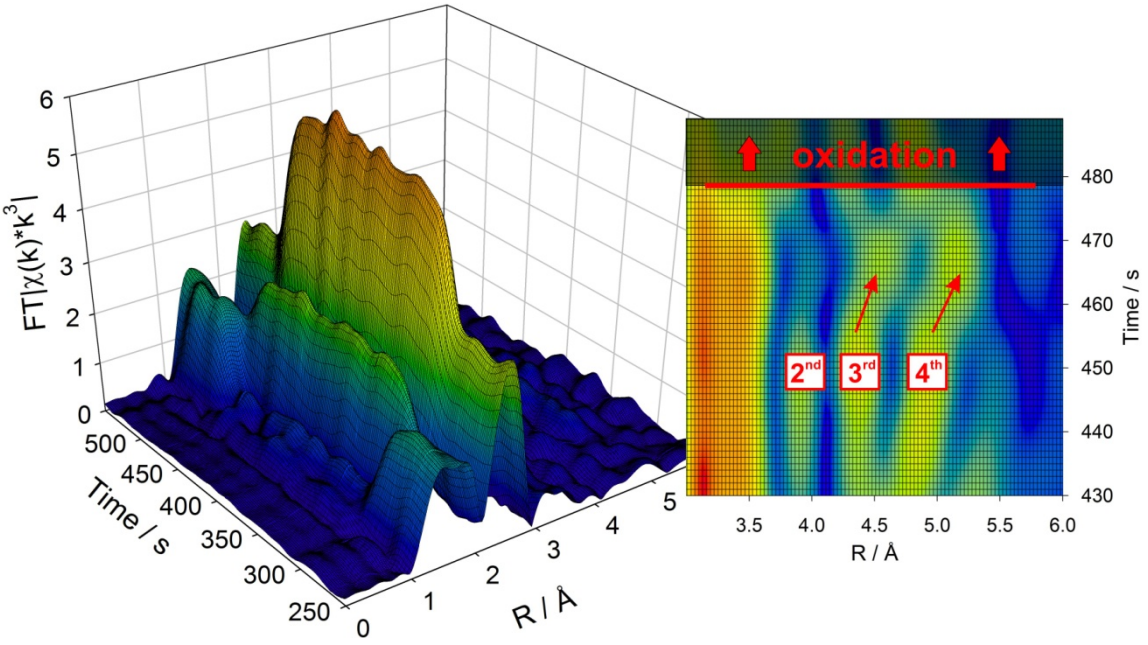

Figure 4.25: Fourier transformed QEXAFS data acquired during one period of the CPO oscillations and smoothed with the Gaussian filter: 3D overview showing the dominant first Pd shell during the reduced state (left side) and contour plot for studying the higher shells prior to the oxidation (right side). The arrows mark the evolution of the 2nd, 3rd and 4th shell.

the oxidation and also shortly after the reduction, which is a strong evidence that two independent states are present during the reduced state. A forth component yields only minor improvements in the middle of the oxidized state, which are too small to be assigned to any additional species.

Due to the PCA results, the reduced state was further analyzed with the help of Fourier transformed EXAFS spectra after applying the Gaussian 40 spectra filter. The results for one depicted oscillation are shown in Figure 4.25. The 3D overview demonstrates the rather dominant first Pd shell at about 2.5 Å during the reduced state. In the top-view contour plot of the region between 3 Å and 6 Å it is possible to study the evolution of the second, third and fourth shell prior to the oxidation. First of all, the typical fcc structure, which is expected for metallic Pd, is only observable in a short time frame around about 450 s (and shortly prior to the oxidation). Thereafter, the third and the fourth shell move to higher distances, while the second one only slightly decreases in intensity. This behavior can be explained with a lattice expansion due to the intercalation of C. Carbon diffusion to a maximum C/Pd ratio of ~0.13, before the C is oxidized to CO_2, was recently predicted by Bychkov et al. [Byc09].

McCaulley performed EXAFS measurements of $PdC_{0.13}$ in comparison to metallic Pd and has shown that the third and fourth shell are shifted to higher R-values in a similar way as observed here in Figure 4.25b [McC93a]. Furthermore the second shell vanishes in $PdC_{0.13}$

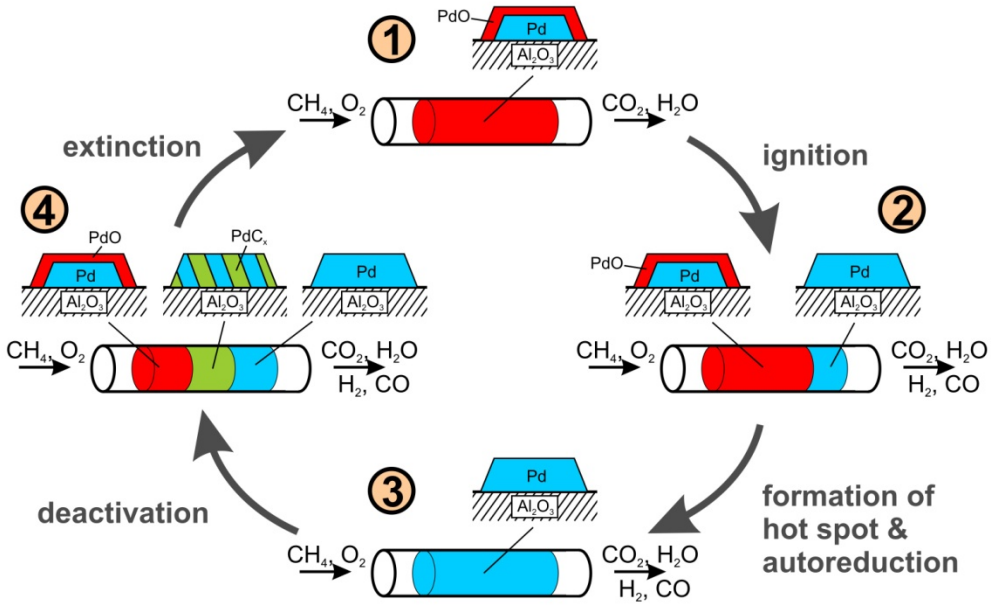

Figure 4.26: Oscillations of CPO on a fixed bed Pd/Al_2O_3 catalyst described in a scheme consisting of four stages: (1) oxidized catalyst and total oxidation of methane, (2) ignition of CPO and start of reduction at the end of the catalyst bed, (3) fully reduced catalyst after autoreduction caused by hot spot formation, (4) oxidation from the beginning of the catalyst bed with an intermediate PdC state appearing shortly prior to the oxidation. As soon as the entire catalyst is reduced, a new cycle begins.

which agrees well with the decreased intensity of the second shell that was observed above. Thus, it is suggested that poisonous carbonaceous species in the Pd lattice are observable in a short time frame prior to the oxidation, which also agrees well with the PCA results shown in Figure 4.24. Evidences for C incorporation can also be seen after EXAFS fitting the first shell, which is also shifting to higher R-values (see [Stö12a]). In this report it was also shown that the XANES features do not vary significantly in parallel to the lattice expansion, which would be expected in the case of hydrogen instead of carbon incorporation [McC93b].

Discussion

The results obtained by QEXAFS data analysis show that a front of Pd nanoparticle reduction oscillates along the catalyst bed. Two different states are separated by this front. In the more oxidized state, which was characterized as Pd nanoparticles with partly oxidized surface atoms, only total oxidation of methane can be observed (extinguished state). The other state corresponds to fully reduced Pd particles (plus adsorbed reactants) on which the CPO occurs (ignited state). The whole process is summarized within four steps as shown in Figure 4.26. First, the catalyst is oxidized and only total oxidation occurs, which means that no hydrogen is produced (state 1). With the total consumption of

oxygen no more oxygen reaches the end of the catalyst bed after a while. This leads to reduction and the start of the CPO from the end of the catalyst bed towards the beginning, which was also assumed in previous studies [Han07, Kim09, Gru09b]. It was shown here, that the start of the reduction is also favored by higher temperatures, which is thus the responsible effect determining the temperature dependence of the oscillation frequency. This dependency could be described by the Arrhenius equation, so that it is possible to control the oscillation frequency by the applied temperature. At the same time when the end of the catalyst bed starts to reduce, the region of total oxidation is contracted to the very beginning of the catalyst bed and a hot spot with a locally increased temperature evolves within this region [Kim10] (state 2). A self-acceleration of the total oxidation reaction occurs due to the non-linear Arrhenius term and a further increase of temperature can be observed within the more and more contracted region of total oxidation, while the reduction front moves further upstream.

Finally the autoreduction temperature of Pd is reached and the catalyst fully reduces (state 3). It was detected that the frequency of the oscillation is higher for smaller particles, which is probably the case because of a faster autoreduction, respectively the higher density of defects [Joh04]. Furthermore, a higher O_2 : CH_4 ratio increases the frequency as it leads to a faster and larger hot spot evolution, and thus again a faster autoreduction. As soon as the catalyst is fully reduced, the activity of methane oxidation drops and thus also the corresponding heat production. As soon as the temperature is lowered to a sufficient extent, the catalyst re-oxidizes again from the beginning of the catalyst bed, where the oxygen concentration is highest, downstream towards the end, while the CPO extinguishes at the same time (state 4). This can be seen as proof of the combustion-reforming mechanism also shown on other noble metal catalysts [Har11, Dal11]. During the oxidation process it was shown that only shortly prior to the re-oxidation the typical structure of bulk Pd is recognizable in all shells, probably due to desorption of the reactants. Prior to the re-oxidation, a lattice expansion could be observed, which was assigned to carbon incorporation into the Pd lattice. This is also displayed as part of the fourth state in Figure 4.26. The observed sintering of the catalyst in the gas stream can be explained with the high exothermicity of the reduction process [Gru07], although in principle the re-oxidation could also lead to a re-dispersion in each oscillation.

4.1.3 Chemical oscillations during extinction of CO oxidation

Oscillations in the conversion of a reaction gas on catalysts can also be detected during the famous catalytic reaction of CO oxidation on Pt catalysts [Ert82, Ert08]. While this reaction is mainly known to be applied in automobiles to clean the exhaust emissions [Far99], it is also e.g. used to remove CO from hydrogen streams in fuel cell applications [Kah97]. Oscillations during CO oxidation on Pt have been observed on single crystal

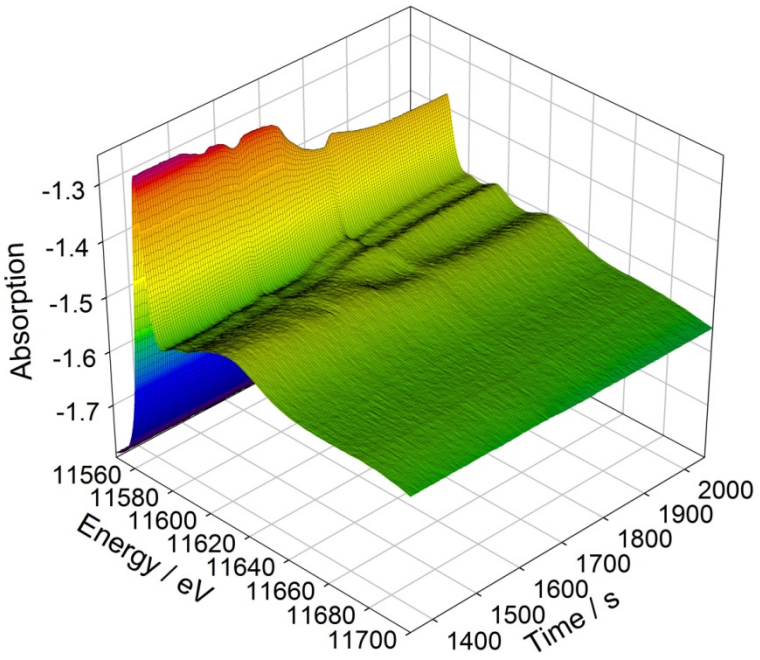

Figure 4.27: 3D plot of the QEXAFS spectra measured during the extinction of CO oxidation on Pt/Al_2O_3 at the Pt L_3-edge revealing oscillations within the crystal structure.

surfaces [Eis86] and also under technically relevant conditions [Beu72]. The herein studied oscillations appear shortly before and during the extinction of the catalytic process. Therefore, the catalyst was slowly cooled down with 1 $Kmin^{-1}$ from 395 K, where the oxidized catalyst showed high activity and full conversion of CO, to 350 K, where the catalyst was reduced and inactive. Details about the preparation of the used 1.9 wt% Pt/Al_2O_3 catalyst, the catalytic reactor used for the X-ray absorption experiments and the applied conditions to achieve the oscillatory behavior can be found in [Sin10]. The mass spectrometer signal of CO_2, which is displayed in Figure 4.28, demonstrates the oscillatory behavior of the catalyst during the experiments. These oscillations start with a decrease in CO conversion followed by a sudden increase above the full conversion level before the CO_2 signal returns to the 100% conversion level. Thereby the question arises, whether these oscillations in gas conversion are accompanied by oscillatory structural changes of the Pt catalyst.

The acquired QEXAFS spectra at the Pt L_3-edge during the extinction measured at a position about 1 mm downstream from the beginning of the catalyst bed are shown in Figure 4.27. Here it is obvious by considering the varying XANES features that structural oscillations can be observed during the reduction of Pt, corresponding to the extinction of the catalytic reaction. As already indicated in section 3.3.4, the white line feature represents transitions to free d-orbitals and is thus an indicator of the oxidation state of Pt. Thus, to study the dynamics of the observed oscillations it is a convenient approach to analyze the white line intensity as function of time, respectively temperature, as shown in

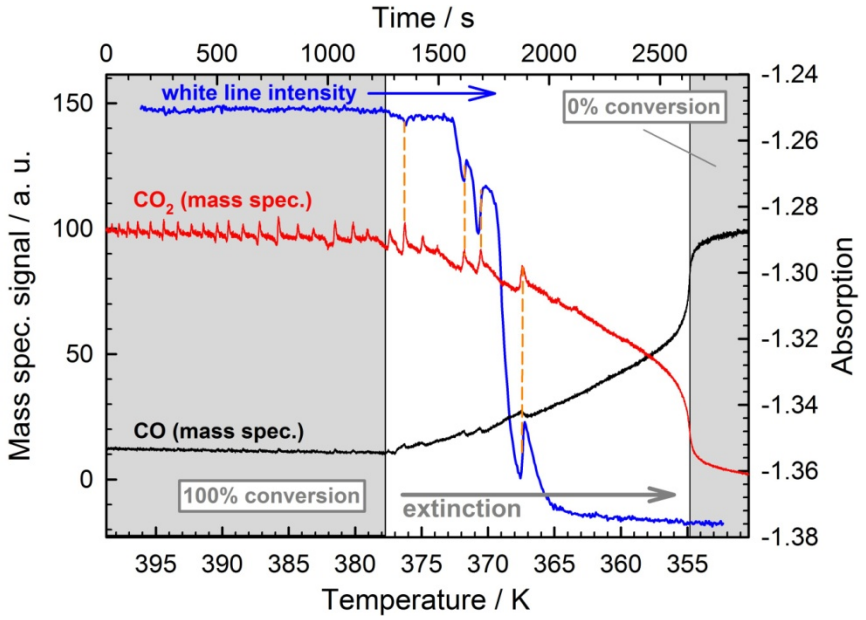

Figure 4.28: Mass spectrometer signal of CO and CO_2 representing the oscillations in conversion of CO on Pt/Al_2O_3 during the extinction of the catalytic reaction. Additionally, the synchronized white line intensity derived from the QEXAFS spectra, which were measured simultaneously, is shown. The orange lines mark the regions, where a partly re-oxidation of the catalyst could be observed together with an increase in conversion.

Figure 4.28 synchronized to the signal of the mass spectrometer. Above 378 K the oscillations in the CO_2 signal are not complemented by corresponding effects in the measured white line intensity. Thereafter, several oscillations can be observed in the MS signal as well as in the white line intensity. These oscillations start with a decrease of CO_2, which is accompanied by a decrease in white line intensity, suggesting the start of reduction. Afterwards, simultaneously to the sudden increase of CO_2 also the white line increases again.

To quantitatively verify the observations presented in Figure 4.28, the QEXAFS spectra acquired during the extinction were fitted with a linear combination of the reduced CO-covered Pt appearing during the inactive state of the catalyst and the partially oxidized state of the active catalyst. In general, the results, which are shown in Figure 4.29, confirm the previous conclusions derived from the white line intensity. However, by plotting the mean square deviations between the linear combination fits and the measured spectra sharp peaks appear at the positions of re-oxidation during the described oscillations. Comparing the marked positions 1 and 2 in Figure 4.29, it is noteworthy that these deviations are only observable during the re-oxidation and not during the reduction, although the LCA results suggest the same sample composition here. The XANES regions of the two measured spectra assigned to the marked positions exhibit an energy shift of 0.2 eV. This chemical shift can be explained with an additional sudden release of CO from the surface of the

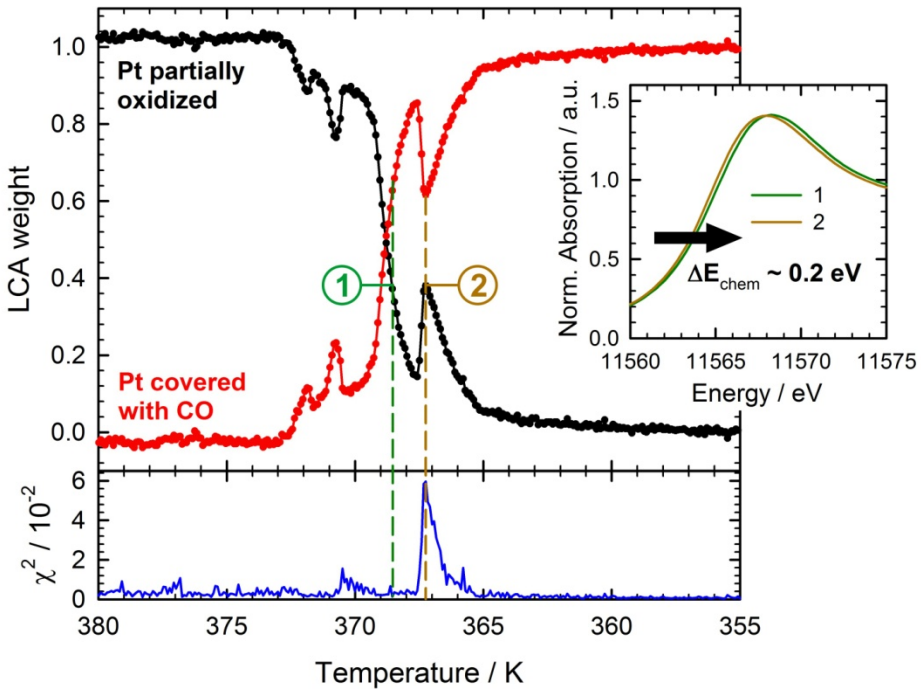

Figure 4.29: Linear combination fits of all spectra during the extinction of CO oxidation with spectra of partially oxidized and CO covered Pt. Additionally, the mean square deviation between fits and measured data is plotted and the XANES spectra at two different positions, where the LCA results suggest the same sample composition, while the fit errors are very different.

catalytic particles during the re-oxidation. Desorption of CO during re-oxidation could also be confirmed by additional investigations using infrared spectroscopy [Sin10].

In Figure 4.28 it can be further observed that the catalyst still shows activity between 365 K and 355 K, although it is fully reduced at this position along the catalyst bed. Measuring at various positions revealed that the reduction of the catalyst moves further towards the total extinction of the catalytic reaction, when measuring closer to the outlet of the reactor. Thus, the oscillations can be explained by an oscillating reduction front that slowly moves downstream over the entire catalyst bed. The results indicate that each oscillation starts with the catalyst in a partially oxidized state, whereby the surface oxygen reacts with CO to CO_2. The thereby generated free lattice sites are immediately replenished either by oxygen from the gas stream according to the Mars-van-Krevelen mechanism or by CO at lower temperatures. The CO further reduces the catalyst by reacting with the lattice oxygen until only CO-covered Pt remains, which is the inactive state of the catalyst. During this process, the catalyst can partly re-ignite, which is paralleled by a removal of CO and a re-oxidation of the surface. Shortly after these re-ignitions, the catalyst temporarily shows high activity until it is poisoned by CO again and the reduction/deactivation further proceeds.

4.1.4 Modulated excitation of reactions on catalysts

Many interesting phenomena in catalysis, as e.g. oxidation and reduction processes, are reproducible, whenever the same conditions are applied. Thus, it is often possible to modulate the system by periodically varying the experimental conditions as e.g. the temperature or the gas composition inside the catalytic reactor. The advantages of this approach are, on the one hand, that it is possible to average over several cycles and thus to improve the statistics without losing time resolution. On the other hand, the advanced data analysis techniques of MES/PSD as introduced in section 3.3.7 can be applied to the data. In this section two modulated experiments with catalytic systems will be discussed. In both cases, two different gas compositions that were streamed over the catalyst in a fixed bed capillary reactor, which has already been introduced in section 4.1.2, were switched periodically. The first experiment was performed with a Pt-Rh/Al_2O_3 catalyst during the active state of methane conversion by CPO [Gru09a]. In this case the reaction gas 6% CH_4 / 3% O_2 / He and the reducing gas mixture 5% H_2 / He were interchanged. As second system a Cu/Al_2O_3 catalyst has been periodically oxidized and reduced by switching 21% O_2 / He and 5% H_2 / He gas streams at various temperatures inside the catalytic reactor and with various Cu loadings. Cu catalysts are interesting for methanol synthesis, steam reforming and gas phase oxychlorination.

Experimental

The QEXAFS spectra during both experiments were acquired at the SuperXAS beamline with the Si(111) channel-cut crystal installed inside the QEXAFS monochromator. The used eccentricity, yielding peak-to-peak Bragg angle amplitude of about 0.6°, resulted in spectra from 11.5 keV to 12.3 keV at the Pt L_3-edge and from 8960 eV to 9440 eV at the Cu K-edge. The beam, originating at the bending magnet, was collimated vertically on the monochromator crystal and focused on the sample by toroidal X-ray mirrors. As a result, the catalysts were studied with a beam size of about 100 µm x 100 µm and a flux of about 10^{12} photons/s. The incident and transmitted beam was measured with two short (15 cm) ionization chambers, while a third long (30 cm) chamber was used to measure Pt, respectively Cu, metal foils to calibrate the angular encoder data with the corresponding edge positions. The chambers were all filled with air at ambient pressure and connected to the high voltage supply, which was set to 1 kV.

The 5% Pt - 5% Rh/Al_2O_3 catalyst was prepared by flame spray pyrolysis as described in [Han07]. The Cu/Al_2O_3 catalysts were prepared by impregnating alumina pellets with cylindrical shape (3.2 x 3.5 mm, Engelhard) in a $CuCl_2$ solution with different impregnation times, before the pellets were dried and crushed into about 100 µm large particles [Bai83]. Thereby, the pellets that were impregnated only 4 min exhibit a rather sharp impregnation profile (shell-impregnated), while the ones impregnated for 90 min,

respectively 210 min, were fully impregnated with increasing loading. Similar for all catalysts, about 5 mg of the material was filled into quartz capillaries with 1 mm diameter (Markröhrchen, Hilgenberg GmbH) between to quartz wool plugs. Heating of the capillaries was performed with the reactor cell as described in [Gru04] and in Figure 4.15, while the gas mixture at the outlet of the cell was connected to a quadrupole mass spectrometer (Balzers Thermostar) to monitor the products.

CPO on Pt-Rh

To start the CPO on the Pt-Rh/Al_2O_3 catalyst, the capillary reactor was heated to 330 °C, which is slightly above the ignition temperature as already known from earlier studies [Gru09a, Gru09b]. These studies also revealed that the catalyst is oxidized and inactive prior to the ignition, while a reduction of the Pt can be observed during the ignition, leading to the active state of the catalyst for CPO. Time-resolved investigations of the ignition behavior with QEXAFS were performed in [Stö09b] in comparison to a Pt/Al_2O_3 catalyst, and revealed that the reduction process is completed during only 3 s and leaves the catalyst in a still slightly oxidized state afterwards. This can be explained by the adsorbed reactants during the active CPO of methane on the catalyst surface, to which dissociated O_2 naturally belongs. Thus, it should be possible to analyze the effect of adsorbed oxygen, respectively absorbed carbonyl species, by investigating the changes in the X-ray absorption spectra, when streaming H_2 over the sample. This removes e.g. the dissociated oxygen on the surface by initializing the reaction to water.

In the active state of the catalyst at 330 °C, the composition of the applied gas stream was interchanged between 6% CH_4 / 3% O_2 / He and 5% H_2 / He every 60 s. The evolution of the white line intensity of the normalized spectra measured at the Pt L_3-edge is displayed in Figure 4.30 during a measurement that took about 12 min. As already shown in section 4.1.3, analyzing the Pt white line feature is a very convenient approach to detect changes in the oxidation state of the Pt. Indeed, in the herein presented experiment it is also possible to see dips in the white line intensity of the normalized spectra every 120 s, which suggest a partial reduction at these moments. As the signal-to-noise ratio is not that good, the data was averaged over three cycles resulting in the data shown in Figure 4.30b and it is noteworthy that the data quality could be significantly improved, without any loss of time resolution as would be the case with the other smoothing techniques that were introduced in section 3.3.3.

Considering the results in Figure 4.30b, it is evident that the small effects of adsorbed and desorbed oxygen really can be analyzed with the acquired QEXAFS data. As soon as the H_2 gas stream is applied to the sample, the H_2 starts to react with the adsorbed oxygen and/or carbonyls at the beginning of the catalyst bed. After a while, when all oxygen is removed from the upper part of the catalyst, H_2 also reaches the position further

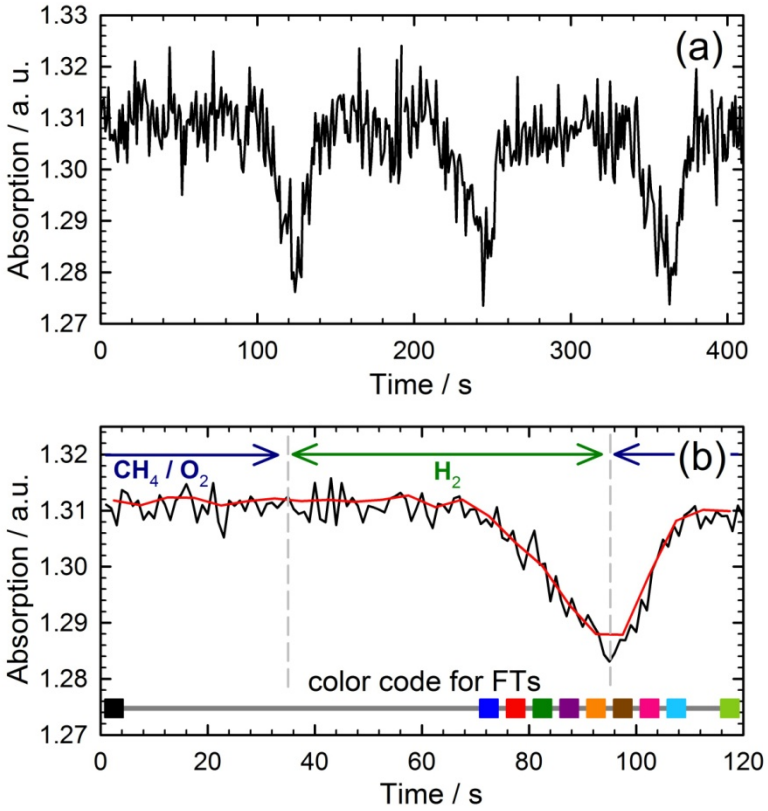

Figure 4.30: White line intensity of the normalized X-ray absorption spectra acquired during cyclic modulation of the Pt-Rh/Al_2O_3 catalyst by periodically changing the gas composition that was streamed over the catalyst: (a) data without any applied smoothing, (b) data after averaging over three modulation cycles (black) and additional flattening by averaging over 5 spectra (red). The colors at the bottom correspond to the colors of the Fourier transformed spectra, as shown in Figure 4.34.

downstream, where the beam passes the sample. Here it also removes the oxygen and/or carbonyls, as evidenced by the observed decrease in white line intensity. As soon as the gas composition is switched back to CH_4 / O_2, the now reduced and empty catalytic surface is immediately covered by methane and oxygen again, leading to an increase in white line intensity due to the increased oxidation state of the Pt. The experiments were also performed with a Pt/Al_2O_3 catalyst at 405 °C and the results are presented in [Stö09b]. Here, averaging over several cycles is even more important, because otherwise it would not have been possible to see any effects in the white line intensity at all. Due to the averaging it becomes obvious that the same effect as observed for the Pt-Rh/Al_2O_3 catalyst is also present for Pt/Al_2O_3, though to a lesser extent. This could be explained by the fact that the adsorption of O_2 and/or carbonyl species is promoted by the larger Rh atoms, providing more active sites. In fact, the formation of Rh-carbonyls on pure Rh catalysts was also observed in other studies by IR and EXAFS investigations [Bas00, Gru01c].

To build up an argumentation of oxidizing and reducing Pt solely on the white line feature is not reasonable, because the white line intensity is also affected by the local geometry

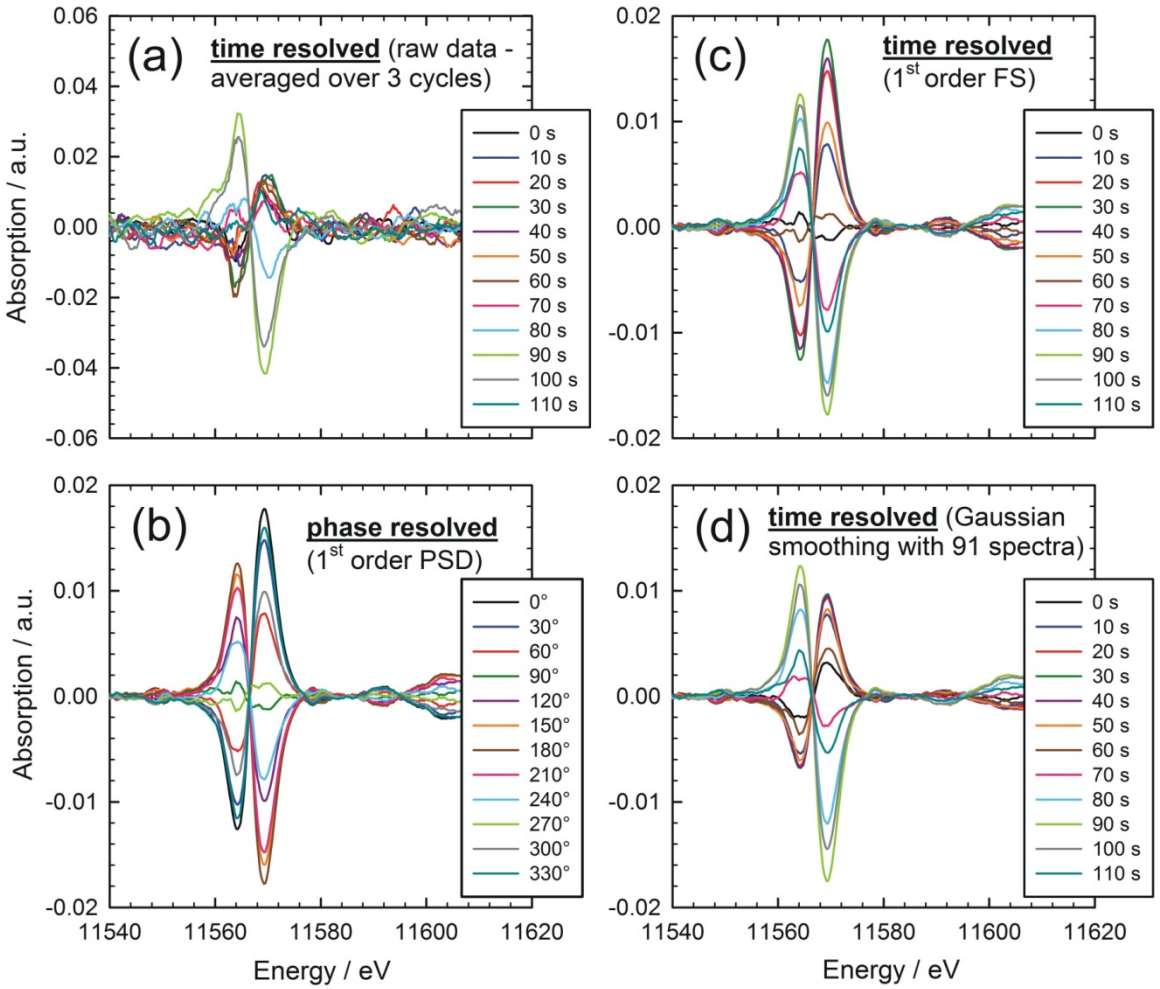

Figure 4.31: (a) Difference normalized absorption spectra of the Pt-Rh/Al_2O_3 catalyst during the gas switching modulation cycle after performing averaging over 3 cycles, (b) results of 1st order PSD, (c) results of 1st order FS and (d) resulting difference spectra after Gaussian smoothing with a width of 91 spectra.

around the Pt atoms, the particle size and the temperature. Thus, it is important to either analyze the XANES region with LCA or the EXAFS of the acquired spectra. For the present system both paths are difficult to follow, since the differences in the spectra are rather small with respect to the noise level. Averaging over several cycles has already proven to be helpful in increasing signal-to-noise ratios, but for an EXAFS analysis every improvement is welcome in order to get a good quality even at high k-values. Thus, further improvements in data quality are desirable.

The reproduction of the spectra with Fourier series (FS) built up on frequencies of the modulation, respectively the calculation of PSD spectra, are two possibilities to improve data quality (see section 3.3.7), smoothing the spectra with low pass algorithms is another one (see section 3.3.3) and all three approaches were applied to the data. Thereafter, the spectrum resulting from averaging over all considered spectra, which is actually the a_0 as defined in Eq. (3.15), was subtracted from the data to achieve a higher sensitivity for noise

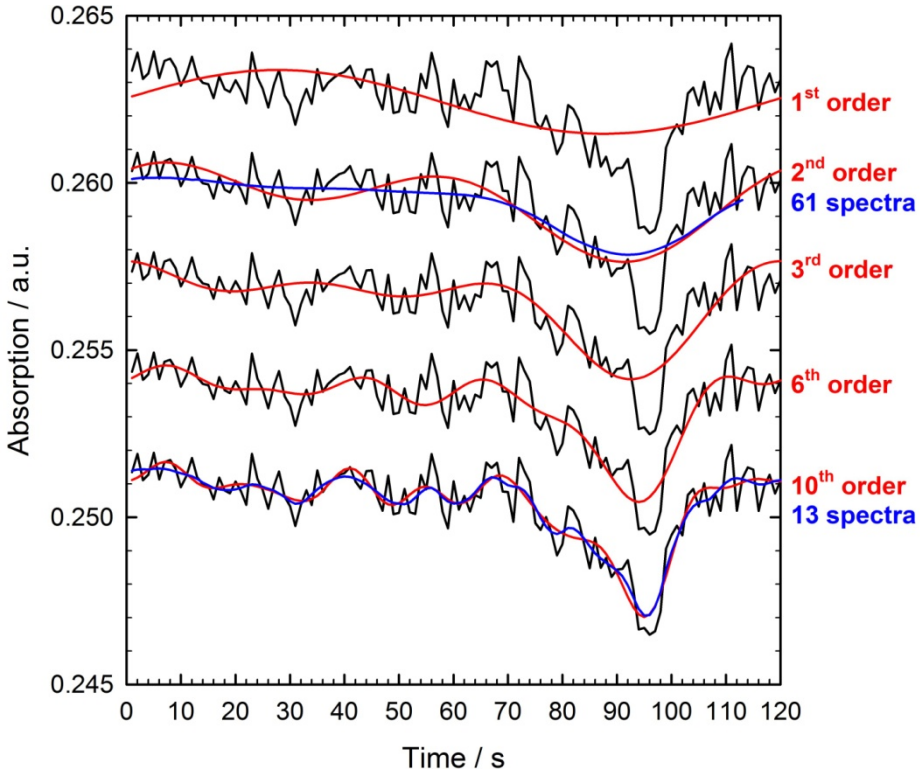

Figure 4.32: White line intensity of the spectra of the Pt-Rh/Al_2O_3 catalyst during one modulation cycle after reproducing the spectra with Fourier series of various orders (red) and after smoothing the spectra with the moving Gauss filter by using various window widths (blue).

observations, which would be scaled down by the edge jump otherwise. The results are shown in Figure 4.31 and several important observations can be made:

(i) FS and PSD spectra are practically the same within the displayed first order calculations with respect to noise as well as dynamics. Since the phase information is by no means superior to the time information, there is actually no reason to apply PSD to the absorption spectra at all.

(ii) The achievable noise reduction is the same for FS/PSD and Gaussian filtering.

(iii) FS/PSD approaches yield symmetric results according to the sinusoidal character of first order FS, while the Gaussian filtering reproduces the dynamics more correctly, as obvious by comparison to the raw data (averaged over three cycles), where the only deviations are clearly localized at 90 s.

According to these results, FS and PSD approaches are rather not recognized as valuable addition to conventional QEXAFS analysis. However, it has to be further evaluated, whether the addition of more orders, respectively weaker low pass filtering, changes things in favor of the FS approach.

To find the most reasonable filter settings with respect to the reaction dynamics, the white line intensity was determined again, this time of the FS reproduced and Gaussian smoothed

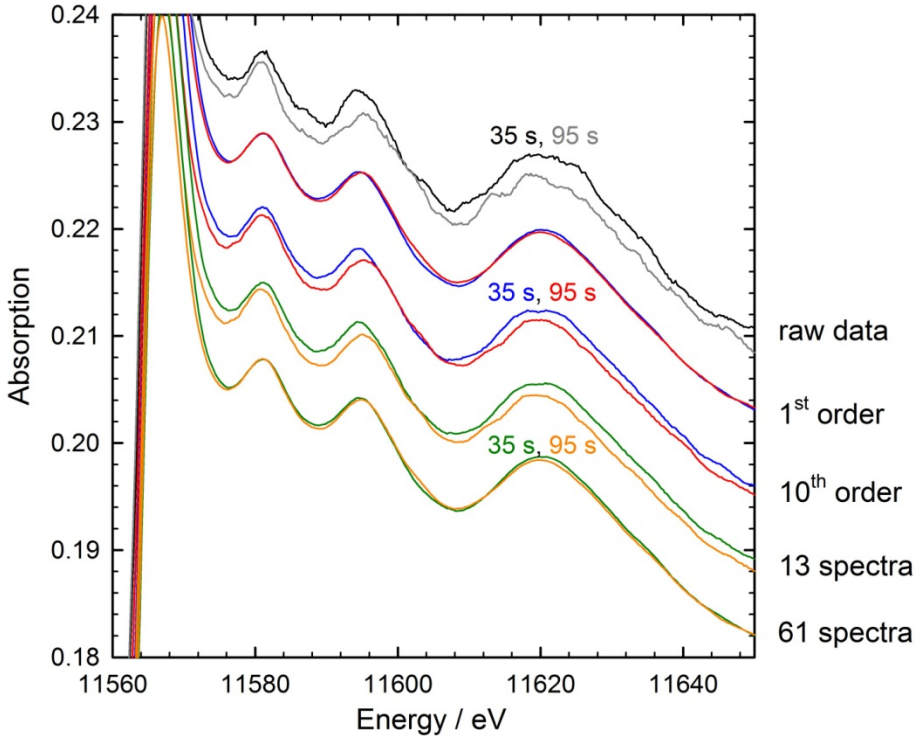

Figure 4.33: Zoomed view on X-ray absorption spectra of the Pt-Rh catalyst during the modulation cycle after 35 s and 95 s (see Figure 4.32) after applying various filter techniques including 1st and 10th order Fourier series (blue/red) as well as 13 and 61 spectra Gauss filtering (green/yellow).

spectra, resulting in the curves presented in Figure 4.32. In order to evaluate the capabilities of the chosen approaches to reduce noise, additional averaging over several cycles was not performed, so that the black curves represent the white line intensity measured during only one cycle. Very smooth curves can be obtained e.g. by Gaussian smoothing with a window width of 61 spectra and FS up to the second order. These two results are comparable, because they exhibit approximately the same cut-off frequency. However, the corresponding curves are both not reproducing the actual dynamics of the white line feature correctly, which is especially well recognizable at the sharp minimum at about 95 s. Instead, 10 orders have to be considered for the FS, and accordingly a window width of only 13 spectra for the Gauss filter, to get reasonable results.

A zoomed view on the absorption spectra at 35 s and 95 s after applying the various filters on the entire spectra are shown in Figure 4.33. Generally, the observations made for the white line feature are confirmed, as the differences between the two spectra are more significant with the application of the 10th order FS, respectively the 13 spectra Gaussian smoothing, than what is achievable with stronger filtering. Compared to the unfiltered spectra, even the weaker filtering yields much smoother spectra and is thus a reasonable approach. However, it is not really possible to conclude, which filter performs better in noise reduction. On the one hand, the FS approach exhibits the advantage, that all frequencies that are not caused by the modulation are suppressed. On the other hand, the

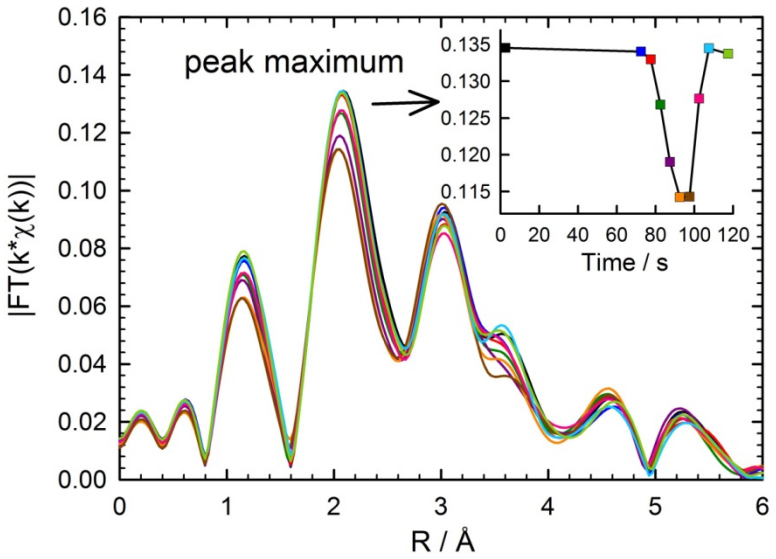

Figure 4.34: Fourier transformations of the k-weighted EXAFS during the modulation cycle applied to the Pt-Rh catalyst. The colors of the spectra correspond to the times as marked in Figure 4.30b and the inset in this graph, which shows the maximum of the FTs as function of time.

FS approach is not able to reproduce constant contributions in the data correctly, as long as only low orders are considered. This can be seen clearly in Figure 4.32 for the second order FS reproduction, where significant deviations appear at about 35 s, while the Gauss filter has no problem to reproduce this region correctly. Using only first order FS/PSD as presented in [Fer10] makes the situation even worse, as the dynamics are forced to follow a sinusoidal shape, which can lead to completely wrong conclusions, as e.g. in the present case to a maximum in white line intensity at 35 s.

Applying FS or PSD to the data also means that each energy value is dealt with individually, so that correlations in energy might get lost. As a consequence, the resulting spectra do not longer necessarily correspond to real chemical states and are thus difficult to analyze correctly. Such problems do not occur when the full spectra are taken into account as in the herein presented low pass filtering approaches. Thus, it can be concluded that MES is a powerful tool for noise reduction, as long as averaging over several cycles is performed, which definitely improves the statistics. Apart from this, using the frequencies of the modulation via FS or PSD with a reasonable amount of orders to reproduce the dynamics correctly does not yield a significantly better noise reduction than low pass filtering with the same cut-off frequencies. The latter one remains the better solution for absorption spectra, since no correlations in energy get lost and constant signals can be reproduced correctly.

In order to finalize the discussion about the observed chemical effect that appears during the modulation cycle, the sample structure has to be studied in more detail by investigating the EXAFS. Mainly due to the averaging over several cycles, it is possible not only to

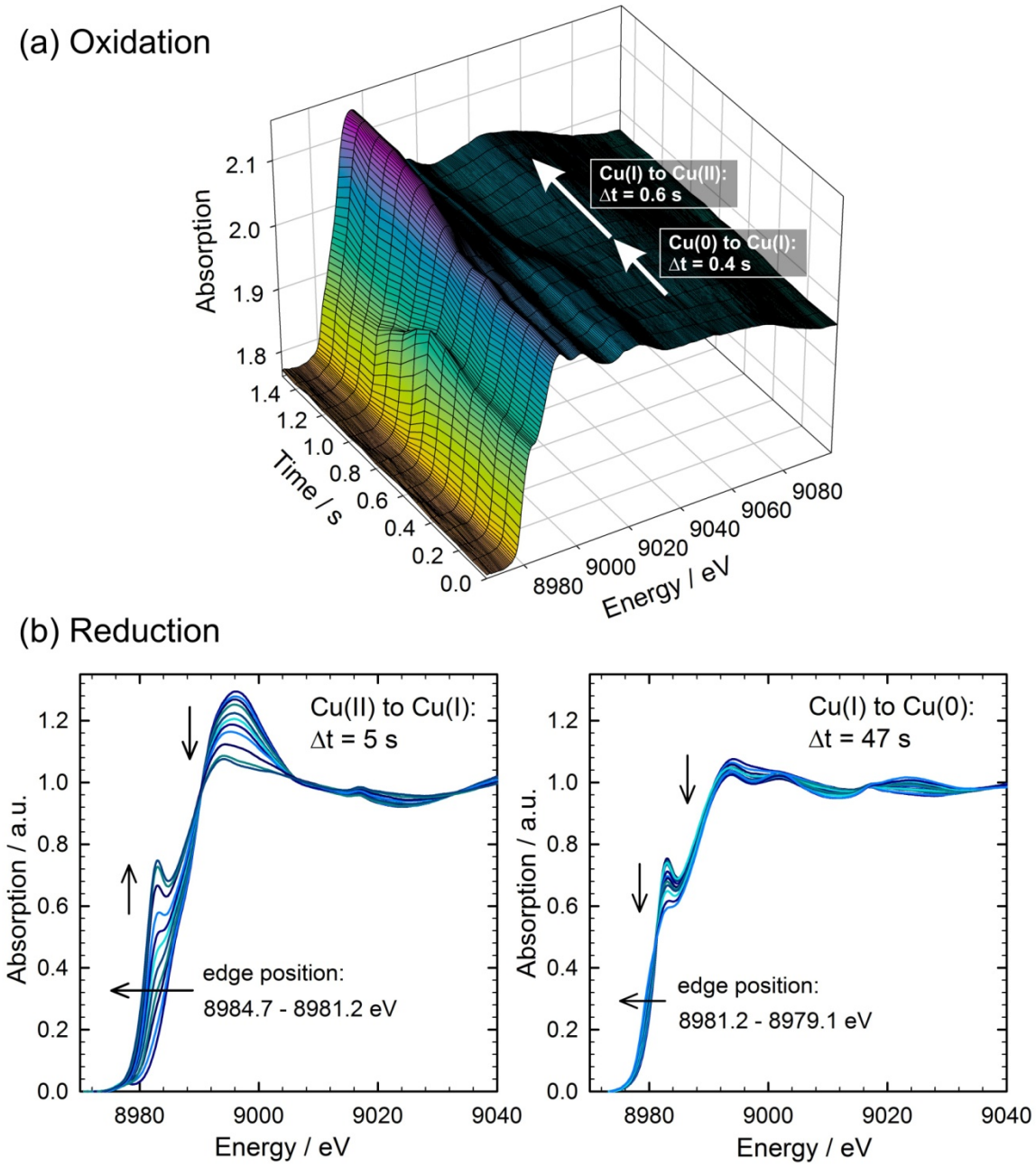

Figure 4.35: (a) Oxidation and (b) reduction of 90 min impregnated Cu/Al_2O_3 at 350 °C followed with normalized XANES spectra. Two transitions are recognizable in both cases, indicating an intermediate Cu(I) state.

follow the changes in the X-ray absorption spectra but also in the Fourier transformed EXAFS as shown in Figure 4.34. The transformations were performed on the raw data after averaging over three cycles and additionally over 5 spectra, as already applied to study the white line intensity in Figure 4.30b (red line). A decrease in the first shells can be observed in parallel to the minimum in the white line intensity. This can be well explained by decreasing oxygen coordination and/or removal of adsorbed carbonyl species, when applying the H_2 gas stream.

Oxidation and reduction behavior of Cu/Al_2O_3

The Cu/Al_2O_3 catalyst inside the capillary reactor was heated to various temperatures between 300 °C and 450 °C, before the gas composition was periodically interchanged between 21% O_2 / He and 5% H_2 / He every 60 s. Earlier QEXAFS studies on Cu/ZnO catalysts indicated a short living intermediate Cu(I) species [Bor99, Gru01a], which is more stable, as soon as spinels can be formed [Kap01, Gru01b]. It was also observed that the reduction behavior of Cu catalysts varies as function of impregnation time [Bai83]. The herein presented studies were performed to find out more about the reduction and oxidation behavior of pure Cu catalysts with different impregnation times and to compare these results to the Cu/ZnO system. One period of the gas changing cycle amounted to 120 s, the spectra were measured with 10 Hz crystal oscillation frequency and data was typically acquired during at least three complete cycles. Thus, each measurement resulted in more than 7200 full X-ray absorption spectra at the Cu K-edge. Accordingly, this experiment is a good example of how important advanced data analysis tools are, in order to investigate fast reactions during a reasonable amount of time with the QEXAFS technique.

Spectra during oxidation and reduction of the 90 min impregnated catalyst at 350 °C are shown in Figure 4.35. First of all, it can be observed that the oxidation process is very fast and it only takes about one second to almost completely oxidize the Cu, while the reduction process is far slower and completes after about one minute. The data quality is sufficient to study details even during the fast oxidation process. Thereby, an increase in the edge feature intensity for about 0.4 s can be detected, before the feature completely disappears for the next 0.6 s to yield spectra similar to the absorption spectrum of the fully oxidized Cu(II) state (see Figure 4.36a). This behavior of the edge feature can be assigned to an intermediate Cu(I) state, which is observable only for about 0.5 s during the oxidation. Thus, the applied time resolution of one spectrum each 50 ms was a prerequisite for detecting this intermediate state at all. During the reduction, it is also possible to see Cu(I), but in this case the detection is much easier due to the much slower transition first from Cu(II) to Cu(I) within about 5 s and thereafter from Cu(I) to Cu(0) within the next 47 s. To verify, that the detected intermediate state can really be assigned to Cu(I), the EXAFS of this state has to be analyzed, as presented within the next paragraph.

In order to quantify the results derived from Figure 4.35, LCA was applied to the shown data and also to the data where the identical catalyst and catalysts with different Cu loadings were measured at various temperatures. As has already been discussed in previous application examples, the choice of reasonable reference spectra is the crucial step of LCA. In the present case the references were directly picked from the experimental data. Thereby, the Cu(0) state was selected from spectra measured at the highest temperature in reducing atmosphere, while the most oxidized Cu(II) state was selected at the highest

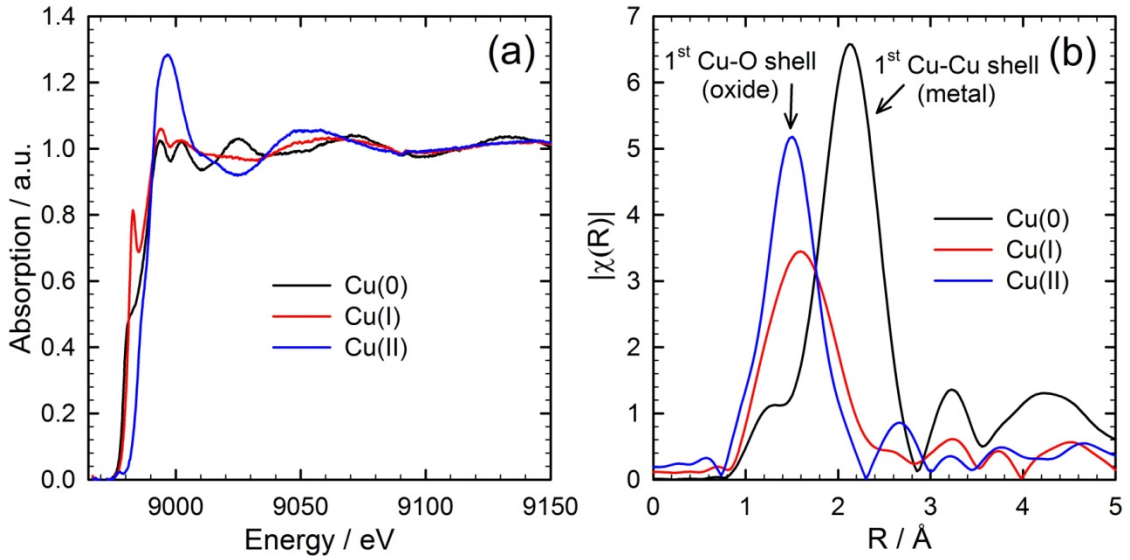

Figure 4.36: References for the LCA of Cu(0), Cu(I) and Cu(II) states selected from the measurements during the modulation cycles: (a) XANES spectra and (b) Fourier transformations of the k^3-weighted EXAFS functions $\chi(k)$.

temperature in oxidizing atmosphere. The spectrum representing the Cu(I) state was chosen as the one with the most intense edge feature. The reference spectra and their Fourier transformed EXAFS spectra are shown in Figure 4.36. Obviously, the references were chosen well as recognizable in the amplitude of the first oxygen peak at about 1.4 Å, which decreases towards the most reduced state. Thereby, the amplitude in the Cu(I) state is located approximately in the middle between the amplitudes detected for the Cu(0) and the Cu(II) states.

The results of LCA during the reduction at 300 °C, 350 °C, 400 °C and 450 °C are shown in Figure 4.37 for catalysts impregnated for 4 min, 90 min and 210 min. It is now possible to study the dynamics of Cu reduction in more detail and major differences are recognizable at various temperatures as well as with different loadings of catalytic material on the support. Generally, it can be observed that the dynamics of the reduction are faster at higher temperatures as expected for reaction kinetic reasons. Thereby, it is also observable that the dynamics are faster at higher catalyst loadings, probably due to a better mediation process between the Cu particles. Full reduction to pure Cu(0) is only possible at the highest temperature of 450 °C for all loadings and at 400 °C for the 90 min and 210 min impregnated sample, while only 60% Cu(0) was detected for the 4 min impregnated catalyst at 400 °C. At lower temperatures, the sample remains in a mixed state of Cu(0) and Cu(I), respectively of Cu(II) and Cu(I), at the end of the reduction. Thereby, the rule is that the final reduction product is most reduced for the highest loading at each temperature, which leads to the conclusion that the support is stabilizing the catalyst.

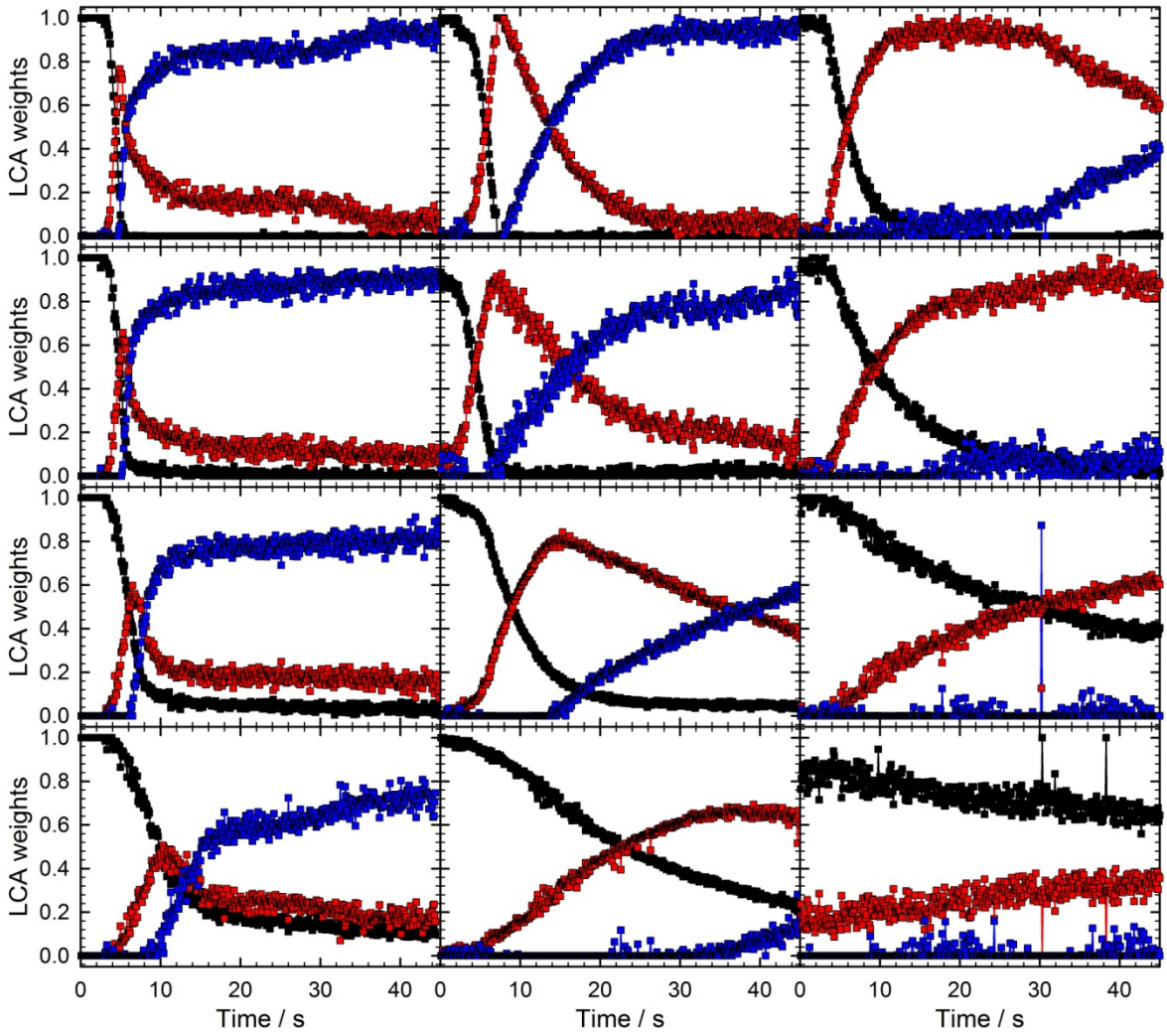

Figure 4.37: LCA weights of Cu(0) (blue), Cu(I) (red) and Cu(II) (black) during the reduction of the Cu/Al_2O_3 catalyst produced with various impregnation times and measured at various temperatures. The columns correspond to the impregnation times of 210 min, 90 min and 4 min from left to right, the rows correspond to the temperatures of 450 °C, 400 °C, 350 °C and 300 °C from top to bottom.

Whenever Cu(0) can be observed, there also appears the intermediate Cu(I) state, which first increases almost linearly in favor of the vanishing amount of Cu(II) and afterwards fades slowly as the Cu(0) state evolves. Thereby, the maximum amount of Cu(I) that appears during the reduction depends on temperature and loading. Only in the case of a full reduction to Cu(0) sample compositions close to pure Cu(I) are possible. Obviously, a certain amount of Cu(I) has to be reached during the reduction, before the sample can further reduce to Cu(0). The presented LCA results suggest that this threshold is reached at about 50 – 80% Cu(I), which can be recognized especially well at the 90 min impregnation time results, where the maximum of Cu(I) approaches the threshold at lower temperatures, while only very small amounts of Cu(0) are detectable. The Cu(I) state increases to almost stable 100% for the 4 min impregnated sample at high temperatures, because the evolution

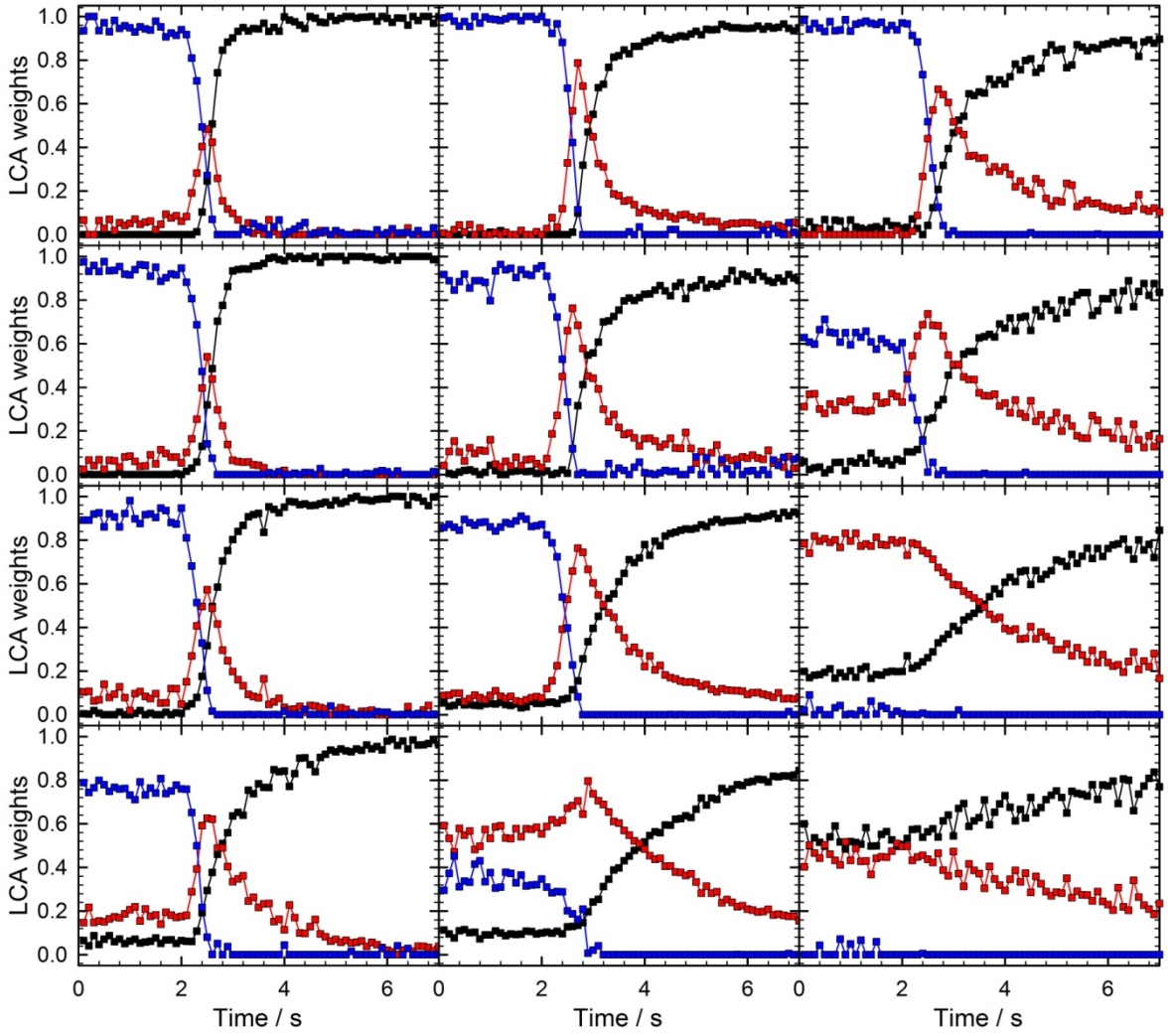

Figure 4.38: LCA results during the oxidation of the Cu/Al_2O_3 catalyst produced with various impregnation times and measured at various temperatures. The rows, columns and colors are defined in the same way as in Figure 4.37.

of Cu(0) is very slow. But even here it is possible to detect the first Cu(0) contribution as soon as the above defined Cu(I) threshold is reached. For the 210 min impregnated sample the threshold is a bit lower than for the samples with shorter impregnation times.

In Figure 4.38 the LCA results for the oxidation process, depicted from the same measurements as the reductions in Figure 4.37, are shown. Since the oxidation proceeds a lot faster than the reduction, the plotted time region was reduced to only 7 s. In contrast to the reduction, the differences in the dynamics of the oxidation at various temperatures and with various loadings are less evident. The sample composition shortly prior to the oxidation has already been discussed as final state of the reduction. Independent of temperature and impregnation time, as long as a Cu(0) state is present at the beginning, it decreases linearly to 0% in favor of the Cu(I) state within about 0.5 s. Simultaneously, the Cu(I) state increases to exactly the same threshold of about 80%, respectively only 50% for the 210 min impregnated sample, which in each case was also observed during the

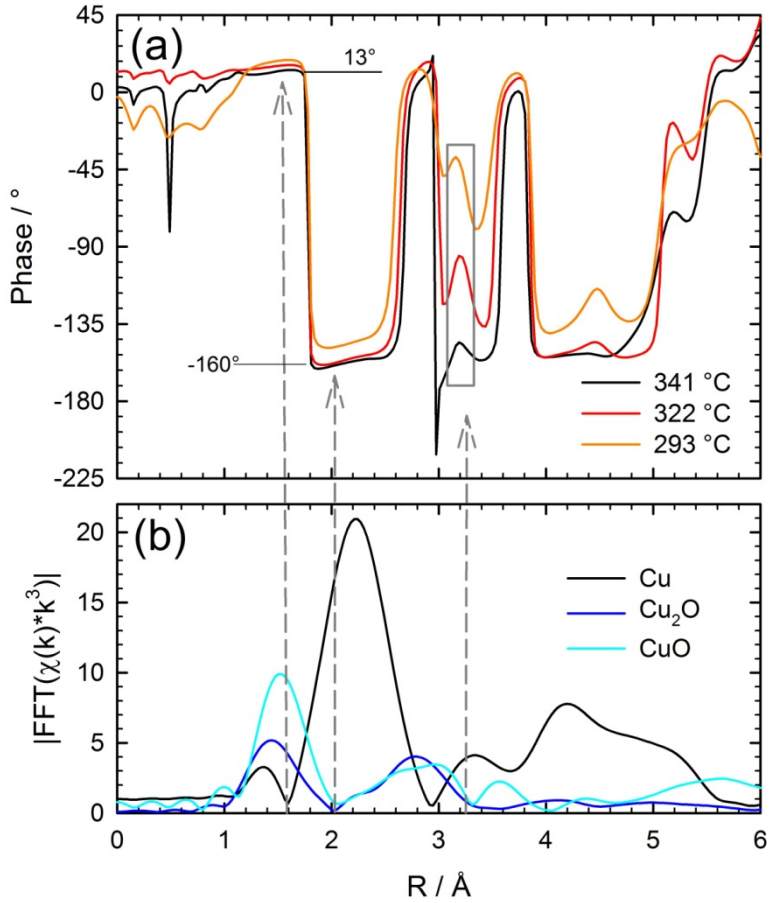

Figure 4.39: Phases calculated with 1st order Fourier series applied to the Fourier transformed data of the 90 min impregnated Cu/Al_2O_3 catalyst at various temperatures: (a) phases in R-space and (b) Fourier transformed spectra of bulk references. See text for details about the arrows and the box.

reduction as threshold for the reduction to Cu(0). After reaching this threshold, which is independent of the applied temperatures, the Cu(I) state immediately decreases and the Cu(II) evolves with a more or less exponential increase. While the vanishing of Cu(0) does not seem to depend on the temperature, the evolution of Cu(II) slows down slightly at lower temperatures.

As shown in the previous paragraphs of this section, the presented experiments can be analyzed excellently with the application of LCA, which is one reasonable approach to deconvolute the contributing species. In contrast to that it is more difficult to perform reliable EXAFS analysis due to the fact that the time resolution is very high which results in low photon statistics and thus noise in the EXAFS signal. On the other hand, the EXAFS provides invaluable information about the sample structure. The LCA is strongly affected by the XANES region, which depends e.g. also on variable bonding angles and on orbital mixing, while the EXAFS is only affected by the bond distances. Thus, the EXAFS is important to either confirm or contradict the LCA results. Since the dynamics of the herein presented experiment, especially during the oxidation, are very fast, it is not possible to

extensively apply the smoothing algorithms introduced in section 3.3.3, in order to improve signal-to-noise ratios. However, it is possible to exploit the periodic modulation of the experiment by applying MES/PSD techniques on the Fourier transformed EXAFS spectra.

Instead of calculating the phase-resolved spectra according to Eq. (3.22), it is also possible to calculate the phases in R-space by reproducing the Fourier transformed EXAFS spectra with 1st order Fourier series and thereafter applying Eq. (3.19). The advantage of this approach is the straight forward access to phase resolution, while it is not required to guess any probing phases, as in the case in Eq. (3.22). The 90 min impregnated catalyst with rather small changes in temperature between 341 °C, 322 °C and 293 °C was investigated with this approach and the calculated phases in R-space are shown in Figure 4.39a. Additionally, the Fourier transformed spectra of bulk Cu, Cu_2O and CuO samples are displayed in Figure 4.39b in order to assign the phases to the shells of the involved components. Thereby, one can distinguish between two rather stable phases, one appearing in the R-regions where the shells of fully reduced Cu are dominant, the other in the regions where the shells of the oxidized Cu species are dominant (marked exemplarily by the first two grey arrows at about 1.6 Å and 2.0 Å). Thus, it is very easy to recognize which phase is attributed to which state and it is also possible to investigate these phases, as further evaluated within the next paragraphs.

In the case of Figure 4.39 the cycles were aligned in such way that they start with the oxidation, which means with the switch to the O_2 / He gas stream. Considering the modulation with a 1st order approach, this means that the O2 / He gas stream represents the part of the sinus curve above zero, as also displayed in Figure 4.40b (grey dashed line). Correspondingly, in a first approximation it can be expected that the phase representing the oxidized Cu will be found close to 0° and the one for reduced Cu close to ± 180°. To determine the phase of the reduced state, the position R = 2 Å was chosen, because at this position both oxidized states, Cu(I) and Cu(II), exhibit a minimum in the radial distribution function, so that everything contributing to the phase at this position can be assigned to Cu(0). At R = 1.6 Å, the reduced Cu exhibits a minimum, while the oxidized Cu species exhibits a rather strong contribution, so that this position was chosen to determine the phase of the oxidized Cu. Comparing the phases at these positions, it can be observed that both values slightly differ from the expected values. Thereby, the reduced contribution exhibits a stronger deviation, which can be assigned to the fact, that the reduction is slower than the oxidation and thus the reduced phase is shifted towards the oxidized one. Furthermore, this deviation becomes more evident for the reduced state at lower temperatures, which is in good agreement with the slower reduction at lower temperatures that was already detected with LCA in Figure 4.37. The 1st order modulation and responses

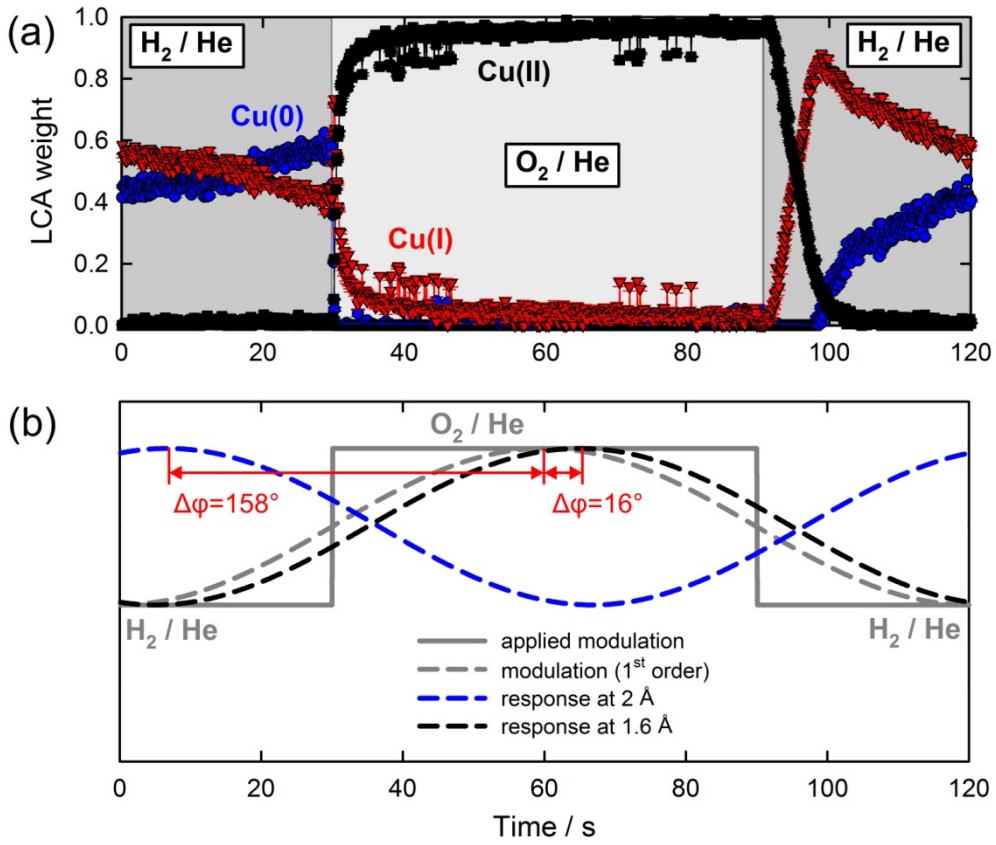

Figure 4.40: 90 min impregnated Cu/Al_2O_3 catalyst at 322 °C: (a) Results of LCA, (b) dynamics of modulation and 1st order responses with phases obtained at different R-values (normalized amplitudes).

with phases obtained at the chosen R-values are displayed in Figure 4.40 for the measurement at 322 °C together with the corresponding LCA results.

To distinguish between Cu(I) and Cu(II) is a difficult matter with the calculated phases. Both components exhibit shells in almost the same R-regions. At R = 3.3 Å a minimum of Cu(II) can be found (see Figure 4.39b), so that only Cu(I) and Cu(0) species should contribute to the phase at this position. Since the phase of Cu(0) can be exactly determined at R = 2.0 Å, any deviation from that phase to the phase at 3.3 Å is an evidence for the presence of a Cu(I) state. Such deviations are observable in Figure 4.39a (marked by the third grey arrow and the grey box) at all temperatures. At the highest temperature, this deviation is rather small, which agrees well with the short appearance of Cu(I). At lower temperatures, the deviation is more significant, again in good agreement with the more enhanced Cu(I) state at lower temperatures, which was also detected by LCA. Thus, the phase resolution can be used to support the stated appearance of a Cu(I) species with the help of the complementary EXAFS information. Thereby, the information of 7200 X-ray absorption spectra contributed to the results, which can be calculated in a straight forward way and significantly faster than the EXAFS fits of all these spectra.

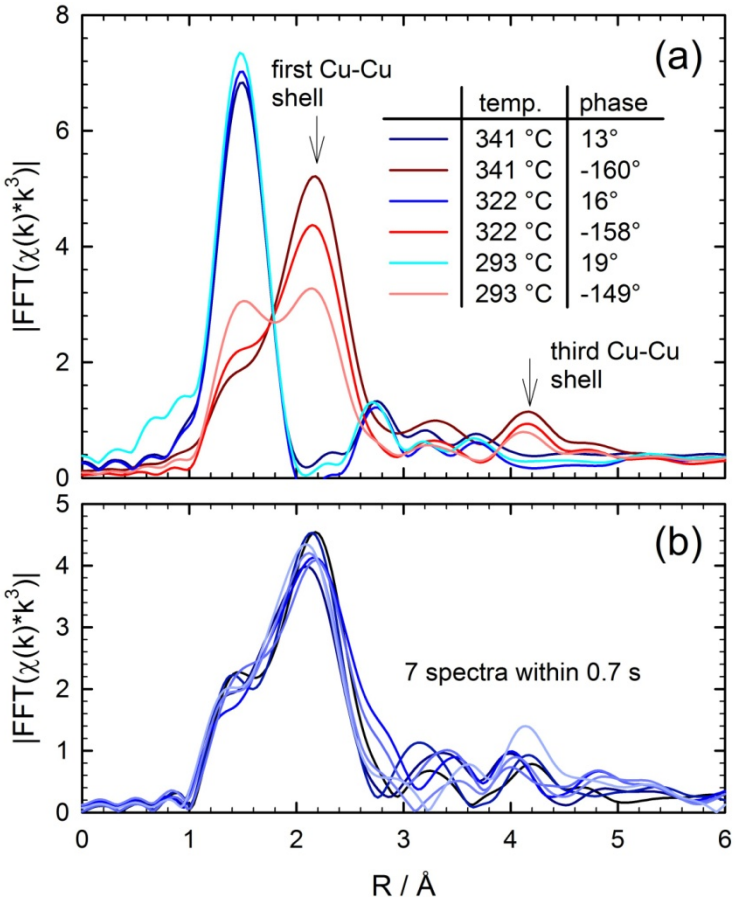

Figure 4.41: (a) PSD-FT spectra calculated with the phases corresponding to the reduced (red) and oxidized (blue) states, (b) Fourier transformations of a randomly selected bunch of 7 time-resolved raw spectra acquired during the reduced state.

Returning once more to Figure 4.39, it is also possible to pick the phases at 2 Å and 1.6 Å and to calculate the corresponding phase-resolved spectra according to Eq. (3.23) plus the added averaged contribution a_0. The results of this procedure are shown in Figure 4.41a and they confirm the previous assumptions about assigning the phases to the oxidized and reduced states of the catalyst. This can be easily recognized by comparing the results to the spectra in Figure 4.39b. In good agreement with the LCA results, it can be observed that the reduced state is shifted towards the oxidized state at lower temperatures, while the oxidized state remains rather stable at all temperatures. Interestingly, such evolutions can be analyzed even up to the third Cu-Cu shell. This would not be possible with the raw time-resolved FT spectra that are exemplarily shown in Figure 4.41b for the reduced state. While this can be attributed to the strong low pass character of 1st order PSD, it must not be forgotten that the fast dynamics of this reaction are not represented well by first order evaluations. This is also plain to see in Figure 4.40 by comparing the LCA weights to the 1st order sinusoidal reproduction of the dynamics.

Although it would also be possible to fit the peaks in Figure 4.41a with calculated EXAFS paths, two issues speak against it. First, due to the strong low pass character of 1st order PSD one would not get the correct amplitudes. Second, the phase resolved spectra do not necessarily correspond to real chemical states. The latter issue is very important and attributed to the fact that the PSD is performed independently for each R-value without considering any correlations along the R-axis. However, since the Fourier transformed EXAFS consists of single and multi-scattering paths and most of them overlap in R-space, such correlations can actually be found almost anywhere. With more than two contributing components there is hardly a chance to extract the Fourier transformed spectra of a true chemical component with PSD.

It also has also to be mentioned that it is not possible to properly extract the FT spectra of the Cu(I) state through the presented approach, since even the phase information obtained at 3.3 Å does not correspond to pure Cu(I). This is a general limitation of PSD in QEXAFS, since it is not always possible to find unique features in the radial distribution function, where all other components exhibit a minimum. It also means that the k-range is a decisive parameter, because a good resolution is required in order to properly separate the shells in the FT. The advantage of the introduced phase-resolution approach, compared e.g. to a PCA, is the fact that it is not only possible to reveal the number of contributing species, but also to obtain information in R-space that can help identifying the chemical nature of these species.

Discussion of MES/PSD as data analysis tools for QEXAFS

The two sample systems studied above were analyzed with different approaches based on the equations in section 3.3.7. It has been shown that modulation experiments combined with QEXAFS provide unique possibilities to analyze fast reproducible processes. This is mainly attributed to the fact that it is possible to average over several modulation cycles and thereby to improve photon statistics without losing time resolution. It has also been shown that the data of modulated experiments can be further evaluated with the techniques provided by MES and PSD, and the various possibilities to include these techniques in QEXAFS data analysis were added schematically in Figure 3.32. With respect to noise reduction, it has clearly been shown that using MES does not yield better signal-to-noise ratios compared to the smoothing techniques introduced in section 3.3.3. Furthermore, since MES operates only along the energy axis, correlations in energy are lost and the results do no longer necessarily represent true chemical states, while it is also difficult to reproduce stable signals with MES. Especially first order MES/PSD can lead to artifacts and misinterpretations in this context. Thus, it is preferable to apply low pass techniques as long as the phase information is not essential. Another argument for the low pass techniques, is the fact that the boundaries can be freely expanded due to the periodic boundary conditions of modulation experiments. It is thus possible to set cut-off

frequencies most accurately, as explained in section 3.3.3 within Figure 3.24. This is also an important argument for the application of modulated experiments in QEXAFS.

The idea of introducing phase-resolution to Fourier transformed QEXAFS data has been evaluated in detail. Since the contributions of backscattering atoms are distributed over the entire EXAFS range as frequencies, it was concluded that it is not reasonable to apply PSD directly to the absorption spectra as function of photon energy. Instead, the radial distribution function was used, where different phases at different R-values can be assigned to specific chemical states due to the characteristic atom shells of each state. In this case it proved to be a reasonable approach to investigate the phases at those R-values where other contributing species exhibit a minimum. Thereby, new insights in the dynamics of the Cu redox experiments could be achieved and it was even possible to find evidence for an intermediate Cu(I) state. By calculating the phase-resolved spectra with selected phases in R-space it is possible to reproduce the FT spectra assigned to these phases. However, correlations in the atomic distance R can get lost by applying the formulas of MES, since they operate along constant R-values. With the appearance of two or more chemical states, each consisting of many single- and multi-scattering paths, it is difficult to find values in R-space where the obtained phases correspond to pure chemical states, even with very good resolution due to a wide k-range. Thus, although intermediate species can be detected with phases in R-space, their identification remains a difficult issue.

In summary, it can be concluded that the application of MES/PSD in QEXAFS is far more difficult than e.g. in IR spectroscopy, XRD or Raman spectroscopy [Bür02, Ura06, Ura08, Ura11], where more or less sharp resonances appear well separated in energy. The LCA technique is a far more powerful tool to investigate the absorption spectra as the correlations in energy are preserved. Even in R-space the contributions of backscattering atoms of several species are not separated well enough for unambiguous interpretations. Furthermore, the reduction of noise is not superior to low pass filters, so that averaging over several cycles and periodic boundary conditions remain the most valuable advantages of modulation experiments in QEXAFS.

4.2 Thermal decompositions

The thermal decomposition of metal oxalates attracts attention due to the provided feasibility of producing metal or metal oxide powders at moderate temperatures, which can be used for catalytic applications. Depending on the process parameters it is possible to control particle size and purity of the reaction products. Although the decomposition process of various metal oxalates was studied extensively (see e.g. [Dol87, Mac00]), it is

still discussed what the primary products are. In this context it is by no means sufficient to analyze the final products, since these might be a result of secondary reactions caused by (i) changing temperatures, (ii) the water generated during the dehydration or (iii) CO/CO_2 gases generated during the primary decomposition reaction. The sample atmosphere further plays a decisive role in the course of the decomposition.

Generally the decomposition of oxalates proceeds in two steps, namely the dehydration of the oxalate, which is always endothermic, and the decomposition itself. The latter can have an overall exothermic character depending on the surrounding gas atmosphere and the thereby induced catalytic reactions in parallel to the endothermic decomposition [Dol87]. It is not possible to treat dehydration and decomposition independently, since it was shown that the dehydration is not completed at the start of the decomposition in many systems [Mal02]. Generally, two reactions are proposed as possible primary decomposition reactions for metal oxalates (not considering alkali and alkali-earth oxalates):

$$MC_2O_4 \longrightarrow M + 2CO_2 \tag{4.3}$$

$$MC_2O_4 \longrightarrow MO + CO + CO_2 \tag{4.4}$$

It depends on the bond strength of M-O and O-C which reaction is favored, whereby a weaker M-O bond supports reaction (4.3) and a weaker O-C bond supports reaction (4.4) [Fuj57].

The decomposition of oxalates and the yielded products are still a matter of discussion in literature. Most existent studies are based on thermogravimetry (TG), differential thermal analysis (DTA) and mass spectrometry (MS) (see e.g. [Coe93, Mac00, Mal02, Maj08]). With these techniques structural information of the metal containing species is only obtained indirectly, either by analyzing the formed gas products or by observing changes in sample energy by means of mass and temperature. This issue was discussed e.g. by Coetzee et al. [Coe94], who pointed out that it is hardly possible to draw confident conclusions with kinetic analysis only. Maciejewski et al. [Mac00] stated that the quantification of the various stages during Co oxalate decomposition based on TG curves is inaccurate and cannot be used to confirm the stoichiometry of these stages. It is also reported that sometimes the DTA cell might act as catalyst, which can lead to misinterpretations of the reaction [Dol87].

The discussions about the applied in situ techniques, plus the fact that contradictive interpretations of the decomposition processes of various oxalates are found in literature, clearly demonstrate that complementary in situ techniques have to be applied. Reasonable alternatives are X-ray in situ techniques like EXAFS and XRD. Thereby, EXAFS seems to

be the more promising approach, since metal nanoparticles and/or amorphous products are expected to be generated. However, conventional EXAFS is too slow to resolve the dynamic changes that were already detected with TG and DTA. Thus, the QEXAFS technique combined with MS were applied in the herein described experiments with a time resolution of two EXAFS spectra each second. This approach allows identifying contributing species during the decomposition. Furthermore, metal oxalate samples exhibit a rather high metal concentration, which makes it possible to study the process time-resolved with a rather good data quality. Thus, this experiment is also adequate to evaluate the capabilities of EXAFS analysis with T-REX, as introduced in section 3.3.9.

In this work, the thermal decomposition of Co oxalate was investigated under non-isothermal conditions in various atmospheres with reducing (H_2), inert (He) and oxidizing (O_2) properties. It has been suggested earlier that in the case of Co the decomposition proceeds to pure metal due to the strength of M-O and C-O bonds, as discussed above. However, Maciejewski et al. [Mac00] have found a significant amount of CoO as reaction product of Co oxalate decomposition in inert atmospheres. Thereby, they emphasized the fact that other in situ investigations are necessary to prove that the oxidized Co is not a result of reactions with residual oxygen. In confirmation to this, Małecka et al. [Mal02] have also shown that the decomposition of Co oxalates proceeds with reaction (4.3) and reaction (4.4) in parallel, while the ratio of both reactions is determined by the conditions of the experiment. In oxidizing atmospheres Maciejewski et al. stated that the freshly formed Co is immediately oxidized to Co_3O_4, which has also been recognized as final product in earlier investigations [Bak74, Nik91]. In hydrogen atmosphere only metallic Co was consistently detected in several studies [Mac00, Mal02, Maj08].

Experimental

The same cell that has already been used in catalytic experiments (see Figure 4.15) was used here to follow the decomposition process. Thus, it was possible to apply temperature ramps and to adjust the gas mixture surrounding the oxalate. The spectra were measured basically with the same experimental settings as the ones chosen for the Cu catalyst in section 4.1.4, except for the crystal oscillation frequency, which was set to 1 Hz in this case. Further averaging over 10 up-spectra was performed, which still provides a sufficient time-resolution (1 spectrum each 10 s) to study all involved processes. The chosen eccentricity yielded spectra at the Co *K*-edge (7709 eV) ranging from 7702 eV to 8044 eV. Accordingly, a Kaiser-Bessel k-window from 2.40 $Å^{-1}$ to 9.15 $Å^{-1}$ was considered for the Fourier transformation applied to the k^3-weighted extracted EXAFS.

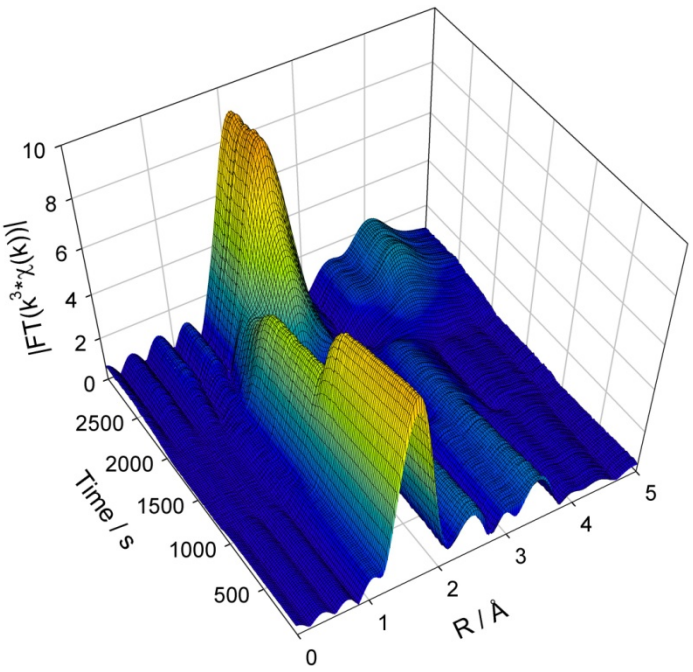

Figure 4.42: Fourier transformed EXAFS at the Co K-edge during the thermal decomposition of Co oxalate in hydrogen atmosphere.

Results

The Fourier transformed EXAFS measured during Co oxalate decomposition in hydrogen atmosphere is shown in Figure 4.42. Two transitions according to dehydration and decomposition are immediately observable. During the dehydration the number of the closest O neighbors around the Co atoms decreases, as can be seen by the decreasing peak at 1.6 Å. In the second step the oxygen peak further decreases while a peak at 2.1 Å evolves which corresponds to a first Co neighbor as expected for pure Co metal. Additionally, the pattern at the end of the reaction is characteristic for the hcp lattice with a strong third shell contribution. These qualitative observations confirm the literature, where only pure Co metal is expected as final product. To quantitatively analyze the spectra in Figure 4.42 refinement fits of the calculated Co-O and Co-Co backscattering paths of Co oxalate (see [Nau96]) and metal Co (see [Kit05]) were performed, as has exemplarily already been shown for the Co-O amplitude in section 3.3.9. Since no Co-Co contribution is expected in the beginning of the reaction all spectra were also fitted without the Co-Co path. Similar considerations can be made at the end of the reaction, where no Co-O contribution is expected in hydrogen atmosphere. However, since there are no other atoms in the distance of the first oxygen shell in the case of pure Co metal, it is not necessary to exclude this scattering path which should simply yield zero amplitude and thus can even be exploited to check the reasonability of the fits.

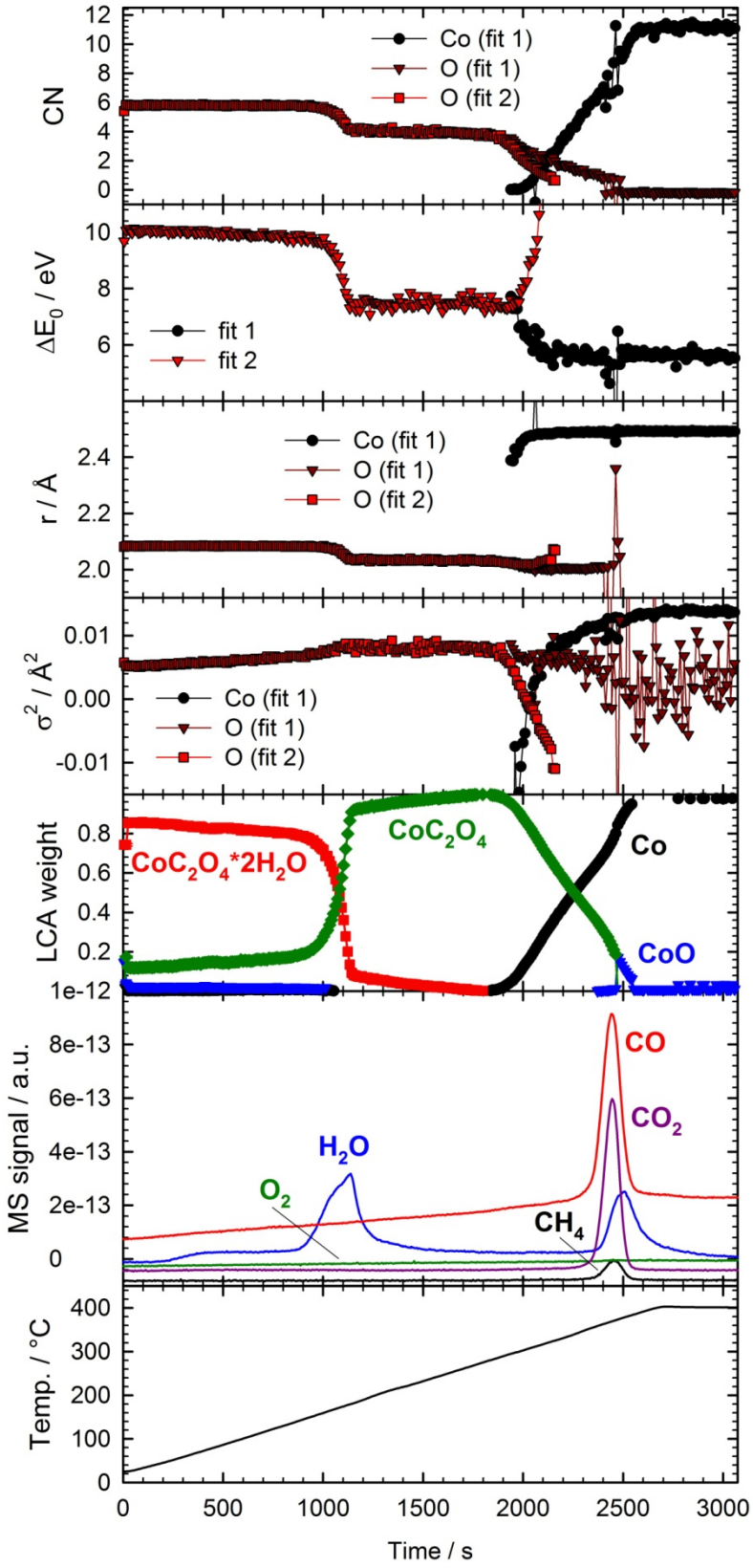

Figure 4.43: Results of synchronized EXAFS analysis, LCA and MS during the thermal decomposition of Co oxalate in hydrogen atmosphere. Displayed are (from top to bottom): Coordination numbers, energy shift, atomic distance, mean square deviation, LCA weights, MS signal and temperature.

The results of the EXAFS fits are displayed in Figure 4.43 as function of time. After about 1000 s the number of oxygen neighbors decreases from 5.8 to about 4.0 during the dehydration, which well agrees with the removal of the initial two water molecules around each Co atom. During the decomposition the number of oxygen neighbors further decreases to zero while the number of Co neighbors increases from 0.0 to about 11.0 – 11.5 at a rather linear rate. Concerning the other fit parameters, it is noteworthy that the fitted E_0 value decreases in two steps. First, a reduction due to the removed water can be observed and afterwards another reduction due to the removed residual oxygen. The Co-O bond length starts with values typical for Co oxalate with inhibited crystal water at about 2.11 Å [Nau96]. After dehydration the decreased number of oxygen neighbors also results in a shorter distance between the O and Co atoms. During decomposition the distance seems to become even smaller, but due to the vanishing oxygen amount these results have to be interpreted carefully. With the evolution of Co metal the corresponding Co-Co distance approaches the typical value expected for Co metal of about 2.50 Å [Kit05]. At the beginning of the reaction the mean square deviation σ^2 contributing to the Debye-Waller factor of the first oxygen scattering path increases. This is in good agreement with the applied temperature ramp resulting in an increased thermal disorder. After the dehydration σ^2 remains on a constant level and decreases again during decomposition. The σ^2 factor of the Co-Co path increases with the increasing number of Co neighbors and the still increasing temperature.

Since it is a matter of discussion whether the Co oxalate decomposition proceeds via reaction (4.3) and/or reaction (4.4), a LCA with Co, hydrated and dehydrated Co oxalate as well as various Co_xO_y references was performed. Due to the changes in the spectra caused by the constant heating, it is difficult to choose reasonable LCA references for the oxalate. As evident in Figure 4.43 the LCA weights of the hydrated and dehydrated oxalates also vary in regions that are not assigned to the dehydration or decomposition. This is attributed to the temperature effect since no corresponding changes appear in the EXAFS analysis, except for the mean square deviation of the Co-O path. No CoO can be observed at the beginning of decomposition, so it either does not appear or it is instantly reduced to Co by the hydrogen. However, at the end of decomposition a small amount of CoO is detected by the LCA. Considering the mass spectroscopy signal, a water peak can be observed, which is appearing with a delay to the CO and CO_2 peaks during the decomposition. The evolution of so much water, at this point of the reaction, cannot be attributed to residual water of the oxalate and can thus only have been produced by the following two reactions:

$$CO_2 + 4H_2 \longrightarrow CH_4 + 2H_2O \tag{4.5}$$

$$CoO + H_2 \longrightarrow Co + H_2O. \tag{4.6}$$

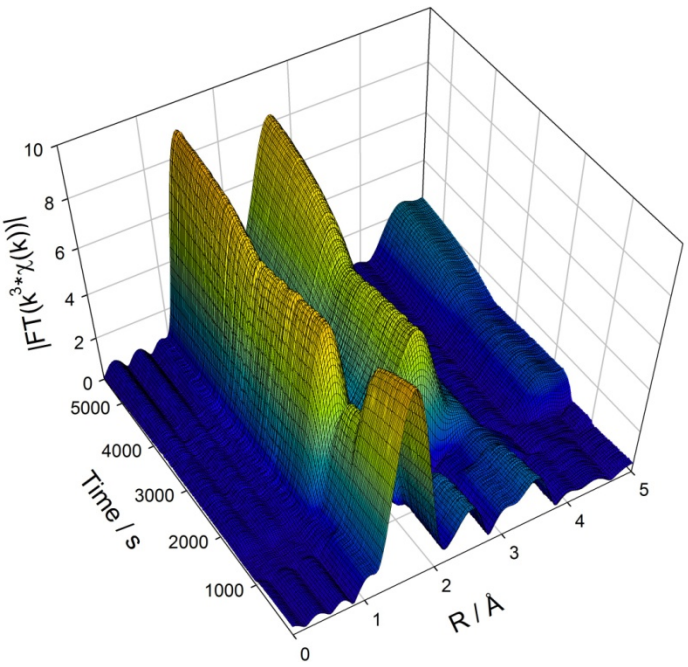

Figure 4.44: Fourier transformed EXAFS at the Co K-edge during the thermal decomposition of Co oxalate in oxygen atmosphere.

Reaction (4.5) is catalyzed by the freshly formed Co and has been confirmed experimentally under isothermal and non-isothermal conditions [Maj08, Mac00]. But since the water peak is not appearing exactly in parallel to the CO_2 peak, reaction (4.6) is also likely to occur, which would be consistent with the detected CoO in the LCA results. That low amounts of CoO are observable at the end of the decomposition can be explained by the high yield of CO_2, which is obviously shortly delaying the reduction of CoO to Co. This also strongly evidences that reaction (4.4) is contributing to the primary decomposition of Co oxalate, since the presence of CoO cannot be explained by oxidized Co under the applied reducing conditions during this experiment. Contrarily, it has to be noted that reaction (4.3) is not necessarily contributing, because the observed Co can also be a secondary product due to CoO reduction by the applied H_2 and/or the evolving CO.

More controversy about the decomposition can be found in the case of vacuum conditions, respectively inert or self-generating atmospheres, as has been summarized by Maciejewski et al. [Mac00] and the references therein. Compounds like CoO, Co_2O_3, $CoO_{0.83}$, $CoO_{0.75}$ or $CoO_{0.16}$ were detected and this fact demonstrates the complexity of the process quite well. In oxidizing atmosphere the decomposition is known to yield Co_3O_4 as final product, but even here the reaction path was not resolved in a direct way using structural in situ techniques. The Fourier transformed spectra measured during Co oxalate decomposition in oxygen are shown in Figure 4.44. Again, the two steps according to dehydration and decomposition are visible without further analysis. In contrast to the measurements in hydrogen atmosphere the oxygen peak does not vanish during decomposition but increases again due to the formation of Co_3O_4 as final product.

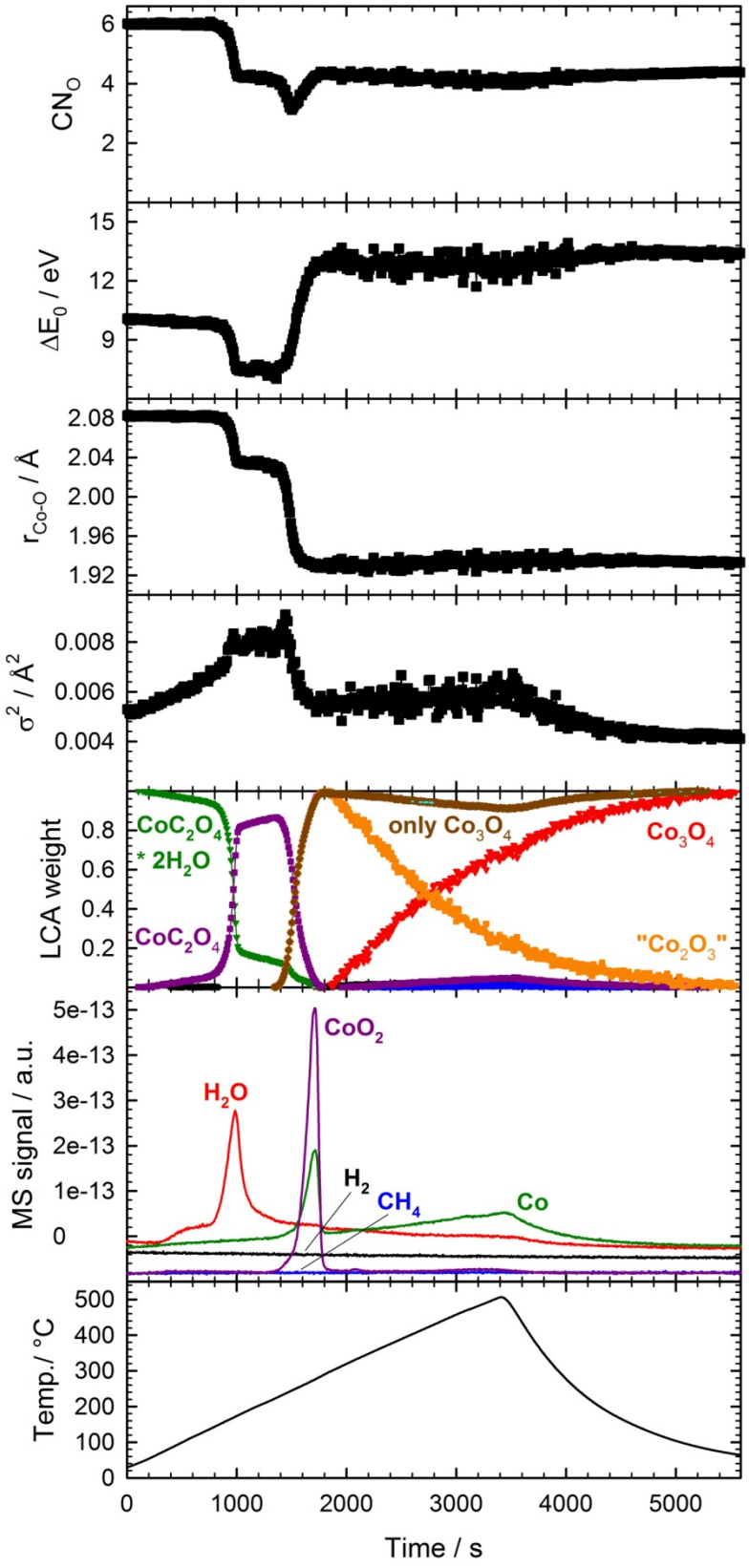

Figure 4.45: Results of synchronized EXAFS analysis, LCA and MS during the thermal decomposition of Co oxalate in oxygen atmosphere. From top to bottom: Coordination numbers, energy shift, atomic distance, mean square deviation, LCA weights, MS signal and temperature.

Fitting the spectra in Figure 4.44 with the first Co-O backscattering path of hydrated Co oxalate yields the results shown in Figure 4.45. Up to the decomposition the results are comparable to those obtained in hydrogen atmosphere and will thus not be further discussed. During the decomposition the number of oxygen neighbors starts to decrease to about 3.1 and then immediately increases again to 4.0 – 4.4 which is slightly below the value expected for the Co_3O_4 structure of about 4.7 [Liu90]. This can be explained either by small Co_3O_4 crystallites or by remaining dehydrated oxalate. The E_0 first decreases in accordance to the partial reduction during the dehydration and then increases towards the highly oxidized Co_3O_4 final state. The Co-O distances are all within the expected values for $CoC_2O_4*2H_2O$ (2.11 Å) [Nau96] and Co_3O_4 (1.94 Å) [Liu90]. Concerning the mean square deviation of the Co-O path length, a maximum is observable in parallel to the minimum in the O coordination number during the decomposition, both well representing the high intermediate disorder due to the structural transition. Furthermore, it is interesting to see that close to the end of the experiment the disorder starts to decrease exponentially, which is in perfect agreement with the exponentially decreasing temperature.

The corresponding LCA was performed with Co, $CoC_2O_4*2H_2O$, CoC_2O_4, CoO and Co_3O_4, whereby the last QEXAFS spectrum of the measurement was selected as Co_3O_4 reference. The LCA results are additionally displayed in Figure 4.45. Although the already proposed decomposition of the oxalate to Co_3O_4 is recognizable (brown line), the appearance of a maximum of Co_3O_4 at about 1775 s followed by a minimum could not be expected and is evidence for a more complex reaction path. The LCA results suggest a rather similar sample composition at 1775 s and 5587 s (about 100% Co_3O_4). However, significant differences in the Fourier transformed EXAFS appear, which cannot solely be attributed to different temperatures. The FT spectra at 1775 s and 5587 s are displayed in Figure 4.46 together with reference spectra of Co_2O_3 and Co_3O_4 [Boy11, Lim08]. All spectra were normalized with respect to the second peak to compensate for different experimental conditions (particle sizes, temperature, calibration, etc.). Although Co_2O_3 and Co_3O_4 look rather similar, certain features in the spectrum at 1775 s significantly resemble those observed for Co_2O_3, as marked by the arrows in Figure 4.46. This leads to the suggestion that Co_2O_3 (or $Co_2O_3*H_2O$) is involved as intermediate state during the decomposition, which further transits to Co_3O_4. Co_2O_3 was e.g. also observed during the ignition of cobalt nitrate where it is also appearing as intermediate, which further reacts to Co_3O_4. It has to be noted, that this conclusion agrees very well with the decomposition in hydrogen, where CoO was detected in parallel to the maximum CO/CO_2 yield. In oxygen atmosphere the suggested transition from Co_2O_3 to Co_3O_4, whereby the latter one is known as Co(II,III) oxide (Co_2O_3*CoO), starts exactly at this maximum and can be explained well by the evolving CoO. Further evidence for intermediate Co_2O_3 is given by the O coordination number, which is first increasing to a maximum at 1775 s during the decomposition and then slightly decreasing again (see Figure 4.45).

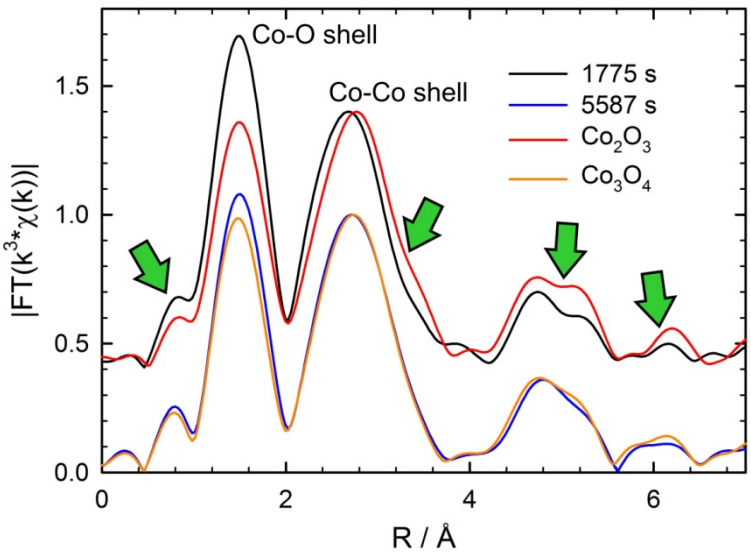

Figure 4.46: Selected Fourier transformed EXAFS during Co oxalate decomposition in oxygen atmosphere compared to Co_2O_3 and Co_3O_4 references, all normalized on the peak at about 2.8 Å.

The results for the decomposition of Co oxalate in He atmosphere are summarized in Figure 4.47. Fitting the spectra with the Co-O backscattering path of Co oxalate yields similar results as under oxidizing conditions by considering only the starting sequence up to the decomposition and the final sample structure of Co_3O_4. However, during the decomposition the number of oxygen neighbors varies significantly, which indicates that several reactions are proceeding here at the same time. This is also confirmed by a sharp maximum in the mean square deviation of the Co-O distance, which indicates that several species and thus Co-O distances are present at the same time. According to the LCA results, Co_3O_4 evolves immediately at the start of decomposition and further increases to a maximum at 2398 s, before it decreases again. A similar behavior has already been observed under oxidizing conditions and is thus evidence for a rapid evolution of initial Co_2O_3. Right after the maximum, which also corresponds to a local maximum of the oxidation state (see E_0 EXAFS results in Figure 4.47), the weight of (probably) Co_2O_3 decreases again in favor of mainly CoO and Co. The CoO also exhibits a maximum and thereafter decreases in favor of the final product Co_3O_4. It is noteworthy that in parallel to the initial Co_2O_3 formation an evolution of Co is also detectable, while the first CoO contribution appears in parallel to the evolving CO/CO_2 peak, which is happening a few hundred seconds later at about 2400 s. A maximum in Co and CoO amount is observable at about 2600 s and the high Co weight is also well evident in the EXAFS results (lowest O coordination number and lowest E_0 value). Co and CoO are further reacting to Co_3O_4, which requires more CoO than Co. In the LCA results this is recognizable by a faster decrease of CoO weight compared to the Co weight. At about 4000 s the heating was stopped resulting in an exponentially decreasing mean square deviation of the Co-O path length, as has already been observed in oxygen atmosphere.

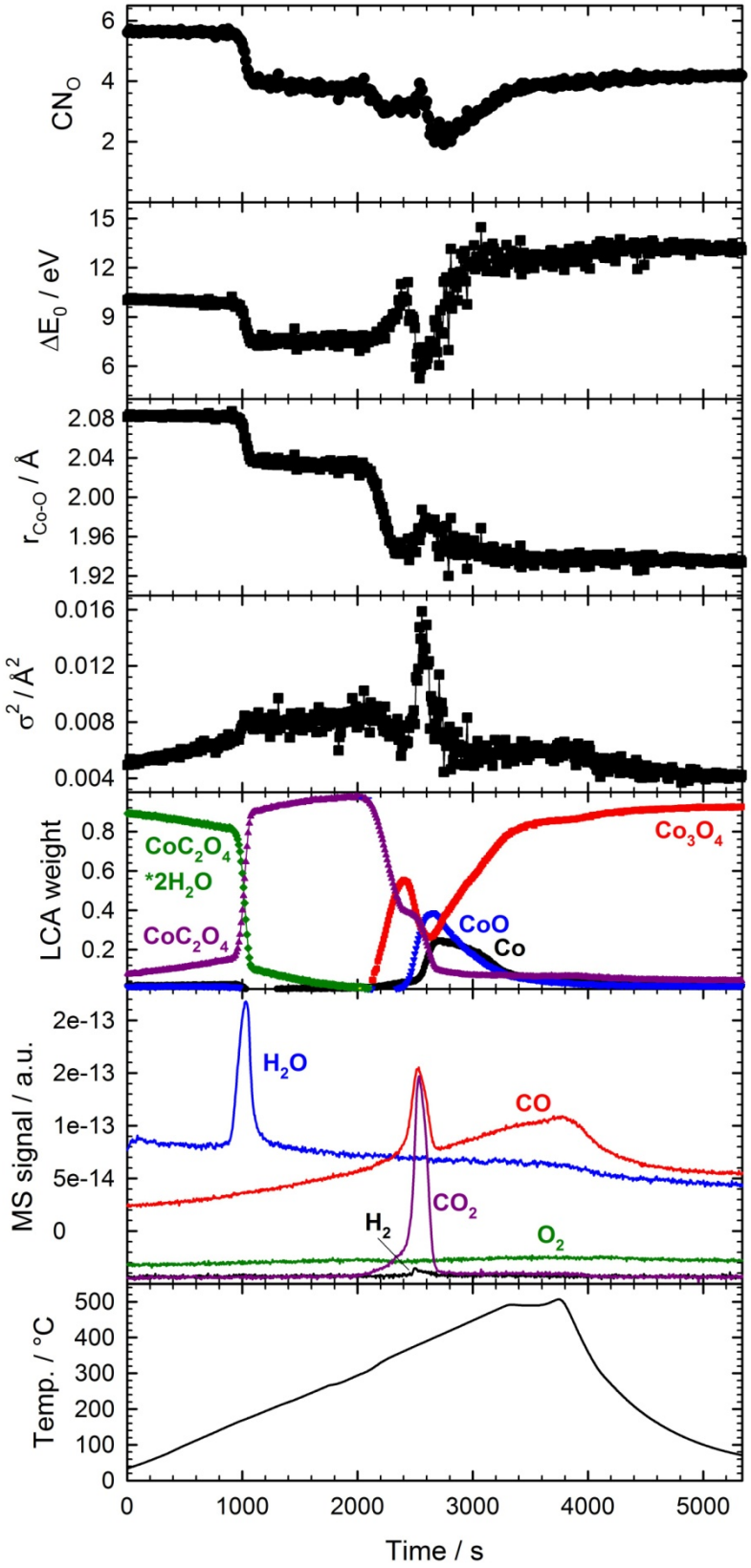

Figure 4.47: Results of synchronized EXAFS analysis, LCA and MS during the thermal decomposition of Co oxalate in helium atmosphere. From top to bottom: Coordination numbers, energy shift, atomic distance, mean square deviation, LCA weights, MS signal and temperature.

Discussion

The presented results suggest a decomposition of Co oxalate in two steps starting with a separation of metal and oxalate ions before the oxalate decomposes. This assumption is supported by the fact that the structure changes long before a maximum in CO/CO_2 evolution can be observed. A few oxalate ions seem to decompose early on, as e.g. evident from the results in inert atmosphere. Here the early formation of Co_2O_3 can only be explained by Co, which is oxidized with O_2 yielded by the evolving CO_2. However, as soon as the oxalate ions really start to decompose (at a higher temperature), as indicated by the sharp CO/CO_2 maximum within the MS signal, CoO is observable. Probably, the CoO evolves from remaining CoC_2O_4, where the oxalate decomposes rather close to the Co atom and not separated from it. This can be observed especially well in the experiment performed under reducing conditions, but the late CoO evolution has also been observed in inert atmosphere and also indirectly under oxidizing conditions. To further understand the decomposition and validate the presented experiments, it would be helpful to repeat the experiment with more rapid heating, to check whether the evolution of CoO starts earlier in the course of the decomposition. Respectively a slower heating could be applied, to check whether a CoO evolution is still observable at all. The herein presented results already explain well why the Co oxalate decomposition has been occupying scientists for so many years. Moreover, they show that QEXAFS is an adequate tool to better understand the underlying processes during thermal decompositions.

4.3 Layer growth and surface reactions

The application of thin solid films becomes more and more important in various industrial fields. Nowadays, active elements are constructed via thin film deposition processes in the semi-conductor industry (see e.g. [Jos07, Zha09]) and with the ongoing trend to smaller components the properties of very thin films have to be understood in detail. Thin films are equally important e.g. as corrosion protection for tools and medical implants, in catalytic applications and for the construction of X-ray optics (see e.g. [Sta02, Mar09, Kal10]). The structure of thin films plays a crucial role for the physical and chemical properties as e.g. the electrical and thermal conductivity, durability or the supply of active sites for chemical reactions on the surface. It is well-known that the structure of thin films is often significantly different from bulk material because of surface defects and roughness. With controllable process parameters during the deposition process, as e.g. temperature, pressure or gas composition, and also with subsequent heat treatment it is possible to manipulate the structure and/or stoichiometry (see e.g. [Tho74, Hot98, Wil04]). A deeper knowledge of film growth processes is important to improve production processes as well as the quality and stability of thin films.

The sputter technique is one important method to deposit thin films. In a vacuum chamber, high energy ions, generated typically by low pressure electric discharge of noble gases, are accelerated towards a target material. During the impact of ions on the target, material is released and settles down on the substrate as thin film. The application of various targets and the addition of reactive gasses as e.g. oxygen or nitrogen can be used effectively to produce oxide or nitride layers with a determined stoichiometry or multilayer systems. An in situ observation of the layer structure during deposition is feasible with X-ray absorption spectroscopy in grazing incidence as explained in section 2.2. With the addition of time resolution provided by the QEXAFS technique, it is possible to follow the deposition process in situ, so that structural changes during the film growth can be investigated in detail without stopping the deposition. Additionally, it is possible to investigate structural changes during heat treatments, which are often used to optimize the layer structure.

The first QEXAFS measurements during sputtering processes have been performed with stepper motor monochromators during Cu layer deposition in fluorescence [Fra91] and more recently during the preparation of tin nitride and tantalum oxide with a time resolution of about 20 – 30 s for each spectrum in absorption [Bru05, Lüt05b, Lüt06]. These experiments have demonstrated the benefits of this technique and proven that detailed information of layers with a thickness of less than 1 – 2 nm can be obtained. With the latest advancements in the QEXAFS technique, as presented within this work, it should also be possible to follow the layer deposition with sub-second time resolution. For that purpose, the deposition of Cu layers during dc sputtering was investigated. Initial experiments were performed at the BW1 beamline at the DORISIII storage ring, where the QEXAFS monochromator presented in this work was temporarily installed together with the reflectometer introduced in the next section. Thereafter, the permanently installed QEXAFS monochromator at the SuperXAS beamline at the SLS was used for more detailed investigations. In earlier studies the same sample system was investigated with the important difference that layer deposition was stopped for each measurement [Fra91]. Based on existent theories of layer growth mechanisms, differences in layer morphology can be expected when outperforming a continuous deposition [San86, Rui03]. In a second experiment, the oxidation of freshly sputtered Cu films in oxidizing atmosphere was investigated at different temperatures, in order to evaluate the benefits of studying surface reactions with grazing incidence QEXAFS.

4.3.1 Experimental setup and sample alignment

Compared to transmission measurements, which were performed in all previously presented applications, the setup required for grazing incidence experiments is somewhat more sophisticated. An accurate alignment of the sample in the X-ray beam is an essential prerequisite. For this purpose a reflectometer was used as drawn schematically in Figure

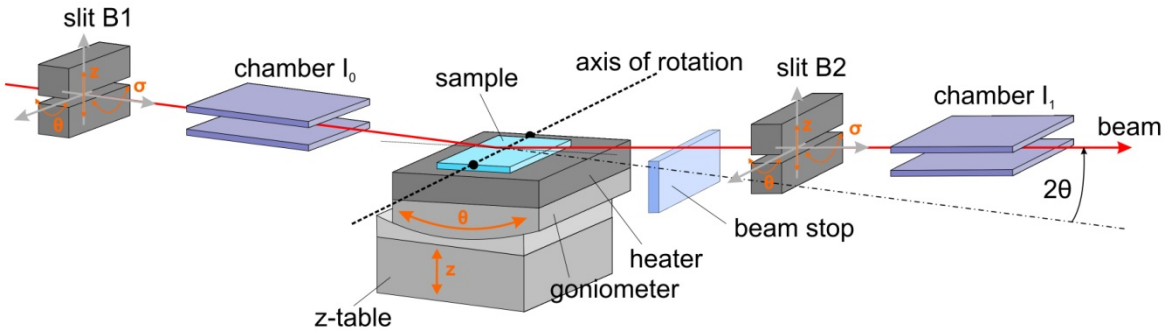

Figure 4.48: Schematic representation of the reflectometer (see also [Hec97]).

4.48. Slit $B1$ defines the height of the beam h before it hits the sample and according to the grazing incidence angle θ, h should amount to less than

$$h = l \sin \theta, \tag{4.7}$$

whereby l is the length of the sample along the beam path. Otherwise, not all of the measured incident beam intensity I_0 hits the surface, which causes errors as soon as normalization of the spectra with I_0 is carried out. An ionization chamber follows next in the beam path to measure the incident beam intensity I_0 before the beam is reflected on the sample. The sample can be translated vertically (z-direction) to adjust the height, and rotated to adjust the incident angle θ, respectively the roll angle along the beam axis (not shown in Figure 4.48). All three movements are performed with linear tables and goniometers, which are controlled by the data acquisition software. Following the path of the reflected beam, a beam stop is used to make sure that no intensity of the direct beam, which might pass above the sample, reaches the detector. Next, the second slit $B2$ can be used to define the acceptance of the following ionization chamber, measuring the reflected signal I_1. Slit $B2$, the following ionization chamber and eventually a reference sample followed by another chamber are mounted on the 2θ arm, which can be adjusted to the specified θ value. During the presented experiments a Cu metal foil was measured as reference sample to calibrate the energy. More details about the reflectometer, including the accuracy of adjustments, can e.g. be found in [Kei05].

The reflectometer allows installing an in situ chamber at the sample position. In the presented experiments, a sputter chamber for dc magnetron sputtering was used for the deposition of thin Cu films on glass substrates and the oxidation of sputtered Cu films. The substrates were cut out of 3 mm thick glass plates with lengths of 48 mm and 22 mm and accordingly, the slit B1 was set to 240 µm and 120 µm, adapted to typical incident angles of about 0.25°. The substrates were cleaned in the following steps: (i) removing dust and glass shards with pressurized air, (ii) washing the substrates in an ultrasonic bath with Tickopur RW77 and (iii) flushing the substrates with ethanol followed by rapid drying.

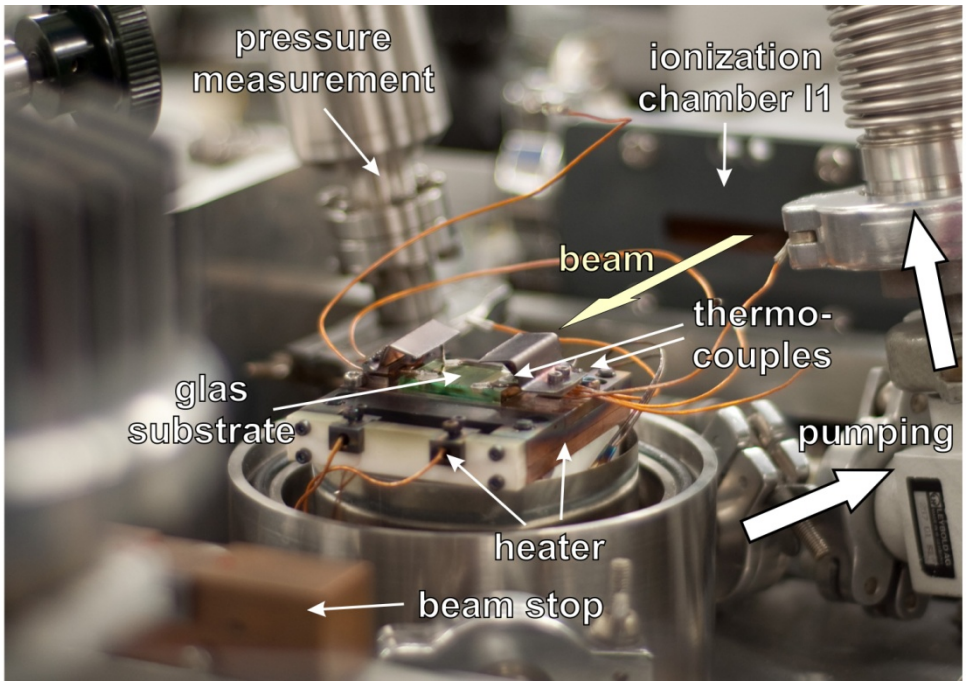

Figure 4.49: In situ sputter cell for layer growth and layer oxidation experiments.

Inside the chamber the glass substrates were placed on a copper table which could be heated by an integrated tungsten wire connected to a current source. Two thermocouples were used to control the temperature, one fixed to the heater and one fixed to the glass substrate with silver conducting paint. A close-up view on the interior of the cell is shown in Figure 4.49. The vacuum system allowed pressures down to about 10^{-5} mbar inside the sputter chamber. With a fine dosage valve Ar was filled into the chamber as sputter gas up to a pressure of about 0.08 mbar. At this pressure, Cu sputtering was performed with currents of about 10 mA.

The entire setup with the reflectometer and the dc magnetron sputter chamber as installed during the preparing experiments at the BW1 beamline at DORIS III is shown in Figure 4.50. The sputter chamber was fixed to the tilt and translation tables used to align the substrates in the beam. The connected pumping station, consisting of a rotary pump followed by a turbo molecular pump, was mounted close to the chamber but mechanically decoupled from the experimental table. This turned out to be an important refinement in order to minimize the disturbing effect of sample vibrations induced by the pump. However, it was not possible to completely avoid sample vibrations, which is a serious problem in combination with QEXAFS, because the vibration frequencies cannot be filtered out of the time-resolved data without affecting the EXAFS signal.

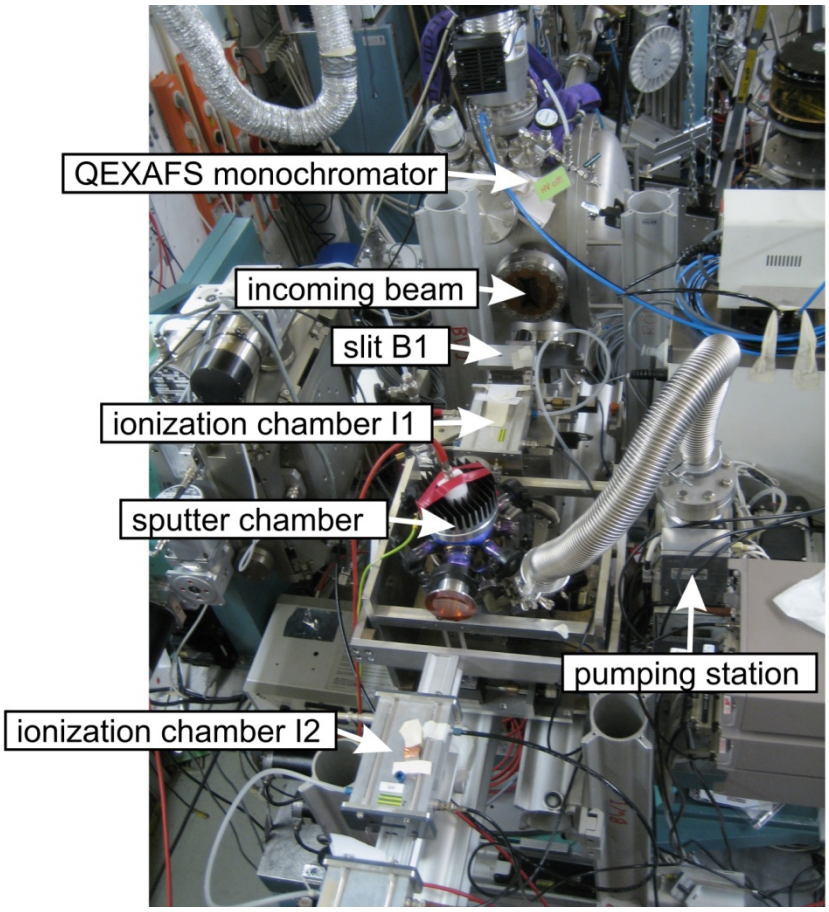

Figure 4.50: Reflectometer and QEXAFS monochromator installed at the BW1 beamline at DORIS III.

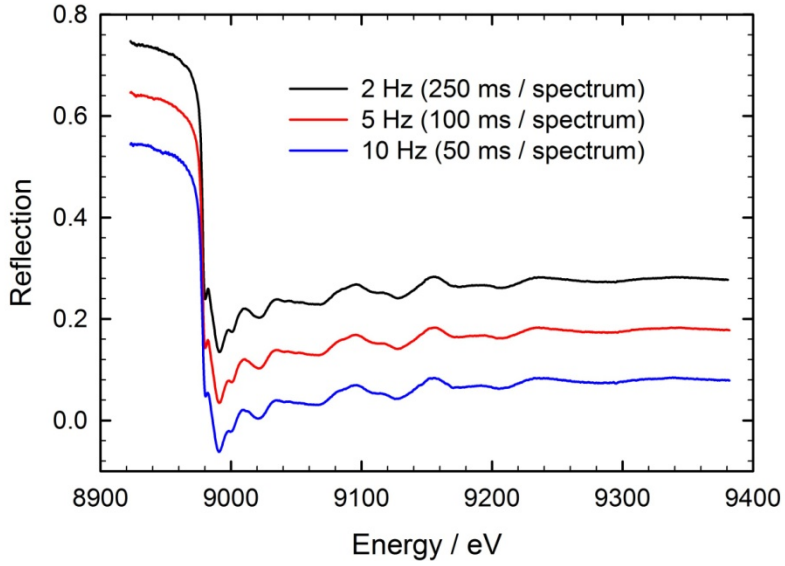

Figure 4.51: ReflEXAFS spectra of a Cu surface measured with varying time resolution. The spectra measured with 5 Hz and 10 Hz crystal oscillation frequency are shifted downwards.

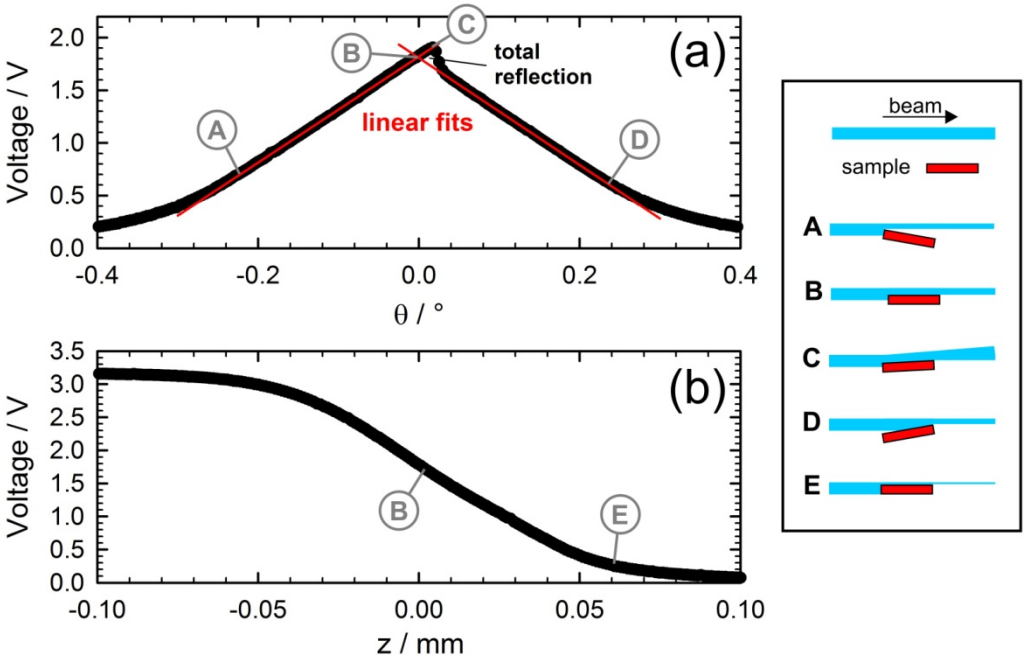

Figure 4.52: (a) Rocking scan and (b) z-scan of the sample in the X-ray beam with fixed photon energy. Both steps have to be repeated iteratively to align the sample, before the incident angle can be adjusted accurately. The sample positions at different steps of the scans (A-E) are represented by the graphics on the right side.

The presented data in the following sections were all collected at the SuperXAS beamline at the SLS, where the QEXAFS monochromator was equipped with a 0.3° eccentric disc yielding spectra from about 8920 eV to 9380 eV at the Cu K-edge. The crystal oscillation frequency was adjusted to different values during the experiments, and in Figure 4.51 typical reflection spectra of a Cu film, measured with the presented setup, are shown. It can be observed that even with very good time resolution below 100 ms a good data quality can be achieved using QEXAFS in grazing incidence reflection mode. This was the first time that such high time resolutions were applied with this technique.

Each sample alignment was performed in the following steps. First, the whole sputter chamber was moved downwards until maximum intensity was measured in the ionization chamber mounted on the 2θ arm adjusted to $2\theta = 0$. Thereafter, a z-scan was performed, which means that the sputter chamber was moved upwards while data was acquired as function of the momentary motor position. The resulting intensity behind the sample is exemplarily shown in Figure 4.52b. The motor position, where half of the maximum intensity is measured, corresponds to the position where half of the beam profile is covered by the sample. After setting the motor to this position, data was acquired as function of the θ angle during the so-called rocking scan. Thereby a shadowing triangle evolves and is exemplarily shown in Figure 4.52a. The linearly increasing and decreasing legs can be explained directly by a shadowing of the beam when θ deviates from zero. At the peak of

the triangle an asymmetric feature evolves, which can be explained by total reflection occurring for θ angles close to zero. Thus the maximum in the signal does not correspond to $\theta = 0$, but to a small positive angle, so that some of the measured beam is actually reflected intensity. In accordance, the true $\theta = 0$ position can only be determined by fitting the increasing and decreasing legs, yielding the correct peak of the triangle. After moving θ to the new angle the intensity was checked again to see whether it still amounted to half of the maximum intensity. If that was not the case the z-scan and also the subsequent rocking scan eventually had to be repeated in several iteration steps. After this procedure, the sample was aligned and it was possible to accurately select the θ angle of interest.

Data analysis was performed with the same code that has also been used for the T-REX software and especially with the simulation tool introduced in section 3.3.10. In contrast to the absorption spectra, the reflection mode spectra were in this case calculated by dividing the intensity I_1 by I_0. Another difference to absorption experiments is the importance to measure a spectrum I_1^*/I_0^* with the direct beam by moving the sample out of the beam path. Thereafter, all measured spectra with the same energy range have to be normalized to this spectrum according to

$$R(E) = \left(\frac{I_1(E)}{I_0(E)}\right) / \left(\frac{I_1^*(E)}{I_0^*(E)}\right), \tag{4.8}$$

in order to obtain true reflectivity values ranging from 0 to 1.

4.3.2 Deposition of Cu films

In this first example copper was deposited on glass via dc sputtering. After aligning the substrate in the beam, Ar was fed into the sputter chamber as sputter gas. Before the start of measurement the Ar pressure was adjusted to ca. 0.08 mbar with a fine dosage valve. About 30 s after starting the measurement the plasma in the sputter chamber was ignited and thus the deposition of Cu started. The sputter process was kept alive for about 5 min and data was acquired continuously at typically 5 Hz crystal oscillation frequency (1 spectrum in 100 ms). The measured reflection mode spectra during Cu deposition at room temperature after performing normalization according to Eq. (4.8) and averaging over 10 spectra are shown exemplarily in Figure 4.53. The incident angle was set to 0.225° for this measurement.

It can be observed that the edge jump of the spectra is increasing in correspondence to the growing layer thickness. Furthermore, it is possible to follow the evolution of the EXAFS features, which are becoming more enhanced with increasing sputter time, as the lattice structure evolves with increasing layer thickness. As recognizable by observing the pre-

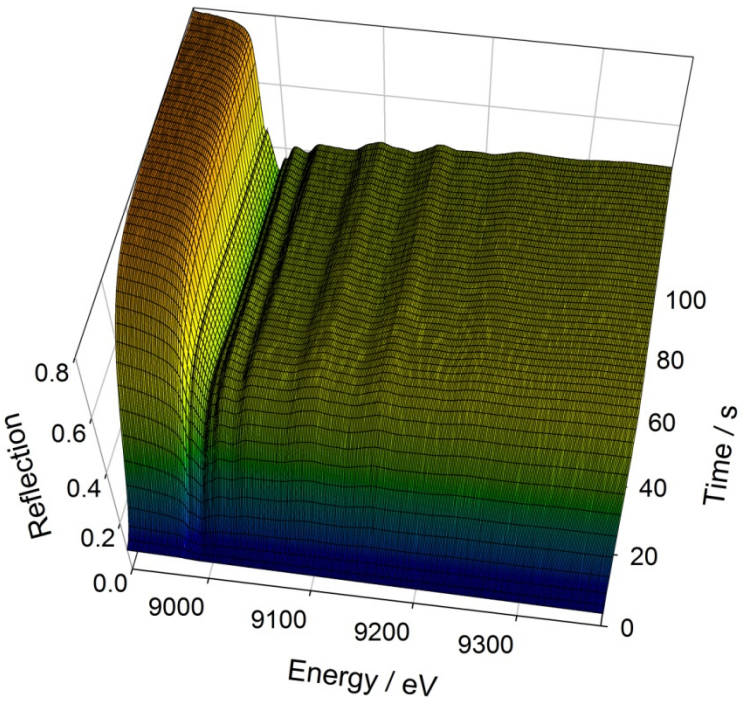

Figure 4.53: ReflEXAFS spectra after averaging over ten spectra during the first 100 s of data acquisition while sputtering Cu on glass at room temperature. The spectra were measured under grazing incidence with an angle of about 0.225°.

edge, the reflectivity first increases, since the chosen incident angle is above the value for total reflection on glass, but still below the corresponding value for Cu. Thus, more beam intensity is reflected with an increasing Cu contribution. After a while (ca. 80 s), the reflectivity slowly starts to decrease, which is explainable by the increasing surface roughness of the growing layer. When keeping the sputter process alive for a longer time, the roughness further increases until it is no longer possible to get a specular reflex strong enough for EXAFS studies.

To determine the structure of the growing layer, and to monitor the evolution of layer thickness and roughness, the spectra in Figure 4.53 were fitted by calculating reflection spectra of various compositions using the optical data of Cu, Cu_2O and CuO. Fitting with pure Cu did not yield reasonable results, while the addition of 30% Cu_2O and 10% CuO led to a better congruence of simulated and measured spectra. This implies a model structure in which the entire volume of the film is composed of a homogeneous mixture of Cu, Cu_2O and CuO. Due to the fact that the sputter gas may contain traces of oxygen and the sputter-chamber only had a base pressure of about 10^{-5} mbar, the incorporation of oxygen species and a possible reaction with Cu within the film is very likely. Exemplary fits and the results of all fits performed during the first 30 s of sputtering are shown in Figure 4.54 for the data after averaging over 10 spectra. First of all, it can be observed that the fits result in a linear layer growth. This linear increase of film thickness was expected

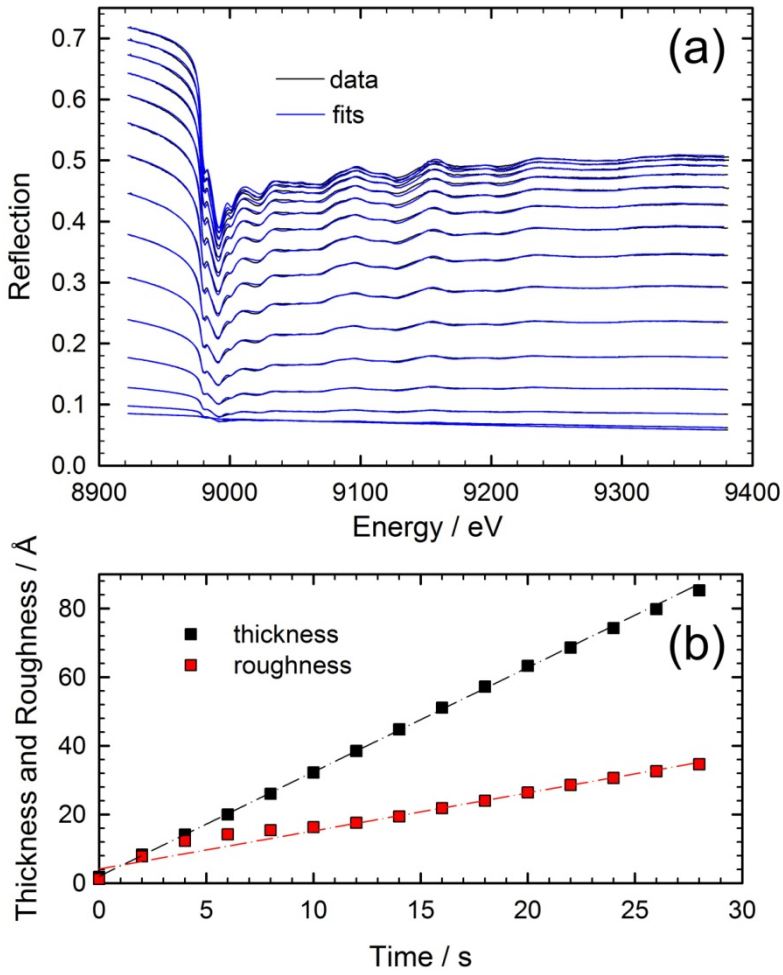

Figure 4.54: (a) Reflection spectra and fits during the first 28 s of sputtering after averaging over ten spectra, (b) evolution of thickness and roughness as function of time as determined by the fits in (a).

due to the constant sputter current and confirms that the performed fits are reasonable. In order to further support this conclusion, it still has to be shown whether the growth rate, which was determined to (0.30 ± 0.02) nm/s in Figure 4.54b, is quantitatively correct.

For this purpose, the sputtered layer was additionally investigated ex situ with an atomic force microscope (AFM) (Q-Scope 250, Quesant) by cutting the layer down to the substrate and thereafter scanning over the produced gap. A typical AFM scan is shown in Figure 4.55. In this case the layer thickness could be determined to be about 370 nm, which is the result of sputtering 910 s and consequently yields an averaged growth rate of 0.41 nm/s of the sputter process. The value is higher than determined with the fits for the first 25 s, which can e.g. be explained by the removal of oxygen inside the chamber and especially on the Cu-metal target during the sputter process, leading to improved sputter efficiency. This is supported by considering the EXAFS investigations during the start of surface oxidation, as presented in the next section, where no more oxidized Cu could be observed at the surface of very thick Cu layers. Additionally, the sputter target typically

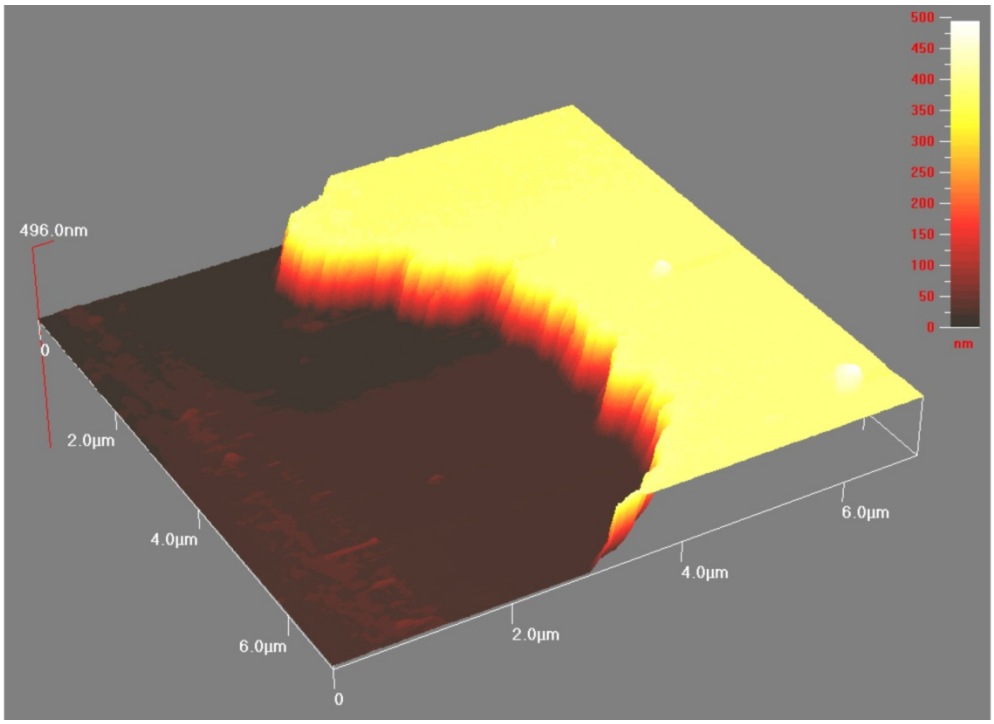

Figure 4.55: 3D topographic plot resulting from AFM investigations.

heats up during the sputter process, which might also result in an increasing growth rate over time.

The roughness of the layers, which is also shown in Figure 4.54b, rapidly increases as long as the layer thickness amount to approximately the same value as the roughness of the substrate, which was determined to about 5.2 Å by additional AFM investigations. Thereafter, at about 15 Å the roughness hardly shows any changes for some seconds, before it again starts to increase linearly for $t \gtrsim 10s$ from the indicated red dashed line in Figure 4.54b.

Generally, it was recognized as a good approach to first perform averaging over several spectra in order to obtain smooth reflection spectra, which allow determining the layer structure accurately. However, as soon as the structure is known, the fitting can also be carried out with spectra that exhibit some noise, because the variation of layer thickness and roughness only affects roughly the shape of the absorption spectra and not the EXAFS oscillations. Thus, the simulations were repeated for the original reflection spectra that were each measured in only 100 ms. Thereby it is possible to follow the start of the sputter process with a surface growth of only about 0.6 Å from one spectrum to the next, which corresponds to about 0.24 monolayers.

The results are shown in Figure 4.56 for the time region up to 13 s. Now it is more obvious that there is a time period, where absolutely no increase in roughness occurs for layer thicknesses between about 2 – 3 nm. It was not possible to detect this behavior with the

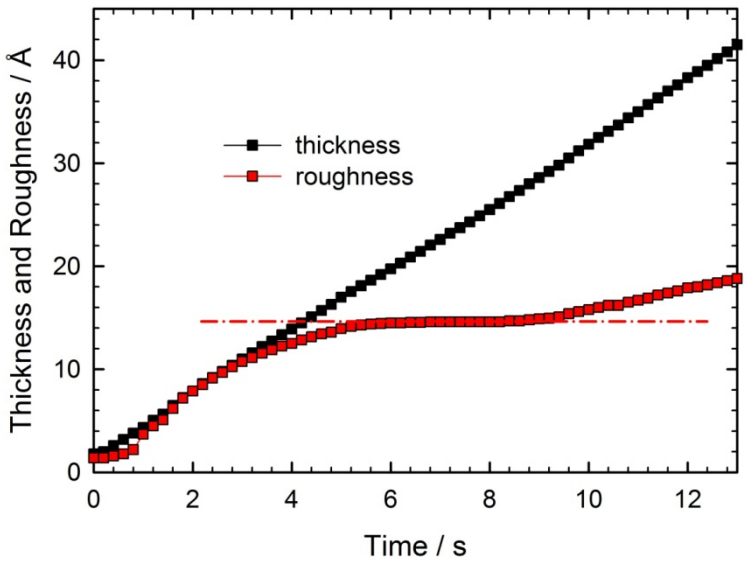

Figure 4.56: Thickness and roughness determined for the first 13 s of Cu deposition on glass at room temperature with a time resolution of 0.2 s.

averaged data in Figure 4.54, where only a slower increase of roughness could be observed. It is also noteworthy that the values resulting from the fits do not scatter strongly, although the unfiltered data is more difficult to fit due to a worse signal-to-noise ratio. This is partly due to the still acceptable data quality, but also due to the fact that it is possible to predict the layer thicknesses for each spectrum with the linear growth rate as determined in Figure 4.54b. Thus, it is much easier to refine the fits with these already rather accurate starting values.

Discussion

In a previous study, the growth of ion beam sputtered Cu layers on graphite was investigated by Marcus et al. [Mar97]. Thereby, it was concluded that the growth of Cu proceeds in a layer-by-layer fashion, which is also known as Franck-van-der-Merwe type of growth [Fra49]. Considering the data presented in Figure 4.56, where a region with stable surface roughness was observed during the initial step of layer deposition, it is difficult to explain this behavior with such a growth mechanism in thin layers. The growth in clusters, which is known as Volmer-Weber mechanism [Vol26], is more suitable to explain the data presented here. Since the roughness value is the mean square deviation of the surface height profile, it can be expected that it increases rapidly at the beginning of layer deposition due to island formation. Thereafter, the roughness might increase more slowly (or even not at all), as soon as the clusters on the surface start to coalesce. At that moment, the gaps between the islands disappear, which slows down the overall increase of roughness. As soon as no more islands exist, the roughness increases steadily parallel to the layer growth, which agrees with the Franck-van-der-Merwe type of growth.

Evidently, QEXAFS in reflection mode can be effectively used to study surface growth processes in detail. Thereby, it is not only possible to follow the layer thickness and roughness but also the layer structure in situ. Further data analysis of experiments with Cu sputtered on glass at various temperatures are expected to reveal additional interesting results compared to those presented in this work. It also has to be evaluated whether fluorescence measurements are more suitable to follow the deposition of the very first monolayers due to the low amounts of material in the beam path. Furthermore, currently each spectrum has to be fitted manually, which is rather laborious and significantly slows down the data analysis process. Thus, fit algorithms are required to automatically fit a bunch of a few hundred reflection spectra in order to use this approach more effectively. Additionally, a code to transform the EXAFS signal into absorption EXAFS by Kramers-Kronig transformations would help to exploit the EXAFS information in a better way and e.g. study the coordination numbers as function of time. The herein presented data demonstrates the potential of such investigations, which could become a much more important tool in the discipline of thin film deposition surface science with adequate software tools.

4.3.3 Oxidation of Cu films

The second example of grazing incidence QEXAFS measurements in reflection mode deals with the oxidation of the Cu films that were studied in the previous section during sputter deposition. Oxidation of metallic films has been a scientific topic for several decades and is still a matter of discussion. Mainly, this is due to the many technological applications, as for example in corrosion and catalysis. In general, the oxidation of a smooth and clean surface is supposed to start with the chemisorption of oxygen on the surface, followed by nucleation of oxygen and ending in the growth of bulk metal oxide over several surface layers [Zho10b]. Due to the catalysis science, there are many investigations of O chemisorption on perfect Cu surfaces under UHV conditions, so that much is known about these mechanisms (see e.g. [Ert67a, Ert67b, Ove98]). However, similar to the material and pressure gap in catalysis, as described in section 4.1, industrially relevant conditions for metal film oxidation are much higher oxygen pressures and rough metal layers instead of perfect crystal planes. Thus, it is not surprising that improvements in the understanding of initial metal oxide growth were mainly accomplished in the last decade with in situ X-ray techniques (see e.g. [Lun04, Eas05, Mar05]).

One important result of recent studies is the existence of a kinetic hindrance that prevents the oxide formation at low oxygen pressures. It was shown for Pd(001) and also for Cu(001) surfaces, that an oxygen pressure is required for surface oxidation which is several orders of magnitude higher than expected from thermodynamics, e.g. by considering the Cu-Cu_2O phase boundary in the phase diagram of the bulk material [Lun04, Eas05]. More

specifically, Lahtonen et al. [Lah08] have shown with XPS and STM that a Cu(001) surface at 100 °C exhibits only an oxygen coverage of about 0.3 monolayers (ML) at pressures in the order of 10^{-7} mbar. They also explained that this layer is very stable and passivates the surface up to pressures in the order of 10^{-2} mbar, before nucleation occurs and (3D) islands of Cu_2O are formed. Such behavior cannot be explained with earlier theoretical models that suggest an appearance of a metal oxygen phase as soon as thermodynamically feasible [Bro98, Car00]. While it was speculated that this kinetic hindrance is caused by the requirements of surface restructuring [Lun04], more recent modeling of the nucleation by Zhou [Zho10b] suggests that the nucleation rate is negligible for low oxygen pressures up to a specific threshold, after which the rate increases drastically. Studies during the oxidation of Rh(111) surface at various pressures and temperatures revealed that the oxidation starts at step defects on the surface to form a O-Rh-O trilayer, which prevents further oxidation until significantly higher pressures and temperatures are applied [Gus04]. Thereby it was suggested that such trilayer structures, which were e.g. also detected as VO_x on Pd(111) [Sur01], are a favorable transient structure that may act in general as protective layer preventing further oxidation of metals under certain conditions. More recently it was also shown for Rh that a 1D oxide formed at steps may also act as a kinetic barrier, which prevents 2D oxidation of the adjacent Rh(111) terraces [Kli08]. All these studies demonstrate the complicated initial steps of metal surface oxidation quite well. It is thus interesting to evaluate, how QEXAFS in reflection mode can help studying such effects.

After the initial O chemisorption and the nucleation step, the oxide layer on Cu is known to grow as Cu_2O structure within the investigated temperature range of up to about 200 °C. This layer growth and the related self-limiting effects are also a matter of discussion in the literature. For many years, the growth of oxide layers on metal surfaces was explained with the Cabrera-Mott model [Cab48], which suggests that at low temperatures the oxide layers grow to a critical thickness of some hundreds of angstroms, driven by an induced electric field. In this scenario the initial oxidation is accelerated by field-enhanced ionic transport, while for thick layers the field becomes too weak for further oxidation. According to the Cabrera-Mott model, the growth rate can be described via [Cab48]

$$\frac{1}{d(t)} = A - B\ ln(t), \tag{4.9}$$

where d is the layer thickness, t the time and A and B are fit parameters inhibiting the cation formation energy and the potential difference that controls the O ion diffusion. More recent studies revealed that in the case of Cu the oxide layer growth does not proceed in a uniform layer-by-layer fashion, but via an island growth followed by coalescence [Yan98]. In this context it was suggested that the diffusion of oxygen occurs along the interfaces

between the 3D Cu_2O islands and the Cu, while the limitation in Cu_2O growth is determined by the coalescence, which cuts off the diffusion channels into the bulk Cu. Very recent studies describe the kinetics of Cu_2O layer growth, at temperatures between 100 °C and 260 °C, by [Ram11]

$$d(t) = kt^n + d_0, \tag{4.10}$$

where d_0 is the initial copper oxide layer thickness (typically about 4 nm), while n is an empirical power factor. Thereby, the growth rate constant k is given by

$$k = k_0 exp\left(-\frac{E_0}{RT}\right) \tag{4.11}$$

with the initial oxide growth constant k_0 and the oxide growth activation energy E_0. In this report, XPS studies additionally revealed a CuO surface layer of about 2 nm thickness, which was also detected by Cho et al. [Cho97] at various temperatures. Further studies revealed a Cu-Cu_2O-CuO layer system also at room temperature [Kei10].

Results

To follow the oxidation of the freshly sputtered Cu films, the vacuum pump was turned off 60 s after starting a new measurement and a gas flow of pure oxygen was applied to the gas inlet of the sputter chamber at the same time. The experiment was performed at room temperature as well as at temperatures of about 150 °C and 200 °C. In each case the same temperature was also applied during the fresh deposition of the Cu layer via sputtering prior to the oxidation experiment. Again, all measurements were performed with a crystal oscillation frequency of 5 Hz. The resulting reflection spectra exhibit major differences between the various runs. At room temperature only minor changes can be tracked during the arrival of the first oxygen at the sample. At 150 °C more significant changes are observable, which proceed for about 300 s. At 200 °C first only small changes occur, but close to the end of the measurement the spectra are looking quite similar compared to the last spectra acquired at the end of the measurement at 150 °C.

As explained in section 2.2, a Kramers-Kronig transformation is required in order to transform the reflection spectra into absorption spectra and thereafter to properly extract the contained structural information by conventional EXAFS analysis. However, if the absolute coordination numbers are not required, it is also possible to directly analyze the EXAFS oscillations of the reflection spectra. Therefore, a spline function is used to extract the oscillations before fitting them with calculated paths, exactly as it is typically done with conventional EXAFS data. Bond lengths can be determined accurately by this approach as long as the penetration depth of the beam is small compared to the layer

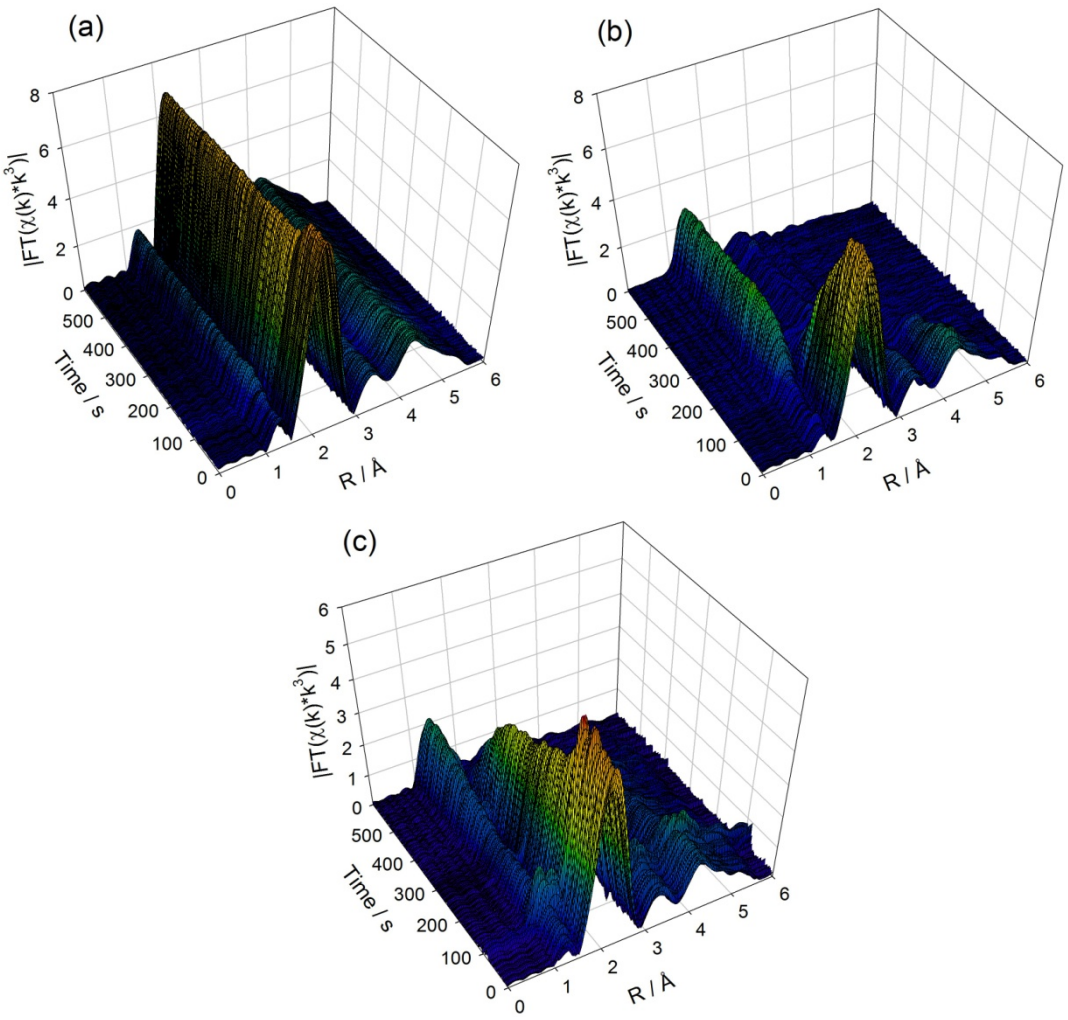

Figure 4.57: Fourier transformed EXAFS extracted directly from the reflection spectra acquired during Cu surface oxidation at (a) room temperature, (b) 150 °C and (c) 200 °C.

thickness. Furthermore, the relative coordination numbers can be determined as long as the geometry of the reflection experiment is not changed, which is the case in the experiments described in this section. In Figure 4.57 the Fourier transformed EXAFS data extracted from the reflection data is shown for all three performed experiments at different temperatures. The Fourier transformation was carried out in a k-range of 1.6 – 9.2 Å after applying a k^3-weighting. In the case of the 150 °C and the 200 °C measurement it is obvious that the first Cu-Cu shell of the metal vanishes, since the peak at about 2.2 Å decreases. At the same time a peak at 1.5 Å evolves, which can be unambiguously assigned to the first Cu-O shell of a surface oxide. At room temperature things are not that obvious, since only small differences between the start and the end of the measurement are recognizable. Here the metal contributions still dominate the spectra at the end of the experiment.

To resolve the structure during the oxidation, the data of Figure 4.57 was fitted with the first copper shell of Cu and the first oxygen shell of CuO/Cu_2O yielding the amplitudes for

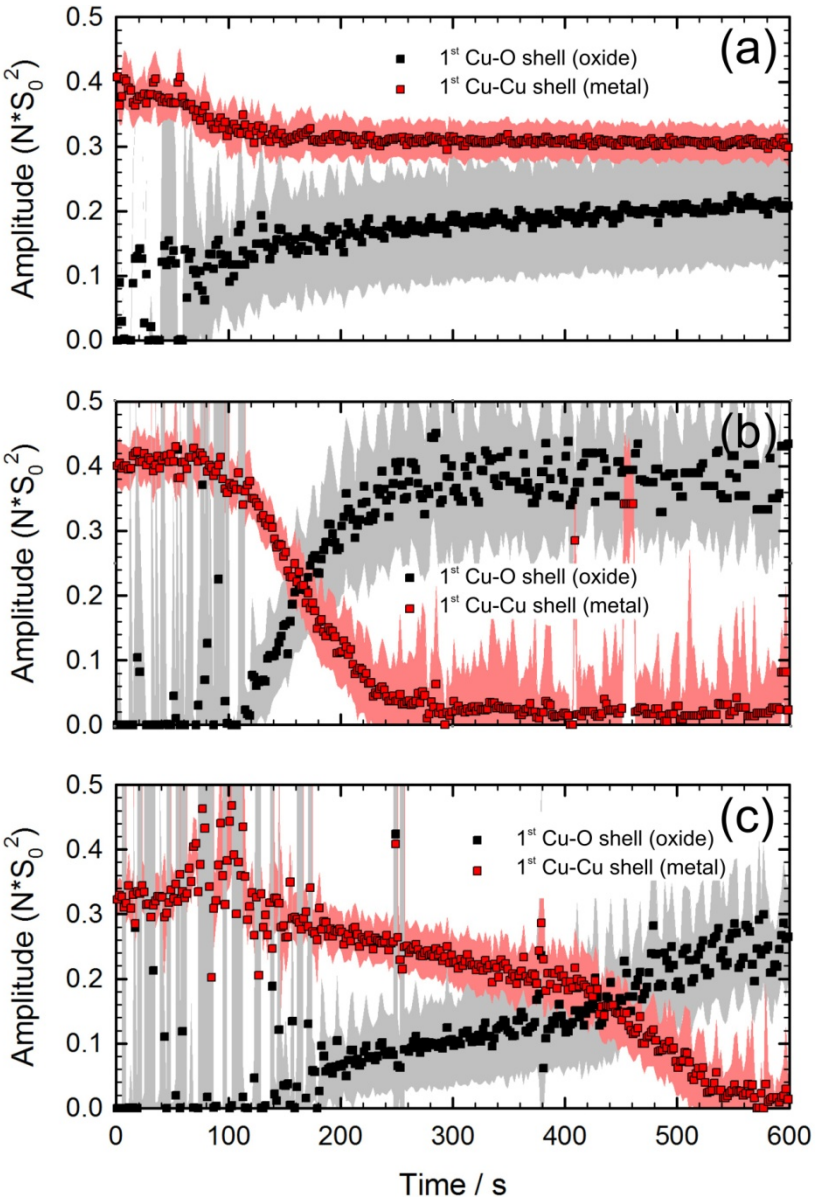

Figure 4.58: Amplitudes calculated with EXAFS fits during the first 600 s of Cu surface oxidation at (a) room temperature, (b) 150 °C and (c) 200 °C.

these shells as plotted in Figure 4.58. At all temperatures, the fits at the beginning of the experiment indicate that the sputtered layers consist of only metallic Cu, since only a few isolated fits yield a significant oxygen contribution. The amplitude of the Cu-O shell increases as soon as oxygen reaches the sample at room temperature and slightly delayed also at higher temperatures. In parallel the contribution of the first Cu-Cu shell decreases. This evolution is most enhanced at 150 °C, where the contribution of the Cu shell decreases to almost zero during the first 300 s. However, even in that case the Cu contribution does not vanish completely, indicating that the oxide layer only grows to a finite thickness.

At 200 °C the Cu contribution also decreases to almost zero, but with about 550 s it takes significantly more time than it is the case at 150 °C. Interestingly, there is a sharp bend in

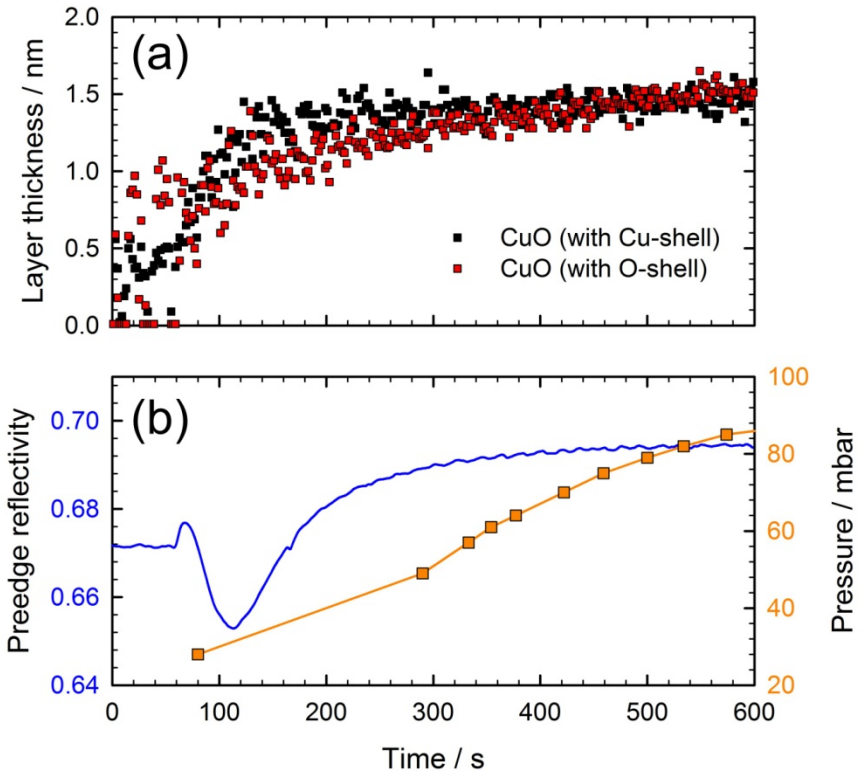

Figure 4.59: (a) CuO layer thickness, (b) pre-edge reflectivity and pressure in the sputter cell as function of time during the start of Cu surface oxidation at room temperature.

the decrease at about 400 s, indicating that there is more than one process observable during the oxidation. At room temperature the amplitude of the Cu-Cu shell of Cu metal decreases rapidly with the contact of first oxygen. Thereafter the decrease proceeds more slowly and during the overall 600 s reaction time only from about 0.4 to 0.3. Obviously, the oxide layer is much thinner at this temperature. At the same time the oxygen contribution increases from 0 to 0.2, indicating that the formed oxide is CuO in this case and not Cu_2O as the EXAFS results suggest at higher temperatures.

To further analyze the fit results the penetration depth of the beam and the relative amount of Cu_2O, respectively CuO, have to be correlated, so that it is possible to determine how exactly the oxidation front moves into the Cu layer. It has to be kept in mind, that the measured spectra are a result of integrating over the sample volume down to a depth that is penetrated by the beam. Thus, according to Eq. (2.35) an exponential decrease of the signal in z-direction has to be considered, so that the overall strength of the signal contributing to the resulting spectra can be written as

$$I = I_0 \left[\int_0^{z_0} \exp\left(-\frac{z}{l_{Cu_2O}}\right) dz + \exp\left(-\frac{z_0}{l_{Cu_2O}}\right) \int_{z_0}^{\infty} \exp\left(-\frac{z - z_0}{l_{Cu}}\right) dz \right] \tag{4.12}$$

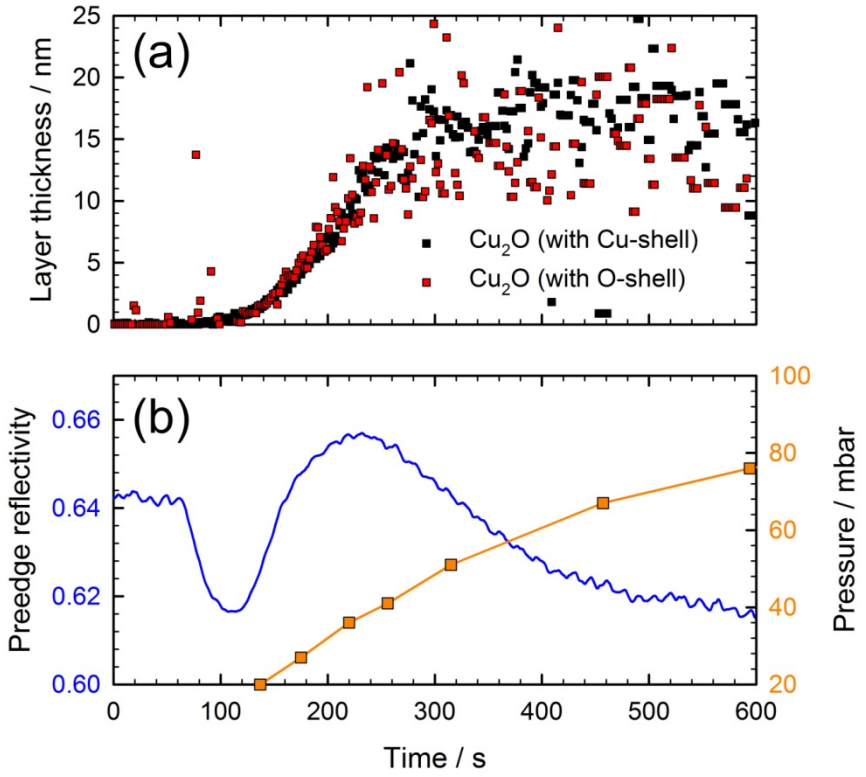

Figure 4.60: (a) Cu_2O layer thickness, (b) pre-edge reflectivity and pressure in the sputter cell as function of time during the start of Cu surface oxidation at 150 °C.

$$= I_0 \left[l_{Cu_2O} \left(1 - \exp\left(-\frac{z_0}{l_{Cu_2O}} \right) \right) + l_{Cu} \exp\left(-\frac{z_0}{l_{Cu_2O}} \right) \right],$$

where it is first integrated over the uppermost Cu_2O layer and thereafter over the Cu layer beneath. The l-values are the penetration depths (see Eq. (2.35)) for both present materials and are a function of energy with the contributions of $\beta(E)$ and $\delta(E)$, whereas z_0 is the thickness of the Cu_2O layer. With Eq. (4.12) the relative amount of Cu_2O contributing to the reflection spectrum can be calculated to

$$p(Cu_2O) = \frac{l_{Cu_2O} \left(1 - \exp\left(-\frac{z_0}{l_{Cu_2O}} \right) \right)}{l_{Cu_2O} \left(1 - \exp\left(-\frac{z_0}{l_{Cu_2O}} \right) \right) + l_{Cu} \exp\left(-\frac{z_0}{l_{Cu_2O}} \right)} \tag{4.13}$$

Since it is possible to determine the relative amounts of Cu_2O (or CuO) and Cu with the EXAFS fit results in Figure 4.58, z_0 can be determined via Eq. (4.13), which yields the results shown in Figure 4.59 – Figure 4.61. Thus, it can be studied how the oxidation front moves into the surface as function of time. Thereby, the calculations can either be performed with the results for the Cu-shell or the O-shell, because the reference values for the bulk materials can be deduced from the start of the reaction, where only pure Cu was detected. In all three measurements both ways lead to similar results, which can be seen as

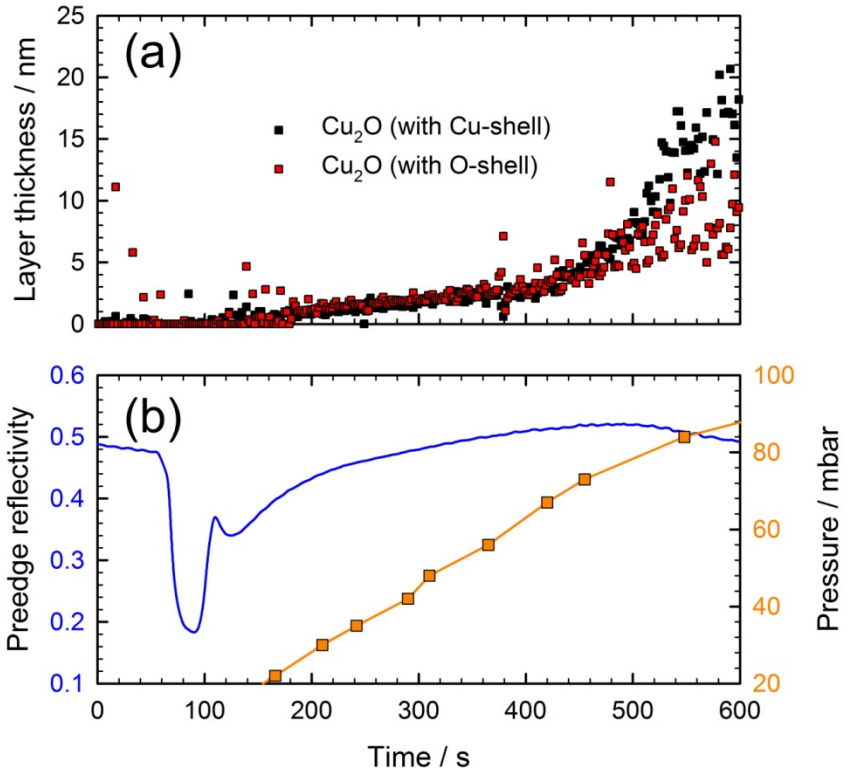

Figure 4.61: (a) Cu_2O layer thickness, (b) pre-edge reflectivity and pressure in the sputter cell as function of time during the start of Cu surface oxidation at 200 °C.

confirmation for the EXAFS fits and the approach using Eq. (4.13). In addition to the layer thickness of the oxide films, the reflection in the pre-edge region was determined by averaging over all reflection values between 8926 eV and 8936 eV in each spectrum and these results are displayed in Figure 4.59b – Figure 4.61b together with the pressure inside the sputter chamber during the experiments. The pressure curves demonstrate that the experiments were all performed under similar conditions except for the substrate temperature and the initial surface roughness.

At all temperatures it can be observed that the reflection decreases as soon as the pump station is turned off. This initial decrease is most enhanced at the highest temperature and scarcely observable at room temperature. After a while, the reflectivity increases again in all cases, but at room temperature this increase proceeds to the end of the measurement, which is not the case at the higher temperatures. Another difference between the various temperatures is the structure of the formed surface layer. At room temperature the EXAFS data indicates the growth of a CuO layer, with only about 1.5 nm thickness on the Cu. At 150 °C a rapid growth of a Cu_2O layer can be observed. Interestingly, at 200°C the layer formation proceeds in two steps. First, there is only a very slow layer growth up to a few nm, before a sudden increase in the Cu_2O layer thickness can be detected. At 150 °C and 200 °C a maximum in the pre-edge reflection is observable, which appears in both cases approximately in parallel to the inflection point during the Cu_2O layer growth. However,

the inflection point appears at a partial oxygen pressure of about 40 mbar at 150 °C and at a pressure of about 80 mbar at 200 °C.

Discussion

The very different results summarized in Figure 4.59 – Figure 4.61 cannot easily be explained, as it is difficult to recognize systematic effects as function of temperature. However, with the contributions of other groups, many congruencies can be found and a detailed discussion is possible. For example, O´Reilly et al. [ORe95] observed an oxidation resistance at 50 °C, a simple Cu_2O layer between 100 °C and 150 °C and two layers at temperatures higher than 300 °C, which indicates a similar complicated temperature dependency of Cu oxidation as detected within this work. However, the herein presented in situ measurements help to draw more conclusions about this behavior within an atomistic and a macroscopic description, as will be presented in the next paragraphs.

First of all, the initial decrease of reflectivity at all temperatures can be explained with an increasing surface coverage by adsorbed atoms and molecules, which have to be mainly oxygen in molecular and dissociated form due to the applied experimental conditions. The following increase in reflectivity can only be explained by the fact that the adsorbed oxygen starts to form a bulk oxide at the surface of the Cu film. This means that at the beginning a certain amount of adsorbed O is required on the surface before Cu oxidation is initiated. Such behavior is in good agreement with recent investigations that revealed a hindrance barrier for the oxidation of Cu surfaces based on the nucleation rate of O [Zho10b]. The presented data also shows that this nucleation step is faster at higher temperatures, since the increase in pre-edge reflectivity after the minimum proceeds more rapidly at increasing temperatures. However, it is interesting to see that at room temperature the surface oxidation starts before the minimum in reflection appears which means that the nucleation has already started. This also explains that the minimum is less enhanced in comparison to the higher temperatures. In agreement to that, the oxidation also starts later at 200 °C than it is the case at 150 °C.

In order to carry out a reasonable discussion, the roughness of the Cu surfaces also has to be taken into consideration, since the films were sputtered at various temperatures. Thus, AFM measurements were performed at different positions on the surface, which yielded a roughness of about 5 nm at room temperature, 7 nm at 150 °C, and 11 nm at 200 °C with an estimated uncertainty of about ±1 nm. Although these measurements were performed ex situ after the oxidation process, it can be expected that the detected trends are also true for the freshly-sputtered films. This is also in agreement with other studies dealing with temperature dependent roughness profiles of deposited transition metal films with thicknesses in the order of a few hundred nanometers [Sea85]. The importance of roughness for surface reactions was recognized a long time ago, and is e.g. discussed in

detail by Zambelli et al. [Zam96]. Thereby, STM measurements showed that monoatomic steps on single crystal surfaces are the source of chemisorption and dissociation of molecules. Considering nanoparticles the effects of defects were found to be enormous as the density of defects drastically increases in such systems [Hon05]. The same can be expected for very rough surfaces, as it is the case for the 200 °C measurement here. With respect to surface oxidation, it was shown that monolayer steps are also the active sites for 1D oxide formation, which is generated by the first arrival of oxygen at the surface [Kli08]. It was also shown in this study that these 1D oxides act as barriers impeding the formation of 2D oxides on the adjacent terraces in analogy to 2D oxides, which are known to inhibit 3D oxidation [Gus04]. Although these studies were performed for Rh, similar effects on other metal surfaces like e.g. Cu are not unlikely. Last year it was shown that defects also play an important role on catalytic surfaces in non-linear surface kinetics as reaction oscillations [Hen10]. Thereby, it was shown that a significantly more oxidizing CO/O_2 atmosphere is required to oxidize a rough surface in comparison to a smooth surface. Such a trend is kinetically not expected, but explainable by the influence of steps on the thermodynamics of the process.

In order to explain the fact that oxidation starts with less adsorbed oxygen at lower temperatures, the surface roughness might well be responsible for this effect. It was shown that O nucleates to islands on surface terraces [Zam96], and it was also shown that this nucleation is required for the start of bulk oxide formation [Zho10b]. On rather smooth surfaces the O_2 dissociates at defects and nucleates on the terraces, whereby the nucleation rate increases as function of the temperature due to the O mobility. However, the more defects exist, the more O is initially adsorbed at these defects, which is also in good agreement with the decrease in reflectivity, which is more enhanced for the rougher surfaces at higher temperatures. Thus, it may be that all defect sites have to be occupied by O, before it starts to nucleate on the terraces. Or maybe the 1D oxide formation plays an important role in the case of Cu and acts as barrier for 2D oxide formation [Kli08], whereby a higher defect density leads to a stronger barrier. In this context, it would be most interesting to perform more experiments of this kind with a constant roughness and variable temperature, respectively a constant temperature and variable roughness.

After the nucleation step, the bulk surface oxidation proceeds in very different ways at the different surface temperatures. At room temperature, a CuO layer with a maximum thickness of 1.5 nm was observed. While the layer is still growing at the end of the measurement, the CuO layer obviously acts as protective passivation layer inhibiting further oxidation, while no such effect is observable during the measurements at higher temperatures. Thus, the oxidation to CuO at room temperature can actually only be explained by the much smoother surface, which inhibits an initial formation of 3D Cu_2O islands, as described by Yang et al. [Yan98]. Obviously, the additional O that reaches the

surface cannot diffuse into the surface, which additionally exhibits a less thermal disorder due to suppressed lattice vibrations. Instead the O further oxidizes the very thin surface layer to Cu(II). Since thin CuO layers were also observed in other studies as coverage on top of a Cu_2O layer [Cho97, Kei10, Ram11], it is interesting to note that the CuO is initially formed in the presented experiments and not after the growth of a Cu_2O layer, which would also be a reasonable possibility. This fact is especially interesting for corrosion applications.

At 150 °C the surface is rougher and the atoms are oscillating stronger around their lattice positions. Additionally, the initially adsorbed oxygen is consumed more rapidly as it is the case at room temperature. All in all, this leads to a rapid growth of 3D Cu_2O islands down to more than 10 nm inside the sample after only about 220 s and with only 40 mbar of O inside the chamber. This island growth was suggested by Yang et al. [Yan98] who also explained the observable self-limiting effect of surface oxidation with coalescence of the 3D islands that suppresses O diffusion into the surface. The decreasing O diffusion leads to increasing O adsorbed at the surface. This is well observable in the data, since the reflectivity decreases again after 220 s – 240 s (Figure 4.60b). At this point the Cu_2O layer thickness amounts to almost 15 nm and thereafter starts to grow more slowly. This is in perfect agreement with recent Cu oxidation studies performed with sheet resistance and optical transmittance at 140 °C, where a decrease in Cu_2O layer growth was observed at thicknesses of about 14 nm [Zho09]. They described the initial growth up to 14 nm with Wagner´s parabolic law [Wag33] and the following growth by an inverse logarithmic rate according to the Cabrera-Mott model as presented in Eq. (4.9).

The question arises, why things look that different at 200 °C, where one could expect an even more rapid Cu_2O layer growth for reaction kinetic reasons. During this measurement the surface is even rougher and the Cu lattice is also stronger affected by thermal disorder. However, similar to the measurement at room temperature, a protective layer is formed in the beginning, this time in a Cu_2O structure. It has already been discussed that the nucleation starts later at 200 °C and therefore overall more O is adsorbed, which is in good agreement with the initial stronger decrease in reflectivity up to about 90 s. By considering the higher quantity of defect sites at 200 °C, it is evident that the amount of initially adsorbed O corresponds to the number of defects and thus the surface roughness. However, in correspondence to the following rapid increase of reflectivity after 90 s (see Figure 4.61b) a rather rapid nucleation on the terraces seems to occur. Considering the much smaller terraces, also due to the higher roughness, this might result in a 2D Cu_2O layer, respectively an even more complicated Cu-O composite layer, before any 3D islands can start to grow. Such layers are well known to appear on transition metals under certain conditions [Lun06, Nol08], as well as their effect as barrier inhibiting further 3D oxidation [Gus04], respectively their role as precursor for bulk Cu_2O formation [Ove98]. In the latter

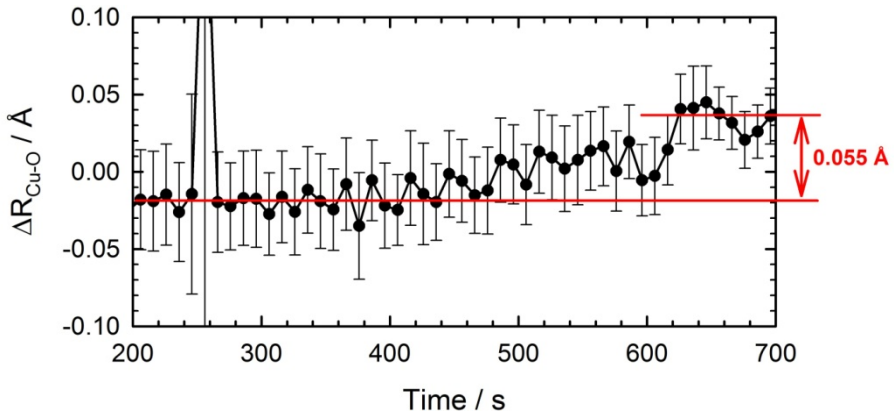

Figure 4.62: Distance difference between Cu and first neighboring O atoms calculated with EXAFS fits as function of time during oxidation at 200 °C. It was averaged over 5 subsequent distance values and the assigned error bars for this graph.

study it was also shown that Cu surface oxides exhibit structures similar to those of Cu_2O, however with slightly decreased Cu-O distances in the order of 0.05 Å (see Table 6 in [Ove98]). Due to the performed EXAFS fits, this can also be analyzed as shown in Figure 4.62. Although the data was rather noisy, it is possible to observe an increase of Cu-O distance after 400 s, which amounts to about 0.055 Å and thus confirms the theory that a transition from 2D surface oxide structures to bulk 3D Cu_2O oxide is the relevant process during this stage.

Since the initially formed Cu_2O layer at 200 °C is very thin, the oxidation potential will further increase until the field gradient is high enough, so that the oxygen starts do diffuse into the layer and oxidation proceeds. At this point it can only be speculated why the overcoming of this second oxidation hindrance barrier is followed by a much faster increase of Cu_2O formation. One possible explanation is that new diffusion paths evolve at the positions, where the initial Cu_2O layer is thinnest and that thereafter surface growth proceeds via the 3D island formation as explained in [Yan98] and as already observed at 150 °C. This would also well agree with the fact that a doubled O pressure is required to start 3D Cu_2O layer growth compared to the measurement at 150 °C. In summary, the evolution in the oxidation of the Cu surface at 200 °C can be described in two steps, from 1D oxide to 2D oxide and thereafter from 2D oxide to 3D oxide. The different mechanisms of oxidation suggested for the 150 °C and the 200 °C measurements are schematically summarized in Figure 4.63.

The discussion indicates that the surface roughness has to be considered as decisive parameter to explain the effects of surface oxidation. It was shown in the past that the laws of first order thermodynamics are not sufficient for a reasonable explanation of these phenomena, so the results obtained with the QEXAFS technique are an interesting addition to the still very up-to-date discussion of surface oxidation and the effect of surface defects

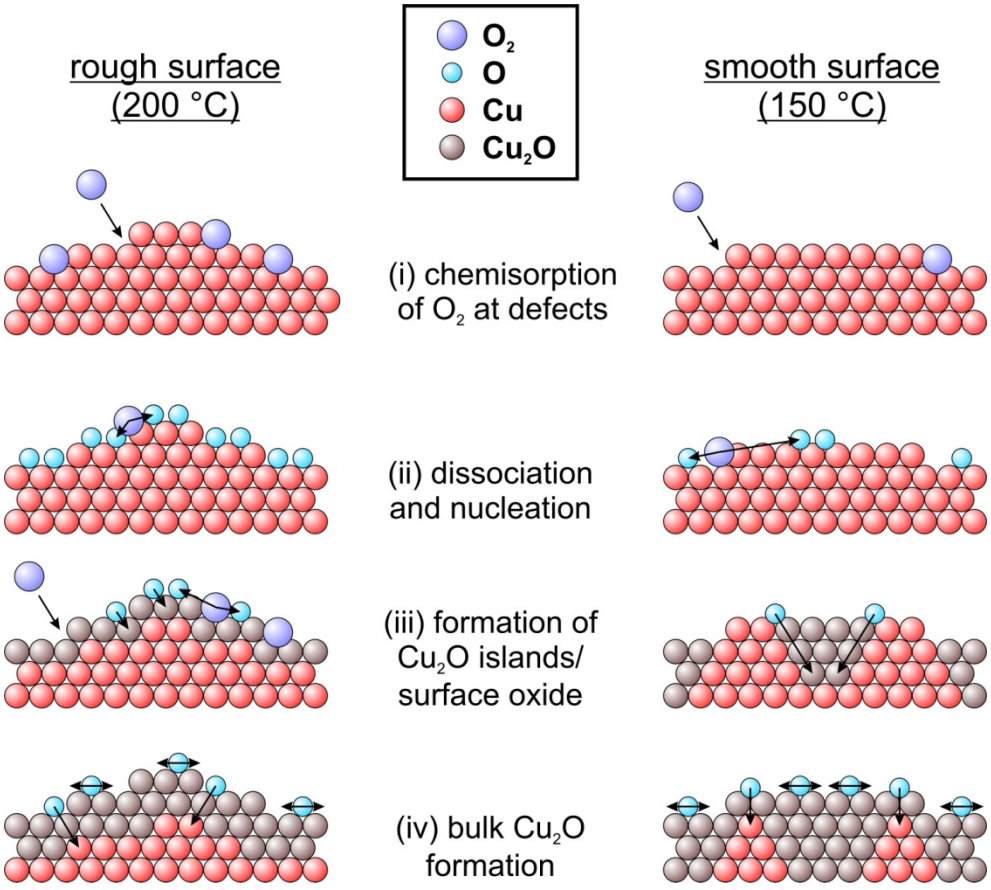

Figure 4.63: Schematic drawing of proposed oxidation mechanisms dependent on surface roughness.

in surface reactions. In Figure 4.60a and Figure 4.61a it can be observed that the layer thickness values scatter strongly, as soon as the thickness increases to about 20 nm, which is due to the exponential decreases of the signal in z-direction and thus lower statistics for deeper regions. Thus, it is e.g. more difficult to determine layer growth constants as in [Ram11], although it can be clearly recognized that the layer growth is approaching a limiting value. All in all, with the possibilities (i) to investigate the samples in situ, (ii) without the requirements of perfectly plane single crystal surfaces or vacuum conditions, (iii) with time resolutions in the sub-second time regime and (iv) also the option to vary the surface sensitivity by the chosen incident angle the presented technique is a unique tool to study surface reactions and it is highly recommendable to perform further experiments in this field.

5 Summary and outlook

Recent experimental advances and developments in the QEXAFS technique were presented along with new applications in the disciplines of catalysis and surface science. Both performance and user-friendliness of the QEXAFS method were significantly improved, while the applicability of QEXAFS was extended by newly designed mechanics. The application of a fast angular encoder proved to be capable to sample the continuously changing Bragg angle of the monochromator crystal synchronized to the acquired absorption data. This was recognized as a prerequisite to obtain highly accurate spectra that can be reliably analyzed with the typical procedures of EXAFS analysis and also as a starting point for more flexible monochromator mechanics. Previous monochromator driving mechanics working with rotating eccentric discs were restricted to fixed energy ranges defined by the applied disc. New mechanics with a continuously changeable eccentricity were designed and have proven to be capable to overcome this limitation. Now, it is possible to flexibly adjust the energy range of the acquired spectra to arbitrary values within seconds. Neither the usage of fixed eccentric discs is required anymore, nor the opening of the vacuum vessel to change the energy range. Thus, the few days typically available for a user group at a QEXAFS beamline can be used much more efficiently. Furthermore, flexible QEXAFS measurements with varying energy ranges and time resolutions are possible now, making new applications possible.

A new data acquisition system was designed, based on a multifunctional ADC board, which provides high acquisition frequencies, while low noise acquisition could be achieved due to the provided differential acquisition mode. The therefore designed acquisition software allows visualizing the sampled data instantly and can continuously save it to the hard disc for several hours if required. Additionally, control of all experimental devices as current amplifiers, monochromator motors and sample stages were implemented to further increase the efficiency of the experimental setup for QEXAFS measurements. In order to simplify the processing of the huge generated QEXAFS raw data files, a completely new

software tool for data analysis was designed, which provides not only the basic procedures of EXAFS data analysis, but also many approaches customized for time-resolved data. It is now possible to apply all data analysis procedures that were presented in this work to QEXAFS files with an organized graphical user interface, which provides easy navigation and high transparency concerning the performed operations. For the first time a thorough data analysis on QEXAFS files with sizes of several Gigabytes can be performed with a single program, which is a crucial advancement for an efficient application of the QEXAFS technique.

Apart from technical advances, various experiments were performed with QEXAFS to gain new insights into the complex processes of several catalytic reactions, the thermal decomposition of metal oxalates, as well as layer growth processes and reactions on rough surfaces. It was possible to study the complex mechanism of the Heck reaction by time-resolved probing the reaction solution and the catalyst bed. Thereby, it was shown that the Pd catalyst has to be completely reduced, before leaching of Pd into the reaction solution can be observed and the Heck reaction starts. It could also be proven that the Pd atoms at the end of the Heck reaction start to agglomerate and the dissolution of Pd from these agglomerates is the rate determining step when converting bromo benzene. Furthermore, it was shown that the composition of the reaction solution shifts towards homogeneous Pd complexes as the reaction fades and that the Pd particles start to grow during the redeposition of Pd. A new median filter has proven to be a powerful tool for the investigation of heterogeneous reaction mixtures as it is capable to filter out random distortions in the spectra. This is an important advancement e.g. for QEXAFS investigations during the preparation of catalysts under liquid conditions. Moreover, the filter can also be used to remove other unexpected runaway values as e.g. induced by beam losses or sudden sample vibrations.

Supported Pd catalysts were investigated during catalytic partial oxidation of methane, whereby oscillations in the conversion were linked to structural changes of the catalyst. With a time and space resolved approach it was observed that a reduction front moves from the end of the catalyst bed to the front. The thereby generated hot spot leads to autoreduction of the whole catalyst bed, before the catalyst re-oxidizes again towards the end of the catalyst bed. The dynamics of these oscillations were studied as function of temperature, gas composition and age of the catalyst. Kinetic oscillations were also investigated on a supported Pt catalyst during the extinction of CO oxidation induced by decreasing temperature. Thereby, it was shown that the observed oscillations in the CO oxidation are caused by an oscillating reduction front that moves downstream over the catalyst bed. In both cases, various approaches to analyze QEXAFS data were presented, which well demonstrates that QEXAFS in combination with advanced analysis software tools is most suitable to study dynamic effects in catalysis.

Modulated experiments were investigated (i) on supported Pt-Rh/Al_2O_3 catalysts during active catalytic partial oxidation in switching gas atmospheres of methane and hydrogen, and (ii) Cu/Al_2O_3 catalysts with different Cu loadings at various temperatures under switching oxidizing and reducing conditions. In the case of the Pt-Rh system minute changes could be observed, which can evidently be linked to the removal of oxygen and/or carbonyls from the catalyst surface. In the case of Cu/Al_2O_3 an intermediate Cu(I) state could be observed during reduction and also shortly during oxidation, which was only possible with a high time resolution of 50 ms/spectrum. Both modulation experiments were also investigated with the approaches of modulation excitation spectroscopy and phase-sensitive detection. The benefits of these approaches for QEXAFS were shown to be rather low, due to correlations in energy as well as R-space, which make it hardly possible to use the phase-information effectively. By considering only low orders of the modulation frequency it is possible to achieve better signal-to-noise ratios. However, similar improvements can be obtained with low pass filter approaches, which are the preferable choice in this context as they do not operate on each energy value separately, so that no correlations in energy can get lost. Nevertheless, it could be shown that modulated experiments are a promising approach to study reproducible processes, as the statistics can be improved drastically by averaging over several modulation cycles, which e.g. improves the surface sensitivity of QEXAFS.

The decomposition of Co oxalate could be studied in reducing, oxidizing and inert gas atmospheres. All non-isothermal measurements suggest a decomposition route starting with a partly separation of Co and oxalate. Towards the end of decomposition also CoO could either be detected directly or indirectly by the reaction products. For the first time, in oxidizing and inert atmospheres, it was possible to find evidences for an intermediate Co_2O_3 state, which is further reacting to Co_3O_4 as final product of the decomposition. This example well demonstrates the unique possibilities of EXAFS analysis applied to several hundred spectra, as bond lengths, bond distances as well as structural and thermal disorder can be followed in detail during complex reactions.

Layer deposition and surface reactions were investigated in situ with the QEXAFS technique in grazing-incidence reflection geometry down to the sub-second time regime for the first time. It was possible to acquire good data with a time-resolution of 100 ms/spectrum during the deposition of Cu layers on glass, using dc magnetron sputtering. Thereby, the layer structure, thickness and roughness could be determined by fitting the acquired spectra with simulated data based on the distorted-wave Born approximation. It was possible to detect a plateau in the roughness between layer thicknesses of about 2 – 3 nm, leading to the conclusion that the Cu layers rather grow in islands than in a layer-by-layer fashion on glass. It was also possible to follow the oxidation of sputtered Cu layers under defined conditions at various temperatures. Only a

few nanometers of CuO could be detected during the initial oxidation at room temperature, while a thick Cu_2O layer evolves at 150 °C. At 200 °C only a thin Cu_2O layer appears in the beginning, which starts to grow rapidly after a few hundred seconds. A model involving the roughness as crucial parameter was suggested to explain these observations, which are in good agreement with other recent studies in this field. The possibilities to rapidly measure surface processes were evaluated within these experiments and highlight the unique opportunities of this approach in surface science.

As future development for QEXAFS monochromators it is recommended to mount both a Si(111) and a Si(311) channel-cut crystal on the tilt table with an additional positioning unit to switch between both crystals. Thereafter, in combination with the flexible eccentricity it will be possible to adjust the energy range for QEXAFS spectra almost arbitrarily in an overall energy range from 4 keV to 40 keV during few seconds. Furthermore, the time-resolution of QEXAFS could be further increased in the near future even to regions below 1 ms for one spectrum. Prerequisites are new hardware developments to decrease the rise time of current amplifiers and ionization chambers, as was also evaluated within this work. The newly designed and herein presented flexible QEXAFS mechanics could be further upgraded by moving the oscillation motor with the mounted cylinder instead of the coupling piece, so that the Teflon contacts and one of the linear bearing would become obsolete. Last but not least, the data analysis software can be further extended by adding new algorithms, especially for the analysis of data measured in reflection mode.

In summary, it was shown with several application examples that QEXAFS is an invaluable tool to study time-resolved processes in physics and chemistry and materials science. With the presented hardware and software improvements it is now possible for potential users (i) to effectively acquire huge amounts of QEXAFS data in a comfortable and transparent way, and (ii) to analyze the acquired data without further programming skills. Furthermore, with the new monochromator mechanics developed in this work the QEXAFS technique can be applied in a very flexible way, as the user can now arbitrarily select the absorption edge and adjust the energy range and time-resolution. By considering all these technical advances and with respect to the also demonstrated high scientific output of beamlines with QEXAFS instrumentation, it can be expected that a growing number of users from the manifold disciplines in basic and applied material sciences will benefit from the QEXAFS method in the future.

6 Literature

[Als00] J. Als-Nielsen and D. McMorrow, *Elements of Modern X-Ray Physics*, 1st, New York, USA, Wiley (2000).

[Asc03] I. Ascone, W. Meyer-Klaucke and L. Murphy, *Experimental aspects of biological X-ray absorption spectroscopy*, J. Synchrotron Rad. **10**, 16 (2003).

[Ast07] D. Astruc, *Palladium nanoparticles as efficient green homogeneous and heterogeneous carbon−carbon coupling precatalysts: A unifying view*, Inorg. Chem. **46**, 1884 (2007).

[Aug95] R. L. Augustine and S. T. Oleary, *Heterogeneous catalysis in organic chemistry. Part 10. Effect of the catalyst support on the regiochemistry of the Heck arylation reaction*, J. Mol. Catal. A: Chem. **95**, 277 (1995).

[Aut04] A. Authier, *Dynamical Theory of X-Ray Diffraction*, New York, USA, Oxford University Press (2004).

[Bai83] A. Baiker and W. L. Holstein, *Impregnation of alumina with copper chloride-modeling of impregnation kinetics and internal copper profiles*, J. Catal. **84**, 178 (1983).

[Bak74] G. Bakcsy and A. J. Hegedüs, *Zur thermischen Zersetzung der 3d-Übergangsmetalloxalate*, Thermochim. Acta **10**, 399 (1974).

[Ban09] K. K. Bando, T. Wada, T. Miyamoto, K. Miyazaki, S. Takakusagi, T. Gott, A. Yamaguchi, M. Nomura, S. T. Oyama and K. Asakura, *Combined in situ analysis of Ni_2P/MCM-41 under hydrodesulfurization conditions – Simultaneous observation of QXAFS and FTIR –*, J. Phys. Conf. Ser. **190**, 012158 (2009).

[Bas00] L. Basini, A. Guarinoni and A. Aragno, *Molecular and temperature aspects in catalytic partial oxidation of methane*, J. Catal. **190**, 284 (2000).

[Bas01] L. Basini, K. Aasberg-Petersen, A. Guarinoni and M. Ostberg, *Catalytic partial oxidation of natural gas at elevated pressure and low residence time*, Catal. Today **64**, 9 (2001).

[Bau10] M. Bauer, G. Heusel, S. Mangold and H. Bertagnolli, *Spectroscopic set-up for simultaneous UV-Vis/(Q)EXAFS in situ and in operando studies of homogeneous reactions under laboratory conditions*, J. Synchrotron Rad. **17**, 273 (2010).

[Bau01] D. Baurecht and U. P. Fringeli, *Quantitative modulated excitation Fourier transform infrared spectroscopy*, Rev. Sci. Instrum. **72**, 3782 (2001).

[Bea74] J. H. Beaumont and M. Hart, *Multiple Bragg reflection monochromators for synchrotron X radiation*, J. Phys. E: Sci. Instrum. **7**, 823 (1974).

[Ber11] M. J. Berger, J. H. Hubbell, S. M. Seltzer, J. Chang, J. S. Coursey, R. Sukumar, D. S. Zucker and K. Olsen, *NIST XCOM: Photon Cross Sections Database*, http://www.nist.gov/pml/data/xcom/index.cfm (2011).

[Beu72] H. Beusch, D. Fieguth and E. Wicke, *Thermisch und kinetisch verursachte Instabilitäten im Reaktionsverhalten einzelner Katalysatorkörner*, Chem. Ing. Tech. **44**, 445 (1972).

[Bif01] A. Biffis, M. Zecca and M. Basato, *Metallic palladium in the Heck reaction: Active catalyst or convenient precursor?*, Eur. J. Inorg. Chem., 1131 (2001).

[Bil00] D. H. Bilderback, A. K. Freund, G. S. Knapp and D. M. Mills, *The historical development of cryogenically cooled monochromators for third-generation synchrotron radiation sources*, J. Synchrotron Rad. **7**, 53 (2000).

[Bin98] N. Binsted, *EXCURV*, CCLRC Daresbury Laboratory computer program (1998).

[Blu08] W. Blum, W. Riegler and L. Rolandi, *Particle detection with drift chambers*, Berlin, Heidelberg, Germany, Springer (2008).

[Bor80] M. Born and E. Wolf, *Principles of optics*, London, UK, Pergamon Press (1980).

[Bor99] H. Bornebusch, B. S. Clausen, G. Steffensen, D. Lützenkirchen-Hecht and R. Frahm, *A new approach for QEXAFS data acquisition*, J. Synchrotron Rad. **6**, 209 (1999).

[Boy11] B. Boyanov and C. Segre, *Farrel Lytle Database*, http://ixs.csrri.iit.edu/database/data/Farrel_Lytle_data/ (2011).

[Bri05] V. Briois, D. Lützenkirchen-Hecht, F. Villain, E. Fonda, S. Belin, B. Griesebock and R. Frahm, *Time-resolved study of the oxidation of ethanol by cerium(IV) using combined quick-XANES, UV−Vis, and Raman spectroscopies*, J. Phys. Chem. A **109**, 320 (2005).

[Bri11] V. Briois, E. Fonda, S. Belin, L. Barthe, C. La Fontaine, F. Langlois, M. Ribbens and F. Villain, *SAMBA: The 4–40 keV X-ray absorption spectroscopy beamline at SOLEIL*, EDP Sciences **UVX 2010**, 41 (2011).

[Bro98] W. A. Brown, R. Kose and D. A. King, *Femtomole Adsorption Calorimetry on Single-Crystal Surfaces*, Chem. Rev. **98**, 797 (1998).

[Bru11] Bruker EST, *Monochromator Systems | Bruker EST*, http://www.bruker-est.com/monochromator-systems.html (2011).

[Bru05] K. Bruder, P. Keil, D. Lützenkirchen-Hecht and R. Frahm, *In situ investigations of thin film formation by reactive sputtering*, Phys. Scr. **T115**, 963 (2005).

[Bür02] T. Bürgi and A. Baiker, *In situ infrared spectroscopy of catalytic solid−liquid interfaces using phase-sensitive detection: Enantioselective hydrogenation of a pyrone over Pd/TiO_2*, J. Phys. Chem. B **106**, 10649 (2002).

[Byc06] V. Y. Bychkov, Y. P. Tyulenin, V. N. Korchak and E. L. Aptekar, *Study of nickel catalyst in oscillating regime of methane oxidation by means of gravimetry and mass-spectrometry*, Appl. Catal. A **304**, 21 (2006).

[Byc07] V. Y. Bychkov, Y. P. Tyulenin, M. M. Slinko and V. N. Korchak, *Autonomous and forced oscillations during methane oxidation over cobalt catalysts*, Appl. Catal. A **321**, 180 (2007).

[Byc09] V. Y. Bychkov, Y. P. Tyulenin, M. M. Slinko, D. P. Shashkin and V. N. Korchak, *The study of the oscillatory behavior during methane oxidation over Pd catalysts*, J. Catal. **267**, 181 (2009).

[Cab48] N. Cabrera and N. F. Mott, *Theory of the oxidation of metals*, Rep. Prog. Phys. **12**, 163 (1948).

[Cam06] R. Cammack, T. Atwood, P. Campbell, H. Parish, T. Smith, J. Stirling and F. Vella, *Oxford dictionary of biochemistry and molecular biology*, 2nd ed., Oxford, USA, Oxford University Press (2006).

[Car00] C. I. Carlisle, T. Fujimoto, W. S. Sim and D. A. King, *Atomic imaging of the transition between oxygen chemisorption and oxide film growth on Ag{111}*, Surf. Sci. **470**, 15 (2000).

[Cat66] R. B. Cattell, *The scree test for the number of factors*, Multivar. Behav. Res. **1**, 245 (1966).

[Cho97] S. Cho, K. Paik and Y. Kim, *The effect of the oxidation of Cu-base leadframe on the interface adhesion between Cu metal and epoxy molding compound*, IEEE Trans.: Compon. Packag. Manuf. Technol. Part B **20**, 167 (1997).

[Cho03] I. Chorkendorff and J. W. Niemantsverdriet, *Concepts of modern catalysis and kinetics*, Weinheim, Germany, WILEY-VCH (2003).

[Cla98] B. S. Clausen, H. Topsøe and R. Frahm, *Application of combined X-ray diffraction and absorption techniques for in situ catalyst characterization*, Adv. Catal. **42**, 315 (1998).

[Cla00] B. S. Clausen and J. K. Nørskov, *Asymmetric pair distribution functions in catalysts*, Top. Catal. **10**, 221 (2000).

[Coe93] A. Coetzee, D. J. Eve and M. E. Brown, *Thermal analysis of some mixed metal oxalates*, J. Therm. Anal. **39**, 947 (1993).

[Coe94] A. Coetzee, M. E. Brown, D. J. Eve and C. A. Strydom, *Kinetics of the thermal dehydrations and decompositions of some mixed metal oxalates*, J. Therm. Analysis and Calorimetry **41**, 357 (1994).

[Col87] N. A. Collins, S. Sundaresan and Y. J. Chabal, *Studies on self-sustained reaction-rate oscillations: III. The carbon model*, Surf. Sci. **180**, 136 (1987).

[Dal11] D. Dalle Nogare, N. J. Degenstein, R. Horn, P. Canu and L. D. Schmidt, *Modeling spatially resolved data of methane catalytic partial oxidation on Rh foam catalyst at different inlet compositions and flowrates*, J. Catal. **277**, 134 (2011).

[Dan96] S. J. Danishefsky, J. J. Masters, W. B. Young, J. T. Link, L. B. Snyder, T. V. Magee, D. K. Jung, R. C. A. Isaacs, W. G. Bornmann, C. A. Alaimo, C. A. Coburn and M. J. Di Grandi, *Total synthesis of Baccatin III and Taxol*, J. Am. Chem. Soc. **118**, 2843 (1996).

[Dat06] Data Translation GmbH, *DT – Open Layers for.NET – Class Library – User´s Manual*, Data Translation Document Number: UM-22161-B (2006).

[deB91] D. K. G. de Boer, *Glancing-incidence X-ray fluorescence of layered materials*, Phys. Rev. B **44**, 498 (1991).

[deB94] D. K. G. de Boer, *Influence of the roughness profile on the specular reflectivity of X-rays and neutrons*, Phys. Rev. B **49**, 5817 (1994).

[deV06] J. G. de Vries, *A unifying mechanism for all high-temperature Heck reactions. The role of palladium colloids and anionic species*, Dalton Trans., 421 (2006).

[Dem08] O. Demoulin, B. Le Clef, M. Navez and P. Ruiz, *Combustion of methane, ethane and propane and of mixtures of methane with ethane or propane on Pd/γ-Al_2O_3 catalysts*, Appl. Catal. A **344**, 1 (2008).

[Den99] Y. Deng and T. G. Nevell, *Oscillations of methane combustion over alumina-supported palladium catalysts under oxygen-deficient conditions*, J. Mol. Catal. A **142**, 51 (1999).

[Den95] A. J. Dent, M. Oversluizen, G. N. Greaves, M. A. Roberts, G. Sankar, C. R. A. Catlow and J. M. Thomas, *A furnace design for use in combined X-ray absorption and diffraction up to a temperature of 1200°C: Study of cordierite ceramic formation using fluorescence QEXAFS/XRD*, Physica B **208-209**, 253 (1995).

[Den02] A. J. Dent, *Development of time-resolved XAFS instrumentation for quick EXAFS and energy-dispersive EXAFS measurements on catalytic systems*, Top. Catal. **18**, 27 (2002).

[Dil84] W. R. Dillon and M. Goldstein, *Multivariate analysis: Methods and applications*, New York, United States, John Wiley & Sons (1984).

[Dol87] D. Dollimore, *The thermal decomposition of oxalates. A review*, Thermochim. Acta **117**, 331 (1987).

[Eas05] J. A. Eastman, P. H. Fuss, L. E. Rehn, P. M. Baldo, G. W. Zhou, D. D. Fong and L. J. Thompson, *Early-stage suppression of Cu(001) oxidation*, Appl. Phys. Lett. **87**, 051914 (2005).

[Eis86] M. Eiswirth and G. Ertl, *Kinetic oscillations in the catalytic CO oxidation on a Pt(110) surface*, Surf. Sci. **177**, 90 (1986).

[Ert67a] G. Ertl, *Untersuchung von Oberflächenreaktionen an Kupfer mittels Beugung langsamer Elektronen (LEED) - Teil 1*, Surf. Sci. **6**, 208 (1967).

[Ert67b] G. Ertl, *Untersuchung von Oberflächenreaktionen an Kupfer mittels Beugung langsamer Elektronen (LEED) - Teil 2*, Surf. Sci. **7**, 309 (1967).

[Ert82] G. Ertl, P. R. Norton and J. Rüstig, *Kinetic oscillations in the platinum-catalyzed oxidation of Co*, Phys. Rev. Lett. **49**, 177 (1982).

[Ert08] G. Ertl, *Reactions at surfaces: From atoms to complexity (Nobel lecture)*, Angew. Chem. Int. Ed. **47**, 3524 (2008).

[Far99] R. J. Farrauto and R. M. Heck, *Catalytic converters: state of the art and perspectives*, Catal. Today **51**, 351 (1999).

[Fay92] M. J. Fay, A. Proctor, D. P. Hoffmann, M. Houalla and D. M. Hercules, *Determination of the Mo surface environment of Mo/TiO_2 catalysts by EXAFS, XANES and PCA*, Mikrochim. Acta **109**, 281 (1992).

[Fer95] M. Fernández-García, C. Márquez and G. L. Haller, *XANES-TPR study of Cu-Pd bimetallic catalysts: Application of factor analysis*, J. Phys. Chem. **99**, 12565 (1995).

[Fer10] D. Ferri, M. S. Kumar, R. Wirz, A. Eyssler, O. Korsak, P. Hug, A. Weidenkaff and M. A. Newton, *First steps in combining modulation excitation spectroscopy with synchronous dispersive EXAFS/DRIFTS/mass spectrometry for in situ time resolved study of heterogeneous catalysts*, Phys. Chem. Chem. Phys. **12**, 5634 (2010).

[Fer11] D. Ferri, M. A. Newton and M. Nachtegaal, *Modulation excitation X-ray absorption spectroscopy to probe surface species on heterogeneous catalysts*, Top. Catal. **54**, 1070 (2011).

[Fle09] U. Flechsig, A. Jaggi, S. Spielmann, H. A. Padmore and A. A. MacDowell, *The optics beamline at the Swiss Light Source*, Nucl. Instrum. Methods Phys. Res. A **609**, 281 (2009).

[FMB07] FMB Oxford Ltd., *FMB Oxford - Catalogue Download - Ion Chambers - Page 5: IC Spec Ionisation Chamber*, http://www.fmb-oxford.com/page.php?page=3 (2009).

[Föt11] K. Föttinger, J. A. van Bokhoven, M. Nachtegaal and G. Rupprechter, *Dynamic structure of a working methanol steam reforming catalyst: In situ quick-EXAFS on Pd/ZnO nanoparticles*, J. Phys. Chem. Lett. **2**, 428 (2011).

[Fra88] R. Frahm, *Quick scanning EXAFS: First experiments*, Nucl. Instrum. Meth. A **270**, 578 (1988).

[Fra89] R. Frahm, *New method for time dependent X-ray absorption studies*, Rev. Sci. Instrum. **60**, 2515 (1989).

[Fra91] R. Frahm, T. W. Barbee Jr. and W. Warburton, *In situ structural study of thin-film growth by quick-scanning X-ray absorption spectroscopy*, Phys. Rev. B **44**, 2822 (1991).

[Fra92] R. Frahm, J. Wong, J. B. Holt, E. M. Larson, B. Rupp and P. A. Waide, *Real-time probe of reaction centers in solid combustions on the subsecond time scale*, Phys. Rev. B **46**, 9205 (1992).

[Fra04] R. Frahm, B. Griesebock, M. Richwin and D. Lützenkirchen-Hecht, *Status and new applications of time-resolved X-ray absorption spectroscopy*, AIP Conf. Proc. **705**, 1411 (2004).

[Fra05] R. Frahm, M. Richwin and D. Lützenkirchen-Hecht, *Recent advances and new applications of time-resolved X-ray absorption spectroscopy*, Phys. Scr. **T115**, 974 (2005).

[Fra09a] R. Frahm, M. Nachtegaal, J. Stötzel, M. Harfouche, J. A. van Bokhoven and J.-D. Grunwaldt, *The dedicated QEXAFS facility at the SLS: Performance and scientific opportunities*, AIP Conf. Proc. **1234**, 251 (2009).

[Fra09b] R. Frahm, J. Stötzel and D. Lützenkirchen-Hecht, *Advancing time-resolved methods in monitoring and characterization of catalysts*, Synchrotron Rad. News **22 No. 2**, 6 (2009).

[Fra09c] R. Frahm, D. Lützenkirchen-Hecht, M. Jentschel, W. Urban, J. Krempel and K. Schreckenbach, *Positron-Electron Pair Creation Near Threshold*, AIP Conf. Proc. **1090**, 554 (2009).

[Fra49] F. C. Frank and J. H. van der Merwe, *One-dimensional dislocations*, Proc. R. Soc. London, Ser. A **198**, 205 (1949).

[Fuj09] T. Fujimori, M. Takaoka, Y. Tanino, K. Oshita and S. Morisawa, *A metal mixture lowers the reaction temperature of copper chloride as shown using in situ quick XAFS*, J. Phys. Conf. Ser. **190**, 012183 (2009).

[Fuj57] J. Fujita, K. Nakamoto and M. Kaboyashi, *Infrared spectra of metallic complexes. III. The infrared spectra of metallic oxalates*, J. Phys. Chem. **61**, 1014 (1957).

[Gni05] A. Gniewek, A. M. Trzeciak, J. J. Ziolkowski, L. Kepinski, J. Wrzyszcz and W. Tylus, *Pd-PVP colloid as catalyst for Heck and carbonylation reactions: TEM and XPS studies*, J. Catal. **229**, 332 (2005).

[Gol11] R. Golovchak, A. Kovalskiy, O. Shpotyuk and J. Himanshu, *In search of energy landscape for network glasses*, Appl. Phys. Lett. **98**, 171905 (2011).

[Gra99] G. W. Graham, D. König, B. D. Poindexter, J. T. Remillard and W. H. Weber, *Ellipsometric study of a palladium catalyst during the oxidation of carbon monoxide and methane*, Top. Catal. **8**, 35 (1999).

[Gru00] J.-D. Grunwaldt, A. M. Molenbroek, N.-Y. Topsøe, H. Topsøe and B. S. Clausen, *In situ investigations of structural changes in Cu/ZnO catalysts*, J. Catal. **194**, 452 (2000).

[Gru01a] J.-D. Grunwaldt, D. Lützenkirchen-Hecht, M. Richwin, S. Grundmann, B. S. Clausen and R. Frahm, *Piezo X-ray absorption spectroscopy for the investigation of solid-state transformations in the millisecond range*, J. Phys. Chem. B **105**, 5161 (2001).

[Gru01b] J.-D. Grunwaldt, P. Kappen, B. S. Hammershøj, L. Tröger and B. S. Clausen, *Fluorescence EXAFS for the in situ study on the state of promotors in catalysis*, J. Synchrotron Rad. **8**, 572 (2001).

[Gru01c] J.-D. Grunwaldt, L. Basini and B. S. Clausen, *In situ EXAFS study of Rh/Al_2O_3 catalysts for catalytic partial oxidation of methane*, J. Catal. **200**, 321 (2001).

[Gru04] J.-D. Grunwaldt, M. Caravati, S. Hannemann and A. Baiker, *X-ray absorption spectroscopy under reaction conditions: Suitability of different reaction cells for combined catalyst characterization and time-resolved studies*, Phys. Chem. Chem. Phys. **6**, 3037 (2004).

[Gru05a] J.-D. Grunwaldt, M. Ramin, M. Rohr, A. Michailovski, G. R. Patzke and A. Baiker, *High pressure in situ X-ray absorption spectroscopy cell for studying simultaneously the liquid phase and the solid/liquid interface*, Rev. Sci. Instrum. **76**, 054104 (2005).

[Gru05b] J.-D. Grunwaldt and A. Baiker, *Axial variation of the oxidation state of Pt-Rh/Al_2O_3 during partial methane oxidation in a fixed-bed reactor: An in situ X-ray absorption spectroscopy study*, Catal. Lett. **99**, 5 (2005).

[Gru07] J.-D. Grunwaldt, N. van Vegten and A. Baiker, *Insight into the structure of supported palladium catalysts during the total oxidation of methane*, Chem. Commun., 4635 (2007).

[Gru09a] J.-D. Grunwaldt, M. Beier, B. Kimmerle, A. Baiker, M. Nachtegaal, B. Griesebock, D. Lützenkirchen-Hecht, J. Stötzel and R. Frahm, *Structural changes of noble metal catalysts during ignition and extinction of the partial oxidation of methane studied by advanced QEXAFS techniques*, Phys. Chem. Chem. Phys. **11**, 8779 (2009).

[Gru09b] J.-D. Grunwaldt, B. Kimmerle, A. Baiker, P. Boye, C. G. Schroer, P. Glatzel, C. N. Borca and F. Beckmann, *Catalysts at work: From integral to spatially resolved X-ray absorption spectroscopy*, Catal. Today **145**, 267 (2009).

[Gru10] J.-D. Grunwaldt and C. G. Schroer, *Hard and soft X-ray microscopy and tomography in catalysis: Bridging the different time and length scales*, Chem. Soc. Rev. **39**, 4741 (2010).

[Gru97] M. Gruyters and D. A. King, *Effects of restructuring in adsorption and reactiondynamics at metal surfaces*, J. Chem. Soc., Faraday Trans. **93**, 2947 (1997).

[Gus04] J. Gustafson, A. Mikkelsen, M. Borg, E. Lundgren, L. Köhler, G. Kresse, M. Schmid, P. Varga, J. Yuhara, X. Torrelles, C. Quirós and J. N. Andersen, *Self-limited growth of a thin oxide layer on Rh(111)*, Phys. Rev. Lett. **92**, 126102 (2004).

[Hag89] M. Hagelstein, S. Cunis, R. Frahm, W. Niemann and P. Rabe, *The energy dispersive X-ray absorption spectrometer DEXAFS at HASYLAB*, Physica B **158**, 324 (1989).

[Han07] S. Hannemann, J.-D. Grunwaldt, P. Lienemann, D. Gunther, F. Krumeich, S. E. Pratsinis and A. Baiker, *Combination of flame synthesis and high-throughput experimentation: The preparation of alumina-supported noble metal particles and their application in the partial oxidation of methane*, Appl. Catal. A **316**, 226 (2007).

[Han02] P. L. Hansen, J. B. Wagner, S. Helveg, J. R. Rostrup-Nielsen, B. S. Clausen and H. Topsøe, *Atom-resolved imaging of dynamic shape changes in supported copper nanocrystals*, Science **295**, 2053 (2002).

[Har11] M. Hartmann, L. Maier and O. Deutschmann, *Hydrogen production by catalytic partial oxidation of iso-octane at varying flow rate and fuel/oxygen ratio: From detailed kinetics to reactor behavior*, Appl. Catal. A **391**, 144 (2011).

[Hau05] M. Haumann, P. Liebisch, C. Müller, M. Barra, M. Grabolle and H. Dau, *Photosynthetic O_2 formation tracked by time-resolved X-ray experiments*, Science **310**, 1019 (2005).

[Hay04] J. C. Hayton, D. G. Allen and V. Scarpello, *Factor retention decisions in exploratory factor analysis: A tutorial on parallel analysis*, Organizational Research Methods **7**, 191 (2004).

[Hec96] D. Hecht, R. Frahm and H.-H. Strehblow, *Quick-scanning EXAFS in the reflection mode as a probe for structural information with time resolution: A study of anodic silver oxide layers*, J. Phys. Chem. **100**, 10831 (1996).

[Hec97] D. Hecht, *Oberflächenanalytische und röntgenabsorptionsspektroskopische Untersuchungen zur Adsorption und Deckschichtbildung auf Ag-Elektroden*, Heinrich-Heine Universität Düsseldorf, Düsseldorf, doctoral thesis (1997).

[Hec68] R. F. Heck, *Acylation, methylation, and carboxyalkylation of olefins by Group VIII metal derivatives*, J. Am. Chem. Soc. **90**, 5518 (1968).

[Hen10] B. L. M. Hendriksen, M. D. Ackermann, R. van Rijn, D. Stoltz, I. Popa, O. Balmes, A. Resta, D. Wermeille, R. Felici, S. Ferrer and J. W. M. Frenken, *The role of steps in surface catalysis and reaction oscillations*, Nature Chemistry **2**, 730 (2010).

[Hol93] V. Holý, J. Kubéna, I. Ohlídal, K. Lischka and W. Plotz, *X-ray reflection from rough layered systems*, Phys. Rev. B **47**, 15896 (1993).

[Hol94] V. Holý and T. Baumbach, *Nonspecular X-ray reflection from rough multilayers*, Phys. Rev. B **49**, 10668 (1994).

[Hon93] C. Y. Hong, N. Kado and L. E. Overman, *Asymmetric synthesis of either enantiomer of opium alkaloids and morphinans. Total synthesis of (-)- and (+)-dihydrocodeinone and (-)- and (+)-morphine*, J. Am. Chem. Soc. **115**, 11028 (1993).

[Hon05] K. Honkala, A. Hellman, I. N. Remediakis, A. Logadottir, A. Carlsson, S. Dahl, C. H. Christensen and J. K. Nørskov, *Ammonia synthesis from first-principles calculations*, Science **307**, 555 (2005).

[Hor65] J. L. Horn, *A rationale and test for the number of factors in factor analysis*, Psychometrika **30**, 179 (1965).

[Hot98] I. Hotovy, J. Huran, J. Janik and A. P. Kobzev, *Deposition and properties of nickel oxide films produced by DC reactive magnetron sputtering*, Vacuum **51**, 157 (1998).

[IFE11] The University of Chicago, *Documentation IFEFFIT*, http://cars9.uchicago.edu/ifeffit/Documentation (2011).

[Igl11] A. Iglesias-Juez, A. Kubacka, M. Fernández-García, M. Di Michiel and M. A. Newton, *Nanoparticulate Pd supported catalysts: Size-dependent formation of Pd(I)/Pd(0) and their role in CO elimination*, J. Am. Chem. Soc. **133**, 4484 (2011).

[Imb95] R. Imbihl and G. Ertl, *Oscillatory kinetics in heterogeneous catalysis*, Chem. Rev. **95**, 697 (1995).

[Imb08] R. Imbihl, *Handbook of surface science - Chapter 9*, Amsterdam, Netherlands, Elsevier (2008).

[Jac06] J. D. Jackson, *Klassische Elektrodynamik*, 4th ed., Berlin, Germany, de Gruyter (2006).

[Jam67] R. W. James, *The optical principles of X-ray diffraction*, Ithaca, New York, USA, Cornell University Press (1967).

[JCh07] JChampion, *The Code Project*, http://www.codeproject.com/KB/graphics/zedgraph.aspx (2007).

[Jen11] M. Jentschel, W. Urban, P. Mutti, P. Courtois, G. S. Simpson and R. Frahm, *Measurements of the pair production cross section close to the threshold energy*, Phys. Rev. C **84**, 052501 (2011).

[Jen99] A. Jentys, *Estimation of mean size and shape of small metal particles by EXAFS*, Phys. Chem. Chem. Phys. **1**, 4059 (1999).

[Joh04] V. Johánek, M. Laurin, A. W. Grant, B. Kasemo, C. R. Henry and J. Libuda, *Fluctuations and bistabilities on catalyst nanoparticles*, Science **304**, 1639 (2004).

[Jos07] J. Joseph, V. Mathew and K. E. Abraham, *Studies on Cu, Fe, and Mn doped SnO_2 semi-conducting transparent films prepared by a vapour deposition technique*, Chin. J. Phys. **45**, 84 (2007).

[Kah97] M. J. Kahlich, H. A. Gasteiger and R. J. Behm, *Kinetics of the selective CO oxidation in H_2-rich gas on Pt/Al_2O_3*, J. Catal. **171**, 93 (1997).

[Kal10] E. E. Kalu, R. Bell and M. Dupree, *Improvement of the corrosion behavior of electrodeposited CoFeCu thin films*, Mater. Chem. Phys. **124**, 689 (2010).

[Kam02] K.-D. Kammeyer and K. Kroschel, *Digitale Signalverarbeitung*, 5th ed., Stuttgart, Leipzig, Wiesbaden, Germany, B. G. Teubner (2002).

[Kan90] K. Kaneda, M. Higuchi and T. Imanaka, *Highly dispersed Pd on MgO as catalyst for activation of phenyl-chlorine bonds leading to carbon-carbon bond formation*, J. Mol. Catal. **63**, L33 (1990).

[Kap01] P. Kappen, J.-D. Grunwaldt, B. S. Hammershøj, L. Tröger, G. Materlik and B. S. Clausen, *The state of Cu promoter atoms in high-temperature shift catalysts—An in situ fluorescence XAFS study*, J. Catal. **198**, 56 (2001).

[Kat09] K. Kato, K. Okumura, T. Sanada, T. Murakami, S. Ito and M. Niwa, *In situ Quick XAFS studies on the structure of Rh supported on zeolites*, J. Phys. Conf. Ser. **190**, 012170 (2009).

[Kei06] Keithley Instruments Inc., *KUSB-3116 - User´s Manual*, Keithley Instruments Document Number: KUSB3116-900-01 Rev. D (2006).

[Kei05] P. Keil, *Neue Methoden oberflächenempfindlicher Röntgenabsorptions-spektroskopie bei streifendem Einfall*, Bergische Universität Wuppertal, doctoral thesis (2005).

[Kei10] P. Keil, R. Frahm and D. Lützenkirchen-Hecht, *Native oxidation of sputter deposited polycrystalline copper thin films during short and long exposure times: Comparative investigation by specular and non-specular grazing incidence X-ray absorption spectroscopy*, Corros. Sci. **52**, 1305 (2010).

[Kei99] Keithley Instruments Inc., *Model 428 Current Amplifier*, 4th printing, Cleveland (1999).

[Kes74] O. Keski-Rahkomen and M. O. Krause, *Total and partial atomic-level widths*, At. Data Nucl. Data Tables **14**, 139 (1974).

[Kha10] S. Khalid, W. Caliebe, P. Siddons, I. So, B. Clay, T. Lenhard, J. Hanson, Q. Wang, A. I. Frenkel, N. Marinkovic, N. Hould, M. Ginder-Vogel, G. L. Landrot, D. L. Sparks and A. Ganjoo, *Quick extended X-ray absorption fine structure instrument with millisecond time scale, optimized for in situ applications*, Rev. Sci. Instrum. **81**, 015105 (2010).

[Kim09] B. Kimmerle, J.-D. Grunwaldt, A. Baiker, P. Glatzel, P. Boye, S. Stephan and C. G. Schroer, *Visualizing a catalyst at work during the ignition of the catalytic partial oxidation of methane*, J. Phys. Chem. C **113**, 3037 (2009).

[Kim10] B. Kimmerle, A. Baiker and J.-D. Grunwaldt, *Oscillatory behaviour of catalytic properties, structure and temperature during the catalytic partial oxidation of methane on Pd/Al_2O_3*, Phys. Chem. Chem. Phys. **12**, 2288 (2010).

[Kit05] C. Kittel, *Introduction to solid state physics*, 8th ed., New York, USA, John Wiley & Sons (2005).

[Kle08] W. Kleist, S. S. Pröckl and K. Köhler, *Heck reactions of aryl chlorides catalyzed by ligand free palladium salts*, Catal. Lett. **125**, 197 (2008).

[Kli08] J. Klikovits, M. Schmid, L. R. Merte, P. Varga, R. Westerström, A. Resta, J. N. Andersen, J. Gustafson, A. Mikkelsen, E. Lundgren, F. Mittendorfer and G. Kresse, *Step-orientation-dependent oxidation: From 1D to 2D oxides*, Phys. Rev. Lett. **101**, 266104 (2008).

[Kno00] G. F. Knoll, *Radiation detection and measurement*, 3rd ed., New York, USA, Wiley (2000).

[Köh06] K. Köhler, S. S. Pröckl and W. Kleist, *Supported palladium catalysts in Heck coupling reactions - Problems, potential and recent advances*, Curr. Org. Chem. **10**, 1585 (2006).

[Köh07] K. Köhler, W. Kleist and S. S. Pröckl, *Genesis of coordinatively unsaturated palladium complexes dissolved from solid precursors during Heck coupling reactions and their role as catalytically active species*, Inorg. Chem. **46**, 1876 (2007).

[Kön94] D. König, W. H. Weber, B. D. Poindexter, J. R. Mcbride, G. W. Graham and K. Otto, *In situ ellipsometric study of a palladium catalyst during the oxidation of methane*, Catal. Lett. **29**, 329 (1994).

[Kon88] D. C. Koningsberger and R. Prins, *X-Ray absorption: Principles, applications, techniques of EXAFS, SEXAFS and XANES*, New York, USA, Wiley (1988).

[Kon00] D. C. Koningsberger, B. L. Mojet, G. E. van Dorssen and D. E. Ramaker, *XAFS spectroscopy: Fundamental principles and data analysis*, Top. Catal. **10**, 143 (2000).

[Kro91] H. Kronmüller, *Digitale Signalverarbeitung: Grundlagen, Theorie, Anwendungen in der Automatisierungstechnik*, Berlin, Heidelberg, New York, Germany, Springer (1991).

[Lab07] J.-C. Labiche, O. Mathon, S. Pascarelli, M. A. Newton, G. G. Ferre, C. Curfs, G. Vaughan, A. Horns and D. F. Carreiras, *Invited article: The fast readout low noise camera as a versatile X-ray detector for time resolved dispersive extended X-ray absorption fine structure and diffraction studies of dynamic problems in materials science, chemistry, and catalysis*, Rev. Sci. Instrum. **78**, 091301 (2007).

[Lah08] K. Lahtonen, M. Hirsimaki, M. Lampimaki and M. Valden, *Oxygen adsorption-induced nanostructures and island formation on Cu{100}: Bridging the gap between the formation of surface confined oxygen chemisorption layer and oxide formation*, J. Chem. Phys. **2008**, 124703 (2008).

[Lan06] E. Lanthier, C. Reber and T. Carrington Jr., *Vibronic coupling in square planar complexes of palladium(II) and platinum(II)*, Chem. Phys. **329**, 90 (2006).

[Lee77] P. A. Lee and G. Beni, *New method for the calculation of atomic phase shifts: Application to extended x-ray absorption fine structure (EXAFS) in molecules and crystals*, Phys. Rev. B **15**, 2862 (1977).

[Lee81] P. A. Lee, P. H. Citrin, P. Eisenberger and B. M. Kincaid, *Extended x-ray absorption fine structure - its strengths and limitations as a structural tool*, Rev. Mod. Phys. **53**, 769 (1981).

[Lee94] W.-K. Lee and D. M. Mills, *High heat load X-ray optics research and development at the Advanced Photon Source - an overview*, Nucl. Instrum. Meth. A **347**, 618 (1994).

[Len99] B. Lengeler, C. G. Schroer, J. Tümmler, B. Benner, M. Richwin, A. Snigirev, I. Snigireva and M. Drakopoulus, *Imaging by parabolic refractive lenses in the hard X-ray range*, J. Synchrotron Rad. **6**, 1153 (1999).

[Len01] B. Lengeler, C. G. Schroer, B. Benner, T. F. Günzler, M. Kuhlmann, J. Tümmler, A. S. Simionovici, M. Drakopoulos, A. Snigirev and I. Snigireva, *Parabolic refractive X-ray lenses: A breakthrough in X-ray optics*, Nucl. Instrum. Methods Phys. Res., Sect. A **467-468**, 944 (2001).

[LiG95] G. G. Li, F. Bridges and C. H. Booth, *X-ray-absorption fine-structure standards: A comparison of experiment and theory*, Phys. Rev. B **52**, 6332 (1995).

[Lim08] S. H. Lim, N. Phonthammachai, T. Liu and T. J. White, *X-ray absorption spectroscopy studies of phase transformations and amorphicity in nanotitania powder and silica-titania core-shell photocatalysts*, J. Appl. Crystallogr. **41**, 1009 (2008).

[Liu90] X. Liu and C. T. Prewitt, *High-temperature X-ray diffraction study of Co_3O_4: Transition from normal to disordered spinel*, Phys. Chem. Miner. **17**, 168 (1990).

[Lop04] N. Lopez, J. K. Nørskov, T. V. W. Janssens, A. Carlsson, A. Puig-Molina, B. S. Clausen and J.-D. Grunwaldt, *The adhesion and shape of nanosized Au particles in a Au/TiO_2 catalyst*, J. Catal. **225**, 86 (2004).

[Lüt01] D. Lützenkirchen-Hecht, S. Grundmann and R. Frahm, *Piezo-QEXAFS with fluorescence detection: fast time-resolved investigations of dilute specimens*, J. Synchrotron Rad. **8**, 6 (2001).

[Lüt05a] D. Lützenkirchen-Hecht, J.-D. Grunwaldt, M. Richwin, B. Griesebock, A. Baiker and R. Frahm, *Monitoring of fast transformations in solid state chemistry and heterogeneous catalysis by QEXAFS in the second scale*, Phys. Scr. **T115**, 831 (2005).

[Lüt05b] D. Lützenkirchen-Hecht and R. Frahm, *Structure of reactively sputter deposited tin-nitride thin films: A combined X-ray photoelectron spectroscopy, in situ X-ray reflectivity and X-ray absorption spectroscopy study*, Thin Solid Films **493**, 67 (2005).

[Lüt06] D. Lützenkirchen-Hecht and R. Frahm, *Time-resolved in situ investigations of reactive sputtering processes by grazing incidence X-ray absorption spectroscopy*, Surf. Sci. **600**, 4380 (2006).

[Lüt09] D. Lützenkirchen-Hecht, R. Wagner, U. Haake, A. Watenphul and R. Frahm, *The materials science X-ray beamline BL8 at the DELTA storage ring*, J. Synchrotron Rad. **16**, 1 (2009).

[Lun04] E. Lundgren, J. Gustafson, A. Mikkelsen, J. N. Andersen, A. Stierle, H. Dosch, M. Todorova, J. Rogal, K. Reuter and M. Scheffler, *Kinetic hindrance during the initial oxidation of Pd(100) at ambient pressures*, Phys. Rev. Lett. **92**, 046101 (2004).

[Lun06] E. Lundgren, A. Mikkelsen, J. N. Andersen, G. Kresse, M. Schmid and P. Varga, *Surface oxides on close-packed surfaces of late transition metals*, J. Phys. Condens. Matter **18**, R481 (2006).

[Lyt65] F. Lytle, *Physics of non-crystalline solids*, Amsterdam, North Holland, Prins, J. (1965).

[Mac00] M. Maciejewski, E. Ingier-Stocka, W.-D. Emmerich and A. Baiker, *Monitoring of the gas phase composition: A prerequisite for unravelling the mechanism of decomposition of solids. Thermal decomposition of cobalt oxalate dihydrate*, J. Therm. Anal. Calorim. **60**, 735 (2000).

[Mac62] A. L. Mackay, *A dense non-crystallographic packing of equal spheres*, Acta Crystallogr. **15**, 916 (1962).

[Maj08] S. Majumdar, I. G. Sharma, A. C. Bidaye and A. K. Suri, *A study on isothermal kinetics of thermal decomposition of cobalt oxalate to cobalt*, Thermochim. Acta **473**, 45 (2008).

[Mal02] B. Małecka, E. Drożdż-Cieśla and A. Małecki, *Non-isothermal studies on mechanism and kinetics of thermal decomposition of cobalt(II) oxalate dihydrate*, J. Therm. Anal. Calorim. **68**, 819 (2002).

[Mar97] P. Marcus and C. Hinnen, *XPS study of the early stages of deposition of Ni, Cu and Pt on HOPG*, Surf. Sci. **392**, 134 (1997).

[Mar05] P. Marcus and F. B. Mansfeld, *Analytical methods in corrosion science and engineering*, Baton Rouge, Florida, USA, CRC Press (2005).

[Mar54] P. Mars and D. W. van Krevelen, *Oxidation carried out by means of vanadium oxide catalysts*, Chem. Eng. Sci. Spec. Suppl. **3**, 41 (1954).

[Mar75] D. S. Martin Jr., J. L. Bonte, R. M. Rush and R. A. Jacobson, *Potassium tetrabromopalladate(II)*, Acta Cryst. B **31**, 2538 (1975).

[Mar04] M. Martin, U. Koops and N. Lakshmi, *Reactivity of solids studied by in situ XAS and XRD*, Solid State Ionics, Diffusion & Reactions **172**, 357 (2004).

[Mar07] M. Martin, N. Lakshmi, U. Koops and H.-I. Yoo, *In situ investigations on the oxidation of metals*, Z. Phys. Chem. **221**, 1499 (2007).

[Mar09] M. Marton, E. Zdravecká, M. Vojs, T. Ižák, M. Veselý, R. Redhammer, M. Varga and A. Šatka, *Study of adhesion of carbon nitride thin films on medical alloy substrates*, Vacuum **84**, 65 (2009).

[Mat80] T. Matsushita and U. Kaminaga, *A systematic method of estimating the performance of X-ray optical systems for synchrotron radiation. I. Description of various optical elements in position-angle space for ideally monochromatic X-rays*, J. Appl. Crystallogr. **13**, 465 (1980).

[Mat81] T. Matsushita and R. P. Phizackerley, *A fast X-ray absorption spectrometer for use with synchrotron radiation*, Jpn. J. Appl. Phys. **20**, 2223 (1981).

[McC93a] J. A. McCaulley, *Temperature dependence of the Pd K-edge extended x-ray-absorption fine structure of PdC_x ($x \sim 0.13$)*, Phys. Rev. B **47**, 4873 (1993).

[McC93b] J. A. McCaulley, *In-situ X-ray absorption spectroscopy studies of hydride and carbide formation in supported palladium catalysts*, J. Phys. Chem. **97**, 10372 (1993).

[Mic10] Microsoft Corporation, *Free Developer Tools - Visual Studio 2010 Express | Microsoft Visual Studio*, http://www.microsoft.com/visualstudio/en-us/products/2010-editions/express (2010).

[Mic05] A. Michailovski, J.-D. Grunwaldt, A. Baiker, R. Kiebach, W. Bensch and G. R. Patzke, *Studying the solvothermal formation of MoO_3 fibers by complementary in situ EXAFS/EDXRD techniques*, Angew. Chem. Int. Ed. **44**, 5643 (2005).

[Mül10] O. Müller, *Ion chambers for time resolved X-ray absorption spectroscopy*, Bergische Universität Wuppertal, dipoma thesis (2010).

[Mur95] L. M. Murphy, B. R. Dobson, M. Neu, C. A. Ramsdale, R. W. Strange and S. S. Hasnain, *Quick fluorescence-EXAFS: An improved method for collection of conventional XAFS data, an improved method for collection of conventional XAFS data and for studying reaction intermediates in dilute systems*, J. Synchrotron Rad. **2**, 64 (1995).

[Nau96] D. Y. Naumov, N. V. Podberezskaya, E. V. Boldyreva and A. V. Virovets, *Crystal-chemical analysis of the structures of oxalic acid and its salts $M_x(C_2O_4)_y \cdot nH_2O$ (n=0−3)*, J. Struct. Chem. **37**, 480 (1996).

[Név80] L. Névot and P. Croce, *Charactérisation de surfaces par réflexion rasante rayons X. Application á l'étude du polissage de quelque verres silicates*, Rev. Phys. Appl. **15**, 761 (1980).

[New02] M. A. Newton, A. J. Dent and J. Evans, *Bringing time resolution to EXAFS: Recent developments and application to chemical systems*, Chem. Soc. Rev. **31**, 83 (2002).

[New07] M. A. Newton, C. Belver-Coldeira, A. Martínez-Arias and M. Fernández-García, *Dynamic in situ observation of rapid size and shape change of supported Pd nanoparticles during CO/NO cycling*, Nat. Mater. **6**, 528 (2007).

[New10] M. A. Newton, M. Di Michiel, A. Kubacka and M. Fernández-Garciá, *Combining time-resolved hard X-ray diffraction and diffuse reflectance infrared spectroscopy to illuminate CO dissociation and transient carbon storage by supported Pd nanoparticles during CO/NO cycling*, J. Am. Chem. Soc. **132**, 4540 (2010).

[New01] M. Newville, *IFEFFIT: Interactive XAFS analysis and FEFF fitting*, J. Synchrotron Rad. **8**, 322 (2001).

[Nik91] A. K. Nikumbh, A. E. Athare and V. B. Raut, *A study of the thermal decomposition of cobalt(II) and nickel(II) oxalate dihydrate using direct current electrical conductivity measurements*, Thermochim. Acta **186**, 217 (1991).

[Nob10] The Royal Swedish Academy of Science, *The Nobel Prize in Chemistry 2010 - Illustrated Information*, http://nobelprize.org (2010).

[Nol08] P. Nolte, A. Stierle, N. Y. Jin-Phillipp, N. Kasper, T. U. Schulli and H. Dosch, *Shape changes of supported Rh nanoparticles during oxidation and reduction cycles*, Science **321**, 1654 (2008).

[ORe95] M. O´Reilly, X. Jiang, J. T. Beechinor, S. Lynch, C. Ní Dheasuna, J. C. Patterson and G. M. Crean, *Investigation of the oxidation behaviour of thin film and bulk copper*, Appl. Surf. Sci. **91**, 152 (1995).

[Oes09] M. Oestreich, *The Mizoroki-Heck reaction*, Chichester, UK, John Wiley & Sons (2009).

[Oku08] K. Okumura, T. Honma, S. Hirayama, T. Sanada and M. Niwa, *Stepwise growth of Pd clusters in USY zeolite at room temperature analyzed by QXAFS*, J. Phys. Chem. C **112**, 16740 (2008).

[Oll12] I. Olliges-Stadler, J. Stötzel, D. Koziej, M. D. Rossell, J.-D. Grunwaldt, R. Frahm and M. Niederberger, *Chemical mechanism of tungstite formation in benzyl alcohol studied by advanced QEXAFS technique*, Chem. Eur. J., DOI: 10.1002/chem.201101514 (2012).

[Ove98] H. Over, *Crystallographic study of interaction between adspecies on metal surfaces*, Prog. Surf. Sci. **58**, 249 (1998).

[Ozk97] U. S. Ozkan, M. W. Kumthekar and G. Karakas, *Self-sustained oscillatory behavior of $NO+CH_4+O_2$ reaction over titania-supported Pd catalysts*, J. Catal. **171**, 67 (1997).

[Par11] J. K. Park, K. H. Lee, J. S. Park, J. H. Seo, Y. K. Kim and S. S. Yoon, *Highly efficient blue light-emitting diodes based on diarylanthracene/triphenylsilane compounds*, J. Nanosci. Nanotechnol. **11**, 4357 (2011).

[Par54] L. G. Parratt, *Surface studies of solids by total reflection of X-rays*, Phys. Rev. **95**, 359 (1954).

[Pau11] Paul Scherrer Institut, *SuperXAS - X10DA*, http://www.psi.ch/sls/superxas/superxas (2011).

[Pic00] D. M. Pickup, G. Mountjoy, M. A. Holland, G. W. Wallidge, R. J. Newport and M. E. Smith, *In situ EXAFS and XANES measurements of the change in Ti coordination during the calcination of a $(TiO_2)_{0.18}(SiO_2)_{0.82}$ aerogel*, J. Phys. Condens. Matter **12**, 9751 (2000).

[Pop03] P. Popíšil, M. Haumann, J. Dittmer, V. A. Solé and H. Dau, *Stepwise transition of the tetra-manganese complex of photosystem II to a binuclear $Mn_2(\mu\text{-}O)_2$ complex in response to a temperature jump: A time-resolved structural investigation employing X-ray absorption spectroscopy*, Biophys. J. **84**, 1370 (2003).

[Ram11] M. Ramirez, L. Henneken and S. Virtanen, *Oxidation kinetics of thin copper films and wetting behaviour of copper and Organic Solderability Preservatives (OSP) with lead-free solder*, Appl. Surf. Sci. **257**, 6481 (2011).

[Rav05] B. Ravel and M. Newville, *ATHENA, ARTEMIS, HEPHAESTUS: Data analysis for X-ray absorption spectroscopy using IFEFFIT*, J. Synchrotron Rad. **12**, 537 (2005).

[Rec98] V. Recupero, L. Pino, R. Di Leonardo, M. Lagana and G. Maggio, *Hydrogen generator, via catalytic partial oxidation of methane for fuel cells*, J. Power Sources **71**, 208 (1998).

[Ree00] M. T. Reetz and E. Westermann, *Phosphane-free palladium-catalyzed coupling reactions: The decisive role of Pd nanoparticles*, Angew. Chem. Int. Ed. **39**, 165 (2000).

[Reh86] J. J. Rehr, R. C. Albers, C. R. Natoli and E. A. Stern, *New high-energy approximation for X-ray absorption near-edge structure*, Phys. Rev. B **34**, 4350 (1986).

[Reh90] J. J. Rehr and R. C. Albers, *Scattering-matrix formulation of curved-wave multiple-scattering theory: Application to X-ray absorption fine structure*, Phys. Rev. B **41**, 8139 (1990).

[Reh91] J. J. Rehr, J. Mustre de Leon, S. I. Zabinsky and R. C. Albers, *Theoretical X-ray absorption fine structure standards*, J. Am. Chem. Soc. **113**, 5135 (1991).

[Reh92] J. J. Rehr, S. I. Zabinsky and R. C. Albers, *High-order multiple-scattering calculations of X-ray absorption fine structure*, Phys. Rev. Lett. **69**, 3397 (1992).

[Reh00] J. J. Rehr and R. C. Albers, *Theoretical approaches to X-ray absorption fine structure*, Rev. Mod. Phys. **72**, 621 (2000).

[Rei10] S. Reimann, J.-D. Grunwaldt, T. Mallat and A. Baiker, *Asymmetric CC bond-formation reaction with Pd: How to favor heterogeneous or homogeneous catalysis?*, Chem. Eur. J. **16**, 9658 (2010).

[Rei11] S. Reimann, J. Stötzel, R. Frahm, W. Kleist, J.-D. Grunwaldt and A. Baiker, *Identification of the active species generated from supported Pd catalysts in Heck reactions: An in situ quick scanning EXAFS investigation*, J. Am. Chem. Soc. **133**, 3921 (2011).

[Ren07] Renishaw, *RGH25U UHV, RGH25F UHV, RGH20F UHV – Ultra high vacuum compatible readhead systems*, Data sheet L-9517-9164-03-B (2007).

[Res97] T. Ressler, M. Hagelstein, U. Hatje and W. Metz, *In situ X-ray absorption spectroscopy studies on chemical oscillations in the CO/O_2 system on supported Pd catalysts*, J. Phys. Chem. B **101**, 6680 (1997).

[Res98] T. Ressler, *WinXAS: A program for X-ray absorption spectroscopy data analysis under MS-Windows*, J. Synchrotron Rad. **5**, 118 (1998).

[Reu03a] K. Reuter and M. Scheffler, *First-principles atomistic thermodynamics for oxidation catalysis: Surface phase diagrams and catalytically interesting regions*, Phys. Rev. Lett. **90**, 046103 (2003).

[Reu03b] K. Reuter and M. Scheffler, *Composition and structure of the RuO_2(110) surface in an O_2 and CO environment: Implications for the catalytic formation of CO_2*, Phys. Rev. B **68**, 045407 (2003).

[Ric01] M. Richwin, R. Zaeper, D. Lützenkirchen-Hecht and R. Frahm, *Piezo-QEXAFS: Advances in time-resolved X-ray absorption spectroscopy*, J. Synchrotron Rad. **8**, 354 (2001).

[Ric02] M. Richwin, R. Zaeper, D. Lützenkirchen-Hecht and R. Frahm, *Piezo-XAFS time-resolved X-ray absorption spectroscopy*, Rev. Sci. Instrum. **73**, 1668 (2002).

[Ric03] M. Richwin, *Entwicklung und Anwendung neuer Verfahren zur zeitaufgelösten Röntgenabsorptionsspektroskopie mit Synchrotronstrahlung*, Bergische Universität Wuppertal, doctoral thesis (2003).

[Rui03] R. Ruiz, B. Nickel, N. Koch, L. C. Feldman, R. F. Haglund, A. Kahn, F. Family and G. Scoles, *Dynamic scaling, island size distribution, and morphology in the aggregation regime of submonolayer pentacene films*, Phys. Rev. Lett. **91**, 136102 (2003).

[Sal82] B. C. Sales, J. E. Turner and M. B. Maple, *Oscillatory oxidation of CO over Pt, Pd and Ir catalysts: Theory*, Surf. Sci. **114**, 381 (1982).

[Sal88] E. B. Saloman, J. H. Hubbell and J. H. Scofield, *X-ray attenuation cross sections for energies 100 eV to 100 keV and elements Z = 1 to Z = 92*, At Data Nucl. Data Tables **38**, 1 (1988).

[San04] M. Sanchez del Rio and R. J. Dejus, *XOP 2.11*, http://www.esrf.eu/computing/scientific/xop2.1/ (2004).

[San86] L. M. Sander, *Fractal growth processes*, Nature **322**, 789 (1986).

[Sap00] A. V. Sapelkin, S. C. Bayliss, D. Russell, S. M. Clark and A. Dent, *In situ EXAFS, X-ray diffraction and photoluminescence for high-pressure studies*, J. Synchrotron Rad. **7**, 257 (2000).

[Say71] D. E. Sayers, E. A. Stern and F. W. Lytle, *New technique for investigating noncrystalline structures: Fourier analysis of the extended X-Ray absorption fine structure*, Phys. Rev. Lett. **27**, 1204 (1971).

[Sch03b] R. Schlögl, *Katalytische Ammoniaksynthese – eine "unendliche Geschichte"?*, Angew. Chem. **115**, 2050 (2003).

[Sch03a] C. G. Schroer, M. Kuhlmann, T. F. Günzler, B. Lengeler, M. Richwin, B. Griesebock, D. Lützenkirchen-Hecht, R. Frahm, E. Ziegler, A. Mashayekhi, D. R. Haeffner, J.-D. Grunwaldt and A. Baiker, *Mapping the chemical states of an element inside a sample using tomographic X-ray absorption spectroscopy*, Appl. Phys. Lett. **82**, 3360 (2003).

[Sch93] F. Schüth, B. E. Henry and L. D. Schmidt, *Oscillatory reactions in heterogeneous catalysis*, Adv. Catal. **39**, 51 (1993).

[Sea85] M. P. Seah and M. Kühlein, *Temperature, roughness and depth resolution in ion sputter profiles*, Surf. Sci. **150**, 273 (1985).

[Sil09] G. Silversmit, H. Poelman, V. Balcaen, P. M. Heynderickx, M. Olea, S. Nikitenko, W. Bras, P. F. Smet, D. Poelman, R. de Gryse, M.-F. Reniers and G. B. Marin, *In-situ XAS study on the Cu and Ce local structural changes in a $CuO–CeO_2/Al_2O_3$ catalyst under propane reduction and re-oxidation*, J. Phys. Chem. Solids **70**, 1274 (2009).

[Sin08] J. Singh, E. M. C. Alayon, M. Tromp, O. V. Safonova, P. Glatzel, M. Nachtegaal, R. Frahm and J. A. van Bokhoven, *Generating highly active partially oxidized platinum during oxidation of carbon monoxide over Pt/Al_2O_3: In situ, time-resolved, and high-energy-resolution X-ray absorption spectroscopy*, Angew. Chem. Int. Ed. **47**, 9260 (2008).

[Sin10] J. Singh, M. Nachtegaal, E. M. C. Alayon, J. Stötzel and J. A. van Bokhoven, *Dynamic structure changes of a heterogeneous catalyst within a reactor: Oscillations in CO oxidation over a supported platinum catalyst*, ChemCatChem **2**, 653 (2010).

[Sit93] B. Sitar, G. I. Merson, V. A. Chechin and Y. A. Budagov, *Ionization measurements in high energy physics*, Berlin, Germany, Springer tracts in modern physics 124 (1993).

[Sli94] M. M. Slin'ko and N. I. Jaeger, *Oscillating heterogeneous catalytic systems*, Amsterdam, Netherlands, Elsevier (1994).

[Smi02] L. I. Smith, *Department of Computer Science - University of Otago*, http://www.cs.otago.ac.nz/cosc453/student_tutorials/principal_components.pdf (2002).

[Sta02] C. Stampfl, M. V. Ganduglia-Pirovano, K. Reuter and M. Scheffler, *Catalysis and corrosion: The theoretical surface-science context*, Surf. Sci. **500**, 368 (2002).

[Stö08a] J. Stötzel, *Entwicklung und Charakterisierung neuer Konzepte der zeitaufgelösten Röntgenabsorptionsspektroskopie*, Bergische Universität Wuppertal, diploma thesis (2008).

[Stö08b] J. Stötzel, D. Lützenkirchen-Hecht, E. Fonda, N. de Oliveira, V. Briois and R. Frahm, *Novel angular encoder for a quick-extended X-ray absorption fine structure monochromator*, Rev. Sci. Instrum. **79**, 083107 (2008).

[Stö09a] J. Stötzel, D. Lützenkirchen-Hecht, R. Frahm, B. Kimmerle, A. Baiker, M. Nachtegaal, M. J. Beier and J.-D. Grunwaldt, *Reduction and re-oxidation of Cu/Al_2O_3 catalysts investigated with quick-scanning XANES and EXAFS*, J. Phys. Conf. Ser. **190**, 012153 (2009).

[Stö09b] J. Stötzel, D. Lützenkirchen-Hecht, R. Frahm, B. Kimmerle, A. Baiker, M. Nachtegaal, M. J. Beier and J.-D. Grunwaldt, *Investigation of the ignition behaviour of the noble metal catalyzed catalytic partial oxidation of methane*, J. Phys. Conf. Ser. **190**, 012162 (2009).

[Stö10a] J. Stötzel, D. Lützenkirchen-Hecht and R. Frahm, *A new flexible monochromator setup for quick scanning X-ray absorption spectroscopy*, Rev. Sci. Instrum. **81**, 073109 (2010).

[Stö10b] J. Stötzel, D. Lützenkirchen-Hecht, R. Frahm, C. V. Santilli, S. H. Pulcinelli, R. Kaminski, E. Fonda, F. Villain and V. Briois, *QEXAFS and UV/vis simultaneous monitoring of the TiO_2-nanoparticles formation by hydrolytic sol-gel route*, J. Phys. Chem. C **114**, 6228 (2010).

[Stö11] J. Stötzel, D. Lützenkirchen-Hecht and R. Frahm, *A new stand-alone QEXAFS data acquisition system for in situ studies*, J. Synchrotron Rad. **18**, 165 (2011).

[Stö12a] J. Stötzel, R. Frahm, B. Kimmerle, M. Nachtegaal and J.-D. Grunwaldt, *Oscillatory behavior during the catalytic partial oxidation of methane: Following dynamic structural changes of palladium using the QEXAFS technique*, J. Phys. Chem. C **116**, 599 (2012).

[Stö12b] J. Stötzel, D. Lützenkirchen-Hecht and R. Frahm, *T-REX - New software for advanced QEXAFS data analysis*, J. Synchrotron Rad., submitted (2012).

[Str05] R. Strobel, J.-D. Grunwaldt, A. Camenzind, S. E. Pratsinis and A. Baiker, *Flame-made alumina supported Pd–Pt nanoparticles: Structural properties and catalytic behavior in methane combustion*, Catal. Lett. **104**, 9 (2005).

[Sur01] S. Surnev, G. Kresse, M. G. Ramsey and F. P. Netzer, *Novel interface-mediated metastable oxide phases: Vanadium oxides on Pd(111)*, Phys. Rev. Lett. **87**, 086102 (2001).

[Szm78] F. Szmulowicz and D. M. Pease, *Augmented-plane-wave calculation and measurements of K and L X-ray spectra for solid Ni*, Phys. Rev. B **17**, 3341 (1978).

[Teo86] B. K. Teo, *EXAFS: Basic principles and data analysis*, Berlin, Heidelberg, New York, Tokyo, Springer (1986).

[Tho09] A. Thompson and D. Vaughan, *X-ray Data Booklet*, 3rd ed., Berkeley, USA, Center of X-ray Optics and Advanced Light, University of California (2009).

[Tho74] J. A. Thornton, *Influence of apparatus geometry and deposition conditions on the structure and topography of thick sputtered coatings*, J. Vac. Sci. Technol. **11**, 666 (1974).

[Ura06] A. Urakawa, T. Bürgi and A. Baiker, *Kinetic analysis using square-wave stimulation in modulation excitation spectroscopy: Mixing property of a flow-through PM-IRRAS cell*, Chem. Phys. **324**, 653 (2006).

[Ura08] A. Urakawa, T. Bürgi and A. Baiker, *Sensitivity enhancement and dynamic behavior analysis by modulation excitation spectroscopy: Principle and application in heterogeneous catalysis*, Chem. Eng. Sci. **63**, 4902 (2008).

[Ura11] A. Urakawa, W. van Beek, M. Monrabal-Capilla, J. R. Galán-Mascarós, L. Palin and M. Milanesio, *Combined, modulation enhanced X-ray powder diffraction and Raman spectroscopic study of structural transitions in the spin crossover material [Fe(Htrz)$_2$(trz)](BF$_4$)*, J. Phys. Chem. C **115**, 1323 (2011).

[Uru07] T. Uruga, H. Tanida, K. Inoue, H. Kamazaki and T. Irie, *Quick XAFS system using quasimonochromatic undulator radiation at SPring-8*, AIP Conf. Proc. **882**, 914 (2007).

[Vic48] J. A. Victoreen, *The absorption of incident quanta by atoms as defined by the mass ohotoelectric absorption coefficient and the mass scattering coefficient*, J. Appl. Phys. **19**, 855 (1948).

[Vog11] W. Vogel, *Interaction of a nanosized Pd catalyst with active C from the carbon support: An advanced in situ XRD study*, J. Phys. Chem. C **115**, 1506 (2011).

[Vol26] M. Volmer and A. Weber, *Keimbildung in übersättigten Gebilden*, Z. Phys. Chem. **119**, 277 (1926).

[Wag33] C. Wagner, *Beitrag zur Theorie des Anlaufvorgangs*, Z. Phys. Chem. B. **21**, 25 (1933).

[Wan08] Q. Wang, J. C. Hanson and A. I. Frenkel, *Solving the structure of reaction intermediates by time-resolved synchrotron X-ray absorption spectroscopy*, J. Chem. Phys. **129**, 234502 (2008).

[War91] B. E. Warren, *X-Ray Diffraction*, New York, USA, Dover Publications (1991).

[Was53] J. Waser, H. A. Levy and S. W. Peterson, *The structure of PdO*, Acta Crystallogr. **6**, 661 (1953).

[Wen04] A. Wendemuth, *Grundlagen der digitalen Signalverarbeitung*, Berlin, Heidelberg, Germany, Springer (2004).

[Wil96] K. Wille, *Physik der Teilchenbeschleuniger und Synchrotronstrahlungsquellen*, 2nd ed., Stuttgart, Germany, B. G. Teubner (1996).

[Wil04] P. R. Willmott, *Deposition of complex multielemental thin films*, Prog. Surf. Sci. **76**, 163 (2004).

[Yan98] J. C. Yang, B. Kolasa and J. M. Gibson, *Self-limiting oxidation of copper*, Appl. Phys. Lett. **73**, 2841 (1998).

[Yev10] A. Yevick and A. I. Frenkel, *Effects of surface disorder on EXAFS modeling of metallic clusters*, Phys. Rev. B **81**, 115451 (2010).

[Yon63] Y. Yoneda, *Anomalous surface reflection of X-rays*, Phys. Rev. **131**, 2010 (1963).

[Zab95] S. I. Zabinsky, J. J. Rehr, A. Ankudinov, R. C. Albers and M. J. Eller, *Multiple-scattering calculations of X-ray absorption spectra*, Phys. Rev. B **52**, 2995 (1995).

[Zam96] T. Zambelli, J. Wintterlin, J. Trost and G. Ertl, *Identification of the "Active Sites" of a surface-catalyzed reaction*, Science **273**, 1688 (1996).

[Zha03] X. Zhang, C. S.-M. Lee, D. M. P. Mingos and D. O. Hayward, *Oscillatory behaviour during the oxidation of methane over palladium metal catalysts*, Appl. Catal. A **240**, 183 (2003).

[Zha05] X. Zhang, C. S.-M. Lee, D. O. Hayward and D. M. P. Mingos, *Oscillatory behaviour observed in the rate of oxidation of methane over metal catalysts*, Catal. Today **105**, 283 (2005).

[Zha09] J. Zhao, X. W. Sun and S. T. Tan, *Bandgap-engineered Ga-rich GaZnO thin films for UV transparent electronics*, IEEE Trans. Electron Devices **56**, 2995 (2009).

[Zhd99] V. P. Zhdanov, *Surface restructuring and kinetic oscillations in heterogeneous catalytic reactions*, Phys. Rev. E **60**, 7554 (1999).

[Zhd02] V. P. Zhdanov, *Impact of surface science on the understanding of kinetics of heterogeneous catalytic reactions*, Surf. Sci. **500**, 966 (2002).

[Zho09] C. Zhong, Y. M. Jiang, D. M. Sun, J. Gong, B. Deng, S. Cao and J. Li, *Oxidation kinetics of nanoscale copper thin films at low temperature characterized by sheet resistance and optical transmittance*, Chin. J. Phys. **47**, 253 (2009).

[Zho10a] Y. Zhou, J.-D. Grunwaldt, F. Krumeich, K. Zheng, G. Chen, J. Stötzel, R. Frahm and G. R. Patzke, *Hydrothermal synthesis of $Bi_6S_2O_{15}$ nanowires: Structural, in situ EXAFS, and humidity-sensing studies*, Small **6**, 1173 (2010).

[Zho10b] G. Zhou, *Nucleation-induced kinetic hindrance to the oxide formation during the initial oxidation of metals*, Phys. Rev. B **81**, 195440 (2010).

[Zhu07] Y.-L. Zhu, L.-S. Wang, Q. Li and Y.-G. Wei, *Bis(tetrabutylammonium) di-μ-bromido-bis[dibromidopalladate(II)]*, Acta Cryst. E **63**, m1004 (2007).

Acknowledgements

I thank Prof. Dr. Ronald Frahm for providing me the topic for this dissertation and the opportunity to write it in his working group. His support during the last years was an invaluable help not only due to the many fruitful discussions, but also due to the granted freedom and confidence. These were crucial parameters for the steady progress of this work and created a comfortable as well as productive working atmosphere.

Moreover, I thank Prof. Dr. Jan-Dierk Grunwaldt for being second referee and for the fantastic collaboration work during the last three years. Without his commitment and motivation in the field of catalysis research with QEXAFS it would neither have been possible to present that many application examples, nor to develop the various presented data analysis tools.

Furthermore, I thank Dr. Dirk Lützenkirchen-Hecht for his always amicable and unselfish support, especially in the context of the presented ReflEXAFS experiments. Actual and former members of the group also contributed to this work with their support during the various beamtimes and also in the home laboratories. Benjamin Bornmann, Jan Gasse, Uli Haake, Justus Just, Daniel Krämer, Christian Markert, Oliver Müller, Stefanie Pfleiderer, Dr. Clemens Ringpfeil, Jakob Schmidtke, Sebastian Szillat, Ralph Wagner and Iwona Wüster are acknowledged for their invaluable help. Furthermore, the working shop of the Bergische Universität Wuppertal is acknowledged for discussing and constructing the various parts of the herein presented construction designs.

Various applications presented or cited in this dissertation are the result of collaborative work with people from various working groups. With the complementary scientific backgrounds of these collaborations it was possible to perform experiments in a very efficient way and to carry out a proper analysis of the results. In this context I thank Prof. Dr. Alfons Baiker, Dr. Bertram Kimmerle, Dr. Sven Reimann, Dr. Wolfgang Kleist, Dr. Matthias Bauer, Alexey Boubnov, Matthias Beier, Prof. Dr. Jeroen van Bokhoven, Jagdeep

Singh, Prof. Dr. Markus Niederberger, Dr. Dorota Koziej, Inga Olliges-Stadler, Prof. Dr. Greta R. Patzke and Ying Zhou for the interesting experiments and all the enlightening discussions.

For extra beamtimes at the SLS special thanks go to Dr. Maarten Nachtegaal, who significantly supported the developments presented in this work with his enthusiasm towards all progress in QEXAFS. In this context, thanks appertain also to Dr. Messaoud Harfouche, Markus Willimann and all further members at the SLS for their support during the many beamtimes at the SuperXAS beamline. Special thanks go to Dr. Uwe Flechsig, who provided us beamtime at the Optics Beamline of the SLS, which was invaluable to evaluate the new monochromator mechanics, and to Andreas Jaggi for his support during this beamtime. For his support during experiments at the BW1 beamline at DESY I thank Dr. Dmitri Novikov.

Last but not least, I am indebted to my parents and Sabrina Schmidt, who patiently accompanied me during the last years. Their support and love were a decisive and irreplaceable contribution to this work.